2020

Electrokinetic focusing of charged and neutral species for bioanalytical applications

Beatrise Berzina
Iowa State University

Recommended Citation

Berzina, Beatrise, "Electrokinetic focusing of charged and neutral species for bioanalytical applications" (2020). *Graduate Theses and Dissertations*. 18097.
https://lib.dr.iastate.edu/etd/18097

Electrokinetic focusing of charged and neutral species for bioanalytical applications

by

Beatrise Berzina

A dissertation submitted to the graduate faculty

in partial fulfillment of the requirements for the degree of

DOCTOR OF PHILOSOPHY

Major: Analytical Chemistry

Program of Study Committee:
Robbyn Anand, Major Professor
Jared Anderson
Young-Jin Lee
Nicole Hashemi
Emily Smith

The student author, whose presentation of the scholarship herein was approved by the program of study committee, is solely responsible for the content of this dissertation. The Graduate College will ensure this dissertation is globally accessible and will not permit alterations after a degree is conferred.

Iowa State University

Ames, Iowa

2020

DEDICATION

Maniem mīļajiem.

To my loved ones.

TABLE OF CONTENTS

Page

ACKNOWLEDGMENTS vi

ABSTRACT.. viii

CHAPTER 1. GENERAL INTRODUCTION 1
  Electrokinetics 3
  Governing equations describing ionic species transport 5
  Continuous electrokinetic focusing for rapid and sensitive analysis of low abundance analytes in point-of-care testing 7
  Electrokinetic spent dialysate recycler for portable/wearable peritoneal dialysis..................... 9
  Organization of the dissertation.. 11

CHAPTER 2. TUTORIAL REVIEW: ENRICHMENT AND SEPARATION OF CHARGED AND NEUTRAL SPECIES BY ION CONCENTRATION POLARIZATION FOCUSING......13
  Abstract.. 13
  Introduction 14
  Fundamental aspects of ICP 17
    Mechanism of ICP.. 18
    Mechanism of faradaic ICP.. 21
    Electric and flow fields that drive ICPF... 24
    Secondary EOF or vortex flow... 31
    Propagation of the IDZ boundary... 35
    Spatiotemporal pH dynamics near ion selective membranes and electrodes during ICP.. 38
  Practical aspects of implementing ICP-based techniques 41
    Device design and fabrication methods.. 41
    Ion selective features and their fabrication... 47
    Sample composition 52
    Analyte encapsulation following ICPF 56
    In-droplet ICP... 58
    Multistage and high throughput preconcentration.. 60
  Integration of other analytical methods with ICPF 63
    Immunoassay.. 63
    Enzymatic assay 64
    Electrochemical sensing.. 64
    The ICP current-voltage curve as a non-optical sensor... 67
  Summary of tips and tricks.. 69
  Conclusions and future outlook.. 69
  References 72

CHAPTER 3. AN ELECTROKINETIC SEPARATION ROUTE TO SOURCE DIALYSATE FROM EXCESS FLUID IN BLOOD 91
Abstract 91
Introduction 91
Experimental section 95
Chemicals 95
Device Fabrication 96
Ion Concentration Polarization 96
Fluorescence Measurements 97
Results and discussion 97
ICP-Based Separation of Albumin from a Neutral Dye in Model Blood Plasma 97
ICP-Based Separation in Blood Plasma 98
Development of an Enhanced Scheme for Separation in Blood Plasma 100
Evaluation of Device Lifetime 102
Influence of Flow Rate and Voltage on Separation Efficiency 103
Evaluation of the Output of the Neutral Stream 104
Summary and conclusions 106
References 107
Supporting information 109

CHAPTER 4. CONTINUOUS MICELLAR ELECTROKINETIC FOCUSING OF NEUTRAL SPECIES BY ION CONCENTRATION POLARIZATION 119
Abstract 119
Introduction 119
Materials and methods 123
Chemicals 123
Device fabrication 123
Electrokinetic separation experiments 124
Fluorescence measurements 124
Results and discussion 125
Response of neutral species to ICP in the absence of surfactants 125
Surfactant influence on the extraction of neutral compounds by ICP 126
Influence of neutral species concentration on extraction efficiency 127
Local formation of micelles by enrichment of surfactant 129
Conclusions 134
References 135
Supporting information 137
References 151

CHAPTER 5. ENRICHMENT OF CHARGED SPECIES BY OUT OF PLANE FARADAIC ION CONCENTRATION POLARIZATION 152
Abstract 152
Introduction 153
Results and discussion 159
Mechanism of faradaic ion concentration polarization 159
3D structures for fICP 163
Comparison of current transients and CVCs for the three device architectures 165

        Enrichment of charged species under constant flow 166
        Scalability of the PSC/Ag/Au device 168
        Electrokinetic enrichment of nucleic acids. 169
    Conclusions 171
    References 172
    Supporting Information 178
    References 190

CHAPTER 6. GENERAL CONCLUSIONS..191

REFERENCES 194

ACKNOWLEDGMENTS

I would like to thank my committee chair and mentor, Dr. Robbyn Anand, for entrusting me with exciting yet challenging projects, and giving me guidance, encouragement, and support throughout my graduate career. Further, I would like to thank my committee members, Drs. Jared Anderson, Young-Jin Lee, Nicole Hashemi, and Emily Smith, for their guidance and support throughout the course of this research. In addition, I would like to thank my colleagues, Anand research group members, the department faculty, and staff for making my time at Iowa State University a wonderful experience.

I would like to acknowledge several funding agencies and donor families that supported the course of this research, curriculum development and travel to conferences. Work summarized in this dissertation was supported by the Fulbright Fellowship, American Chemical Society (ACS) Division of Analytical Chemistry (DAC) and the Society for Analytical Chemists of Pittsburgh (SACP) Graduate Fellowship, NSF CAREER grant, Mary K. and Velmer A. Fassel Fellowship, Mary Helen Merriam Stewart Scholarship, and GPSS and Fassel travel grants.

Additionally, I would like to extend my heartful gratitude to my previous mentors, Drs. Ilga Mutule and Edgars Suna,at the University of Latvia and the Latvian Institute of Organic Synthesis, who were the first to introduce me and guide me towards a researcher path. I would also like to thank my colleagues and friends, Drs. Eduards Bakis, Matiss Reinfelds, Toms Rekis, and Kaspars Leduskrasts, for their support and late-night scientific discussions.

Lastly, I would like to thank my family and friends for their continuous encouragement. Thanks to ED, EV, KD, MG, MM, MS, SP and RR for reminding me about the world outside the lab. Finally, thanks to my brothers, my sisters in law, and my biggest cheerleaders, my parents

Dace and Janis. And to Jeff, thank you for the patience and love throughout this adventure.

Without any of you this would not be possible.

ABSTRACT

Despite the continuous advancement of analytical techniques, low analyte concentration, limited sample volume, and complexity of matrices still present major challenges in clinical, bioanalytical, and environmental sample preparation and separation. The need for improved limits of detection (LOD), specificity, and decreased analysis time are the main challenges that drive the development of new technologies.

For the past few decades, microfluidic platforms have enabled the development of high impact technologies, such as wearable devices for diabetes and for chronic heart disease management. Microfluidic or lab-on-chip devices can be integrated with fluidic structures, electrodes, and chemically-modified surfaces to confer several distinct advantages including efficient handling of small volumes, rapid analysis, and access to surface-driven physical phenomena such as electrokinetics. Electrokinetic forces are ideal for manipulating transport of charged species, e.g., nucleic acids, proteins, and cells, which are often used as important biomarkers for disease diagnosis.

Ion concentration polarization (ICP) is an electrokinetic phenomenon that occurs due to a simultaneous enrichment and depletion of ions at opposing ends of an ion permselective structure, ether a membrane (ICP) or an electrode (faradaic ICP, fICP), when an electrical field is applied across it. A locally enhanced electric field forms within the ion depleted region due to low ionic conductivity. The sharp spatial variation in background electrolyte concentration at the boundary of this region results in a steep electric gradient that has been employed for enrichment and separation of charged species for analysis, mainly in simple media (buffer solutions).

Despite recent advancements in ICP and fICP, a few challenges remain. For example, focusing of neutral (uncharged) species, application of ICP in highly conductive or complex

media (e.g., biological fluids), development of strategies to decrease fluidic instability in the high electric field zone, improvement of volumetric throughput, and integration with downstream analysis are all active areas of research.

The objectives of this dissertation address the current limitations of ICP by developing 1) ICP-based methods for chemical separations in biological fluids, 2) methods for the separation and enrichment of neutral (uncharged) species, 3) fundamental strategies to increase the stability of ICP, thereby allowing for increased device throughput, and 4) a platform that can be integrated with downstream analysis for low abundance analyte detection in POC settings. The outcome of this work will be broader application of ICP for the analysis of a wide range of biological species, especially for point-of-need applications.

CHAPTER 1. GENERAL INTRODUCTION

Analysis of samples with complex matrices (e.g., biological fluids and environmental samples) is still one of the main challenges in analytical chemistry due to interfering compounds and time-consuming sample preparation. The goals for new analytical method development are to scale down sample sizes, decrease sample matrix effects, and increase sensitivity, all while obtaining a fast response. Various electric field-assisted extraction and separation techniques have been developed to address these challenges, and one of the main benefits of employing electric field techniques is the ease of their integration and implementation with lab-on-chip (LOC) devices.

Electric field-assisted extraction techniques can be separated into liquid-, solid-, and membrane-based.[1,2] Application of an electric field has been shown to improve the efficiencies of membrane-based techniques, such as electrodialysis,[3] electrokinetic membrane extraction,[4] and electrofiltration.[5] However, membrane degradation and bubble formation are common when a strong electric field is applied.[6] Electric field-assisted liquid extractions are based on enhancing analyte dispersion, or by transporting charged species across a phase boundary between two immiscible liquids (e.g., aqueous solution-organic solvent, or electrolyte-electrolyte phases).[7] Use of an electric field in solid-phase extraction (SPE) and solid-phase microextraction (SPME) has opened new avenues of synthesis and fine-tuning of sorbents materials (e.g., thickness, morphology, conductivity), as well as enhancing the extraction efficiency. Extraction efficiency is improved by electrokinetic migration of analytes towards the solid phase or facilitating the desorption of the analyte by altering the potential of conductive polymer-coated electrodes.[2,8,9]

Electric field-based separations like capillary electrophoresis (CE),[10] capillary electrochromatography (CEC),[11] microfluidic chip-based electrophoresis,[12] and electrochromatography[13] have been known for decades. However, poor sensitivity has been one of the main limitations of these electrophoretic separation techniques. Several preconcentration or analyte stacking approaches have been developed to address this limitation and improve the sensitivity by several orders of magnitude.[14]

On-chip electrokinetic preconcentration techniques such as field amplified sample stacking (FASS),[15] isotachophoresis (ITP),[16] isoelectric focusing (IEF),[17] and electric field gradient focusing (EFGF)[18] have been developed for analyte preconcentration and separation to improve the limits of detection of low abundance analytes. All of these electrokinetic techniques are able to achieve focusing of analyte bands at defined spatial locations along the electric field based on background electrolyte (BGE) and analyte electrophoretic properties.[19] For example, the migration velocity of charged analytes in an electric field gradient is dependent on the electrophoretic mobility of the species employed. In the presence of a constant opposing force, like hydrodynamic flow, analytes are enriched at a specific location along the channel where electrophoretic and convective forces are equal, but opposite. In this way, because a field gradient is used rather than a constant electric field, both the enrichment and separation of analytes with different mobilities is achieved.[20]

Ion concentration polarization (ICP) is one of the most recently developed electrokinetic approaches for enrichment and separation of charged species. It perpetually generates and maintains a steep electric field gradient that is caused by a gradient in BGE concentration. Further, it allows for a constant supply of analyte to the stacking location. These features improve the preconcentration factor for low abundance analytes such as biomarkers (proteins, DNA), for which relevant concentrations may be atto- to nano- molar.[21] The gradient in BGE concentration is achieved via selective ion transport through a membrane,[22] or via an electron transfer reaction involving ions of the BGE at the electrode (faradaic ICP, fICP), when an electric field is applied.[23–25] In this dissertation, ICP and fICP are each employed to demonstrate electrokinetic focusing of both charged and uncharged species, while tackling major limitations important to the successful analysis of bioanalytical samples.

More detailed information on fundamental mechanisms underpinning the ICP and fICP phenomena, a summary of recent advancements and new applications, and a list of practical tips and tricks are summarized in Chapter 2 of this dissertation. To fully interpret this information, a few basic principles of electrokinetics (electroosmosis and electrophoresis), and governing equations of ionic species transport, especially in the context of microfluidics, are summarized in further paragraphs as this information is not included in Chapter 2. Lastly, two major applications of electrokinetic flow focusing, as well as the motivation of this dissertation, are included in this chapter.

Electrokinetics

Electrokinetic effects include the transport of liquid (electroosmosis) and charged analytes (electrophoresis) in response to an electric field, among other phenomena. Electroosmotic flow (EOF) originates in the electrical double layer (EDL) formed at a solid-liquid interface, in which the solid has a net surface charge (Figure 1). The EDL thickness can vary from a few to tens of nanometers depending on the ionic strength of the bulk solution.[26,27]

If the surface is positively charged, there will be an excess of anions in the adjacent liquid (slipping plane). Once the electric field is applied, the excess anions will move, drawing the fluid along (EOF). The resulting fluid velocity increases from zero near the surface, due to a high shear rate, to bulk velocity at the edge of the EDL. The bulk electroosmotic velocity (v_{eo}) is proportional to the applied electric field (E_x) and can be described using electroosmotic mobility (μ_{eo}) which is a function of both surface and solution properties.

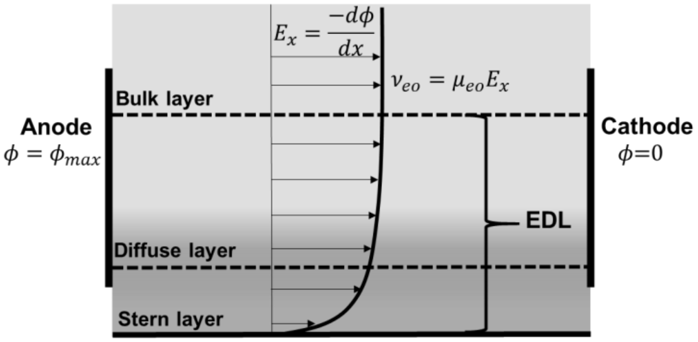

Figure 1. Illustration of the velocity profile of the EOF within an EDL formed near a solid surface positioned between an anode and cathode. Illustration reproduced from ref. [27].

The main disadvantage of the use of EOF is the need to apply a high electric field to generate significant flow velocity. Usually, μ_{eo} is in the range of 10^{-8} m^2 $V^{-1}s^{-1}$, and therefore, about 100 V applied over a 1.0 cm channel is required to reach a flow rate of 100 µm s^{-1}. Additionally, high electric field strength and current result in Joule heating which can lead to local changes in viscosity, and uneven thermal conditions within the microfluidic channels. Thus, although EOF has a lower flow resistance and plug-like velocity profile, pressure-driven flow is more commonly used in LOC applications.

Electrophoresis is a movement of charged species in a fluid under the influence of an applied electric field.[28] Electrophoresis is a valuable tool for transport of charged species, such as proteins and DNA. Under certain conditions, charged species can be separated based on their size or surface charge and zeta potential. The electrostatic force (F_{es}) acting on an ion depends not only its charge but also the electric field strength (E), such that $F_{es}=QE$, where Q is charge. The ion reaches its terminal velocity when the drag force exerted on it by the solution ($F_d=\xi v$) is equal in magnitude and opposite in sign to F_{es}. Here, ξ is the drag coefficient and v the velocity of the ion. Therefore, the electrophoretic velocity (v_{ep}) of an ion can be expressed as,

$$v_{ep} = QE/\xi \tag{1}$$

For a spherical species with hydrated radius a, in a solution with kinematic viscosity, η, ξ can be estimated by,

$$\xi = 6\pi\eta a \tag{2}$$

Each species is most appropriately characterized by its electrophoretic mobility (μ_{ep}) because it is constant relating the variables v_{ep} and E.

$$\mu_{ep} = v_{ep}/E = Q/6\pi\eta a \tag{3}$$

Owing to this relationship, multiple species with distinct μ_{ep} can be spatially separated in an electric field. In the context of electrokinetic focusing, these species will stack at distinct axial locations along an electric field gradient.

Governing equations describing ionic species transport

Modeling and simulation work has enabled researchers to forecast experimental results beforehand and explain the underlying physical mechanisms observed in experiments.[29] Additionally, a fundamental understanding of ionic species transport in various systems is needed to shift electrokinetic focusing from research, to a routine analysis platform.

There are two approaches employed when modeling flow and transport in micro-/nanochannels: the continuum and molecular models.[30] The molecular model or molecular dynamics (MD) has shown promising results when studying ionic transport and electroosmotic flow in nanochannels with a diameter of 3.5 nm or smaller.[31–33] However, due to the computational cost, MD is not applicable to simulate transport in channels larger than 10 nm, and therefore, the continuum model, that statistically averages molecular interactions, is used more often instead.[34–36] Continuum models describe fluidics and the distribution of species in the electrolyte using quantities, such as concentration ($c_{(x,t)}$) of a given species, which are continuous functions of space and time. The most relevant equations to the continuum models that describe ionic transport are the Nernst-Planck, Poisson, and Navier-Stokes equations.

The total ion flux of species *i* (j_i) can be described by the Nernst-Planck (NP) expression (eq. 4) that consists of three components – diffusion against a concentration gradient, migration of a charged species along a gradient in electrical potential, and convection due to a fluid flow.

$$j_i = -D_i \nabla c_i - \mu_i z_i F c_i \nabla \varphi + c_i v, \text{ where} \tag{4}$$

D_i is the diffusion coefficient, c_i the concentration, and z_i the valence of species *i*. *F* is Faraday's constant, μ_i is the ionic mobility, *v* is the velocity vector of the bulk flow, and φ is the electrical potential.

Potential, φ, is related to charge density through the Poisson equation:

$$\varepsilon_r \nabla^2 \varphi = -\rho_e / \varepsilon_0, \text{ where} \tag{5}$$

ε_r is the relative permittivity of the medium, ε_0 is the permittivity of vacuum, and ρ_e is the net charge density of ions. The net charge density of ions can be found using,

$$\rho_e = F \sum_{i=1}^{m} z_i c_i, \text{ where} \tag{6}$$

m is the total number of species in the system.

Electrokinetic fluid flow can be described by the Navier-Stokes equation:

$$\rho_0(\partial_t v + v \nabla v) = -\nabla p + \eta \nabla^2 v - \rho_e \nabla \varphi \text{ , where} \tag{7}$$

ρ_0 is density of water and *p* is the pressure.

Coupling of the Nernst-Planck, Poisson, and Navier-Stokes expressions by computational methods can provide insights into electric potential, ion concentration, velocity, and pressure profiles in the system, which in turn improves our fundamental understanding of electrokinetic transport in micro-/nanofluidic devices. Several reviews summarize advances in computational modeling of ICP.[37–39] Ultimately, a comprehensive model would provide valuable information that is critical for the design of microfluidic devices which can function as sensing, preconcentration, and separation devices in clinical and bioanalytical applications.

Continuous electrokinetic focusing for rapid and sensitive analysis of low abundance analytes in point-of-care testing

Point-of-care testing (POCT) detects analytes at the time and place of patient care, which improves access to accurate diagnosis, close monitoring, and timely management of various diseases.[40–42] It enables quick medical decisions, as the diseases can be diagnosed at a very early stage, leading to improved health outcomes for patients. Several POCT platforms, such as lateral flow assays, dipsticks, and microfluidics have been rapidly evolving over the past few decades. According to a Market&Market global forecast, the POCT market will reach USD 46.7 billion by 2024, which is doubled from USD 28.5 billion in 2019.[43] The SARS-CoV-2 pandemic that began in late 2019 is likely to increase that market further.

Microfluidic techniques enable development of new and high impact technologies from POC devices to the detection and manipulation of single entities like cells and molecules. Lab-on-chip (LOC) devices integrate fluidic structures with electrodes or chemically-modified surfaces possessing several distinct advantages including efficient handling of small volumes, rapid analysis, and access to surface-driven physical phenomena.

The detection of biomarkers for early diagnosis or prognosis of diseases is often challenging due to their extremely low abundance in biological fluids. It is especially important for POC devices that require development of an analysis platform sensitive enough to detect antigens, ssDNA, or viral RNA (e.g., SARS-CoV-2) natively found in the fM range. With a growing need for rapid detection of cancer, infectious and cardiovascular diseases, several on-chip electrokinetic preconcentration and separation techniques, such as ICP and dielectrophoresis, have been used to advance single-cell capture and analysis,[44–46] and enrichment, separation and quantification of both charged and neutral target species.[22,47–51]

By electrokinetically increasing the local concentration of the analyte, the sensitivity and rate of biological assays can be improved by several orders of magnitude. For example, ICP focusing has been used to enhance the sensitivity of multiplexed enzyme-linked immunosorbent assay (ELISA) for prostate cancer detection.[52] The sensitivity of this assay was improved by up to 100-fold by incorporating a preconcentration step. Similarly, Wang et al. demonstrated increased sensitivity of a bead bed immunoassay from 50 pM to sub-fM range for fluorescently tagged proteins.[53] Lee et al. demonstrated an increased enzymatic assay rate and decreased assay time from 1 h to 10 min along with a 100-fold enhancement of the sensitivity for trypsin (1.0 pg mL-1).[54] Likewise, ICP focusing (ICPF) was used to enhance an assay for kinase in cell lysate. The protocol yielded a 25-fold increase in reaction rate and a 65-fold enhancement in sensitivity.[55] However, most of these methods require the use of sensitive instrumentation for detection, mostly found only in research laboratories, as well as a high applied potential to drive ICP preconcentration (commonly, greater than 100 V).[22,56]

Electrochemical detection methods are sensitive and can be used as an alternative to spectroscopic methods. Hong et al. developed a valve-based microfluidic chip, in which methylated DNA (a promising biomarker for early diagnosis of cancer) was preconcentrated by ICP and then further quantified using a nanostructured gold biosensor. This microfluidic chip yielded 100- to 120-fold sample preconcentration in 10 min, which improved the LOD of methylated DNA from 475 pM to 350 fM in a buffer solution. Another appealing approach is to use ICP itself as a sensing mechanism. Senapati et al. demonstrated that the binding of charged molecules to the surface of an ion selective membrane causes a substantial shift in the current-voltage response of the preconcentrators.[57,58] Since then, this phenomenon has been used as a reporting mechanism for several surface-based assays for the detection of nucleic acids.[59,60]

In this dissertation, a POCT flow-through device with an in-line bead bed is developed to simultaneously drive fICP focusing and add specificity towards biomolecules. This approach allows for a reduction of required potential and an increase in the stability of the focused analyte plug. The applicability of this platform is demonstrated using the V600E mutant of the BRAF gene, but it can be modified for various applications and targets. The BRAF gene is important in signaling pathways responsible for cell growth, and mutation in this gene is known to lead to unchecked growth and spread of cancer cells. The V600E mutation can be found in melanoma and colorectal cancer, and therefore, checking for this mutation in tumor tissue or liquid biopsy may help with early diagnosis and planned treatment. More details about this platform can be found in Chapter 5 of this dissertation.

Electrokinetic spent dialysate recycler for portable/wearable peritoneal dialysis

According to the World Health Organization only 10% per year of those in need receive a kidney transplant.[61] While waiting, many patients require either peritoneal or hemodialysis several times per week. Between dialysis sessions, patients suffer from fluid retention and a gradual increase in blood concentration of excess salts and waste products, such as urea and creatinine. Short term effects of fluid retention include edema, shortness of breath, and rapid pulse. However, repeated episodes of fluid retention may cause permanent damage to the heart and lungs. As a result, cardiac failure is a leading cause of mortality in dialysis patients.[62] Increased dialysis dosage or continuous slow dialysis would potentially have a positive impact on therapy and improve prognosis for kidney disease patients.[63,64]

A recent breakthrough for continuous dialysis treatment is the development of the wearable artificial kidney (WAK), which is the first truly portable hemodialysis device.[65–67] The WAK is a system with all components attached to a belt (similar in size to a back brace), and was shown in its first clinical trials to successfully maintain blood components at healthy levels over a 24-hr period. Two similar systems for continuous peritoneal dialysis, the Vicenza wearable artificial kidney for peritoneal dialysis (ViWAK PD)[68] and automated wearable artificial kidney (AWAK),[69] were engineered to consume a reduced dialysate volume based on sorbent-assisted dialysate regeneration. In general, sorbent-assisted dialysate regeneration efficiency depends on specific and non-specific interactions between a composite material and waste products in the dialysate.[70–75] Despite these huge advancements, these systems suffer from biofouling, and still require a dialysate reservoir, which is heavy and cumbersome. Continuous dialysis systems, such as the WAK, utilize approximately 40 mL min^{-1}, thus requiring the wearer to carry liters of fluid.

To reduce the amount of sorbent, some research groups have developed electrochemical dialysate regeneration pathways.[76–79] Dialysate regeneration in these systems is based on the electrochemical oxidation of nitrogen-containing organic compounds, like urea and creatinine, to nitrogen and carbon dioxide. Although these systems sufficiently remove nitrogen-containing organic compounds and simplify the composition of spent dialysate, they still require sorbent cartridges (e.g., activated carbon) to remove other contaminants.

Several wearable devices and sensors, such as sensors for diabetes or for chronic heart disease management, have been developed using microfluidic platforms and are successfully implemented as diagnostic or therapeutic tools in patient care.[80–82] The Anand group is developing a membrane-free reservoir-free wearable hemodialysis device for patients with kidney disease. The aim is to reduce the excess fluid by sourcing and regenerating spent dialysate using a series of electrochemical and electrokinetic processes such as ion concentration polarization (ICP). Recently, Kim et al. reported preliminary findings regarding the performance of a nanoelectrokinetic purification device intended to be employed as a continuous peritoneal dialysate recycler.[83] In the recycler, regeneration is based on charged species separation by ICP, and urea removal by electrochemical oxidation. Although the small-scale device showed promising results for urea removal and for clearance of small charged species from the dialysate, the overall device performance was poor. Specifically, the efficiency with which waste species (charged and uncharged) were removed from the dialysate was low, especially upon scaling to a larger device and higher volumetric throughput. Furthermore, materials used to build the dialysate recycler are not FDA approved, and therefore could not be implemented in medical devices.

To be able to implement an electrokinetic approach to dialysate regeneration, several challenges have to be addressed, including the implementation of ICP in biological fluids, which are highly conductive and lead to biofouling, the mitigation of uncharged waste components, and the augmentation of volumetric throughput while decreasing the required voltage and power consumption. These challenges are either partially or fully addressed in this dissertation.

Organization of the dissertation

The second chapter surveys the main fundamental and experimental aspects of ICP and fICP that govern selective ion transport, generation and stability of a locally enriched analyte plug, changes in local pH resulting from redistribution of ions and faradaic reactions, as well as practical approaches for on- or off-chip analysis. Recent advancements that target challenges to broad implementation of ICP focusing are also reviewed. Lastly, a tutorial summary on practical aspects of ICP, such as, device fabrication, incorporation of ion selective features, encapsulation of analyte plugs post-enrichment, and quantification of the analyte are provided to aid new practitioners.

Chapter 3 introduces the electrokinetic route for separation of charged from neutral species in undiluted blood plasma by ICP. The reported method demonstrates the potential application of this approach for sourcing dialysate fluid from patients' blood plasma. Moreover, the same method can be used for the regeneration of spent dialysate.

Chapter 4 demonstrates recent advancements in continuous electrokinetic separation and enrichment of neutral compounds, previously not addressed by ICP. Continuous extraction of neutral compounds from aqueous solution was achieved by their partition into an ionic micellar phase.

Chapter 5 describes an approach to increase fluidic stability, decrease applied voltage, and improve the volumetric throughput of electrokinetic preconcentrators by employing out-of-plane fICP. It is believed that these results will enable a route for high-throughput enrichment and separation of biologically and clinically relevant samples. These same advancements are synergistic with the development of scalable devices for dialysate regeneration.

Finally, Chapter 6 summarizes the remaining challenges and future potential for broad application of ICP as a separation and analysis technique, such as for dialysate regeneration, or for the detection and quantification of disease markers in a liquid biopsy.

CHAPTER 2. TUTORIAL REVIEW: ENRICHMENT AND SEPARATION OF CHARGED AND NEUTRAL SPECIES BY ION CONCENTRATION POLARIZATION FOCUSING

Beatrise Berzina, Robbyn K. Anand

Iowa State University, Department of Chemistry

Modified from a manuscript published in *Analytica Chimica Acta*.

Abstract

Ion concentration polarization focusing (ICPF) is an electrokinetic technique, in which analytes are enriched and separated along a localized electric field gradient in the presence of a counter flow. This field gradient is generated by depletion of ions of the background electrolyte at an ion permselective junction. In this tutorial review, we summarize the fundamental principles and experimental parameters that govern selective ion transport and the stability of the enriched analyte plug. We also examine faradaic ICP (fICP), in which local ion concentration is modulated via electrochemical reactions as an attractive alternative to ICP that achieves similar performance with a decrease in both power consumption and Joule heating. The tutorial covers important challenges to the broad application of ICPF including undesired pH gradients, low volumetric throughput, samples that induce biofouling or are highly conductive, and limited approaches to on- or off- chip analysis. Recent developments in the field that seek to address these challenges are reviewed along with new approaches to maximize enrichment, focus uncharged analytes, and achieve enrichment and separation in water-in-oil droplets. For new practitioners, we discuss practical aspects of ICPF, such as strategies for device design and fabrication and the relative advantages of several types of ion selective junctions and electrodes. Lastly, we summarize tips and tricks for tackling common experimental challenges in ICPF.

Introduction

The demands of clinical, environmental, and pharmaceutical applications have long driven the advancement of analytical techniques towards improved limits of detection (LOD), greater specificity, and decreased analysis time. Despite these efforts, low analyte concentration, limited sample volume, and the complexity of matrices still present major challenges and motivate the development of more advanced sample preparation. Lab-on-a-chip (LOC) devices integrate micro- to nanoscale fluidic structures with electrodes or chemically-modified surfaces to confer several distinct advantages including efficient handling of small volumes, rapid analysis, and access to surface-driven physical phenomena. In this context, electrokinetic forces are ideal for performing fluidic operations and for manipulating charged species and/or biological objects such as DNA, proteins, and cells.[1] Due to these features, several miniaturized or on-chip electrokinetic preconcentration techniques such as electric field gradient focusing (EFGF),[2–6] field amplified sample stacking (FASS),[7] isoelectric focusing (IEF),[8] isotachophoresis (ITP),[9,10] dynamic field gradient focusing (DFGF),[2] and temperature gradient focusing (TGF)[11–13] have been developed for analyte preconcentration and/or separation. These methods share an ability to achieve an abrupt change in the velocity of the analyte at a defined spatial location along an electric field. For example, in ITP, charged analytes are introduced between leading and trailing electrolyte (LE and TE), which have co-ions of relative high and low mobility, respectively. The mismatch in mobilities dictates low and high electric field strengths in respective channel segments given the condition that continuity in ionic current must be maintained. Analytes are separated along this electric field gradient into discrete bands based on their electrophoretic mobilities. Importantly, the electrophoretic mobility of an analyte must be less than that of the co-ion of the LE and greater than that of a TE, and therefore, must be known in advance. Ion concentration polarization focusing (ICPF) is among the most recently developed of these techniques and is used for both analyte enrichment and separation. In ICPF, charged analytes are focused along a steep gradient in electric field strength in the presence of opposing fluid flow. ICPF allows for continuous sample supply and perpetually generates and maintains a steep gradient in background electrolyte (BGE) concentration, thus improving the preconcentration factor for low abundance analytes.[14]

Ion concentration polarization (ICP) is the simultaneous enrichment and depletion of ions at opposing ends of an ion permselective structure when an electrical field is applied across it. Leinweber and Tallarek were first to quantify ICP in a packed mesoporous bead bed in a capillary.[15] In microfluidic systems, Pu et al. showed the first reported visualization of CP near nanochannels and presented a qualitative model describing it.[16] Since then, multiple research groups have expanded the application of ICP, and further characterized it as a means for control over species transport. Ion depletion is particularly important because it leads to a localized increase in solution resistance, which by Ohm’s Law, enhances the electric field strength. The resulting electric field gradients at the boundary of this ion depleted zone (IDZ) have been employed extensively for focusing and separation of charged analytes in the presence of counter-flow. If two species with distinct electrophoretic mobilities are introduced into the system (for example two different fluorescent dyes[17] or phosphorylated and unphosphorylated substrates in an enzymatic assay),[18] each species will be focused at a distinct axial location (**Scheme 1**).

Separate reviews provide an account of the theoretical and experimental advances in ICP,[19–21] including various applications.[14,22] Specifically, ICP has been leveraged for desalination,[23–26] enrichment and separation of trace analytes[22] and bioparticles,[27] cellular dielectrophoresis,[28] regeneration of sensing substrates,[29] and biological assays.[18,30]

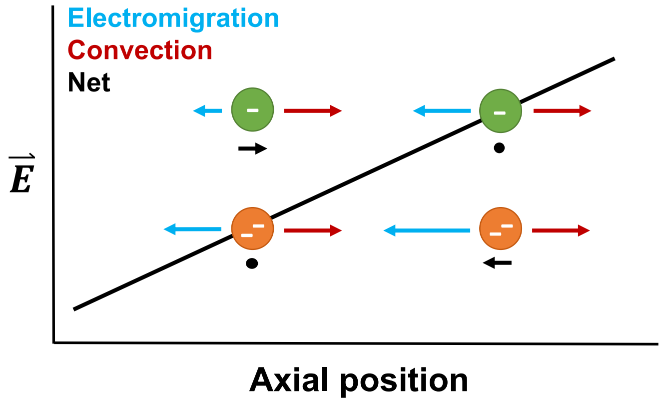

Scheme 1. Illustration of electrokinetic focusing of two anionic species having high (orange) and low (green) electrophoretic mobilities along a gradient in electric field strength. The anions have a convective velocity, from left to right, that is constant as a function of axial position. Their electromigratory velocities (from right to left) are the product of the distinct electrophoretic mobility of each anion as well as the sign and magnitude of the electric field at each location. Therefore, for each anion, there is a position along the electric field gradient at which the net velocity is zero.

Besides analyte focusing and separation, another important application of the ICP phenomenon is micromixing. Mixing solutions at the microscale is slow and often inefficient due to their operation in a laminar flow regime, where mixing is governed by diffusion. The electroconvection generated by ICP near ion selective membranes or nanochannels can be used to mix solutions in neighboring flow laminae. Several active and passive micromixer platforms have been developed for lab-on-chip applications.[31–33]

Faradaic ion concentration polarization (fICP) (called bipolar electrode (BPE) focusing when performed using bipolar electrochemistry) is analogous to ICP with the exception that local ion concentration is controlled electrochemically via charge transfer reactions at an electrode.[34–36] BPE focusing has been used for both enrichment and separation of charged analytes.[35] Recently, fICP has been demonstrated as an alternative to conventional ICP for enrichment of charged species for analysis,[34,35,37] redirection of microbeads,[38] and dielectrophoresis.[28] Techniques that rely on electric field gradients formed by ICP and fICP have shared advantages and limitations, and thus, both will be discussed in this tutorial review.

Despite tremendous advancements in ICP and fICP, some aspects remain challenging. For example, the extension of focusing to neutral (uncharged) species, improvement of volumetric throughput, integration with downstream analysis, application to complex media (e.g., plasma, blood), and the development of strategies to decrease fluidic instability within the IDZ are active areas of research.

In this tutorial review, we briefly introduce physical and chemical aspects of ICP including its theoretical background, primary configurations of the fluidic channel(s) and electric field, the origin of fluidic instability and strategies to mitigate it, propagation of the IDZ boundary (and of the focused analyte bands), and dynamic local pH changes. Next, we describe practical aspects of ICP including methods of device fabrication, prevalent ion selective materials and methods of incorporating them into devices, the influence of sample composition on the selection of device configuration and on the efficiency of focusing, and analyte encapsulation to ‘lock in’ pre-enrichment for off-chip analysis. We further address methods for on-chip analysis, which primarily leverage ICP to control mass transport to/from chemically-modified surfaces. We highlight recent advancements such as multi-staged concentrators, micellar ICPF and an approach for in-droplet enrichment. Lastly, we include a summary of tips and tricks to utilize ICP effectively within its practical and theoretical limits for focusing charged and neutral species.

Fundamental aspects of ICP

In this section, we summarize the key physical and chemical aspects of ICP. We first discuss the mechanisms by which selective ion transport (Donnan exclusion) and, alternatively, faradaic reactions lead to ion depletion in an extended space charge region (the IDZ). Second, we summarize device and electrode configurations employed to achieve the requisite electric field across both the ion selective structure and the microfluidic compartment in which electrokinetic focusing occurs. Third, the transport phenomena that contribute to the formation of disruptive vortex flow and strategies to dampen their effects are described. Next, experimental regimes that promote upstream propagation of the IDZ boundary, which in many applications is undesirable, are delineated, and reported strategies to prevent propagation are discussed. Finally, we describe the processes leading to spatiotemporal shifts in pH, their impact on the sample, and how to control their location and magnitude.

Mechanism of ICP

ICP occurs when a majority of ionic current is selectively carried by either cations or anions between two compartments interconnected by an ion permselective structure when a voltage bias is applied.[14,19] **Scheme 2a** is an illustration of a nanoscale junction, with fixed negative surface sites along its walls, that separates two microfluidic compartments. When a voltage bias is applied across the junction, as shown, cations are selectively transported out of the anodic compartment. Anions migrate towards the anodic driving electrodes, leading to formation of an IDZ in which ion concentration approaches zero. In the cathodic compartment, anions migrate to the junction but are unable to enter, and cations accumulate there to maintain electroneutrality. These processes lead to ion accumulation, thus creating an ion enriched zone (IEZ). A key point is that the low ionic conductivity in the IDZ results in localized electric field enhancement that drives even more rapid depletion, resulting in growth and propagation of the IDZ.

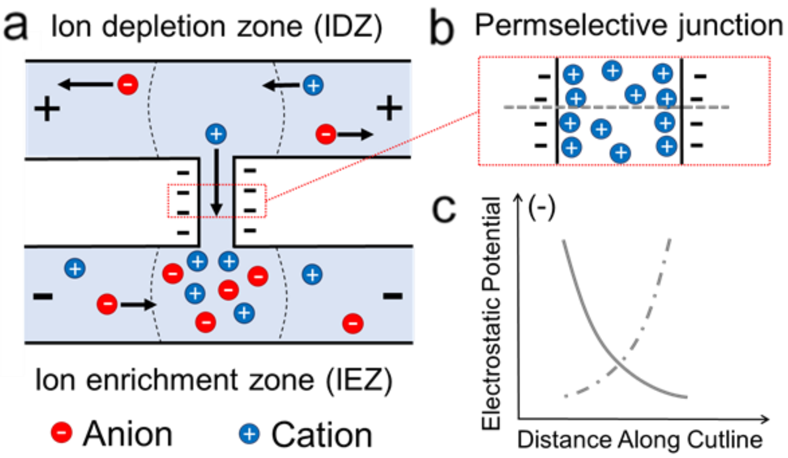

Scheme 2. a) Illustration of IDZ and IEZ formation near a nanoscale junction spanning two microfluidic compartments; b) illustration of the electrical double layers at the negatively charged walls of the nanojunction; and c) a schematic plot of the electrostatic potential as a function of distance from each wall. In this illustration, the electrical double layers overlap, and therefore, the electrostatic potential at every location within the junction is more negative than that of the bulk solution.

Because of this mechanism of permselectivity by Donnan exclusion, the ratio of the channel/pore radius to the Debye length of the electrical double layer (EDL) is a key parameter impacting the initiation of ICP and propagation of the IDZ.[19] An EDL forms at any solid-liquid interface and is on the order of a few nanometers (< 10 nm) in a symmetric electrolyte at a concentration greater than 1.0 mM. If the channel wall is negatively charged, the electrical potential at the wall will be more negative than that of the bulk solution (**Scheme 2b**). If two such walls are in close proximity to each other, the EDLs will overlap and the electric potential in the center of the channel will not reach that of the bulk solution (**Scheme 2c**). A non-zero voltage bias will drive selective transport of cations through the junction. Practically, this condition is satisfied when the ratio of channel/pore height to the Debye length is unity or less ($h/\lambda_d \leq 1$, where h is the height of the channel/pore and λ_d is the Debye length), thus implying that the ICP phenomenon is limited to nanochannels with a critical length on the order of 10 nm or less.

However, Kim et al. demonstrated that strong ICP effects can be achieved with non-overlapped EDLs.[39] They observed ICP at nanochannel with a critical dimension of 40 nm in the presence of an electrolyte concentration of 15 mM, which corresponds to a 3 nm-thick EDL. Additionally, Jacobson and coworkers showed that strong ICP effects can be achieved even with non-overlapped EDLs.[40] Using a poly(ethylene terephthalate) (PET) membrane with track-etched conical nanopores sandwiched between two PDMS microchannels, they showed that despite an estimated EDL thickness of 1-3 nm in a nanopore having a diameter of 130 nm, ICP occurred ($h/\lambda_d \approx 100$). To investigate the ion selective transport mechanism, these authors measured and compared the conductivities of the buffer in the bulk solution, in the microchannel and in the nanopores while varying the concentration of the buffer. Their results demonstrated that the bulk and microchannel conductivities were directly proportional to each other over the entire buffer concentration range, while the nanopore conductivities exhibited a positive deviation at low buffer concentration. This greater than expected conductivity is due to the increased surface-to-volume ratio in the nanopore, which leads to an increased contribution to the nanopore conductivity from the surface charge. This result suggests that under the condition that ion conduction along the surface of the nanopore is a major contributor to the overall current, ICP will occur.

Zangle et al. coupled theoretical and experimental studies to investigate the relationship between surface and bulk conductance in the generation of ICP. They concluded that concentration polarization depends primarily on a nondimensional parameter called the Dukhin number (Du) and not strictly on the ratio of channel/pore radius to Debye length.[19,41] Du is the ratio of the surface (G_σ) to bulk (G_b) conductance:

$$Du = G_\sigma / G_b$$

Mani et al.,[41] Zangle et al.,[42] and Kim et al.[43] further used the inverse Dukhin number (1/Du), to characterize concentration polarization. The *1/Du* relates the number of ions in the bulk to the number of ions associated with the EDL.

$$1/Du \approx Fhzc_0/\sigma, \text{ where}$$

F is the Faraday constant, *h* is channel or pore height, *z* is valence of a symmetric electrolyte, c_0 is bulk concentration of electrolyte ions, and σ is surface charge density. Strong concentration polarization effects have been demonstrated for systems where $Fhzc_0/\sigma \ll 1$. In other words, for ICP to occur, selective conduction of counter-ions along the surface must greatly exceed non-selective bulk conduction, and this ratio depends on the availability of charge carriers to each current path.

Several studies have measured both bulk and ion selective currents, as a function of applied voltage, and have related them to the rate of ion depletion and IDZ propagation.[39,44–46] The depletion zone length increases as the applied voltage bias and the current through a permselective junction increase. Most commonly reported currents through a cation selective membrane in ICP systems are within a range of tens of nA for small channel geometries (with channel cross sectional area of 400 μm^2)[39,47] up to 80 μA for out-of-plane devices (cross sectional area of 0.4 mm^2).[25]

Mechanism of faradaic ICP

Faradaic reactions can be used to generate ion depleted and enriched zones that are analogous to those resulting from ICP at permselective junctions. For example, neutralization of ions of the BGE at an electrode leads to their depletion. In the application of faradaic ICP (fICP), these reactions are most commonly facilitated by a BPE. A BPE is a conductive material, that is not directly connected to an external power supply, and thus is free to float to an equilibrium potential.[48–50] If a potential bias (ΔU_{tot}) is applied across the electrolyte solution in contact with the BPE, an interfacial potential difference will develop between the BPE (U_{BPE}) and the solution at each of its ends (**Scheme 3a**). If the total potential dropped across the BPE (ΔU_{BPE}) is sufficiently large, the electrochemical overpotentials, η_a and η_c, will drive anodic and cathodic reactions that are electrically coupled through the BPE. **Scheme 3b** (top view) and **Scheme 3c** (cross-sectional side view) illustrate a thin film BPE in contact with two parallel microchannels. Reduction of a cation to a neutral product at the BPE cathode (top channel, **Scheme 3b**) results in a decrease in local ion concentration. This process is coupled to an oxidation reaction at the BPE anode (bottom channel). As depicted here, the oxidation of a neutral compound generates a cation, and concurrent inward migration of anions to charge pair with these cations leads to a local increase in ionic strength (an IEZ). This combined process is analogous to selective cation transport. **Scheme 3d** depicts an alternative route to fICP involving acid-base neutralization of buffer ions. Here, water is reduced to generate OH^- (red circle, top, **Scheme 3d**), which accepts a proton from a buffer cation (blue circle, e.g., $TrisH^+$) to generate a neutral species (black circle, e.g., Tris), thus resulting in a local decrease in ionic strength and creation of an IDZ.

Note that for fICP, the degree of selectivity (similar in concept to *Du* in ICP) is the ratio of the faradaic current leading to ion depletion to the bulk ionic current. Therefore, for a system in which the reaction proceeds with 100% faradaic efficiency and in which all current is passed through the electrode that drives CP, there is perfect selectivity (analogous to infinite *Du*). An important limitation of fICP, however, is that faradaic processes are not simply charge selective – they are also species selective, depleting one type of cation (e.g., $TrisH^+$) while leaving another (e.g., Na^+) untouched. The resulting partial depletion is analogous to a low *Du*. This characteristic presents a major challenge for fICP in complex media, and therefore, a key area for growth in fICP is the identification of electrochemical processes that deplete major charge carriers in systems of interest.

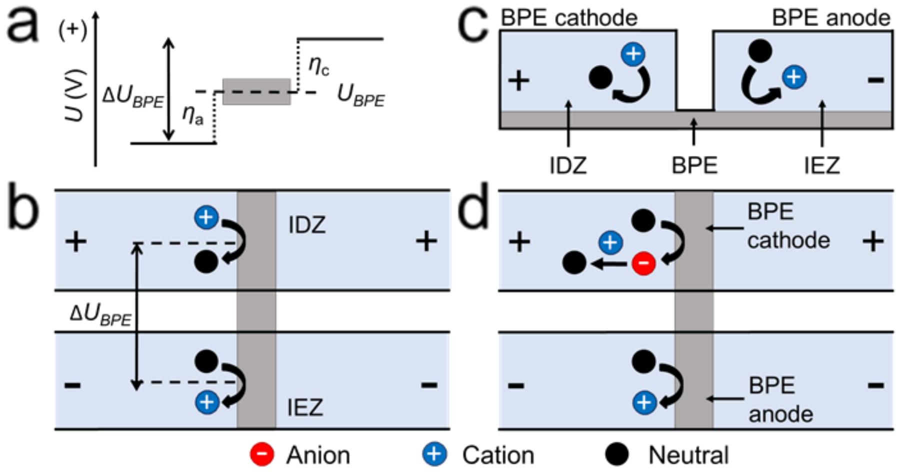

Scheme 3. a) Schematic plot of the electrostatic potential (*U*) of the electrolyte solution and the BPE (U_{BPE}), an equipotential object, along the dashed cutline in (c). In an externally applied field, an interfacial potential difference develops between the BPE and the solution at each of its ends. b) Top view and c) cross-sectional side view schematics of a thin film BPE in contact with two parallel microchannels. Faradaic reactions occur at the BPE cathode and anode, impacting the concentration of cationic (blue circles) and neutral (black circles) species in each compartment. d) Schematic illustration of the device shown in (b), in which an alternative mechanism leads to ion depletion. Faradaic production of anionic species (red circle) leads to depletion of a cations (blue circle) by a following reaction.

When designing a strategy for fICP, there are several key factors to consider. First, it is not required that the electrode be a BPE – any electrode in a confined volume that drives reactions leading to significant removal of ionic charge carriers of the BGE can facilitate the development of an IDZ. Second, the reactions can be either a faradaic oxidation or reduction and can act either directly or indirectly on the ions of the BGE. For example, at an anode, the generation of protons by water oxidation can drive ion depletion indirectly via the neutralization of a buffer anion. Such neutralization can be complete (e.g., CH_3COO^- to CH_3COOH) or partial (e.g., HPO_4^{2-} to $H_2PO_4^-$).[51] However, complete neutralization leads to a more dramatic decrease in local ionic strength, and therefore, to greater electric field enhancement within the IDZ.

Finally, the sign of the excess charge on the electrode determines the direction of the electric field gradient, and therefore, dictates which sign of analyte (cationic or anionic) can be focused. Anions are focused against a counter flow by repulsion from an IDZ generated at a cathode (and vice versa).

Electric and flow fields that drive ICPF

This section focuses on the aspects of the applied electric field and fluid flow that contribute to the rate of ion depletion and the electric field distribution – especially, its magnitude and slope where focusing occurs – and to the rate of convection. In most cases, initiation of ICP requires a voltage bias across an ion permselective junction (E_J).[20] A peak in electric field strength develops at the location where ion depletion is the greatest and forms an electric field gradient extending up to several hundred microns to the edge of the IDZ (**Figure 1**).[52] Hlushkou et al. investigated ICP at hydrogel membranes with varying surface charge densities and the associated electric field formed upon applying a potential bias. **Figure 1a** depicts a single-channel device employed in this study to obtain both numerical and experimental results. At the channel midpoint, a fixed hydrogel plug connects the anodic and the cathodic compartment of the microchannel. Species transport was governed by electroosmosis and electrophoresis. There is convection along the microchannel from left to right (**Figure 1**), and the fluid flows through the hydrogel. A charged hydrogel can drive EOF, acting as a pump. **Figure 1b** shows the result of numerical simulations of the electric field near charged (c_{fix}=c_{res}, and c_{fix}=0.1c_{res}) and uncharged membranes (c_{fix}=0). Focusing of a charged species can be achieved at an axial location along this field gradient, at which the convective and electromigratory velocities of that species are equal in magnitude and opposite in direction.[17]

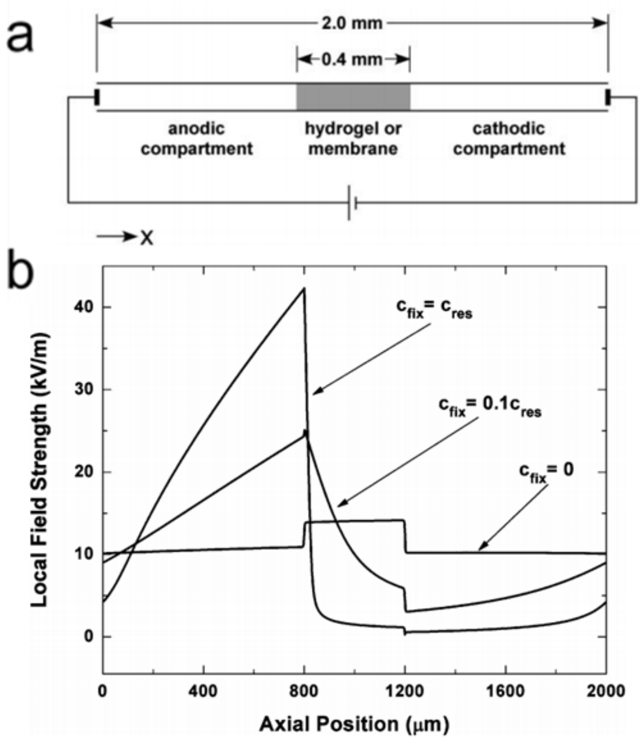

Figure 1. a) Schematic illustration of the system used for analyte concentration enrichment in a microfluidic channel containing a fixed nanoporous (anionic or neutral) membrane. b) Numerical simulation of the steady-state distribution of the local electrical field strength for an externally applied field of 11.1 kV m^{-1}. Three cases are shown, in which the membrane was assigned a negative fixed charge of uniform volume density of $c_{fix}=0$ (neutral), $c_{fix}=0.1c_{res}$ (weakly charged), and $c_{fix}=c_{res}$ (highly charged). c_{res} is the concentration of the BGE in the reservoir. The membrane occupies the region x = 800-1200 µm. Illustration reproduced from ref. [52] with permission.

Kim et al. investigated the current and voltage requirements for inducing ICP in a single microfluidic channel having a surface patterned *Nafion* membrane film along a segment of the channel floor.[53] They found that if cation flux through the patterned membrane was larger than that through the bulk solution (high *Du*), then ICP occurred. **Scheme 4a** and **4b** illustrate a top view and cross-sectional side view of a single microchannel with an embedded membrane, where V_1 and V_2 are the voltages applied in the microchannel reservoirs. Fluid flow is from left to right, and the green band represents a plug of enriched anionic analyte upstream of the membrane. The convective and electrophoretic components of their velocities are indicated as υ_c and υ_{el}, respectively. In the device employed by Kim et al., the channel was 200 µm wide by 20 µm tall and with a membrane, that extended 200 μm along the channel length, spanning the channel centrally. In this configuration, initiation of ICP required 50 V cm^{-1} electric field. In a subsequent publication with a similar device geometry, this same group developed a model to characterize the influence of several experimental parameters on the enrichment factor (EF) in this single-channel ICP device.[54] EF is calculated as the maximum localized concentration observed in the enriched plug of analyte divided by its initial concentration in the sample. These parameters included the voltage bias (V+), electrophoretic mobility of the analyte (μ_{ep}), the charge density in the membrane (**σ**), and the electrolyte concentration (c_0). The authors concluded that, although single-channel ICP devices are simple to fabricate and to operate (two driving electrodes, no auxiliary channel), they are limited to applications with low electrolyte concentrations (≤ 0.1 mM) for sufficiently high *Du*. Additionally, at a spatially averaged electric field strength of 50.0 V cm^{-1} or higher, the *Nafion* membrane (100 μm long and 2 μm thick) was damaged and degraded within 15 min.

In **Scheme 4c** and **4d**, two fluid filled compartments are connected solely by an ion selective junction. Such a system can be achieved experimentally by contacting two microfluidic channels with a cation selective membrane (top view, **Scheme 4c**, and cross-sectional side view, **Scheme 4d**). **Scheme 4c** depicts two anionic analytes with distinct mobilities as focused bands upstream of the membrane in the main (anodic) channel. This dual-channel configuration allows the operator to tune the components of the electric field normal to the membrane (E_J) and tangential to fluid flow (E_T) independently. Therefore, the current through the membrane can be kept below the threshold for damage while maintaining tight focusing. More specifically, when $V_1 > V_2$ (**Scheme 4c**) the magnitude of ET is increased, leading to increased migration velocity and higher EOF-driven flux of the analyte to the enriched band, thereby resulting in greater enrichment.[55] In such a configuration, it is typical that $V_3 = V_4 \leq V_2$ such that $E_J > 0$.

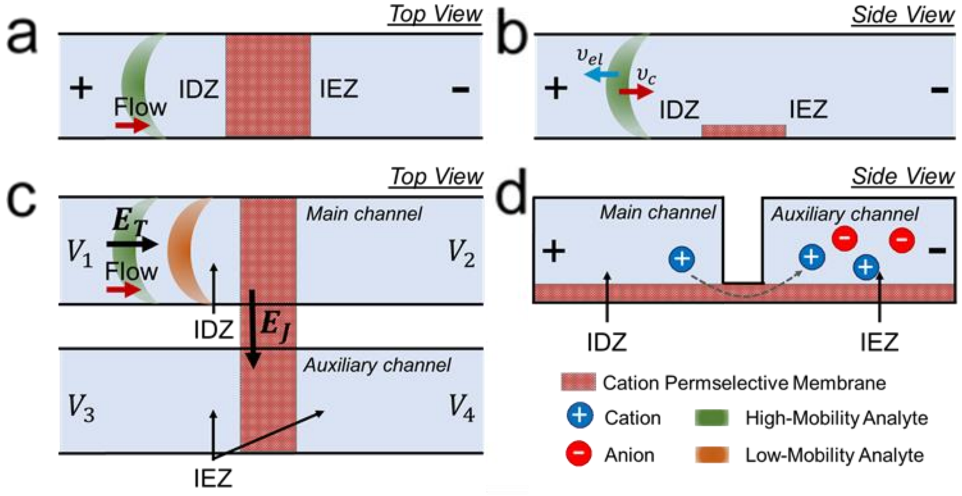

Scheme 4. a) Top view and b) side view illustrations of a single-channel device with an embedded membrane. An analyte (green) is focused upstream of the membrane by a balance of electrophoretic and convective forces. c) Top view and d) side view illustrations of a dual-channel device, in which two parallel microfluidic channels are interconnected by an ion permselective membrane (e.g., *Nafion*). Two analytes (green and yellow) are focused at distinct axial locations determined by their individual electrophoretic mobilities.

This dual-channel configuration has been used to simultaneously preconcentrate and separate multiple species that have distinct electrophoretic mobilities. This approach is especially effective for analysis of biological targets, for which a biorecognition event, such as binding, chemical modification, or cleavage, leads to a shift in mobility. Recent examples include the detection of 1) a protein by the separation of bound and free aptamers,[56] 2) a kinase through discrimination of phosphorylated and unphosphorylated substrates,[18] and 3) a specific DNA sequence by its complexation to Cas9.[57–59] A universal strategy to improve resolution that arose from these methods is the inclusion of spacer molecules (here, peptides comprised of neutral and acidic residues) having mobilities intermediate to those of separands. When enriched to a concentration near that of the BGE, the spacers generated steps in the electric field gradient that push apart analytes that focus at higher and lower field strengths.[18]

fICP similarly has been demonstrated in both single- and dual-channel configurations. A single-channel configuration for fICP, in which the entire BPE is in one channel, has been employed for focusing of either anions or cations (**Scheme 5a,b**)[34–36] and for separation of multiple analytes.[60] Application of voltage bias, ΔU_{tot}, across a single microchannel of length l_{chan} with embedded BPE results in an electric field with a constant value of $E \approx \Delta U_{tot}/l_{chan}$. If there is a sufficient potential dropped across the solution above a BPE (of length, l_{elec}), faradaic electrochemical reactions will occur at the poles of the BPE. Electrochemical reactions will occur when the fraction of ΔU_{tot} dropped over the length of the BPE (approximated by $\Delta U_{BPE} \approx \Delta U_{tot} \times l_{elec}/l_{chan}$ and depicted in **Scheme 5c**) exceeds that required to drive a reduction reaction at the cathodic pole and an oxidation at the anodic pole.[51] In other words, ΔU_{BPE} must exceed the difference in onset potential between the two electrically coupled reactions. By employing a single-channel configuration, small anionic dyes were enriched up to ~500 fold within 400 s.[60]

It has been reported that during fICP in a device configured such that both ends of the BPE lie in a single microchannel, a majority of current flows through the BPE and not through the bulk solution. Importantly, approximately 80% of the total current is diverted through the BPE. For example, at a total current of 328 nA, the current through the BPE was reported to be 271 nA.[36] This high ratio of a faradaic current (that selectively depletes one sign of charge carrier) to bulk current is analogous to a high Du in ICP. This finding is important because it has allowed for focusing in devices lacking nanoscale, or even low microscale, dimensions.

Scheme 3 depicts a BPE in contact with two microchannels. Such dual-channel focusing offers multiple advantages. First, the ability to select either cathodic or anodic reactions leading to ion depletion provides a route to simultaneous enrichment of both cations and anions in the same device. For example, dual IDZs form with indirect neutralization of $TrisH^+$ and CH_3COO^- at the BPE cathode and anode, respectively.[35] Second, E_J and E_T are controlled independently, thereby preventing damage to the electrode caused by Joule heating or by redox reactions of the electrode material itself. A higher E_T allows for an enhanced rate of enrichment via more rapid transport of the analyte to the IDZ boundary and tighter focusing.[34,35] Using dual-channel focusing, up to 143,000-fold EF within 33 min (71-fold/s) of a tracer dye was reported.[35]

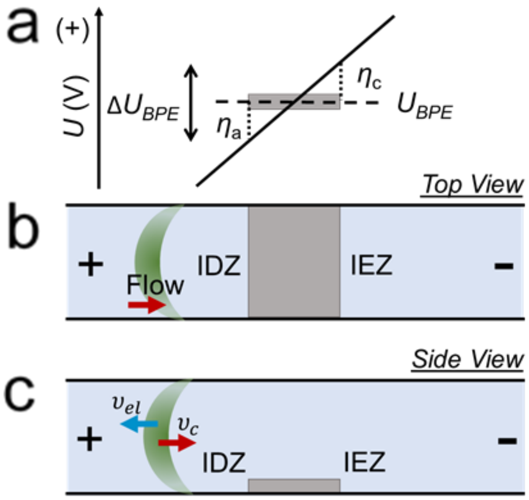

Scheme 5. a) Top view and b) side view illustration of a single-channel fICP device with an embedded BPE. c) Schematic plot of electrostatic potential of the electrolyte solution as a function of axial position along the channel. The potential of the BPE is intermediate to that of the solution it contacts. This simplified schematic assumes no impact of the BPE on the solution potential.

In practice, convection is achieved by electroosmotic flow (EOF), pressure-driven flow (induced by gravity or a syringe pump), or a combination of both. During focusing of a charged species, convection plays the role of carrying it from the inlet reservoir to the location at which opposing electromigration is sufficiently strong to balance it. Therefore, the convective velocity of the species must exceed its spatially averaged electromigratory velocity. For example, a small molecule with an electrophoretic mobility (μ_{ep}) of 3.0 x 10^{-8} m^2 V^{-1} s^{-1} in a 5 kV m^{-1} electric field, will have an electrophoretic velocity of 1.5 x 10^{-4} m s^{-1} (150 µm s^{-1}). In the IDZ, the electric field strength can be 10-fold greater (50 kV m^{-1}) than the average along the channel. Therefore, in the presence of electroosmotic flow (EOF) with a spatially averaged linear velocity of 500 µm s^{-1}, the species described will be carried to the IDZ and focused at an axial location where the electric field reaches 16.7 kV m^{-1}. Native glass, silicon, and materials commonly employed in microfluidics such as polydimethylsiloxane (PDMS) have negatively charged surface groups (Si-O-) over a wide pH range (pK_a 4-6) leading to a surface charge on the order of 10 mC m^2.[61] The resulting negative zeta potential (ζ) drives EOF towards the cathodic driving electrode in the presence of a tangential electric field (E_T). Note that ICPF of cationic analytes near an anion selective membrane would require an anodic EOF, which can be achieved by modifying the channel walls with a cationic coating. Where EOF alone drives convection, E_T is directly proportional to both convective and electromigratory velocities, and in general, a higher field strength leads to tighter focusing – the width of the analyte band is determined by how well these sequestering forces can counter diffusive broadening. However, E_T is practically limited by the onset of fluidic instability, which is discussed in detail in Sections 2.3 and 2.4.

The electroosmotic mobility (μ_{eo}) can vary considerably depending on the pH of the sample and the properties of the microchannel surface, and therefore, it is practical to dampen EOF with an uncharged surface coating (such as poly(ethylene glycol)-block-poly(propylene glycol)-block-poly(ethylene glycol) or Pluronic F108)[62,63] and rely on pressure driven flow instead. However, note that the flow rates required for ICP are very low and therefore difficult to control with a syringe pump. Take for example the 500 µm s^{-1} EOF described above. In a microchannel having typical dimensions (200 µm x 50 µm), the volumetric flow rate is only 5.0 nL min^{-1}. In the absence of a pump that can stably deliver such a low flow rate, gravity-driven flow arising from a fluid height differential across the inlet and outlet reservoirs is often employed.

Secondary EOF or vortex flow

The efficiency of ICPF is limited by a strong secondary electroosmotic flow that develops within the IDZ, creating fluid vortices that cause unwanted mixing. Recently Nam et al. summarized key features of this fluidic instability.[47] The origin of this phenomenon is a sharp decline in the electrolyte concentration within the IDZ. The concentration of ionic charge carriers approaches zero at the limiting current,[16] and the resulting decrease in electrical conductivity leads to a locally amplified electric field.[64] This high local electric field drives fast electrokinetic flow within the IDZ to transport sufficient ions to the junction to satisfy electroneutrality conditions.[39,65] A mismatch in the local driving force for EOF inside versus outside of the IDZ leads to circulating (vortex) flow and results in disruption of concentration gradients. Therefore, the onset of vortices can be detected indirectly as a decrease in the electrical resistance of the IDZ and excursion of current above the limiting value (overlimiting behavior).

Prior to this more recent summary, several research groups proposed multiple mechanisms for fluidic instability. Zaltzman and Rubinstein experimentally investigated changes in current associated with fluidic instability. They found that current through an ion selective membrane increases linearly with increasing applied electric field (ohmic regime), until reaching a voltage-independent current limited by mass transport of ions through the depletion zone (limiting current regime). At still higher voltages, the onset of fluidic instability and mixing decreases resistance in the IDZ, leading to increased current through the nanoporous membrane (overlimiting current regime).[66] They characterized the mechanism of this instability including contributions from thermal fluctuations,[67] non-equilibrium electroosmotic slip,[68] and electro-diffusio-convection.[66]

Mani et al.[41] and Park et al.[69] described factors affecting vortex formation near a nanojunction. These authors concluded that because the ratio of surface to bulk conductance depends on the cross-sectional area of the channel, the EOF profile is non-uniform across the microchannel-nanochannel interface. A local mismatch in EOF causes internal pressure gradients near the interface, thus creating vortices in the channel.

Recently, a more unified theory of the mechanisms contributing to overlimiting current was proposed.[70] Diffusion-limited transport to an ion selective membrane or to an electrode in a microchannel having charged walls was described using three mathematical models: 1. surface conduction (SC) by the excess counterions that screen the wall charge; 2. convection by EOF, which is driven by large electroosmotic slip in the depletion region on the sidewalls; and 3. electroosmotic instability (EOI) or fluid vortices. For the mathematical model, authors used symmetric electrolyte (c_0=1.0 mM), with microfluidic channel length L=1.0 cm, surface charge of 50 mV, and channel height, H. The predicted mechanism for overlimiting current transitions were from SC to EOF at H=8.0 µm, and from EOF to EOI at H=0.4 mm. It was concluded that the SC mechanism dominates for very shallow channels, low ion concentration, and large surface charge, while EOF dominates in taller channels. Further, with increasing channel height, the dominant mechanism switches to EOI because a significant portion of the depleted solution is unaffected by the EOF. These results indicate that the dominant mechanism leading to overlimiting behavior and vortex formation can vary based on microfluidic channel dimensions and ionic strength.[47]

Few experimental approaches have been developed to reduce the impact of vortex formation and fluid mixing on IDZ stability. Reducing the cross-sectional area of the main channel can lead to vortex flow suppression and IDZ zone stabilization. Kim et al. demonstrated that electroconvection can be suppressed by decreasing microchannel depth. Upon decreasing from 20 to 2 µm, the vortex size was constrained to this smaller depth, thus leading to less efficient fluid mixing and a more stable concentration gradient near the permselective membrane.[39] However, this decrease in depth, led to a 10-fold decrease in volumetric flow rate (Q) under the same linear flow velocity, thus detrimentally lowering device throughput.

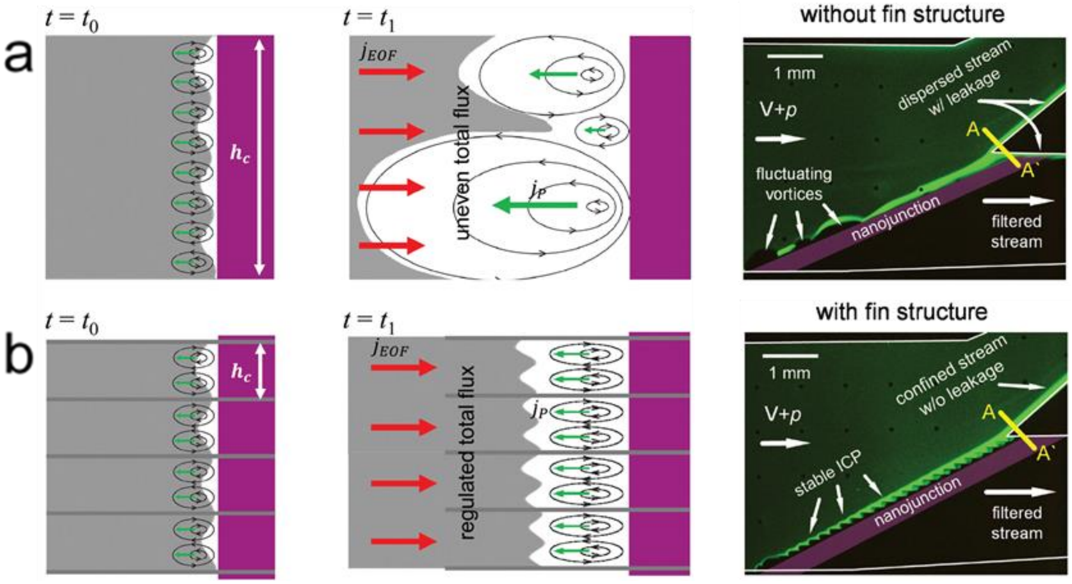

Figure 2. Schematics of vortex formation near a permselective membrane in each a device a) without and b) with the microfin structure. Here, h_c, j_{EOF} and j_P indicate the critical dimension, the ion flux by electroosmotic flow and back pressure due to vortex flow, respectively. Fluorescence micrographs of the high-throughput continuous ICP separator are shown at far right, for each device. Illustration in reproduced from ref. [46] with permission.

Similarly, Kim et al. utilized geometric 'microfin' structures near the ion selective membrane to reduce the size of vortices and increase the stability of the IDZ boundary (**Figure 2**).[46] These microfin structures served to promote SC (instead of EOI) and also physically suppressed the electrokinetic vortices, resulting in a stable IDZ boundary at high voltage (110

V), while maintaining high preconcentration efficiency of charged species and increasing the overall throughput (up to Q=4.0 μL min^{-1}) of the microfluidic device.

As an alternative to geometric restrictions, Kim et al. proposed that increased surface conduction can stabilize the vortex flow.44 In their study, they achieved stable IDZ formation by artificially enhancing the surface charge of the channel by coating the highly conductive polymer (Nafion) inside the glass/PDMS microchannel. Highly conductive materials like *Nafion*, have surface charge in the range of 200-600 mC m^{-2} (higher than glass). Therefore, they created an alternative current path (by enhanced SC) within the IDZ (**Figure 3b,c**). Consequently, the strong electrokinetic flow associated with the amplified electric field inside the IDZ was significantly suppressed.

A recent study by Valença et al revealed that microstructuring of an ion selective membrane facilitates ion transport to the membrane in the overlimiting regime, thereby reducing the need for EOI as a means of transport. The result is smaller fluid vortices.[71] In this study, a caste-molding process was utilized to create 50 µm-tall and 50, 100, 200, 400, or 800 µm-long rectangular square-wave structures in the surface of a cation exchange membrane comprised of sulfonated poly ether ether ketone (SPEEK). Chang and coworkers have shown that device design also plays an important role in determining the degree of instability.[72] They found that a large ratio between the active areas of the driving electrode(s) and membrane leads to larger vortices. Therefore, designs that decrease this ratio and favor low current density are expected to exhibit greater fluidic stability.

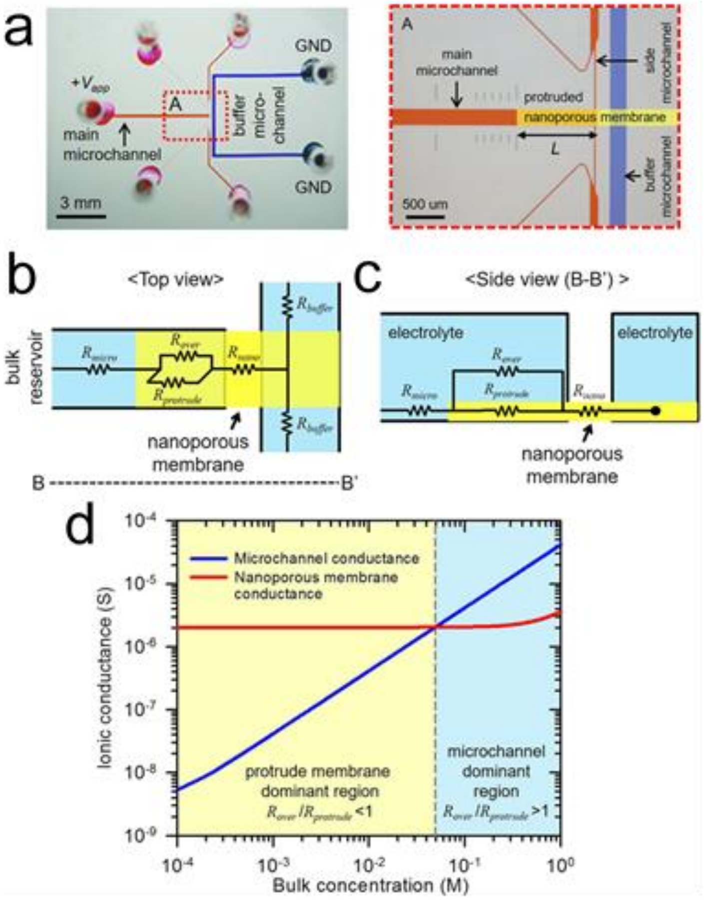

Figure 3. a) Top view image of the fabricated non-destructive cellular preconcentrator and microscopic view of the area indicated by the red box labelled A. L was the length that the nanoporous membrane protruded from the junction into the main microchannel. Schematics of b) top and c) side view of the proposed devices with equivalent electrical resistors (not to scale). d) Calculated ionic conductance of the microchannel and nanoporous membrane as a function of the bulk concentration of the electrolyte. Conduction of ions is dominated by the membrane at bulk concentrations below 4.0×10^{-2} M. Illustration reproduced from ref. [44] with permission.

Propagation of the IDZ boundary

Under certain conditions enrichment and depletion zones in a microfluidic system propagate outwards from the micro/nano-channel interface, creating shock waves.[19,41] These shock waves are propagating boundaries between regions of channel with initial concentration ($c_{0,r}$) and regions where the concentration has been influenced by selective ion transport ($c_{0,r}*$). To be able to incorporate an analyte preconcentration step into a generic benchtop analysis or for point-of-care testing, the specific location of the concentrated analyte band within the microchannel must be known. However, due to propagation of the IDZ, controlling the location can be challenging.

Mani, Zangle, and Santiago developed and experimentally validated a computational model to characterize parameters that define propagating and non-propagating regimes.[19,41,42] They found, that these phenomena are governed by *Du* of the ion selective junction (here a nanochannel) and the mobility of the co-ion (e.g., anions for a negatively charged wall). As described previously, *1/Du* represents the ratio of bulk to surface conductance. This parameter is proportional to nanochannel/pore height (h_n) and background electrolyte concentration ($c_{0,r}$) as supplied from the inlet reservoir and inversely proportional to the surface charge density (σ). For computational purposes, they used non-dimensionalized concentration ($c_{(0,r)}*\ h_n*$) and co-ion mobility (v_2*). They found that CP enrichment and depletion zones will propagate if the following condition is satisfied:

$$1/Du = c^*_{0,r}h^*_n < (v^*_2, 2v^*_2 - 1),\ where$$

$$c^*_{0,r}h^*_n = (v_1 z_1 - v_2 z_2)F h_n c_{0,r}/(-2v_1\sigma),\ and$$

$$v^*_2 = \upsilon_2 z_2 F\eta/\xi_n \varepsilon,\ where$$

v_1 and v_2 are velocities of the counter and co-ion of the BGE, respectively, z_1 and z_2 are the valence of these ions, ξ_n is the zeta potential of the nanochannel, *F* is the Faraday constant, ε permittivity, and η is viscosity. In other words, a highly selective junction (defined as small 1/*Du* and $c_{(0,r)}*\ h_n*$) or a system in which the co-ion (which is repelled from the IDZ) is fast will yield propagation. By processing data from 56 sets of previously published experimental results and comparing them to the developed model, they observed that co-ion mobility values typically vary within two orders of magnitude (from 0.1 to 10) and thus, are not as influential as1/*Du*, which extends over 4 orders of magnitude.[19]

There are practical approaches that can be used to diminish the influence of propagation. For instance, the propagation of the depletion zone can be opposed by introduction of hydrodynamic flow or increase of EOF (by modifying the surface charge). Pressure driven flow is preferred because it is independently tunable. Undesirable “bursting” of the IDZ boundary occurs when the EOF overcomes the repulsive force of the IDZ.[64]

Kwak et al. proposed an alternative method to control the propagation of the IDZ by confining preconcentration to a specific region regardless of the device operating conditions (time, applied voltage, ionic strength and pH).[45] To achieve this goal, they initiated ICP between two ion selective membranes (*Nafion*) located axially along a microchannel (**Figure 4**). These membranes were oppositely polarized such that an IEZ developed at the upstream junction and an IDZ at the downstream junction. This approach generated a preconcentrated plug of a model analyte in the 100 μm-gap between the membranes, thus simplifying in situ or in-line analysis.

Vortex formation and ICP zone propagation can be decreased using capillarity ICP, an approach in which the capillary force of a permselective hydrogel, instead of an electric bias, spontaneously generates an IDZ.[73] Depletion occurs due to selective imbibition of counter ions from the sample solution into the hydrogel matrix, while its co-ions in the fluid are rejected from entering the hydrogel. Due to the difference in mechanism (e.g., passive transport of ions) electric field amplification does not occur inside the IDZ, and thus, no electrokinetic instability is observed. Despite the added stability, only a modest preconcentration rate of 100-fold min^{-1} was achieved for biomolecules, owing to a decrease in the magnitude of electrophoretic and convective forces available for focusing. Capillarity ICP holds promise for applications in which samples are electrically sensitive (e.g., cells) or for point-of-care devices where high voltages are difficult to supply and only modest analyte preconcentration is needed.

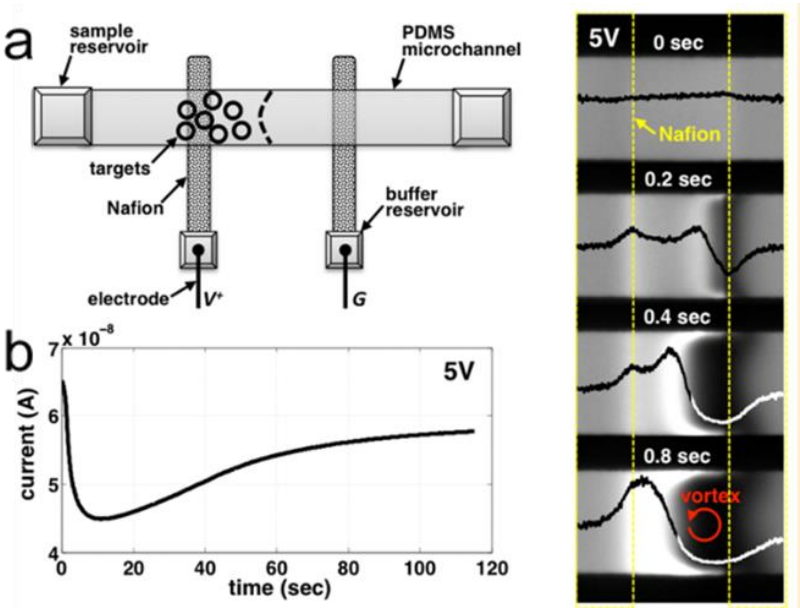

Figure 4. Schematic of a spatiotemporally defined preconcentrator. a) Analyte (black hollow circles) is preconcentrated between two Nafion strips, which are thin films, flow-patterned on the substrate; b) Current-time response obtained during performance of ICP at 5.0 V in this device; c) Fluorescence micrographs of the merged IEZ and IDZ between which an enriched band of a tracer dye develops. Illustration reproduced from ref. [45] with permission.

Spatiotemporal pH dynamics near ion selective membranes and electrodes during ICP

Dynamic, localized changes in acid-base chemistry caused by permselectivity and ion accumulation and depletion at the ion selective structure may contribute significantly to nonlinear behaviors by affecting important system properties, such as analyte charge, local ionic strength and zeta potential of the channel walls, which are all coupled to pH. Further, the pH change may affect the kinetics of chemical reactions and directly interfere with molecular recognition and sensing reactions designated to occur near the ion selective feature. Often, ICP and fICP induce pH shifts on either side of the membrane or electrode as a result of H^+/OH^- ion transport or production, respectively. The degree of change depends on key system parameters including buffer capacity, the pKa and density of charged surface moieties, and the magnitude of the current.

Mai et al. investigated the effect of ionic strength, electric field strength, and buffer composition on pH during CP at a negatively charged polyacrylamide (PAM^-) membrane (**Scheme 6**).[74] The dual emission ratiometric fluorescent dye, carboxyseminaphthorhodafluor (SNARF), was used to monitor pH, while the degree of CP was ascertained based on the decrease in current (in a current vs. time plot) through the ion selective feature. The authors first investigated CP in two distinct buffer systems – 10.0 mM sodium phosphate buffer (PB, pH 7.5) and 10.0 mM phosphate buffer saline (PBS, with 150 mM NaCl, pH 7.5) under an applied electric field of 25 V cm^{-1}. A more rapid decrease in ionic current indicated stronger CP with lower ionic strength PB than with PBS. In one minute after applying the electric field, current through the ion selective feature decreased by 75% in PB system, while in PBS they observed a 55% decrease. This outcome is expected based on the dominance of EDL conductance in the lower ionic strength buffer.

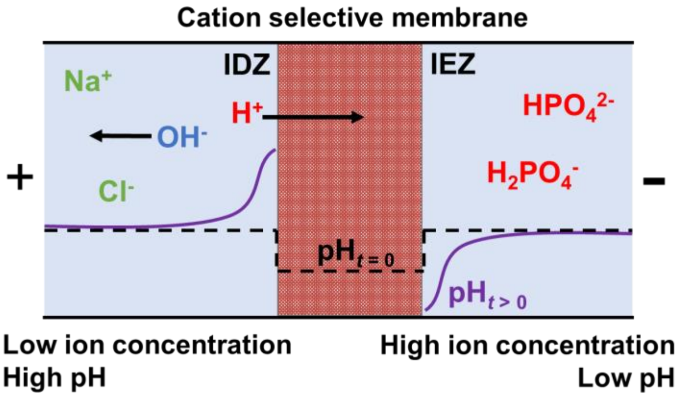

Scheme 6. Illustration of pH change near an ion selective membrane. During ICP, the pH profile evolves from its initial state (black dashed line) to develop a local maximum and minimum pH in regions near the membrane at later times (purple solid line). Illustration modified from ref. [74] with permission.

Further, the authors found that pH changes near the PAM^- structure were more pronounced in PBS than in PB alone. In PBS buffer, and under an applied electric field of 25 V/cm for 30 s, pH on the cathodic side of the PAM^- membrane decreased from 7.5 to 6.

However, in PB, the pH was stable on the cathodic side. On the anodic side, an increase in pH to 8.5 was observed at the outer edge of the IDZ, at more than 500 µm away from the PAM$^-$ membrane. Based on these results, it was concluded that higher ionic strength is correlated to a greater pH change. This result makes sense because a higher ionic strength will support greater overall current, thereby driving greater transport of H^+ between the microfluidic compartments.

Finally, it was observed that the strength and rate of CP and the magnitude of local pH changes were positively correlated with applied electric field. As the field strength was increased, the initial current was higher and decayed more rapidly to its limiting value. These higher currents drive more rapid flux of protons through the membrane supporting greater excursions in pH.[74,75] Andersen et al. further developed a mathematical model to help predict and engineer pH dynamics that can be essential to the performance of ICP systems.[76]

Similarly, the driving electrodes can facilitate electrochemical reactions that influence pH. Recently, Kim and co-workers demonstrated how electrode material and exposed area contribute to this effect. First, they compared Ag/AgCl electrodes with large (26.9 mm^2) and small (0.2 mm^2) electroactive area.[77] Significant pH change was observed only at the small area electrode due to the high current density and resulting Cl^- depletion at the anode. Since the supply of Cl^- limited the oxidation of Ag to AgCl, water oxidation dominated instead, leading to decreased pH. These results were also compared to those obtained using Pt electrodes, where difference in electrode area showed no significant influence on pH, because water oxidation was the only available reaction. Given these findings, selection of electrode materials, dimensions, and reactions is of critical importance for pH sensitive samples (e.g., proteins).

While these publications seek to prevent pH excursions in ICP, a stable pH gradient is useful for several applications, such as microbioreactions, and biomolecular separations. To take advantage of this feature of ICP, Cheng et al. developed a microscale pH actuator platform for pH regulation in a microchamber.[78] A controlled change in the pH of the BGE was achieved by injecting excess H^+ or OH^- ions produced by field-enhanced water dissociation at the membrane upon application of a voltage bias. A stable pH gradient produced in this way was used to separate protein mixtures based on their isoelectric points.[79]

Practical aspects of implementing ICP-based techniques

In this section, we summarize the key practical aspects of ICP. We first discuss the most commonly used device designs and fabrication methods for ICP-based techniques. Second, we provide a brief overview of materials that have been used to achieve selective ion transport. Third, we discuss the key aspects of sample composition, including analyte and electrolyte concentrations and mobilities, that dictate the limit of enrichment by one of two mechanisms (e.g., based on electrokinetics or electroneutrality). Further, we introduce additives that can be used to achieve ICP-based enrichment of neutral (uncharged) species. Finally, we give an overview of methods to encapsulate the preconcentrated analyte plug to prevent it from dispersing once the electric field is removed, thereby preserving it for further on- or off- chip analysis.

Device design and fabrication methods

There have been several reviews published describing microfluidic chip materials and fabrication.[80] Silicon, glass, elastomers, thermoplastics, and paper are used for fabricating microfluidic devices. Two-dimensional (2D) microfluidic systems are commonly used to investigate and demonstrate ICP phenomena. More advanced systems with multiple layers, valves and sensors require complex fabrication techniques (layer stacking, 3D printing), and are therefore used less frequently for fundamental studies.

Soft lithography is one of the most commonly used methods for 2D microfluidic device fabrication. Briefly, in soft lithography a master mold is fabricated by patterning a photoresist film on a Si substrate with a high-resolution photomask (lateral resolution approximately 10 µm for a printed mask and 500 nm for a chrome mask). This master mold is used to create a replica in a thermoplastic, by embossing, or in an elastomer, by cast molding. Polydimethylsiloxane (PDMS) is a frequently used elastomer for microdevice fabrication due to its high thermal stability (stable below 400ºC),[81] elasticity, optical transparency, and ability to seal with itself (stacking) or a glass slide after plasma treatment.[82] PDMS devices are disadvantaged by ready adsorption of small hydrophobic molecules and biomolecules onto channel walls, thereby making quantification of enrichment and separation by ICP a challenge. This problem can be partially addressed by modifying the channel walls to increase hydrophilicity – for example, PDMS can be reversibly coated with a block copolymer such as Pluronic F108 or F127, which are comprised of two ethylene glycol segments flanking polypropylene glycol.[53] The impact of such coatings on zeta potential on the channel walls and other device materials must be considered. For example, Pluronic dampens EOF, thereby requiring supplementation with pressure driven flow when convection is needed.

Three-dimensional microfluidic devices (3D) are fabricated by stacking multiple PDMS layers.[25] Out-of-plane or three-dimensional device designs have allowed large contact area between the sample solution and the membrane, thereby supporting increased volumetric throughput (up to 20 µL min^{-1}),[25] higher enrichment factors,[83] and better interfacing with downstream analysis.[84] 3D printing a thermoplastic material circumvents the need for high resolution photomasks, multilayer alignment, timed exposures, or development.[85] However, lower lateral resolution (about 25 µm)[86] and greater surface roughness restrict its applications in ICP.[87] Additionally, the development of thermoplastic materials that would be comparable in stability, elasticity and transparency with PDMS is still ongoing.

Paper microfluidic devices have a relative advantage for point-of-care applications due to their simplicity, low cost, and ease of fabrication.[88–91] To fabricate paper-based ICP devices, channel designs are printed using wax to define walls. An ion selective feature is incorporated by impregnating the paper with a conductive ink or resin solution. Currently, several groups have reported enrichment of low abundance analytes from 60-fold[92,93] to 1000-fold[94] in paper by ICP, and 500-fold by fICP.[90]

Several configurations of the driving electrodes, fluidic channels and ion selective features have been reported.[22] Choice of device design and ion selective feature is governed by the application. Frequently, only one ion selective membrane or electrode is used to generate an IDZ in a microfluidic device. However, there is precedent for dual membrane configurations, in which a voltage bias applied across the membranes in series generates a neighboring IDZ and IEZ.[45] This format has been further employed to prevent propagation of the IDZ in paper fluidics and to achieve CP in water-in-oil droplets.[95] Also, ion selective membrane coated electrodes have been used for unipolar ICP generation, although larger pH excursions limit their application to pH insensitive samples.[75]

Scheme 7 illustrates the most commonly used device configurations for focusing analytes by ICP[96] and fICP.[34,35,97] Single- and dual-channel preconcentration (**Scheme 7a,b**) and dual gate (**Scheme 7c**) designs, are the most common for preconcentration. The dual gate design has a more uniform electric field distribution across the width of the main channel, than do the single and dual-channel preconcentrators, because the voltage is applied on both sides, and ions are depleted symmetrically.[98,99] The dual gate further allows the driving electrodes to be located in the two electrolyte-filled auxiliary channels that are fluidically isolated from the sample, thereby protecting it from large pH excursions.

Ko et al. developed a U-shaped (**Scheme 7d,f**) device which uses only two driving electrodes.[100] This U-shaped design has been used for biomolecule preconcentration, however the electric field is not uniform across all parallel channels. Stronger ICP is observed in channels contacting the portion of the membrane nearest to the ground lead (**Scheme 7f**).

The techniques supported by the designs shown in **Scheme 7g,h,j** are important because they overcome the limitation that ICPF and fICP are traditionally performed as batch processes that have low volume throughput. Split or branching microfluidic devices provide an additional outlet for continuous extraction of focused charged species, micelle-encapsulated uncharged species, particles, and cells (**Scheme 7g**). The fractionation of the sample can be controlled via the ratio of volumetric flow rates in each outlet. This ratio determines the maximum EF, resulting in much more modest enrichment than does accumulation of the analyte (stacking) over a longer period of time. However, it provides access to a sufficient volume of enriched analyte for downstream or off-chip analysis, while transport of an enriched plug results in considerable diffusive broadening. When this branching scheme is utilized in conjunction with fICP, the ability of BPEs to be reconfigured allows for an enriched plug to be directed along the channel while enrichment is maintained36 or transported on-demand to any outlet(s).[101] This active control of focused analytes into separate branches is one of the key advantages of fICP.

Continuous separation of multiple species is achieved by incorporating multiple channels that are branching at the nanojunction creating a “fan” design (**Scheme 7h**).[102,103] The particles and analytes are deflected from the IDZ to a degree that depends on their electrophoretic mobilities and are thereby directed to distinct outlets. A recent example with important environmental impact is the integration of a multi-outlet device with fICP for sorting of microplastics.[104]

Papadimitriou et al. recently developed a method called free flow ICP (FFICP) that yields high resolution separations in a continuously flowing stream.[105] Their device is conceptually similar to the “fan” design in that it has many outlets (**Scheme 7j**). The key distinction is that the sample solution interacts with the IDZ boundary for a greater duration, which allows for more complete focusing. This outcome is accomplished by employing a combination of pressure driven flow components that, relative the applied electric field, are parallel (for focusing) and perpendicular (to carry the analyte(s) to the outlet).

Scheme 7e,i,l show three variations of a design feature that decouples the sample inlet (indicated as S) from that employed for voltage application and introduction of BGE.[106–108]The sample is introduced in a direction that is orthogonal to focusing. This strategy has two primary advantages. First, a highly conductive sample, such as a biofluid, does not have as great an impact on the electrical resistance of the main (focusing) channel, and therefore, higher spatially-averaged electric field strengths are permitted. The problem of high sample conductivity is conventionally addressed by dilution, which slows mass transport of the analyte to the enriched plug and effectively decreases volumetric throughput. Second, the design prevents biofouling by avoiding contact between the driving electrodes and sensitive samples such as biological cells, bioparticles (such as exosomes)[107]and biomolecules.[106,108] A similar outcome can be achieved in a paper-based device by pipetting the sample onto the paper strip during focusing.[88]

The out-of-plane device shown in **Scheme 7k** recapitulates the branched layout of **Scheme 7g** but is rotated 90° and extruded to allow a greater contact area between the nanoporous membrane and the sample. This design required the use of a CO_2 laser to create a slot for insertion of a *Nafion* membrane. The auxiliary (grounded channel) lies above the main channel, which is used, in this case, for water desalting.[25]

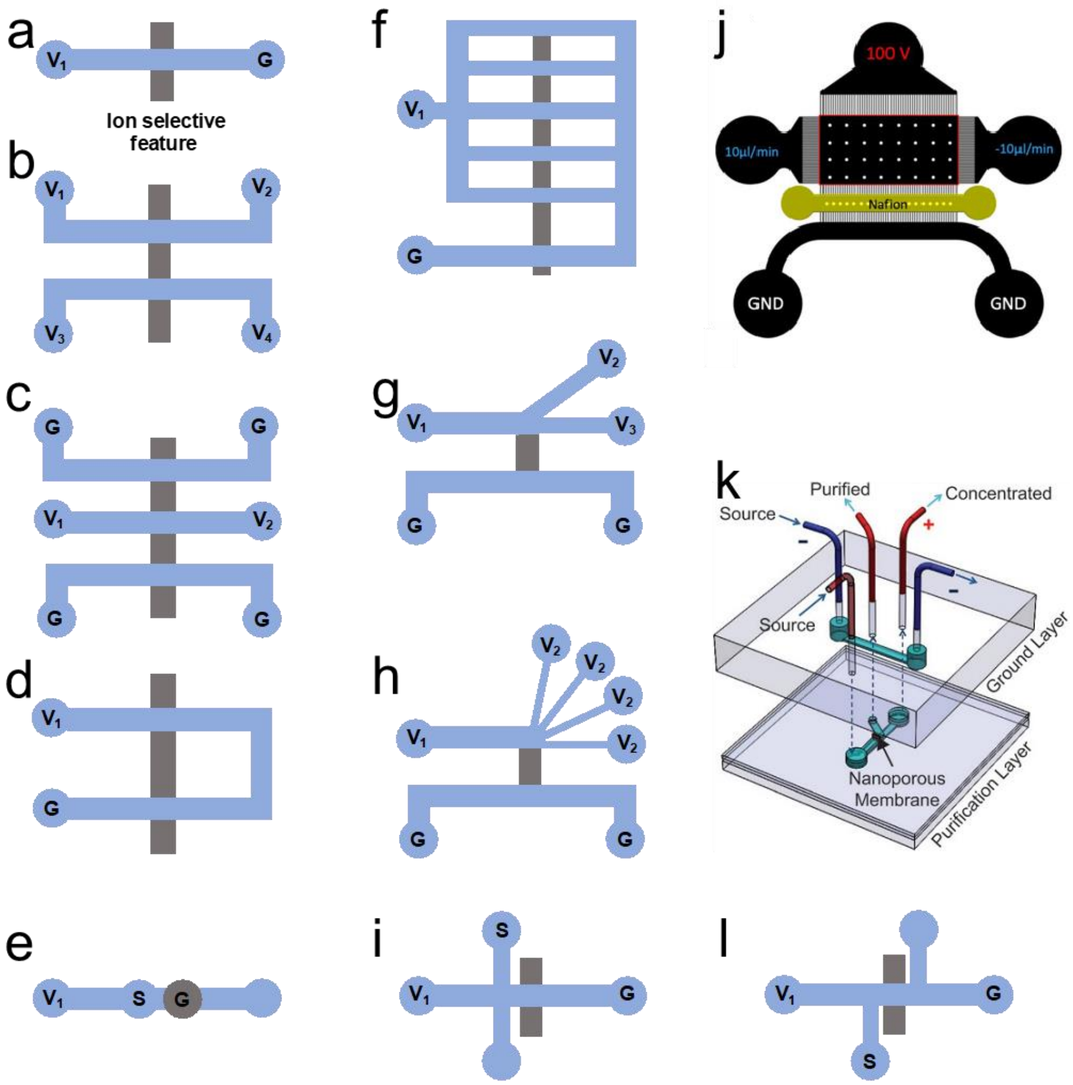

Scheme 7. Schematics of various nanofluidic preconcentration device designs including a) single-channel, b) dual-channel, c) dual gate, d) U-shaped, f) U-shaped with parallel concentrators, g) branched, h) 'fan-shaped', j) FFICP, and k) out-of-plane. e, i, l) Sample inlet (S) distinct from BGE inlet (V_1) and oriented orthogonal to the channel in which focusing occurs. Illustrations in (h) and (i) reproduced from ref. [105] and [25], respectively, with permission.

Ion selective features and their fabrication

Several classes of materials can govern selective ion transport, such as nanoporous membranes and hydrogels, bead beds, nanochannels, and nanotubes. These materials are summarized here, taking into consideration the features relevant to their performance, such as critical dimensions, surface charge density, and exposed area.[53,103]

Ion permselective membranes and hydrogels

Ionic conductivity, hydrophobicity and ease of fabrication are important features to consider when selecting a material for an ion permselective junction. Ion selective resin solutions like *Nafion* (cation selective), and *Sustainion* (anion selective) are commercially available in solution form and therefore are convenient materials for creating nanojunctions. *Nafion* is a sulfonated tetrafluoroethylene-based fluoropolymer with high surface charge of 200-600 mC m^{-2} and has been well characterized owing to its wide application as a proton conductor for proton exchange membrane (PEM) fuel cells. Further, it is highly hydrophobic and resists swelling in water. Therefore, it is an attractive ion selective material. Several methods have been developed to pattern *Nafion*, several of which are briefly summarized in the following paragraph.

The pattern and dimensions of such a resin solution can be defined by microflow patterning, which utilizes a PDMS microfluidic channel that is reversibly bonded to a glass slide.[109] The resin solution is first flushed through the microchannel and then cured to create the membrane (e.g., *Nafion* is cured at 95ºC for 10 min). The microchannel used for patterning is then peeled away, and finally, the glass slide with the patterned membrane is plasma treated and irreversibly bonded to the microchannel to be used for ICP. Importantly, surface area and height of the membrane are governed by the volume and composition of the resin solution and the dimensions of the microchannel dimensions used for patterning. For example, to achieve an approximately 200 nm membrane thickness, Lee et al. filled a 120-µm deep and 200 µm-wide channel with 1.0 µL of the resin solution (5% *Nafion*) and then removed it with suction, leaving only a thin film behind prior to curing.[103] Although membrane dimensions can be controlled well by microflow patterning, this method is restricted to low viscosity resin solutions. Additionally, irreversible bonding of the glass substrate to the PDMS chip can be challenging if the patterned membrane is thicker than 0.5 µm. As the membrane thickness increases, the seal between the glass and PDMS weakens, thus resulting in device failure.

Microcontact printing utilizes a PDMS microstamp to create a surface-patterned ion selective membrane on a glass slide.[110] During this process, the PDMS microstamp is “inked” with the resin solution, which is transferred to the glass slide by applying pressure and is then cured. This patterning method offers less control of the final membrane dimensions, and the membrane dimensions vary due to applied pressure differences while microstamping. The resulting membrane thickness ranges from 0.5 to 1.0 µm, which makes bonding to PDMS challenging.

A mechanical incision method can be utilized to fabricate a high aspect ratio ion selective nanojunction inside a PDMS microchannel.[24,111] In this process, the junction is created by making a mechanical incision across the main and auxiliary channels with a scalpel. The incision is then bent open, filled with ion selective resin (e.g., 20% *Nafion*), sealed, and cured. Residual resin on the PDMS surface is then removed by repeatedly applying low residue tape. Next, the PDMS with embedded nanojunction is irreversibly bonded to a glass slide following plasma treatment.

A fourth approach is to fabricate microdevices with narrow openings between the main channel and a resin- or hydrogel-filled channel.[73,112] In this method, the chip is designed with three parallel microfluidic channels (main, resin, and auxiliary). Resin solution or hydrogel is then injected into the delivery channel and cured. Due to the surface tension at the narrow openings, the resin solution does not fill the neighboring channels. This technique is limited to high viscosity resin solutions (above 12.5% *Nafion* resin solution). The openings must remain small (10-20 µm), and thus fabrication of such microfluidic devices can be somewhat challenging.

Bead beds

As an alternative to ion selective membranes, Syed et al. employed self-assembly of colloidal silica beads (300-900 nm diameter) to create a nanofluidic junction.[99] Self-assembly by evaporation of aqueous phase (1.0 mM phosphate buffer with 0.05 % Tween-20) allowed for creation of a close-packed structure with controlled pore diameter (~45 nm, 15% that of the particle diameter). Additionally, they demonstrated that the surface properties (zeta potential, and therefore ion selectivity) of such colloidal particles can be modified using polyelectrolyte layer-by-layer self-assembly outside the microfluidic chip to achieve high surface charge. Although strong ion depletion occurred and a high EF was achieved (up to 1700-fold), the concentrated plug propagated upstream too rapidly.

Nanotubes

Single-walled carbon nanotubes (SWNTs) provide an alternative nanoporous material for driving ICP.[113] The nanoporous architecture of stacked, entangled SWNTs and the presence of negatively charged carboxy ligands on their surfaces govern ion permselection. It has been demonstrated that a 60 nm-thick SWNT structure exhibits similar conductance to a 500 nm-thick Nafion membrane. The reported SWNT junction was fabricated using a vacuum filtration and film transfer method with the following steps. First, SWNTs were oxidized by suspending them in a strong acid solution (concentrated H_2SO_4:HNO_3 in a 1:3 volume ratio). Second, this SWNT suspension was diluted with ddi water, and the nanotubes were collected on a membrane filter via vacuum filtration. Third, the SWNT and underlying filter were cut to match the junction dimensions and then placed on a clean glass slide. Lastly, the filter was etched with acetone, and the patterned SWNTs were rinsed with isopropyl alcohol. Although the SWNT patterning process is time consuming and labor intensive, the high conductivity, tunable geometry, and chemical properties of the SWNTs can enable the development of high throughput and high aspect ratio ICP devices.

Electrodes for fICP

An electrode can be metallic (e.g., Au, Ag, Pt), carbonaceous (e.g., glassy carbon or graphite), semiconducting (e.g., doped Si, boron doped diamond, indium tin oxide) or nonpolarizable (e.g., Ag/AgCl). Several of these materials have been used to create microband electrodes and BPEs in microfluidic devices using standard photolithographic techniques,[49] such as masking and etching an evaporated metal film or lift-off lithography. Pyrolyzed photoresist carbon (PPC) can be used as an alternative to evaporated metal films.[97,114]

When deciding on the type of electrodes to drive formation of an IDZ, one must consider the composition of the BGE and what electrochemical reactions are available to modulate local ion concentration. Importantly, species that can be neutralized by oxidation or reduction should be present in the sample solution at sufficiently high concentration such that their neutralization significantly decreases ionic strength. For example, Knust and coworkers described depletion driven by water electrolysis.[35] At a cathode, OH^- was generated in sufficient quantities to neutralize a significant fraction of the buffer counter ion $TrisH^+$. Because the cathode is at a negative potential relative to the driving electrode(s), the resulting electric field gradient can be used for anion focusing. Conversely, at an anode, H^+ neutralization of CH_3COO^- forms an electric field gradient that is appropriate in sign for focusing cations. These reactions were carried out on Au electrodes. However, many electrode materials can drive water electrolysis and differ primarily by the overpotential required to achieve a sufficient rate of H^+/OH^- production. If a high field strength is desired, then the best material has a high overpotential for water electrolysis and is resistant to degradation of the electrode itself. The internal resistance of the material should be low to prevent Joule heating. Any chemical reaction that reduces local BGE concentration can be employed for fICP, thus considering available redox reactions in the sample when choosing electrode materials for fICP is important.

Nafion-coated electrodes have been previously used for sensing.[115–117] Kwak et al. employed a *Nafion*-coated electrode to drive half-cell ICP.[75] In this process, the electrode consumes or produces protons by water electrolysis, while the *Nafion* coating prevents hydroxide ion transport. Because of this cation selective transport through the *Nafion*, the faradaic reactions are unipolar. If a *Nafion*-coated cathode is employed, H^+ is consumed at the cathode, resulting in IDZ formation. In contrast, if a *Nafion*-coated anode is used, then H^+ is generated by water splitting, and an IEZ forms. In practice, these electrodes lead to larger shifts in pH than a *Nafion* membrane alone because protons are the only charge carriers (instead of other common BGE cations such as Na^+ or K^+).

To complete the electrical circuit, there must be current at the driving electrodes. The most commonly used driving electrodes are coiled Pt wire, which readily provide current owing to a low overpotential for water electrolysis and a high surface area, or Ag/AgCl electrodes, in which current is supplied without altering the solution pH. While less expensive materials, such as graphite, may be attractive for point-of-care devices, the added overpotential required to drive faradaic processes at their surface necessitates a higher applied voltage, which may not be practical in a low resource setting. Yoon and coworkers reported a TiO_2 photoanode driving electrode, which provides a route to utilize renewable energy.[118] There are opportunities to develop driving electrodes that provide long-lasting current without altering solution pH, for example, by capacitance or pseudocapacitance.[119]

Sample composition

Concentration of the analyte and the electrolyte determine the limit of enrichment

Sample composition has a profound influence on the enrichment and separation of charged analytes. As was discussed in previous subsections of this Tutorial Review, the concentration of the BGE will influence the EDL thickness and Du, which determine the degree of CP. Further, *Du* and co-ion mobility collectively define propagating and non-propagating regimes. The concentration and mobilities of the ions of the BGE and of the analyte(s) are also correlated to the limit of enrichment.

Several studies have shown that a higher EF is achieved for samples with lower initial analyte concentration.[34,37,55] Numerical simulations showed that this limiting behavior is attributable to accumulation of the charged analyte to a sufficiently high concentration to impact the shape of the electric field gradient – i.e., the analyte becomes a significant charge carrier. However, Hong et al. demonstrated that under a distinct set of experimental conditions, the EF is independent of the initial concentration of the analyte.[120] Ouyang et al. explained this phenomenon by introducing two limiting regimes governed by electrokinetics or by electroneutrality.[121] In the electrokinetically limited regime, the distribution of the ions of the BGE defines the electric field profile, and then enrichment is determined by the balance between convective, electrophoretic and diffusive fluxes of the analyte. This regime is defined by a buffer concentration that is several orders of magnitude greater than that of the analyte. In this regime, the EF depends exponentially on both the Péclet number and the mobility of the analyte relative to its co-ion. This dependency means that enrichment is favored by a high mobility analyte, a slow co-ion, and less diffusive broadening. Conversely, when the analyte is a significant charge carrier, the EF will be limited by the availability of counter-ions to pair with the analyte ions to maintain electroneutrality. EF is therefore directly proportional to the counter-ion concentration and is diminished if the analyte and co-ion are highly mobile, which places a greater demand on the counter-ion. After this limit is reached, arrival of additional analyte will lead to widening of the enriched plug while it remains at a fixed concentration.

Complex matrices in biological and environmental applications

Samples relevant to environmental analysis and human health (e.g., blood plasma) can present additional challenges that complicate analyte focusing by ICP. Due to these challenges, only a handful of applications using complex samples have been reported.[29, 111] For example, direct contact to the electrodes or membrane can denature proteins and lead to biofouling of these surfaces. Biofouling can be reduced by initiating IDZ formation prior to injection of a complex sample to repel biomolecules from the junction or by changing the position[111] or material of driving electrodes. For applications in complex matrices, electrode materials that are designed to resist biofouling, such as the nanoporous electrodes developed by Collinson and coworkers, are promising.[122,123] Further ion selective membranes with tunable porosity, ion selectivity, and hydrophilicity have been reported,[124,125] some of which boast high ion conductivity while being comprised of materials more biocompatible than *Nafion*.

Highly abundant proteins, such as albumin in blood, accumulate during ICP-based enrichment and rapidly reach the concentration limit dictated by electroneutrality. In such case, the enriched plug of protein gradually widens, pushing higher mobility species such as nucleic acids back towards the inlet. Han and coworkers addressed this challenge by applying a pulse of pressure at the sample inlet, resulting in the enriched plug of protein being pushed over the IDZ. This approach allowed the protein to be depleted while the enriched band of nucleic acid was retained.[126]

An additional challenge with working in biofluids is their high native ion concentration (~150 mM), which leads to a thin EDL and therefore, to a weak ICP. In such cases, to achieve EDL overlap and strong CP formation, ion selective features with small nanopores (e.g., *Nafion*, 4 nm) must be used. Finally, there are few faradaic reactions available to drive CP in biofluids, such as neutralization of endogenous weak acids and bases, thus limiting implementation of fICP in more complex matrices. Furthermore, neutralization of anionic species such as bicarbonate at an anode will generate an IDZ that is useful for focusing of only cationic analytes.

The high ionic conductivity of biological fluids results in high currents under an applied field, and the result is rapid water electrolysis at the driving electrodes leading to gas bubble formation and Joule heating that can damage a sample or an ion selective membrane, lead to local changes in viscosity, and uneven thermal conditions within the microfluidic channels. High currents in biological fluids can be reduced by dilution with low conductivity electrolytes[88,127]or by introduction of the sample orthogonal to the direction of focusing (as in **Scheme 7e,i,l**).[106–108]

Additives to the sample for sharper IDZ boundary formation

The viscosity of the media or BGE can influence the IDZ stability and propagation. It has been shown that additives that increase the viscosity of the sample can help achieve higher EF by inhibiting Taylor dispersion. To this end, Gao et al. added 0.10% w/v hydroxyethyl cellulose (HEC, *Natrosol*) to the BGE during cation and anion enrichment in a paper microfluidic device.[89] HEC is a nonionic water-soluble polymer commonly used as a thickening agent in cosmetics and pharmaceutical formulations. Addition of HEC to the BGE decreased the enriched dye band width by ~2.5 fold, while increasing the fluorescence intensity of the enriched band by a factor of 3. It is important to note that additives can also change the axial location of the enriched band due to an inverse relationship between viscosity and electrophoretic mobility. Moreover, the authors noticed an approximately 50% decrease in EF (near to that obtained in the absence of HEC) when a HEC concentration above 0.10% w/v was used. The authors did not comment on the cause of the observed decrease, which may be due to excessive dampening of EOF in the paper strip. Thus, the additive concentration for each system must be optimized.

Additives to alter analyte mobility and to achieve focusing of uncharged species

It has been shown previously that uncharged molecules are not affected by the electric field and are therefore unable to be enriched by ICP.[20,128] However, a recent study found that an uncharged dye was repelled from the IDZ during ICP in blood plasma, whereas in phosphate buffer solution, redirection of the dye was not observed. This observation was attributed to intermolecular interactions between the uncharged dye and charged species native to blood plasma.[111] To further investigate this phenomenon and to address the limitation of ICP to only charged analytes, Berzina et al. recently developed continuous micellar electrokinetic focusing (CMEKF), in which uncharged compounds are focused by ICP via their incorporation into an ionic micellar phase.[128] This approach combines concepts of micellar electrokinetic chromatography (MEKC) or micellar capillary electrophoresis (micellar CE) with ICPF.[130] This new technique has enabled a route to further expand the utility of ICP to applications in which focusing of uncharged species is needed, such as water purification, and pharmaceutical and environmental analysis. This approach is generalizable – any binding event that “assigns” charge, can facilitate ICP-based focusing of uncharged species.

Analyte encapsulation following ICPF

A significant challenge to the broad application of ICPF for quantitative analysis is that there have been very few demonstrations of in situ analysis of the focused analyte(s). Further, their transport to a downstream location or off-chip for analysis leads to unwanted dilution due to dispersion. In response to this challenge, several strategies have been developed to “lock in” and collect the enriched analyte band(s) for downstream or off-chip analysis. Here, we summarize recent advancements in the encapsulation of a preconcentrated plug using droplet- and valve-based microfluidic platforms.

Sample preconcentration takes place under continuous flow and therefore, suffers from broadening due to Taylor dispersion when the applied electric field is removed. To remove the need for continuous application of an electric field to sustain the concentrated plug, microfluidic droplet generators can encapsulate the analyte into water-in-oil droplets or gel plugs. Encapsulation offers a straightforward way to preserve the sample concentration for further analysis, such as enzyme activity assays and protein immunoassays.

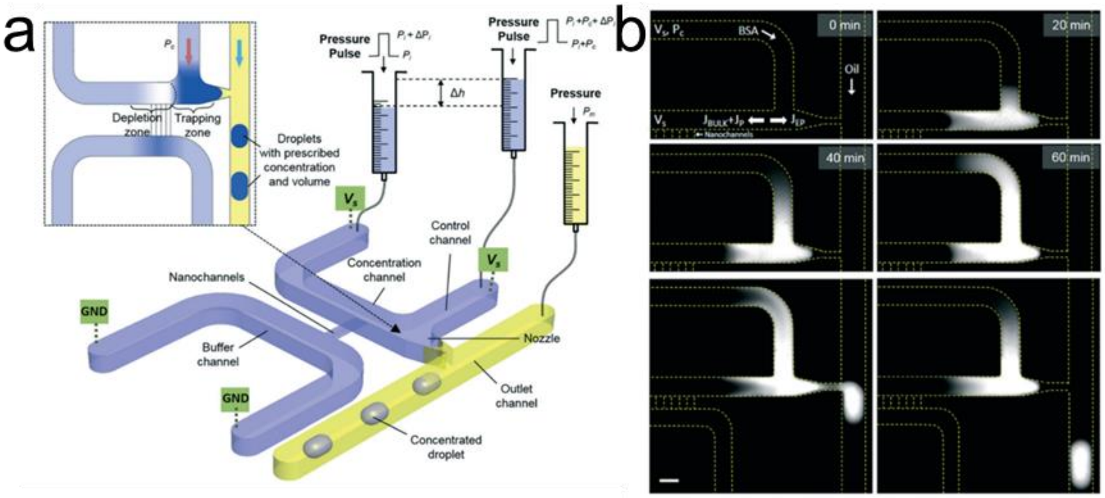

Figure 5. a) Schematic diagram of the nanofluidic concentrator coupled with a droplet-on-demand system; b) Sequential fluorescence images showing the preconcentration process of FITC-BSA in the nanofluidic concentrator at V_s = 120 V and P_c = 1.52 kPa for 60 min. Here, V_s is the voltage bias applied between the sample and the auxiliary channel across the junction, and P_c is the incremental pressure applied to the control channel relative to that at the sample inlet (P_i). Illustration reproduced from ref. [132] with permission.

Phan et al. combined a continuous flow concentrator (branched channel, as in **Scheme 7f**) with a droplet generator in a single device for enriched analyte encapsulation. First, the analyte was preconcentrated by ICP while being redirected into a narrow branching channel. Subsequently, at the end of this channel, the concentrated analyte was enclosed in 25 µm- to 50 µm- water-in-oil droplets.[133] In this device, under a flow rate of 10.0 µL h^{-1} (0.17 µL min^{-1}), 100-fold enrichment of charged species from 1.0 µM to 100 µM was achieved.

Although droplets can serve as an excellent tool to encapsulate concentrated analytes, breaking of the microemulsion is required before some types of analysis. Also, hydrophobic analytes can partition into the oil phase, and thus are not good candidates for droplet-based encapsulation using oil. As an alternative, Deng and coworkers developed a bubble valve device to trap preconcentrated analyte plugs using air (**Figure 6**).[134] To test the device, low abundance C-reactive protein (CRP) (a biomarker for coronary heart disease and atherosclerosis) was successfully preconcentrated and quantified using bead immunoassay. Up to 104-fold enrichment of target analyte was reported, while improving the limit of detection by 4-fold (to 100 pg mL^{-1}).

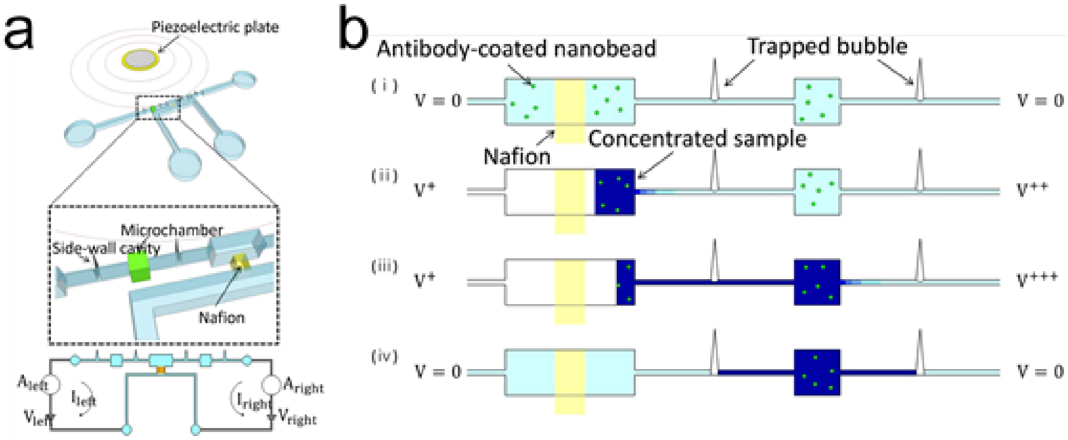

Figure 6. Schematic illustration of a) the electrokinetic preconcentrator with bubble valves, and b) the process by which the concentrated plug of analyte was isolated. Illustration reproduced from ref. [119] with permission.

Choi et al. developed an ICPF device with integrated pneumatic microvalves located between microchambers.[17] The authors demonstrated control over the location of two enriched and separated analyte bands and prevented dispersion after removing the applied voltage. A separation resolution between dyes of 1.75 with an overall EF of up to 100-fold was achieved.

In-droplet ICP

Droplet microfluidics has revolutionized biotechnology owing to an ability to encapsulate individual entities (e.g., single nucleic acids, enzymes, or biological cells) for analysis and to segment a time varying sample (e.g., cell secretions or interstitial fluid from tissues) into pico- to nanoliter aliquots. In this context, concentration enrichment can potentially lead to an increase in the speed of reactions or assay sensitivity. Moreover, manipulation of droplet composition and ion distribution can create opportunities for mobility-based assays. However, extended periods of analyte accumulation from a bulk sample leads to a loss of single-entity isolation or temporal resolution. To address this challenge, Kim et al. developed a method to manipulate concentration profiles inside nanoliter-scale water-in-oil droplets by ICP.[95] This approach achieves both enrichment and separation of charged compounds within a droplet by positioning it between two cation selective membranes that extend along a microchannel like railroad tracks. Each membrane connects the main (droplet) channel to one of two parallel auxiliary channels filled with the BGE (**Figure 7a,b**).

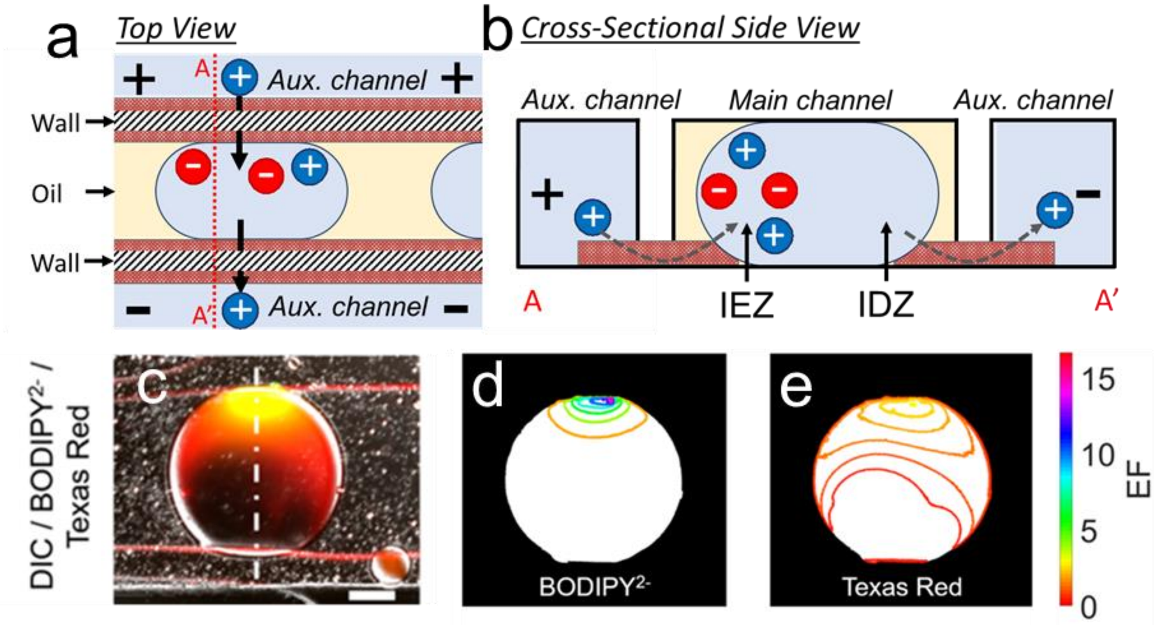

Figure 7. a) Top view and b) cross-sectional side view illustrations of an aqueous droplet positioned between two cation selective membranes (purple) in a microfluidic channel. The membranes interconnect the main (droplet) channel with two parallel auxiliary channels filled with the BGE. Under an applied voltage bias as shown, cations are extracted from and injected into the droplet. Anions migrate toward the anodic membrane to maintain electroneutrality and are therefore enriched, generating an IDZ and IEZ within the droplet. c) Overlay of brightfield and green and red fluorescence micrographs of a droplet containing two fluorescent tracers with distinct electrophoretic mobilities. Isometric contour plots show the distribution of the d) green and e) red dyes in the micrographs shown in (c). Illustration modified from ref. [95] with permission.

A voltage bias applied between the auxiliary channels drives ionic current across the cation selective membrane via the droplet. As a result, cations were depleted from the droplet region nearest to the ground auxiliary channel (cathodic channel), while anions migrated towards the anodic compartment, generating an IDZ and IEZ. 16.7-fold enrichment of an anionic fluorophore (BODIPY disulfonate) and its separation from a second dye (Texas Red) was demonstrated in a 5.5 nL droplet, under 10.0 V voltage bias (**Figure 7c-e**). The in-droplet ICP phenomenon was demonstrated over a wide range of experimental parameters including droplet volume, voltage bias, droplet composition and flow rate. The versatility of this approach indicates a high potential for its application to bioassays, and improvements in speed, sensitivity, and selectivity are expected.

Multistage and high throughput preconcentration

Existing biomolecule nanoconcentrators can achieve 10^2- to 10^6- fold enrichment in one hour, a value limited by the small sample volume (µL scale) from which the analyte is swept during ICP. To increase the volumetric throughput while also increasing the degree of enrichment, devices with staged parallel and serial enrichment units can be used. A microfluidic device with 4 to 64 parallel enrichment channels arranged radially for high throughput enrichment was designed by Lee et al. (**Figure 8**). Here, a buffer channel-less design simplified device fabrication.[135] Ion selection was achieved with printed ion permselective membranes or silver electrodes (for ICP and fICP, respectively) (**Figure 8a,b**). In this device, the diluted sample (35 µL) was injected at the center using a pipette (**Figure 8**, steps *i* and *ii*), and a 10.0 V DC bias was applied between the radial electrode and a wire electrode inserted in the pipette tip. The preconcentrated plugs of analyte migrated backwards towards the center of the device where they were collected with the pipette tip (**Figure 8**, step *iii*). The nanopreconcentrator yielded moderate recovery ratios for polystyrene particles, fluorescent dye, and dsDNA of 85.5%, 79.0%, and 51.3%, respectively, and the preconcentration factor was poor (up to 10-fold).

However, this calculation was based on the concentration of the sample in the collected volume (1 to 5 µL) and not the maximum concentration achieved within the microfluidic channel. The authors indicated that higher enrichment in a shorter time frame can be achieved using a higher initial sample volume and increasing the number of branching channels.

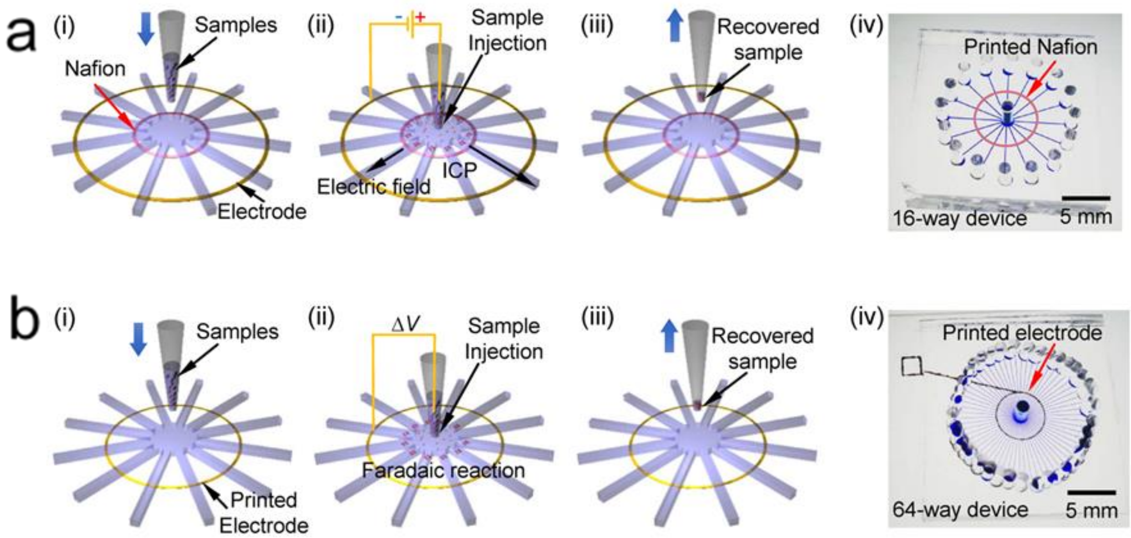

Figure 8. Radial buffer-free preconcentration device with a) *Nafion* junction and b) printed silver electrode. Both devices had the same operating procedure: i) buffer injection and preparation of the sample solution; ii) sample injection and preconcentration of molecules; iii) extraction and recovery of preconcentrated molecules. iv) A photographic image of the devices. Illustration reproduced from ref. [135] with permission.

Recently, Ouyang et al. developed a hierarchical microfluidic molecular enrichment system (HOLMES) that can achieve billion-fold enrichment (10^9) of biomolecules and proteins within 30 min (**Figure 9a**).[83] This high EF is obtained by a four-stage hierarchical concentration process, in which first, parallel nanofluidic concentrators are simultaneously operated to sweep milliliters of sample (up to 10 mL). In this 1st stage, vertically stacked (up to 12) plasma-bonded PDMS layers define chambers, each containing massively parallel microchannels.

A perpendicularly patterned strip of *Nafion* connects these parallel microchannels (blue, **Figure 9b**) to auxiliary channels (green). These concentrators release their contents into successively narrower chambers in the 2nd - 4th stages (**Figure 9c**), in which biomolecule plugs are combined and re-concentrated. The number of parallel microchannels in each chamber is scaled down by 10- or 100-fold per stage.

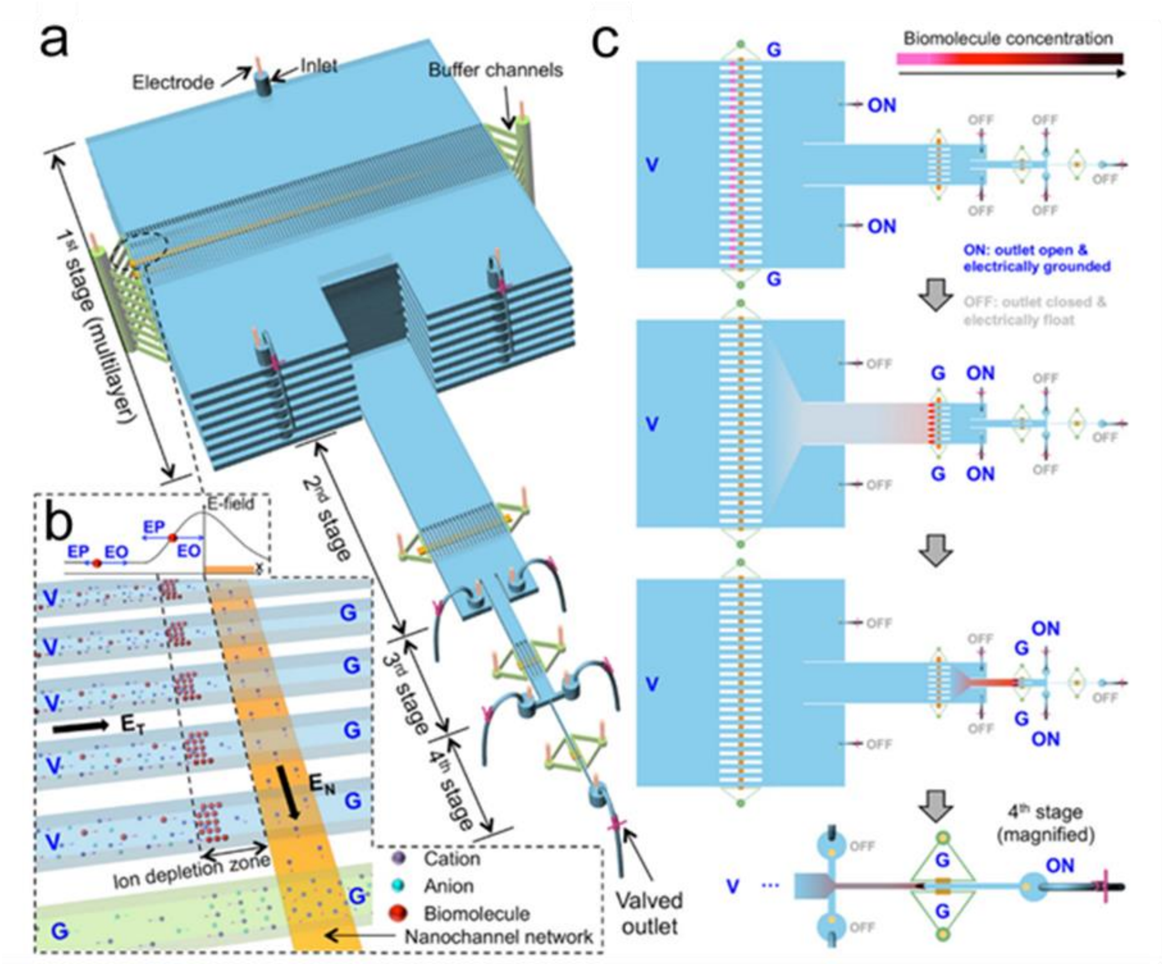

Figure 9. a) Schematic of HOLMES. At each stage, parallel microchannels and buffer channels are bridged by a Nafion membrane. b) Schematic of biomolecule enrichment in the parallel channels. Under the electrical configuration shown, biomolecules are electroosmotically injected into the parallel channels and electrokinetically concentrated just upstream of the IDZs induced at the micro-/nano- channel junctions. The membrane interconnects the microchannels (blue) with an auxiliary channel (green). c) Illustration of staged preconcentration of biomolecules including the locations at which driving electrodes apply positive potentials (ON), ground (G), or are left at a floating potential (OFF). Illustration reproduced from ref. [83] with permission.

Integration of other analytical methods with ICPF

An important hurdle to the broad application of ICPF is the qualitative and quantitative analysis of the enriched target. Thus far, detection has been largely limited to fluorescent or electroactive species. In this section, we summarize in-line detection methods that have been integrated with ICP and discuss how these techniques are applied to various biological systems.

Immunoassay

Several microfluidic devices based on ICP have been developed to preconcentrate biomolecules before detection with immunoassays. The increased concentration of the analyte enhances the sensitivity of these assays. Wang et al. were first to integrate a nanopreconcentrator with a bead bed immunoassay.[98] Following 30 min of enrichment of a sample over antibody-modified beads, they achieved more than 500-fold enhanced sensitivity for the fluorescent protein R-phycoerythrin (PE) from 50 pM to the sub-100 fM range. To test the device with a more complex sample, they added 10 µg mL^{-1} green fluorescent protein (GFP), a non-target protein, to test the influence of an interferent on preconcentration and detection of target molecules. The results indicated that the interferent was co-enriched, but it was not bound to the beads. Thus, this platform shows promise to preconcentrate and detect charged biomolecules in the presence of interferents.

A similar platform was developed for multiplexed enzyme-linked immunosorbent assay (ELISA).[136] In this study, beads modified with antibodies to two prostate cancer-specific antigens were incubated in blood plasma prior to labeling with an enzyme-linked antibody. The beads were then packed into a microchannel, and the substrate for the enzyme flowed across them. ICPF was utilized to enrich the fluorescent product. The sensitivity for the detection of these two cancer markers was enhanced 65- to 100-fold, and five distinct samples were analyzed simultaneously in parallel channels. This same research group later improved multiplexing (up to

128 individually controlled parallel channels) and throughput for this bead-based immunoassay platform.[100]

Enzymatic assay

There have been several reports in which enzymatic assay rate and sensitivity have been be increased by ICPF.[110,137] Lee et al. demonstrated a decreased assay time from 1 h to 10 min along with a 100-fold enhancement of the sensitivity for trypsin (1.0 pg mL^{-1}). Similarly, ICPF was used to enhance an assay for kinase in cell lysate. The protocol yielded a 25-fold increase in reaction rate and a 65-fold enhancement in sensitivity. These improvements allowed a reduction in sample size from 200 μL to 5 μL (equivalent to lysate from ~5 cells) and a shortened assay time (from 1 h to 10-25 min). These results show that ICP can potentially enable a route to single-cell analysis.

Recently, Wei et al. developed a multi-well detection platform with integrated electrokinetic pre-concentrators for enzymatic assays.[30] They integrated 12 ICP preconcentrators with a standard 12-well plate and demonstrated detection of a metalloproteinase (MMP-9) expression in the breast adenocarcinoma cell line MDA-MB-231. Preconcentration by ICP allowed a decreased assay time (by 10 h) and an increase in the overall sensitivity of the assay by an order of magnitude. This result is significant because it demonstrates the practical integration of microfluidic preconcentrators with a microplate assay for standard laboratory use.

Electrochemical sensing

The simultaneous detection of several biomarkers for early diagnosis or prognosis of disease is often challenging due to their extremely low abundance in biological fluids. For example, methylated DNA is believed to be a promising marker for early diagnosis of cancer.

However, the concentration level is found to be in the fM range. Electrochemical biosensors have high sensitivity (on the order of 1 nM), enable quantification, and require minimal equipment. Thus, they are good candidates for point-of-care testing. Techniques like ligase chain reaction[138] and polymerase chain reaction[139] have been used for methylated DNA amplification, previously. However, they are time consuming and tedious. To address the need for a relatively fast and sensitive detection method, Hong et al. developed a valve-based microfluidic chip, in which methylated DNA was preconcentrated by ICPF and then further quantified using a nanostructured gold biosensor (**Figure 10**).[120] Using this microfluidic chip, 100- to 120-fold sample preconcentration was obtained in 10 min, which improved the LOD of methylated DNA from 475 pM to 350 fM in buffer.

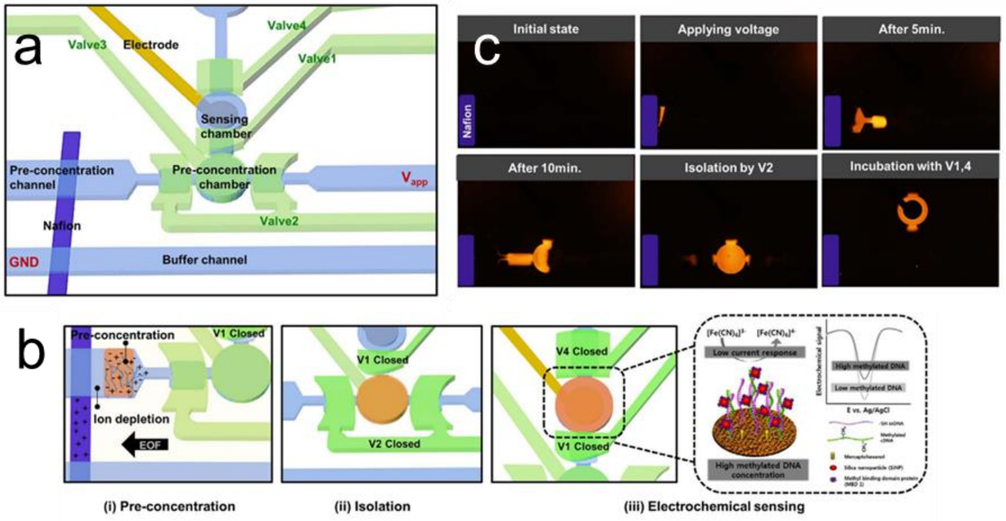

Figure 10. Schematic diagram of the microdevice integrating pre-concentration with electrochemical sensing. a) Schematic diagram of the microfluidic pre-concentration chip; b) working principle of the chip (i) pre-concentration, (ii) isolation and (iii) incubation of the methylated DNA on the electrochemical sensor and in the inset, sensing principle of the electrochemical sensor; c) time-lapse fluorescence images of the DNA pre-concentration and transfer to the sensor. Illustration reproduced from ref. [120] with permission.

Nanostructure-based electrical biosensors have been used for ultrasensitive and label-free biomolecule detection.[140] For example, the electrical resistance of a nanofluidic crystal (NFC) is sensitive to biomolecule binding. However, high sensitivity can only be achieved under low ionic strength conditions, and therefore, sensing under physiological conditions (160 mM) is challenging. At high ionic strength, surface charges are screened by ions of the BGE, and the EDL has a thickness of < 1 nm.

Ouyang et al. demonstrated that electrical detection of biomolecules could be achieved by employing ICP to lower the ionic strength at the NFC biosensor following an initial binding step.[141] Their device consisted of two perpendicular channels with nanofilters located on three sides of the intersection to retain functionalized nanoparticles there (**Figure 11**). After loading the sample at the inlet (**Figure 11**, *I*, at location A), CP was initiated for biomolecule preconcentration near the NFC (**Figure 11**, *II*). Following the incubation step (**Figure 11**, *III*), CP was initiated again to achieve a local decrease in ion concentration by 200-fold near the NFC to facilitate sensing.

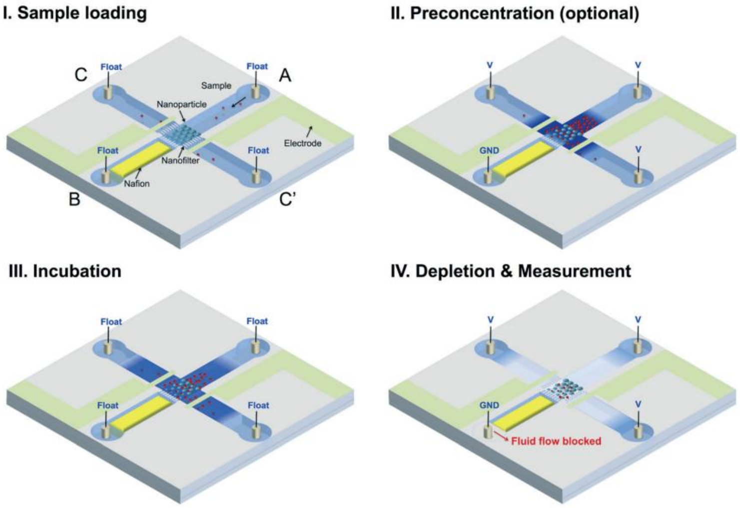

Figure 11. Schematic illustration of the operation of the ICP-coupled nanofluidic crystal for biosensing. Illustration reproduced from ref. [141] with permission.

ICP has been employed not only for analyte preconcentration prior to electrochemical sensing, but also to regenerate sensing substrates. Chen et al. introduced a microfluidic device for real-time continuous bioassays without the requirement of a separate clean buffer solution for rinsing steps (**Figure 12**).[29] In this ‘buffer-free’ device, first, an aptamer sensor was employed for measurement of target biomolecules in human serum. Second, the sensor surface was regenerated to allow repeated assays. To achieve the latter goal, the authors sourced purified water from the human serum by ICP-based repulsion of other plasma components into another microfluidic branch. The results showed that in 10 min after applying the driving voltage, the sensors were completely regenerated.

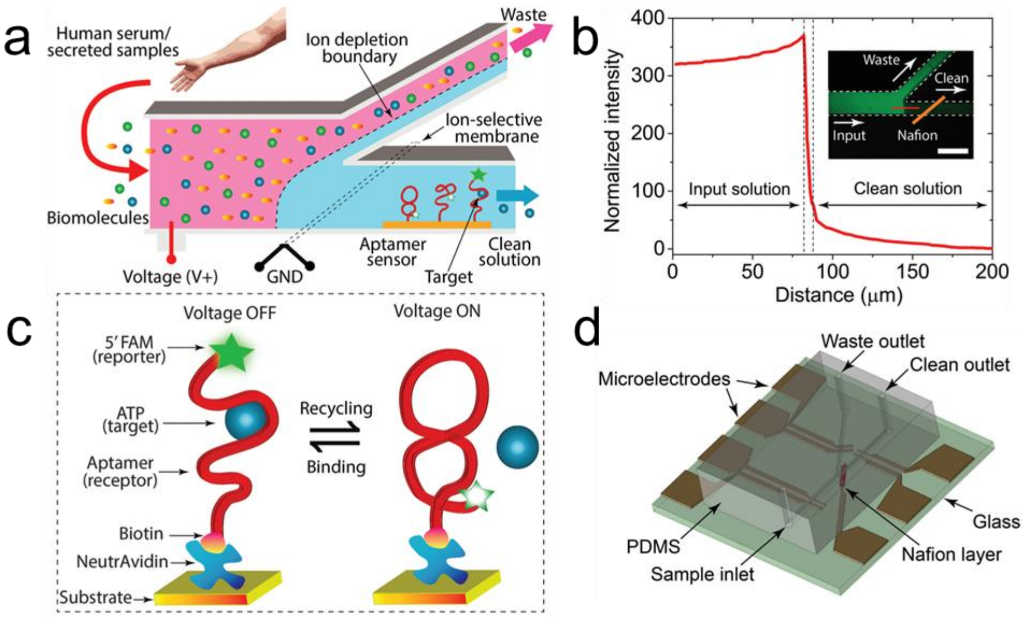

Figure 12. a) Schematic of the nanofluidic device for real-time target biomolecule monitoring; b) the binding of the target biomolecule to the aptamer immobilized on the glass substrate; c) fluorescence micrograph demonstrating ICP-based repulsion of plasma components (green fluorescent dye) into the branching channel (inset scale bar 200 μm); (d) Illustration of the branching microfluidic device with embedded membrane and microelectrodes. Graph demonstrates the normalized fluorescence intensity along the red line across the IDZ. Illustration reproduced from ref. [29] with permission.

The ICP current-voltage curve as a non-optical sensor

A recent innovation overcomes the need for fluorescently labeled targets by leveraging ICP itself as the sensing mechanism. Ion-selective structures respond to a voltage bias with a distinctive nonlinear current-voltage curve that has ohmic, limiting and overlimiting regions

(Section 2.4.). Chang and coworkers demonstrated that binding events that confine charged molecules to the surface of an ion permselective membrane significantly alter the shape of its current-voltage curve.[142,143] For example, hybridization of negatively charged DNA to the surface of an anion selective membrane (positively charged) leads to surface charge inversion and changes ion conductance through the membrane, especially in the overlimiting region.[142,143] These finding suggested that the current-voltage response is sensitive to the presence of charged molecule binding events on the surface of the membrane. Since then, this phenomenon has been used as a reporting mechanism in several assays for biomarkers.[144,145] For example, this method was recently applied to the detection in human serum of ribonucleic acid (RNA) from the mosquito-borne virus that causes dengue fever.[146] The method is label free and requires minimal peripheral equipment, making it well-suited to point-of-care analysis. Four sensors were employed – one specific to each of four serotypes of the dengue virus. Each sensor was an anion selective membrane modified with a probe specific for one serotype. Binding of the target RNA led to a shift in the onset of overlimiting behavior to a higher voltage versus the probe alone. The authors reported excellent specificity, which they attributed to the ability of electroconvection to wash the sensor surface, thereby eliminating non-specific binding. By using this method in concert with upstream one-pot reverse transcriptase PCR (RT-PCR), the authors were able to detect as few as 100 copies of RNA in 1 mL of human plasma.

Summary of tips and tricks

Table 1. Summary of tips and tricks of ICPF

Challenge	Tips and tricks
IDZ instability	➢ Introduce geometric restrictions (decrease channel height and width).[45] ➢ Create an alternate current path through the IDZ by increasing channel surface charge using Nafion coating.[43] ➢ Decrease current density at the ion selective structure by increasing its surface area.[66] ➢ Add microstructuring to the membrane.[65]
IDZ propagation	➢ Apply pressure driven counterflow. ➢ Use dual membranes to define preconcentration in a specific region.[44] ➢ Change ion transport mechanism from ICP to capillarity ICP, in which ion transport is governed by capillary forces and not by an applied external field.[67]
Uncharged analytes not focused	➢ Neutral species do not migrate in response to an electric field gradient. To achieve neutral species separation, ionic surfactants above their critical micelle concentration can be used.[114]
Unwanted pH changes	➢ Change material of the electrode to avoid oxygen evolution reaction (OER) and hydrogen evolution reaction (HER).[71] ➢ Coat the driving electrode with an ion permselective membrane.[64] ➢ Increase the buffer concentration. Change buffer composition (different pKa values for various buffers), and ionic strength.[70]
Sample dispersion once the electric field is removed	➢ Use droplet-based or valve-based encapsulation.[17,117,119,120]
Gas bubble formation and Joule heating	➢ Sample conductivity may be too high. ➢ Dilute the sample to decrease conductivity.[88,127] ➢ Inject the sample orthogonal to the direction of focusing.[106–108] ➢ Apply the voltage between the membrane and an outlet from ion depleted solution exits the device.[111]

Conclusions and future outlook

In this *Tutorial Review*, we have discussed both fundamental and practical aspects of ICP and fICP and summarized recent advancements relevant to the application of ICPF to quantitative analysis. To use ICP effectively, it is important to understand the mechanisms by which ion permselectivity or faradaic reactions can lead to localized depletion of ions of the BGE, and how the resulting electric field gradients facilitate focusing of analytes in the presence of a counter flow. Many distinct device configurations and methods have been developed for applying the requisite electric and flow fields that drive ICPF, and therefore, we have presented the basic principles and relative advantages of each. The greatest experimental challenges in ICPF are the onset of fluid vortices that lead to unwanted mixing, the upstream propagation of the IDZ boundary and analyte plug, unwanted pH excursions near membranes and electrodes, and at high BGE conductivities, Joule heating and gas formation. While strategies to address these challenges are ongoing, there are existing approaches to mitigate their effects, which we discussed throughout the Tutorial Review and included in subsection 5 – *Summary of tips and tricks*.

For new practitioners, we included a brief summary of device design principles and fabrication methods and a more detailed discussion of materials commonly utilized to facilitate selective ion transport or electrochemical reactions. Given the recent push toward high-throughput preconcentrators and the demand for devices that are easier to fabricate (or to manufacture), there is an opportunity to develop materials and device architectures amenable to larger length scales and mass production. As ICPF devices are adopted into broader use, there is a need for user-friendly computational methods that allow device dimensions and experimental parameters to be optimized for a specific application in silico. ICP poses a significant computational challenge including coupled Poisson, Nernst-Planck, and Navier-Stokes equations, and therefore, approaches that reduce computational load are needed.

We further discussed the impact of the sample composition on ICPF. A key advancement in this area is the introduction of scaling laws that describe the theoretical maximum enrichment factor that can be attained. The scaling laws differentiate two distinct regimes that are defined by the ratio of the concentration of the analyte versus that of the BGE. Enrichment is limited by electrokinetics (peak mode) when this ratio is high and electroneutrality (plateau mode) when it is low.[105,121] We also discussed strategies to address the challenges presented by complex biological matrices, such as high ionic conductivity, non-depleted ions (in fICP), and biofouling, and we summarized additives to improve performance, including viscosity modifiers to increase Péclet number and ionic micelles to alter analyte mobility. This latter advancement has allowed for separation of neutral species and can be generalized to any intermolecular interaction that would assign charge, thus expanding the applicability of ICPF.

Owing to the low volumetric throughput of most ICPF devices, integration of focusing with on- or off-chip analysis has been limited. We discuss approaches that address this challenge including encapsulation of analytes in water-in-oil droplets to "lock-in" enrichment during transport off-chip and multi-stage (hierarchical) concentrators that dramatically increase both throughput and enrichment rate. Such increased throughput holds promise to provide sufficient volumes and concentration for integration with mass spectrometric analysis or polymerase chain reaction (PCR). In-droplet ICP allows for enrichment and separation in a confined volume, thereby retaining information from time varying samples and isolation of individual entities (e.g., single nucleic acids, enzymes, or biological cells) and can be integrated into existing droplet microfluidic workflows. Finally, we describe progress in the quantification of analytes by interfacing ICP preconcentrators with immunoassays, enzymatic assays, and electrochemical sensing, and we highlight a very recent advancement, in which binding events at an ion-selective membrane are detected via resulting changes in the current-voltage curve obtained during ICP.

In addition to providing background knowledge of ICPF, this Tutorial Review summarizes "tips and tricks" for new practitioners and provides insight into aspects of ICPF most in need of advancement. We anticipate progress in the following areas: rapid or more facile device construction (especially high-throughput) including biocompatible, high surface area, and

3-dimensional materials for the ion-selective junction; methods for addressing high conductivity and biofouling in complex matrices; the development of user-friendly computational models to aid in customization of devices for new applications; methods that leverage intermolecular interactions (such as analyte encapsulation in micelles); integration of high-throughput ICPF with a wider variety of analytical methods; and extension of recently introduced concepts such as in-droplet ICP and sensing via the ICP current-voltage curve to a wider set of analytical challenges.

CRediT authorship contribution statement

Beatrise Berzina: Writing - original draft. Robbyn Anand: Writing - review & editing.

Declaration of competing interest

The authors declare that they have no known competing financial interests or personal relationships that could have appeared to influence the work reported in this paper.

Acknowledgements

This material is based upon work supported by the National Science Foundation under Grant No. (1849109).

References

1. Wong, P. K.; Wang, T. H.; Deval, J. H.; Ho, C. M. Electrokinetics in Micro Devices for Biotechnology Applications. *IEEE/ASME Trans. Mechatronics* **2004**, *9*, 366–376.

2. Burke, J. M.; Smith, C. D.; Ivory, C. F. Development of a Membrane-Less Dynamic Field Gradient Focusing Device for the Separation of Low-Molecular-Weight Molecules. *Electrophoresis* **2010**, *31*, 902–909.
3. Sun, X.; Farnsworth, P. B.; Tolley, H. D.; Warnick, K. F.; Woolley, A. T.; Lee, M. L. Performance Optimization in Electric Field Gradient Focusing. *J. Chromatogr. A* **2009**, *1216*, 159–164.
4. Lin, S. L.; Li, Y.; Tolley, H. D.; Humble, P. H.; Lee, M. L. Tandem Electric Field Gradient Focusing System for Isolation and Concentration of Target Proteins. *J. Chromatogr. A* **2006**, *1125*, 254–262.
5. Humble, P. H.; Kelly, R. T.; Woolley, A. T.; Tolley, H. D.; Lee, M. L. Electric Field Gradient Focusing of Proteins Based on Shaped Ionically Conductive Acrylic Polymer. *Anal. Chem.* **2004**, *76*, 5641–5648.
6. Koegler, W. S.; Ivory, C. F. Focusing Proteins in an Electric Field Gradient. *J. Chromatogr. A* **1996**, *726*, 229–236.
7. Sustarich, J. M.; Storey, B. D.; Pennathur, S. Field-Amplified Sample Stacking and Focusing in Nanofluidic Channels. *Phys. Fluids* **2010**, *22*, 112003.
8. Li, C.; Yang, Y.; Craighead, H. G.; Lee, K. H. Isoelectric Focusing in Cyclic Olefin Copolymer Microfluidic Channels Coated by Polyacrylamide Using a UV Photografting Method. *Electrophoresis* **2005**, *26*, 1800–1806.
9. Jung, B.; Bharadwaj, R.; Santiago, J. G. On-Chip Millionfold Sample Stacking Using Transient Isotachophoresis. *Anal. Chem.* **2006**, *78*, 2319–2327.
10. Malá, Z.; Gebauer, P.; Boček, P. Recent Progress in Analytical Capillary Isotachophoresis. *Electrophoresis* **2015**, *36*, 2–14.

11. Ross, D.; Locascio, L. E. Microfluidic Temperature Gradient Focusing. *Anal. Chem*. **2002**, *74*, 2556–2564.
12. Hoebel, S. J.; Balss, K. M.; Jones, B. J.; Malliaris, C. O.; Munson, M. S.; Vreeland, W. N.; Ross, D. Scanning Temperature Gradient Focusing. *Anal. Chem*. **2006**, *78*, 7186–7190.
13. Balss, K. M.; Vreeland, W. N.; Phinney, K. W.; Ross, D. Simultaneous Concentration and Separation of Enantiomers with Chiral Temperature Gradient Focusing. *Anal. Chem*. **2004**, *76*, 7243–7249.
14. Li, M.; Anand, R. K. Recent Advancements in Ion Concentration Polarization. *Analyst* **2016**, *141*, 3496–3510.
15. Leinweber, F. C.; Tallarek, U. Nonequilibrium Electrokinetic Effects in Beds of Ion-Permselective Particles. *Langmuir* **2004**, *20*, 11637–11648.
16. Pu, Q.; Yun, J.; Temkin, H.; Liu, S. Ion-Enrichment and Ion-Depletion Effect of Nanochannel Structures. *Nano Lett*. **2004**, *4*, 1099–1103.
17. Choi, J.; Huh, K.; Moon, D. J.; Lee, H.; Son, S. Y.; Kim, K.; Kim, H. C.; Chae, J. H.; Sung, G. Y.; Kim, H. Y.; et al. Selective Preconcentration and Online Collection of Charged Molecules Using Ion Concentration Polarization. *RSC Adv*. **2015**, *5*, 66178–66184.
18. Cheow, L. F.; Sarkar, A.; Kolitz, S.; Lauffenburger, D.; Han, J. Detecting Kinase Activities from Single Cell Lysate Using Concentration-Enhanced Mobility Shift Assay. *Anal. Chem*. **2014**, *86*, 7455–7462.

19. Zangle, T. A.; Mani, A.; Santiago, J. G. Theory and Experiments of Concentration Polarization and Ion Focusing at Microchannel and Nanochannel Interfaces. *Chem. Soc. Rev*. **2010**, *39*, 1014.
20. Kim, S. J.; Song, Y. A.; Han, J. Nanofluidic Concentration Devices for Biomolecules Utilizing Ion Concentration Polarization: Theory, Fabrication, and Applications. *Chem. Soc. Rev*. **2010**, *39*, 912–922.
21. Wang, C.; Wang, Y.; Zhou, Y.; Wu, Z. Q.; Xia, X. H. High-Performance Bioanalysis Based on Ion Concentration Polarization of Micro-/Nanofluidic Devices. *Anal. Bioanal. Chem*. **2019**, *411*, 4007–4016.
22. Fu, L. M.; Hou, H. H.; Chiu, P. H.; Yang, R. J. Sample Preconcentration from Dilute Solutions on Micro/Nanofluidic Platforms: A Review. *Electrophoresis* **2018**, *39*, 289–310.
23. Hlushkou, D.; Knust, K. N.; Crooks, R. M.; Tallarek, U. Numerical Simulation of Electrochemical Desalination. *J. Phys. Condens. Matter* **2016**, *28*, 1–28.
24. Kim, S. J.; Ko, S. H.; Kang, K. H.; Han, J. Direct Seawater Desalination by Ion Concentration Polarization. *Nat. Nanotechnol*. **2010**, *5*, 297–301.
25. MacDonald, B. D.; Gong, M. M.; Zhang, P.; Sinton, D. Out-of-Plane Ion Concentration Polarization for Scalable Water Desalination. *Lab Chip* **2014**, *14*, 681–685.
26. Roelofs, S. H.; Van Den Berg, A.; Odijk, M. Microfluidic Desalination Techniques and Their Potential Applications. *Lab Chip* **2015**, *15*, 3428–3438.
27. Kwak, R.; Kim, S. J.; Han, J. Continuous-Flow Biomolecule and Cell Concentrator by Ion Concentration Polarization. *Anal. Chem*. **2011**, *83*, 7348–7355.

28. Anand, R. K.; Johnson, E. S.; Chiu, D. T. Negative Dielectrophoretic Capture and Repulsion of Single Cells at a Bipolar Electrode: The Impact of Faradaic Ion Enrichment and Depletion. *J. Am. Chem. Soc*. **2015**, *137*, 776–783.
29. Phan, D.-T.; Jin, L.; Wustoni, S.; Chen, C.-H. Buffer-Free Integrative Nanofluidic Device for Real-Time Continuous Flow Bioassays by Ion Concentration Polarization. *Lab Chip* **2018**, *18*, 3962–3979.
30. Wei, X.; Do, V. Q.; Pham, S. V.; Martins, D.; Song, Y. A. A Multiwell-Based Detection Platform with Integrated PDMS Concentrators for Rapid Multiplexed Enzymatic Assays. *Sci. Rep*. **2018**, *8*, 1–11.
31. Yu, S.; Jeon, T. J.; Kim, S. M. Active Micromixer Using Electrokinetic Effects in the Micro/Nanochannel Junction. *Chem. Eng. J*. **2012**, *197*, 289–294.
32. Chiu, P. H.; Chang, C. C.; Yang, R. J. Electrokinetic Micromixing of Charged and Non-Charged Samples near Nano-Microchannel Junction. *Microfluid. Nanofluidics* **2013**, *14*, 839–844.
33. Jännig, O.; Nguyen, N. T. A Polymeric High-Throughput Pressure-Driven Micromixer Using a Nanoporous Membrane. *Microfluid. Nanofluidics* **2011**, *10*, 513–519.
34. Anand, R. K.; Sheridan, E.; Knust, K. N.; Crooks, R. M. Bipolar Electrode Focusing: Faradaic Ion Concentration Polarization. *Anal. Chem*. **2011**, *83*, 2351–2358.
35. Knust, K. N.; Sheridan, E.; Anand, R. K.; Crooks, R. M. Dual-Channel Bipolar Electrode Focusing: Simultaneous Separation and Enrichment of Both Anions and Cations. *Lab Chip* **2012**, *12*, 4107.

36. Perdue, R. K.; Laws, D. R.; Hlushkou, D.; Tallarek, U.; Crooks, R. M. Bipolar Electrode Focusing: The Effect of Current and Electric Field on Concentration Enrichment. *Anal. Chem*. **2009**, *81*, 10149–10155.

37. Hlushkou, D.; Perdue, R. K.; Dhopeshwarkar, R.; Crooks, R. M.; Tallarek, U. Electric Field Gradient Focusing in Microchannels with Embedded Bipolar Electrode. *Lab Chip* **2009**, *9*, 1903–1913.

38. Davies, C. D.; Yoon, E.; Crooks, R. M. Continuous Redirection and Separation of Microbeads by Faradaic Ion Concentration Polarization. *Chem Electro Chem* **2018**, *5*, 877–884.

39. Kim, S. J.; Wang, Y.-C.; Lee, J. H.; Jang, H.; Han, J. Concentration Polarization and Nonlinear Electrokinetic Flow near Nanofluidic Channel. *Phys. Rev. Lett*. **2007**, *99*, 1–9.

40. Zhou, K.; Kovarik, M. L.; Jacobson, S. C. Surface-Charge Induced Ion Depletion and Sample Stacking near Single Nanopores in Microfluidic Devices. *J. Am. Chem. Soc*. **2008**, *130*, 8614–8616.

41. Mani, A.; Zangle, T. A.; Santiago, J. G. On the Propagation of Concentration Polarization from Microchannel-Nanochannel Interfaces. Part I: Analytical Model and Characteristic Analysis. *Langmuir* **2009**, *25*, 3898–3908.

42. Zangle, T. A.; Mani, A.; Santiago, J. G. On the Propagation of Concentration Polarization from Microchannel-Nanochannel Interfaces Part II: Numerical and Experimental Study Thomas. *Langmuir* **2009**, *25*, 3909–3916.

43. Kim, S. M.; Burns, M. A.; Hasselbrink, E. F. Electrokinetic Protein Preconcentration Using a Simple Glass/ Poly(Dimethylsiloxane) Microfluidic Chip. *Anal. Chem*. **2006**, *78*, 4779–4785.

44. Kim, J.; Cho, I.; Lee, H.; Kim, S. J. Ion Concentration Polarization by Bifurcated Current Path. *Sci. Rep*. **2017**, *7*, 1–12.
45. Kwak, R.; Kang, J. Y.; Kim, T. S. Spatiotemporally Defining Biomolecule Preconcentration by Merging Ion Concentration Polarization. *Anal. Chem*. **2016**, *88*, 988–996.
46. Kim, K.; Kim, W.; Lee, H.; Kim, S. J. Stabilization of Ion Concentration Polarization Layer Using Micro Fin Structure for High-Throughput Applications. *Nanoscale* **2017**, *9*, 3466–3475.
47. Nam, S.; Cho, I.; Heo, J.; Lim, G.; Bazant, M. Z.; Moon, D. J.; Sung, G. Y.; Kim, S. J. Experimental Verification of Overlimiting Current by Surface Conduction and Electro-Osmotic Flow in Microchannels. *Phys. Rev. Lett*. **2015**, *114*, 1–5.
48. Crooks, R. M. Principles of Bipolar Electrochemistry. *Chem Electro Chem* **2016**, 3, 357–359.
49. Fosdick, S. E.; Knust, K. N.; Scida, K.; Crooks, R. M. Bipolar Electrochemistry. *Angew. Chemie - Int. Ed*. **2013**, *52*, 10438–10456.
50. Davies, C. D.; Yoon, E.; Crooks, R. M. Continuous Redirection and Separation of Microbeads by Faradaic Ion Concentration Polarization. *Chem Electro Chem* **2017**, *4*, 1–9.
51. Sheridan, E.; Hlushkou, D.; Knust, K. N.; Tallarek, U.; Crooks, R. M. Enrichment of Cations via Bipolar Electrode Focusing. *Anal. Chem*. **2012**, *84*, 7393–7399.
52. Hlushkou, D.; Dhopeshwarkar, R.; Crooks, R. M.; Tallarek, U. The Influence of Membrane Ion-Permselectivity on Electrokinetic Concentration Enrichment in Membrane-Based Preconcentration Units. *Lab Chip* **2008**, *8*, 1153–1162.

53. Kim, M.; Jia, M.; Kim, T. Ion Concentration Polarization in a Single and Open Microchannel Induced by a Surface-Patterned Perm-Selective Film. *Analyst* **2013**, *138*, 1370.

54. Jia, M.; Kim, T. Multiphysics Simulation of Ion Concentration Polarization Induced by a Surface-Patterned Nanoporous Membrane in Single Channel Devices. *Anal. Chem*. **2014**, *86*, 10365–10372.

55. Wang, Y. C.; Stevens, A. L.; Han, J. Million-Fold Preconcentration of Proteins and Peptides by Nanofluidic Filter. *Anal. Chem*. **2005**, *77*, 4293–4299.

56. Cheow, L. F.; Han, J. Continuous Signal Enhancement for Sensitive Aptamer Affinity Probe Electrophoresis Assay Using Electrokinetic Concentration. *Anal. Chem*. **2011**, *83*, 7086–7093.

57. Choi, J.; Baek, S.; Kim, H. C.; Chae, J. H.; Koh, Y.; Seo, S. W.; Lee, H.; Kim, S. J. Nanoelectrokinetic Selective Preconcentration Based on Ion Concentration Polarization. *Biochip J*. **2020**, *14*, 100–109.

58. Baek, S.; Choi, J.; Son, S. Y.; Kim, J.; Hong, S.; Kim, H. C.; Chae, J. H.; Lee, H.; Kim, S. J. Dynamics of Driftless Preconcentration Using Ion Concentration Polarization Leveraged by Convection and Diffusion. *Lab Chip* **2019**, *19*, 3190–3199.

59. Lee, H.; Choi, J.; Jeong, E.; Baek, S.; Kim, H. C.; Chae, J. H.; Koh, Y.; Seo, S. W.; Kim, J. S.; Kim, S. J. DCas9-Mediated Nanoelectrokinetic Direct Detection of Target Gene for Liquid Biopsy. *Nano Lett*. **2018**, *18*, 7642–7650.

60. Tallarek, U.; Perdue, R. K.; Crooks, R. M.; Hlushkou, D.; Laws, D. R. Bipolar Electrode Focusing: Simultaneous Concentration Enrichment and Separation in a Microfluidic Channel Containing a Bipolar Electrode. *Anal. Chem*. **2009**, *81*, 8923–8929.

61. Duffy, D. C.; McDonald, J. C.; Schueller, O. J. A.; Whitesides, G. M. Rapid Prototyping of Microfluidic Systems in Poly(Dimethylsiloxane). *Anal. Chem.* **1998**, *70*, 4974–4984.

62. Hellmich, W.; Regtmeier, J.; Duong, T. T.; Ros, R.; Anselmetti, D.; Ros, A. Poly(Oxyethylene) Based Surface Coatings for Poly(Dimethylsiloxane) Microchannels. *Langmuir* **2005**, *21*, 7551–7557.

63. Doherty, E. A. S.; Meagher, R. J.; Albarghouthi, M. N.; Barron, A. E. Microchannel Wall Coatings for Protein Separations by Capillary and Chip Electrophoresis. *Electrophoresis* **2003**, *24*, 34–54.

64. Kim, S. J.; Li, L. D.; Han, J. Amplified Electrokinetic Response Concentration Polarization near Nanofluidic Channel. *Langmuir* **2009**, *25*, 7759–7765.

65. Yossifon, G.; Chang, H. C. Changing Nanoslot Ion Flux with a Dynamic Nanocolloid Ion-Selective Filter: Secondary Overlimiting Currents Due to Nanocolloid-Nanoslot Interaction. *Phys. Rev. E* **2010**, *81*, 1–6.

66. Zaltzman, B.; Rubinstein, I. Electro-Osmotic Slip and Electroconvective Instability. *J. Fluid Mech.* **2007**, *579*, 173–226.

67. Rubinstein, I.; Shtilman, L. Voltage against Current Curves of Cation Exchange Membranes. *J. Chem. Soc. Faraday Trans. 2 Mol. Chem. Phys.* **1979**, *75*, 231–246.

68. Rubinshtein, I.; Zaltzman, B.; Pretz, J.; Linder, C. Experimental Verification of the Electroosmotic Mechanism of Overlimiting Conductance through a Cation Exchange Electrodialysis Membrane. Russ. *J. Electrochem.* **2002**, *38*, 853–863.

69. Park, S. Y.; Russo, C. J.; Branton, D.; Stone, H. A. Eddies in a Bottleneck: An Arbitrary Debye Length Theory for Capillary Electroosmosis. *J. Colloid Interface Sci.* **2006**, *297*, 832–839.

70. Dydek, E. V.; Zaltzman, B.; Rubinstein, I.; Deng, D. S.; Mani, A.; Bazant, M. Z. Overlimiting Current in a Microchannel. *Phys. Rev. Lett*. **2011**, *107*, 1–5.
71. De Valença, J.; Jõgi, M.; Wagterveld, R. M.; Karatay, E.; Wood, J. A.; Lammertink, R. G. H. Confined Electroconvective Vortices at Structured Ion Exchange Membranes. *Langmuir* **2018**, *34*, 2455–2463.
72. Yossifon, G.; Mushenheim, P.; Chang, Y. C.; Chang, H. C. Eliminating the Limiting-Current Phenomenon by Geometric Field Focusing into Nanopores and Nanoslots. *Phys. Rev. E* **2010**, *81*, 1–13.
73. Oh, Y.; Lee, H.; Son, S. Y.; Kim, S. J.; Kim, P. Capillarity Ion Concentration Polarization for Spontaneous Biomolecular Preconcentration Mechanism. *Biomicrofluidics* **2016**, *10*, 1–12.
74. Mai, J.; Miller, H.; Hatch, A. V. Spatiotemporal Mapping of Concentration Polarization Induced PH Changes at Nanoconstrictions. *ACS Nano* **2012**, *6*, 10206–10215.
75. Kwak, R.; Han, J. Half-Cell Ion Concentration Polarization on Nafion-Coated Electrode. *J. Phys. Chem. Lett*. **2018**, *9*, 2991–2999.
76. Andersen, M. B.; Rogers, D. M.; Mai, J.; Schudel, B.; Hatch, A. V.; Rempe, S. B.; Mani, A. Spatiotemporal PH Dynamics in Concentration Polarization near Ion-Selective Membranes. *Langmuir* **2014**, *30*, 7902–7912.
77. Kim, W.; Oh, J.; Kwon, S.; Kim, K.; Kim, S. J. Quantifying the PH Shift Induced by Selective Anodic Electrochemical Reactions in the Ion Concentration Polarization Phenomenon. *Lab Chip* **2019**, *19*, 1359–1369.
78. Cheng, L. J.; Chang, H. C. Microscale PH Regulation by Splitting Water. *Biomicrofluidics* **2011**, *5*, 046502.

79. Cheng, L. J.; Chang, H. C. Switchable PH Actuators and 3D Integrated Salt Bridges as New Strategies for Reconfigurable Microfluidic Free-Flow Electrophoretic Separation. *Lab Chip* **2014**, *14*, 979–987.
80. Ren, K.; Zhou, J.; Wu, H. Materials for Microfluidic Chip Fabrication. *Acc. Chem. Res.* **2013**, *46*, 2396–2406.
81. Camino, C.; Lomakin, S. M.; Lazzari, M. Polydimethylsiloxane Thermal Degradation Part 1. Kinetic Aspects. *Polymer* **2001**, *42*, 2395–2402.
82. McDonald, J. C.; Whitesides, G. M. Poly (Dimethylsiloxane) as a Material for Fabricating Microfluidic Devices. *Acc. Chem. Res*. **2002**, *35*, 491–499.
83. Ouyang, W.; Han, J. Universal Amplification-Free Molecular Diagnostics by Billion-Fold Hierarchical Nanofluidic Concentration. *Proc. Natl. Acad. Sci*. **2019**, *116*, 16240–16249.
84. Hong, S. A.; Kim, Y.-J.; Kim, S. J.; Yang, S. Electrochemical Detection of Methylated DNA on a Microfluidic Chip with Nanoelectrokinetic Pre-Concentration. *Biosens. Bioelectron*. **2018**, *107*, 103–110.
85. Pi, H.; Tong, J.; Bian, C.; Xia, S. 3D Printed Micro/Nanofluidic Preconcentrator for Charged Sample Based on Ion Concentration Polarization. *J. Micromechanics Microengineering* **2017**, *27*, 055008.
86. O'Neill, P. F.; Azouz, A. Ben; M. Vázquez, J. L.; Marczak, S.; Slouka, Z.; Chang, H. C.; Diamond, D.; Brabazon, D. Advances in Three-Dimensional Rapid Prototyping of Microfluidic Devices for Biological Applications. *Biomicrofluidics* **2014**, 8.

87. Waheed, S.; Cabot, J. M.; Macdonald, N. P.; Lewis, T.; Guijt, R. M.; Paull, B.; Breadmore, M. C. 3D Printed Microfluidic Devices: Enablers and Barriers. *Lab Chip* **2016**, *16*, 1993–2013.

88. Gao, H.; Liu, J. J.; Liu, Y. Q.; Wu, Z. Y. Detection of Urine Protein by a Paper-Based Analytical Device Enhanced with Ion Concentration Polarization Effect. *Microfluid. Nanofluidics* **2019**, *23*, 1–7.

89. Gao, H.; Xie, M. R.; Liu, J. J.; Fang, F.; Wu, Z. Y. Electrokinetic Stacking on Paper-Based Analytical Device by Ion Concentration Polarization with Ion Exchange Membrane Interface. *Microfluid. Nanofluidics* **2018**, *22*, 1–8.

90. Li, X.; Luo, L.; Crooks, R. M. Faradaic Ion Concentration Polarization on a Paper Fluidic Platform. *Anal. Chem*. **2017**, *89*, 4294–4300.

91. Yang, Y.; Noviana, E.; Nguyen, M. P.; Geiss, B. J.; Dandy, D. S.; Henry, C. S. Paper-Based Microfluidic Devices: Emerging Themes and Applications. *Anal. Chem*. **2017**, *89,* 71–91.

92. Son, S. Y.; Lee, H.; Kim, S. J. Paper-Based Ion Concentration Polarization Device for Selective Preconcentration of Muc1 and Lamp-2 Genes. *Micro Nano Syst. Lett*. **2017**, *5*, 1–5.

93. Phan, D. T.; Shaegh, S. A. M.; Yang, C.; Nguyen, N. T. Sample Concentration in a Microfluidic Paper-Based Analytical Device Using Ion Concentration Polarization. *Sensors Actuators, B Chem*. **2016**, *222*, 735–740.

94. Han, S. Il; Hwang, K. S.; Kwak, R.; Lee, J. H. Microfluidic Paper-Based Biomolecule Preconcentrator Based on Ion Concentration Polarization. *Lab Chip* **2016**, *16*, 2219–2227.

95. Kim, S.; Ganapathysubramanian, B.; Anand, R. K. Concentration Enrichment, Separation, and Cation Exchange in Nanoliter-Scale Water-in-Oil Droplets. *J. Am. Chem. Soc*. **2020**, *142*, 3196–3204.

96. Son, S. Y.; Lee, S.; Lee, H.; Kim, S. J. Engineered Nanofluidic Preconcentration Devices by Ion Concentration Polarization. *Biochip J*. **2016**, *10*, 251–261.

97. Knust, K. N.; Hlushkou, D.; Anand, R. K.; Tallarek, U.; Crooks, R. M. Electrochemically Mediated Seawater Desalination. *Angew. Chemie - Int. Ed*. **2013**, *52*, 8107–8110.

98. Wang, Y. C.; Han, J. Pre-Binding Dynamic Range and Sensitivity Enhancement for Immuno-Sensors Using Nanofluidic Preconcentrator. *Lab Chip* **2008**, *8*, 392–394.

99. Syed, A.; Mangano, L.; Mao, P.; Han, J.; Song, Y.-A. Creating Sub-50 Nm Nanofluidic Junctions in a PDMS Microchip via Self-Assembly Process of Colloidal Silica Beads for Electrokinetic Concentration of Biomolecules. *Lab Chip* **2014**, *14*, 4455–4460.

100. Ko, S. H.; Kim, S. J.; Cheow, L. F.; Li, L. D.; Kang, K. H.; Han, J. Massively Parallel Concentration Device for Multiplexed Immunoassays. *Lab Chip* **2011**, *11*, 1351.

101. Scida, K.; Sheridan, E.; Crooks, R. M. Electrochemically-Gated Delivery of Analyte Bands in Microfluidic Devices Using Bipolar Electrodes. *Lab Chip* **2013**, *13*, 2292–2299.

102. Kim, W.; Park, S.; Kim, K.; Kim, S. J. Experimental Verification of Simultaneous Desalting and Molecular Preconcentration by Ion Concentration Polarization. *Lab Chip* **2017**, *17*, 3841–3850.

103. Lee, J. H.; Song, Y. A.; Han, J. Multiplexed Proteomic Sample Preconcentration Device Using Surface-Patterned Ion-Selective Membrane. *Lab Chip* **2008**, *8*, 596–601.

104. Davies, C. D.; Crooks, R. M. Focusing, Sorting, and Separating Microplastics by Serial Faradaic Ion Concentration Polarization. *Chem. Sci.* **2020**.

105. Papadimitriou, V. A.; Segerink, L. I.; Eijkel, J. C. T. Free Flow Ion Concentration Polarization Focusing (FF-ICPF). *Anal. Chem*. **2020**, *92*, 4866–4874.

106. Marczak, S.; Senapati, S.; Slouka, Z.; Chang, H. C. Induced Nanoparticle Aggregation for Short Nucleic Acid Quantification by Depletion Isotachophoresis. *Biosens. Bioelectron*. **2016**, *86*, 840–848.

107. Marczak, S.; Richards, K.; Ramshani, Z.; Smith, E.; Senapati, S.; Hill, R.; Go, D. B.; Chang, H. C. Simultaneous Isolation and Preconcentration of Exosomes by Ion Concentration Polarization. *Electrophoresis* **2018**, *39*, 2029–2038.

108. Zhang, C.; Sun, G.; Senapati, S.; Chang, H. C. A Bifurcated Continuous Field-Flow Fractionation (BCFFF) Chip for High-Yield and High-Throughput Nucleic Acid Extraction and Purification. *Lab Chip* **2019**, *19*, 3853–3861.

109. Kim, E.; Xia, Y.; Whitesides, G. M. Polymer Microstructures Formed by Moulding in Capillaries. *Nature* **1995**, *376*, 581–584.

110. Lee, J. H.; Song, Y. A.; Tannenbaum, S. R.; Han, J. Increase of Reaction Rate and Sensitivity of Low-Abundance Enzyme Assay Using Micro/Nanofluidic Preconcentration Chip. *Anal. Chem*. **2008**, *80*, 3198–3204.

111. Berzina, B.; Anand, R. K. An Electrokinetic Separation Route to Source Dialysate from Excess Fluid in Blood. *Anal. Chem*. **2018**, *90*, 3720–3726.

112. Liu, V.; Song, Y.-A.; Han, J. Capillary-Valve-Based Fabrication of Ion-Selective Membrane Junction for Electrokinetic Sample Preconcentration in PDMS Chip. *Lab Chip* **2010**, *10*, 1485–1490.

113. Kim, B.; Heo, J.; Kwon, H. J.; Kim, I.; An, T.; Lim, G. Fabrication of Entangled Single-Wall Carbon Nanotube Films as Nanoporous Junctions for Ion Concentration Polarization. *J. Appl. Phys*. **2015**, *54*, 035102.

114. Dumitrescu, I.; Yanceya, D.; Crooks, R. Dual-electrode microfluidic cell for characterizing electrocatalysts. *Lab Chip* **2012**, *12*, 986–993.

115. Szentirmay, M. N.; Martin, C. R. Ion-Exchange Selectivity of Nafion Films on Electrode Surfaces. *Anal. Chem*. **1984**, *56*, 1898–1902.

116. Selvaraju, T.; Ramaraj, R. Electrochemically Deposited Nanostructured Platinum on Nafion Coated Electrode for Sensor Applications. *J. Electroanal. Chem*. **2005**, *585*, 290–300.

117. Bobacka, J. Conducting Polymer-Based Solid-State Ion-Selective Electrodes. *Electroanalysis* **2006**, *18*, 7–18.

118. Yoon, E.; Davies, C. D.; Hooper, T. A.; Crooks, R. M. Photoelectrochemical Ion Concentration Polarization: Membraneless Ion Filtration Based on Light-Driven Electrochemical Reactions. *Lab Chip* **2017**, *17*, 2491–2499.

119. Wang, Y.; Song, Y.; Xia, Y. Electrochemical Capacitors: Mechanism, Materials, Systems, Characterization and Applications. *Chem. Soc. Rev*. **2016**, *45*, 5925–5950.

120. Hong, S. A.; Kim, Y. J.; Kim, S. J.; Yang, S. Electrochemical Detection of Methylated DNA on a Microfluidic Chip with Nanoelectrokinetic Pre-Concentration. *Biosens. Bioelectron*. **2018**, *107*, 103–110.

121. Ouyang, W.; Ye, X.; Li, Z.; Han, J. Deciphering Ion Concentration Polarization-Based Electrokinetic Molecular Concentration at the Micro-Nanofluidic Interface: Theoretical Limits and Scaling Laws. *Nanoscale* **2018**, *10*, 15187–15194.

122. Farghaly, A. A.; Lam, M.; Freeman, C. J.; Uppalapati, B.; Collinson, M. M. Potentiometric Measurements in Biofouling Solutions: Comparison of Nanoporous Gold to Planar Gold. *J. Electrochem. Soc*. **2016**, *163*, H3083–H3087.

123. Khan, R. K.; Gadiraju, S. P.; Kumar, M.; Hatmaker, G. A.; Fisher, B. J.; Natarajan, R.; Reiner, J. E.; Collinson, M. M. Redox Potential Measurements in Red Blood Cell Packets Using Nanoporous Gold Electrodes. *ACS Sensors* **2018**, *3*, 1601–1608.

124. Bush, A. M.; Ford, H. O.; Gao, F.; Summe, M. J.; Rouvimov, S.; Schaefer, J. L.; Phillip, W. A.; Guo, R. Tunable Mesoporous Films from Copolymers with Degradable Side Chains as Membrane Precursors. *Journal of Membrane Science* **2018**, 104–114.

125. Ford, H. O.; Cui, C.; Schaefer, J. L. Comparison of Single-Ion Conducting Polymer Gel Electrolytes for Sodium , Potassium , and Calcium Batteries : Influence of Polymer Chemistry , Cation Identity , Charge Density , and Solvent on Conductivity. *Batteries* **2020**, *6*, 1–41.

126. Ouyang, W.; Li, Z.; Han, J. Pressure-Modulated Selective Electrokinetic Trapping for Direct Enrichment, Purification, and Detection of Nucleic Acids in Human Serum. *Anal. Chem*. **2018**, *90*, 11366–11375.

127. Han, S. Il; Yoo, Y. K.; Lee, J.; Kim, C.; Lee, K.; Lee, T. H.; Kim, H.; Yoon, D. S.; Hwang, K. S.; Kwak, R.; et al. High-Ionic-Strength Pre-Concentration via Ion Concentration Polarization for Blood-Based Biofluids. *Sensors and Actuators, B: Chemical.* **2018**, 485–493.

128. Berzina, B.; Anand, R. K. Continuous Micellar Electrokinetic Focusing of Neutral Species Driven by Ion Concentration Polarization. *Lab Chip* **2019**, *19*, 2233-2240.

129. Berzina, B.; Anand, R. K. An Electrokinetic Separation Route to Source Dialysate from Excess Fluid in Blood. *Anal. Chem.* **2018**, *90*, 3720–3726.

130. Muijselaar, P. G.; Otsuka, K.; Terabe, S. Micelles as Pseudo-Stationary Phases in Micellar Electrokinetic Chromatography. *J. Chromatogr. A* **1997**, *780*, 41–61.

131. Chen, C. H.; Sarkar, A.; Song, Y. A.; Miller, M. A.; Kim, S. J.; Griffith, L. G.; Lauffenburger, D. A.; Han, J. Enhancing Protease Activity Assay in Droplet-Based Microfluidics Using a Biomolecule Concentrator. *J. Am. Chem. Soc.* **2011**, *133*, 10368–10371.

132. Yu, M.; Hou, Y.; Zhou, H.; Yao, S. An On-Demand Nanofluidic Concentrator. *Lab Chip* **2015**, *15*, 1524–1532.

133. Phan, D. T.; Chun, Y.; Nguyen, N. T. A Continuous-Flow Droplet-Based Concentrator Using Ion Concentration Polarization. *RSC Adv.* **2015**, *5*, 44336–44341.

134. Deng, C. Z.; Fan, Y. J.; Chung, P. S.; Sheen, H. J. A Novel Thermal Bubble Valve Integrated Nanofluidic Preconcentrator for Highly Sensitive Biomarker Detection. *ACS Sensors* **2018**, *3*, 1409–1415.

135. Lee, S.; Park, S.; Kim, W.; Moon, S.; Kim, H.-Y.; Lee, H.; Kim, S. J. Nanoelectrokinetic Bufferchannel-Less Radial Preconcentrator and Online Extractor by Tunable Ion Depletion Layer. *Biomicrofluidics* **2019**, *13*, 034113.

136. Cheow, L. F.; Ko, S. H.; Kim, S. J.; Kang, K. H.; Han, J. Increasing the Sensitivity of ELISA Using Multiplexed Electrokinetic Concentrator. *Anal. Chem.* **2010**, *82*, 3383–3388.

137. Jeong, H. L.; Cosgrove, B. D.; Lauffenburger, D. A.; Han, J. Microfluidic Concentration-Enhanced Cellular Kinase Activity Assay. *J. Am. Chem. Soc*. **2009**, *131*, 10340–10341.

138. Koo, K. M.; Wee, E. J. H.; Rauf, S.; Shiddiky, M. J. A.; Trau, M. Microdevices for Detecting Locus-Specific DNA Methylation at CpG Resolution. *Biosens. Bioelectron*. **2014**, *56*, 278–285.

139. Haque, M. H.; Gopalan, V.; Yadav, S.; Islam, M. N.; Eftekhari, E.; Li, Q.; Carrascosa, L. G.; Lam, N.-T. N.; Lam, A. K.; Shiddiky, M. J. A. Detection of Regional DNA Methylation Using DNA-Graphene Affinity Interactions. *Biosens. Bioelectron*. **2017**, *87*, 615–621.

140. Luo, X.; Davis, J. J. Electrical Biosensors and the Label Free Detection of Protein Disease Biomarkers. *Chem. Soc. Rev*. **2013**, *42*, 5944–5962.

141. Ouyang, W.; Han, J.; Wang, W. Enabling Electrical Biomolecular Detection in High Ionic Concentrations and Enhancement of the Detection Limit Thereof by Coupling a Nanofluidic Crystal with Reconfigurable Ion Concentration Polarization. *Lab Chip* **2017**, *17*, 3772–3784.

142. Senapati, S.; Slouka, Z.; Shah, S. S.; Behura, S. K.; Shi, Z.; Stack, M. S.; Severson, D. W.; Chang, H. C. An Ion-Exchange Nanomembrane Sensor for Detection of Nucleic Acids Using a Surface Charge Inversion Phenomenon. *Biosens. Bioelectron*. **2014**, *60*, 92–100.

143. Slouka, Z.; Senapati, S.; Shah, S.; Lawler, R.; Shi, Z.; Stack, M. S.; Chang, H. C. Integrated, DC Voltage-Driven Nucleic Acid Diagnostic Platform for Real Sample Analysis: Detection of Oral Cancer. *Talanta* **2015**, *145*, 35–42.

144. Taller, D.; Richards, K.; Slouka, Z.; Senapati, S.; Hill, R.; Go, D. B.; Chang, H. C. On-Chip Surface Acoustic Wave Lysis and Ion-Exchange Nanomembrane Detection of Exosomal RNA for Pancreatic Cancer Study and Diagnosis. *Lab Chip* **2015**, *15*, 1656–1666.

145. Ramshani, Z.; Zhang, C.; Richards, K.; Chen, L.; Xu, G.; Stiles, B. L.; Hill, R.; Senapati, S.; Go, D. B.; Chang, H. C. Extracellular Vesicle MicroRNA Quantification from Plasma Using an Integrated Microfluidic Device. *Commun. Biol.* **2019**, *2*, 1–9.

146. Yin, Z.; Ramshani, Z.; Waggoner, J. J.; Pinsky, B. A.; Senapati, S.; Chang, H. C. A Non-Optical Multiplexed PCR Diagnostic Platform for Serotype-Specific Detection of Dengue Virus. *Sensors Actuators, B Chem.* **2020**, *310*, 127854.

CHAPTER 3. AN ELECTROKINETIC SEPARATION ROUTE TO SOURCE DIALYSATE FROM EXCESS FLUID IN BLOOD

Beatrise Berzina, Robbyn K. Anand

Iowa State University, Department of Chemistry

Modified from a manuscript published in *Analytical Chemistry*, **2018**, *90*, 3720-3726.

Abstract

To improve the health of patients with end- stage renal disease, there is a clear need for slow, continuous hemodialysis, and the primary barrier to a wearable device is the requirement of a large reservoir of dialysate. We describe an electrokinetic means of producing dialysate from the excess fluid extant in the peripheral blood of patients undergoing therapy. A critical feature of this process is the retention of essential components of blood, especially serum albumin. In progress toward this goal, we demonstrate the separation of charged from neutral species in blood plasma at a branched microchannel junction by ion concentration polarization (ICP). Further, we introduce a method that reduces the opportunity for damage to proteins and prevents electrode biofouling. The present approach results in as high as 99.7% retention of albumin and successful separation of neutral metabolites and excess fluid to be utilized as a precursor to dialysate.

Introduction

Despite significant progress in kidney disease management, the requirement for dialysate remains to be the primary barrier to the creation of a wearable device capable of continuously cleansing the blood of metabolic waste. In this paper, we demonstrate the removal of neutral compounds from blood plasma by ion concentration polarization (ICP) in a branched microchannel. This separation can be employed to source fluid from blood plasma that could be utilized downstream, as patient-derived dialysate, to accept metabolic waste during hemodialysis. A key point is that this strategy is much like that employed by the human kidney, which sources excess fluid from the blood to accept waste.

According to the World Health Organization, more than70000 people per year receive a kidney transplant, and most importantly, this number represents only 10% of the total number on the waiting list.[1] The health risks associated with intermittent therapy[2] are a clear indication that slow continuous dialysis would greatly improve quality of life and prognosis for patients with kidney failure. In response to this need, there has been significant advancement toward miniaturized wearable devices for the removal of metabolic waste from the blood. For example, the wearable artificial kidney (WAK) is the first truly portable hemodialysis device,[3] having all components attached to a belt (similar in size to a back brace). The WAK was shown in its first clinical trials to successfully maintain blood components at healthy levels over a 24 h period. Another system, called the Vincenza wearable artificial kidney for peritoneal dialysis (ViWAK PD) was engineered by Ronco et al. to consume a reduced dialysate volume based on sorbent-assisted regeneration.[4] Despite these major advancements, the systems are still heavy and cumbersome. Due to the need for miniaturization, microfluidic technologies are being incorporated into artificial transplantable kidneys and dialysis devices.[4–6] McGrath and co-workers recently published a miniaturized hemodialysis module that uses a lithographically patterned nanomembrane to significantly increase transmembrane diffusion and thereby decrease dialyzer size.[5] In an effort to remove the need for dialysate, Nissenson and co-workers have developed a model for an implantable "human nephron filter" that employs a multimembrane system to mimic the functions of the glomeruli and tubules in the nephron.[6] This technology targets the dialysate reservoir, which is by far the most serious limitation to miniaturization.

However, we think that the same goal can be accomplished by employing ICP at a microfluidic junction to form dialysate directly from human blood or blood plasma.

ICP is the simultaneous enrichment and depletion of ions at opposing ends of an ion permselective membrane[7–10] or bipolar electrode[7,11–13] when an electrical voltage is applied across it. In ICP, the electric field gradient present at the boundary of the ion depletion zone (IDZ) has been employed for concentration enrichment and separation of charged and neutral species for analysis.[11–19] Most relevant to the current work is the ability of ICP to separate charged from neutral species in a branched, flow-through microfluidic device, a feature that has been employed for desalination.[20–22] In such a device (**Scheme 1a**), a main (branched) channel is connected to an auxiliary channel at a junction such as a nanoporous membrane (blue line, **Scheme 1a**) that facilitates selective charge transport.

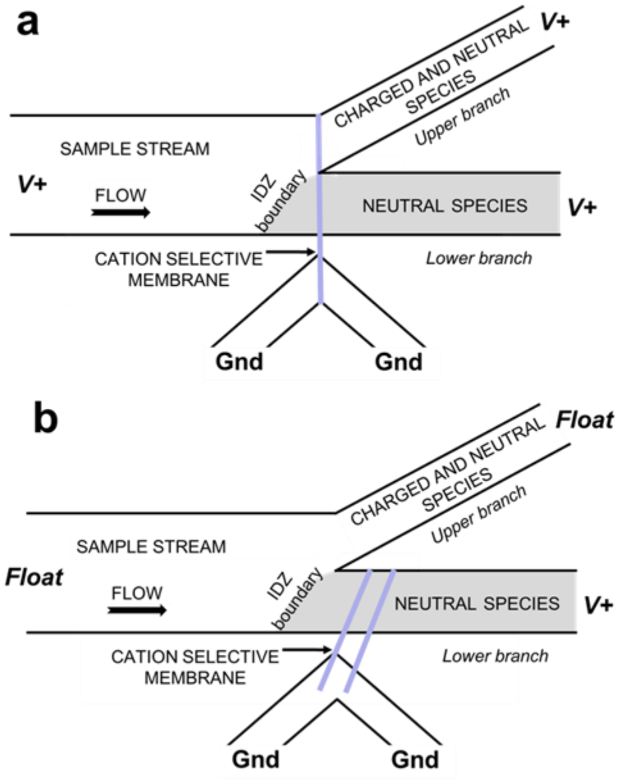

Scheme 1.

To achieve separation, the sample is flowed into the main (branched) channel (left to right, **Scheme 1a**) and a driving voltage (*V*+) is applied between this main channel and the auxiliary channel. If the membrane selectively permits cations, then an IDZ forms in the main channel near the micro/ nanojunction. When employed for desalination, it was shown that charged species are repelled from the IDZ and redirected into the upper microchannel branch ("brine stream") while neutral species are unaffected, passing equally into both branches. A similar branching microchannel was reported by Kwak et al. for the continuous enrichment of green fluorescence protein (rGFP), red blood cells (RBCs), Escherichia coli (E. coli), and fluorescein isothiocyanate (FITC)-conjugated lectin for analytical applications.[19] The authors demonstrated that a narrower upper branch led to enhanced enrichment. While this approach led to enrichment of RBCs, the repulsion of cells from the IDZ can lead to cell damage due to fluidic instability (local vortices) at its boundary. The origin of this instability and strategies for mitigating it are an important focus of ICP-related research. A recent publication by Kim and co-workers indicates that reduced instability can be achieved by extending a Nafion membrane into the IDZ so that it can serve as an alternative current path (versus ion migration through the depleted volume alone).[23] This approach adds a resistance in parallel to the IDZ, thus decreasing both locally high electrokinetic flow and the electric field employed for separation. Therefore, while this approach leads to gentle repulsion of RBCs in whole blood, it may yield a low separation efficiency for ionic species. These studies illustrate the utility of ICP for the enrichment and separation of blood components such as proteins and cells. Given the potential impact of ICP in analytical and medical applications, we characterize here the continuous separation of neutral species in blood plasma. Importantly, we achieve this separation with a device configuration (**Scheme 1b**) that avoids contact between the blood plasma and the driving electrode, thereby reducing the opportunity for plasma components to be damaged and for electrode biofouling to occur. Further, we show that the IDZ can be formed even after extended exposure of the nanoporous membrane to blood plasma (at least 6 h) and can be sustained for up to 11 h. Once formed, the IDZ reduces contact of the membrane with high concentrations of biomolecules (esp. proteins) found in plasma. Tracking of fluorescent dyes of the neutral stream indicate that even some neutral compounds are excluded from the IDZ. This observation is made in blood plasma but not in a simpler buffer medium, indicating that the depletion of uncharged dye may occur by virtue of intermolecular interactions with charged species. We have also quantified separation efficiency (for albumin) as a function of flow rate, applied voltage, and membrane location including an analysis of run-to-run variation. These results demonstrate the viability of ICP as a means of creating patient-derived dialysate as part of a wearable hemodialysis device.

Experimental section

Chemicals. Texas Red dye-linked albumin and the neutral (uncharged) fluorophore BODIPY FL (4,4-difluoro-4-bora- 3a,4a-diaza-S-indacene) were obtained from Molecular Probes (Eugene, OR). Human blood plasma samples (K_2EDTA) were purchased from Discovery Life Sciences (Los Osos, CA), divided into 100 μL aliquots, stored frozen at −80 °C, and thawed at 37 °C before use. All other solutions were made with reagent grade chemicals (Fisher Scientific, Waltham, MA) and diluted with double deionized water (18.2 MΩ·cm, Sartorius Arium Pro, Göttingen, Germany) before use to desired concentration. A solution which modeled the ionic strength and pH of blood plasma consisted of a solution of 50.0 mM NaCl and 5.0 mM KCl in 20.0 mM carbonate buffer adjusted to pH 7.45 with 0.1 M HCl. Poly(dimethylsiloxane) (Sylgard 184 elastomer kit, Dow Corning Corp., Midland, MI) was used for device fabrication.

Platinum electrodes (99.95%) were purchased from Strem Chemicals (Newburyport, MD). A 3.0 µM solution of Pluronic F-108 (poly(ethylene glycol)-block- poly(propylene glycol)-block-poly(ethylene glycol)) (Millipore Sigma, St. Louis, MO) in 10.0 mM phosphate buffer (pH 7.2) was used to coat the microchannels. Nafion perfluorinated resin (20 wt % solution in lower aliphatic alcohols) was purchased from Sigma-Aldrich (St. Louis, MO) and used as received.

Device Fabrication. The PDMS/glass devices were fabricated using standard soft lithography.[24–28] The main (branched) microfluidic channel was 48.0 µm tall and 10.0 mm long, having a 500 µm wide inlet segment leading into two 250 µm wide branches at a location 5.0 mm from the inlet. A 4.0 mm diameter biopsy punch was used to create the inlet and outlet reservoirs. Near the branching junction, at a location indicated as in the Results and Discussion section, a mechanical incision was made using a scalpel blade and subsequently filled with 5.0 µL of Nafion. The Nafion was then cured at 95 °C for 10 min. Excess Nafion was removed by repeating applying and peeling away low residue tape. The PDMS layer and glass slide were treated in an air plasma (PDC-001, Harrick Plasma, Ithaca, NY) for 90 s and then bonded together. Immediately after bonding, all microfluidic devices were rinsed with deionized water and coated by filling with Pluronic solution and incubating at 4.0 °C for at least 18 h. Pluronic coating was used to prevent nonspecific adsorption of blood plasma components onto the channel walls and to suppress electroosmotic flow.

Ion Concentration Polarization. Prior to ICP experiments, each device was rinsed with 10.0 mM phosphate buffer solution for 30 min to remove excess Pluronic. This rinsing step is key to preventing Pluronic from decreasing the performance of the Nafion membrane. The rinsing solution was then replaced with the sample solution. A driving voltage was applied across the nanojunction using a DC power supply (HY3005D, Mastech and DIGI360, Electro

Industries, Westbury, NY) connected to Pt electrode wires positioned in the main (*V*+) and auxiliary (Gnd) channel reservoirs. The volume of solution and voltages employed at each reservoir for individual experiments are indicated in the Results and Discussion section.

Fluorescence Measurements. All fluorescence measurements were performed using an Eclipse Ti-S inverted fluorescence microscope (Nikon Industries, New York, NY) equipped with a digital camera (Orca-4.0, Hamamatsu Corp., Bridgewater, NJ). All images were processed using NIS- Elements 4.6 software (Nikon). Fluorescence measurements used for quantitative comparison of species concentrations were background subtracted. Separation efficiency was calculated as the percentage decrease in concentration of dye-linked albumin in the lower branch as determined by comparing the mean background subtracted fluorescence across the lower branch at a lateral distance 0.20 mm downstream of the Nafion membrane to that obtained prior to the application of the driving voltage.

Results and discussion

We employed fluorescence microscopy to characterize the behavior of charged and neutral compounds in ICP-based separations. The first separation was carried out in a solution of model blood (matched salinity and pH) and the second in undiluted blood plasma. The device was then adapted to decrease the opportunity for damage to proteins and to reduce operating voltage. Finally, we evaluated factors impacting device lifetime and separation efficiency and determined the composition of the output of the lower branch (**Scheme 1b**).

ICP-Based Separation of Albumin from a Neutral Dye in Model Blood Plasma.

Figure 1a shows the separation of albumin (labeled with Texas Red) from an uncharged dye (green, BODIPY FL) at an ion permselective junction (white dashed line) in a solution that models the pH and salinity of blood plasma. The solution contained 0.05 mg mL^{-1} dye-linked albumin (approximately 0.1% of the concentration of albumin in human blood) and 1.0 µM BODIPY in 50.0 mM NaCl, 5.0 mM KCl, and 20.0 mM carbonate at pH 7.45. In this experiment, first, the main channel was rinsed with the sample solution for 2 min. Second, the volume of sample solution in the reservoirs was adjusted to 40.0 µL (inlet) and 15.0 µL (both outlets) to generate flow from left to right (as in **Scheme 1a**). Finally, 40.0 V was applied at all three reservoirs of the main channel versus the auxiliary channel (ground). The IDZ formed immediately upon application of the driving voltage (**Figure 1a**). After the voltage was turned off, the IDZ dissipated and the albumin and uncharged dye uniformly filled the main channel (Figure 1b). It is important to note that the driving voltage is applied in the inlet and both outlets of this branched microchannel (labeled as *V*+), a configuration traditionally employed for desalination.

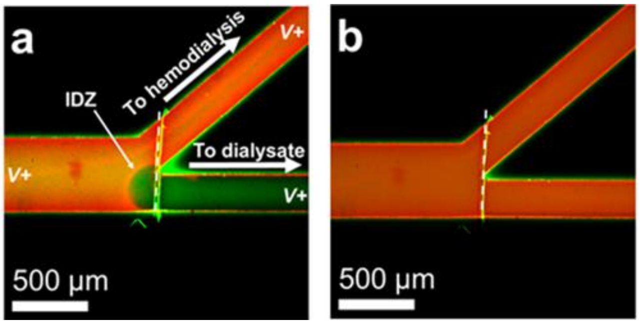

Figure 1. Fluorescence micrograph showing the location of dye-linked albumin and BODIPY FL, which are representative both of the charged species and neutral species present in model blood plasma. a) The dye-linked albumin is redirected into the upper branched channel with an applied voltage of 40.0 V. b) At 0.0 V, the dye-linked albumin flows equally to both outlets.

ICP-Based Separation in Blood Plasma. When this three-driving-electrode configuration was used to perform a similar separation in blood plasma, bright spots were observed in the inlet segment of the main channel and attributed to the formation of aggregates of the dye linked albumin. (**Figure S1**). Such aggregate formation is likely due to interaction of blood components with the products of faradaic reactions at the driving electrode located in the inlet. During this experiment, we also observed that having the *Nafion*-filled cut positioned across the full width of the main channel often led to the formation of a large IDZ, which blocked entrance of charged species to both branches. To investigate the electrode biofouling and plasma component damage due to electrode contact, a prolonged experiment in which a driving electrode was kept in contact with blood plasma was performed (for detailed protocol, see the Supporting Information (SI)). Results showed that device operation time was reduced to 7 h, after which the electrode was fouled by a visible protein coating. A voltammetric study presented in **Figure 2a** shows the ratio of the anodic peak height measured at each time point to its initial value. This data demonstrates that the available electrode area (%) to facilitate the redox reaction decreases by >70% (**Figure 2b**) over 7 h of operation in blood plasma. On the basis of these observations, we adapted the device and separation protocol.

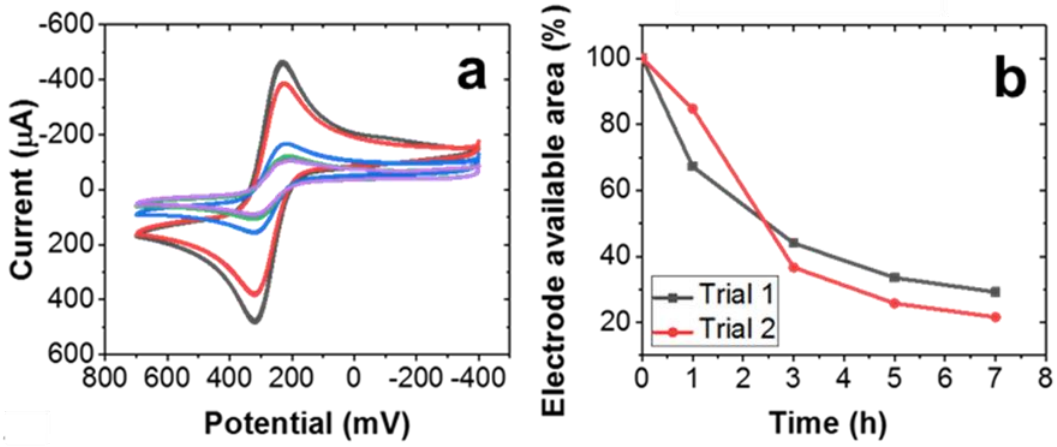

Figure 2. a) Second and third cycles of cyclic voltammograms (CVs) of 5.0 mM each ferricyanide and ferrocyanide in 0.1 M KCl using as the working electrode a Pt wire employed in direct contact with blood plasma to drive ICP for t = 0 (grey), 1 (red), 3 (blue), 5 (green), and 7 h (purple). All potentials are referenced to Ag/AgCl. b) Plot of the percent available area of the Pt wire electrode calculated from the peak currents obtained from these voltammograms.

Development of an Enhanced Scheme for Separation in Blood Plasma. To address the formation of protein aggregates and driving electrode biofouling, we adopted an alternative one-electrode configuration (**Scheme 1b**), which prevents contact of the blood plasma with driving electrodes. In this configuration, the single electrode was located in the outlet of the neutral stream, while the inlet and remaining outlet were at a floating potential. This adaptation is important because contact between blood plasma and electrodes is completely avoided. To avoid blocking both branches with the IDZ, the permselective membrane was relocated to a position past the branching junction into the neutral stream. Using this strategy, the IDZ was more readily contained in the lower branch, which increased tolerance for variations in inflow rates. Further, a double ion-selective junction (**Scheme 1b**, and white dashed lines, **Figure 3**) was employed to increase the rate of ion depletion and the length of the neutral stream branch was shortened from 5.0 to 2.5 mm. In combination, these changes reduced the required driving voltage from 40.0 to 12.0 V while still creating a sufficient IDZ volume to fill the entire cross section of the entrance to the neutral stream. Significantly, this approach resulted in as high as 99.7% retention of albumin and successful separation of neutral metabolites and excess fluid to be utilized as precursor to dialysate.

Figure 3 shows the repulsion of dye-linked albumin from the boundary of an IDZ in undiluted blood plasma. The experiment proceeded as follows. First, the channel was rinsed with 10.0 mM phosphate buffer, after which the buffer in the inlet reservoir was replaced with 40.0 µL of 0.05 mg mL^{-1} dye- linked albumin in model blood plasma. The volume in the outlets was adjusted to 20.0 µL to establish fluid flow. Second, a driving voltage of 24.0 V was applied. This initial step allowed the formation of the IDZ to be observed, indicating proper function of the device, before the addition of blood plasma. After 5 min, the sample solution in the inlet was replaced with 40.0 μL of 0.05 mg mL^{-1} dye-linked albumin in undiluted blood plasma. Third, the flow rate and voltage were adjusted to balance the position of the IDZ boundary relative to the branching junction. Specifically, the inlet volume was adjusted to 33.0 μL and the outlets to 12.0 μL, and the driving voltage decreased to 12.0 V. The change in fluorescence intensity measured in the neutral stream (dashed line, **Figure 3**) 10 min after the voltage was applied indicates exclusion of albumin from this branch. This result is significant because albumin, an essential protein, is retained (repelled) and not lost to the dialysate (neutral stream). An important point is that the exclusion of albumin is representative of the response of other charged species in blood plasma. Further, this separation occurred without apparent damage to components in the blood plasma. No bright spots indicative of protein aggregates were observed.

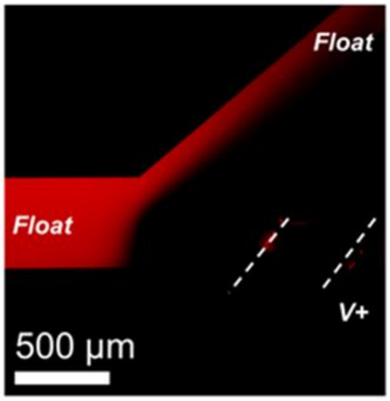

Figure 3 Fluorescence micrograph showing the location of dye-linked albumin in undiluted blood plasma. The dye-linked albumin is redirected into the upper branched channel un-der an applied voltage of 12.0 V.

To investigate electrode biofouling in the one-electrode device configuration (Scheme 1b), a 3 h blood plasma separation experiment with consecutive voltammetric measurements was performed (for detailed protocol, see the SI). Results from the voltammetric study (SI, **Figure S3**) show that the available electrode area remains unchanged over the duration of the experiment. In contrast, when the electrode was kept in the device inlet, in contact with blood plasma, the available electrode area was reduced by about 60% over the same period of time (**Figure 2**). This result demonstrates that using a one-electrode configuration prevents biofouling that results from adhesion of blood components to the electrode. Further supporting this conclusion is the qualitative observation that no protein coating was visible on the driving electrode, even in experiments that continued for 12 h or more. This result underscores the importance of housing the driving electrode in the neutral stream and preventing contact with blood plasma, especially under an applied voltage, to avoid electrode biofouling.

Evaluation of Device Lifetime. Using this single-electrode scheme, we further evaluated device lifetime and the tendency for the membrane to foul. This evaluation consisted of two separate experiments, with and without contact of the membrane with blood plasma prior to IDZ formation. In the first experiment, the device was rinsed with buffer as described in the previous experiment, and then the solution in the channel was replaced with 0.05 mg mL^{-1} dye-linked albumin in undiluted blood plasma. The device was allowed to sit at room temperature with the membrane in contact with the plasma. A driving voltage (12.0 V) was applied intermittently (every 30 min) to determine if the IDZ would still form. The IDZ was stable over the longest times investigated (6 h). This result is significant because it indicates that the device (electrodes and membrane) do not undergo significant biofouling while the voltage source is off Importantly, we anticipated that during operation the IDZ would continuously protect the membrane by preventing its contact with macromolecules in the blood plasma. Therefore, we further tested the device lifetime in the absence of contact between the blood plasma and permselective membrane. This condition was accomplished by establishing an IDZ in buffer solution prior to the introduction of plasma (for detailed protocol, see the SI). Repulsion of the dye-linked albumin at the IDZ boundary was observed as the plasma entered the main channel (SI, **Figure S4**). This observation indicates that contact between the blood plasma proteins and the membrane was avoided. Importantly, previous publications have underscored that all charged species are excluded from the IDZ,[19–21] and therefore, we consider the exclusion of dye-linked albumin to indicate the fate of other charged species. The separation was monitored for 12 h, and separation efficiency evaluated during this time. At 5 h, the driving voltage was increased to 55.0 V (37.5%) to adjust the location of the IDZ boundary. The separation efficiency of >90% was maintained over a 9 h period. After 10 h, the separation efficiency started to decay, reaching 81.7% at 12 h when the experiment was terminated (SI, **Figure S5**). At 12 h, the sharpness of the transition in fluorescence intensity at the IDZ boundary was reduced (SI, **Figure S4**), which could be indicative of changes in the Nafion membrane. The accumulation of dye-linked albumin along the membrane from 6 h onward identifies membrane fouling as a possible cause. However, no increase in resistance was observed when the resistance of the membrane was measured before and after a separation in blood plasma. During these measurements, the device was filled with only 15.0 mM phosphate buffer. In fact, in three such trials, each carried out in a separate device, the resistance actually decreased (307 to 104, 277 to 101, and 272 to 98 MΩ). Therefore, the observed failure of the device at 11 h is more likely due to another cause. In other long duration experiments, we have observed failure attributable to we have observed failure attributable to separation of the *Nafion* membrane from the walls of the PDMS slit and gas bubble formation in the auxiliary channel.

Influence of Flow Rate and Voltage on Separation Efficiency. Using the one-electrode configuration (**Scheme 1b**), we investigated the dependence of separation efficiency on flow rate (5.0 to 70 nL min^{-1}) and applied driving voltage (5.0− 55.0 V). The experimental protocol is described in detail in the SI. Briefly, after establishing a stable flow rate, the voltage (*V*+) was stepped in 5.0 V increments at 1 min intervals. **Figure 4** shows that at 15.0 V and an inlet flow rate of 5.0 nL min^{-1}, >99% separation of dye-linked albumin from the output of the lower branch was achieved. To reach such high separation efficiency at faster flow rates, the voltage must be increased (e.g., 60 nL min^{-1}, 50.0 V, **Figure 4**). Note that for certain flow rates tested, such as for 30 and 50 nL min^{-1} in **Figure 4**, the separation efficiency dropped precipitously to about 60% between 50.0 and 55.0 V. This decreased efficiency is the result of the onset of fluidic instability (local vortices) across the IDZ boundary.23 Due to this instability, we did not extend our measurements beyond 55.0 V. A similar separation efficiency profile can be obtained from run-to-run using the same microfluidic device (compare SI, **Figures S3a** and **S3b**). An evaluation of device-to- device variation and the dependence of separation efficiency on the *Nafion* membrane location (**Figure S4**) is included in the SI.

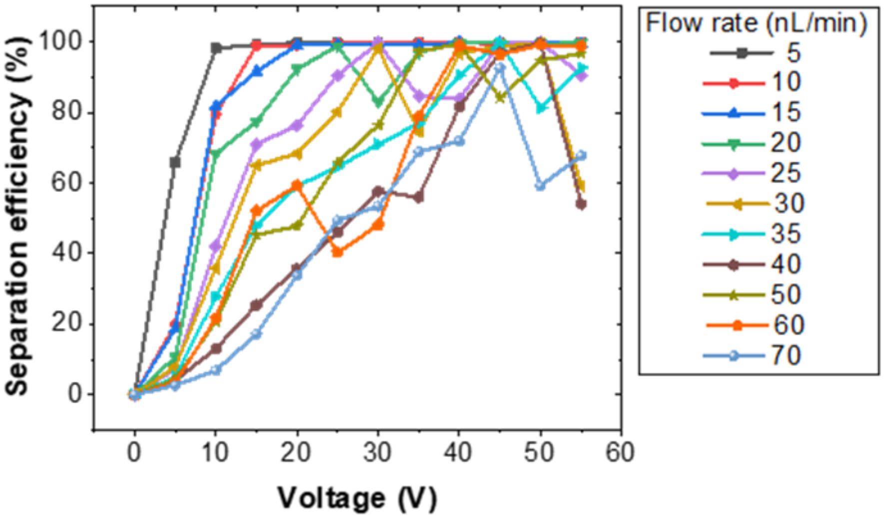

Figure 4. Plots of separation efficiency at distinct inlet flow rates (5.0 to 70 nL min^{-1}) as applied voltage was stepped from 0 V to 55 V in 5 V increments at 1 min intervals.

Evaluation of the Output of the Neutral Stream. While fluorescent tracers indicate the general behavior of charged and neutral compounds in blood plasma, a full characterization of the composition of the outlet streams is necessary to guide further development of this ICP-based separation as a method to source dialysate from blood. Importantly, some neutral compounds are carried into the charged stream by way of intermolecular interactions between these compounds and charged species present in plasma. **Figure 5** demonstrates this concept in that a neutral dye (1.0 µM BODIPY FL) undergoes depletion in blood plasma (96.3%), whereas in model blood plasma (Figure 1a) it did not. This experiment was performed using the same protocol as was used to obtain the results shown in **Figure 3**, but with the addition of 1.0 µM BODIPY FL in the blood plasma. An important consequence of the partial separation of neutral compounds from plasma is that the complexity of the neutral stream is reduced, which in turn simplifies its repurposing as dialysate. To exclude the influence of device configuration on this depletion of neutral dye, control experiments were performed. **Figures S8b** and **S8d** (SI) show that the neutral dye in blood plasma was excluded from the IDZ regardless of whether a one- or three-electrode configuration was employed. Conversely, in model blood plasma, the neutral dye passed through the IDZ and into the lower branch for both electrode configurations (SI, **Figures S8f** and **S8h**). These findings correlate with results obtained in **Figure 1** and, in combination, indicate that the location of the *Nafion* membrane as well has no influence on whether BODIPY FL dye depletes.

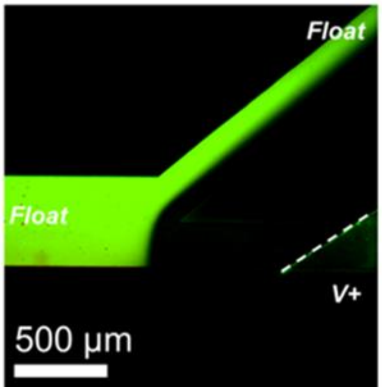

Figure 5. Fluorescence micrograph showing the location of BODIPY FL in undiluted blood plasma. The BODIPY FL is depleted with 40.0 V driving voltage.

We further characterized the output of the lower branch for protein content to answer the critical question of whether the trajectory of the dye-linked albumin is representative of other plasma proteins. To obtain sufficient samples for analysis, the electrokinetic separation in blood plasma was undertaken in a high-throughput device reported by Kim and co-workers,[29] which employs microfins (15 μm wide walls) to define narrow flow laminae (100 μm wide) in a millimeter-scale channel with the aim of stabilizing the IDZ boundary. Using such a device, we were able to collect sufficient sample for a Bradford assay (Micro BCA protein assay kit and Pierce Detergent Compatible Bradford assay kit from Thermo Scientific, Rockford, IL). The measured protein content from experiments conducted in two separate devices indicated high separation efficiencies, which were consistent with the fluorescence images obtained (>90%). More complete characterization of the output fluid (e.g., by LC-MS) may elucidate the detailed composition. An important point is that for the proposed application of this separation, as an in-line source of fluid to repurpose as dialysate, the key metric for success is low protein loss. Passage of molecules below the molecular weight cutoff of hemodialysis into the lower branch is not of concern because their removal from blood is the object of the subsequent hemodialysis step in which this dialysate would be employed.

Summary and conclusions

We have demonstrated that ICP-based separation can continuously remove excess fluid from human blood plasma. These results were achieved using a method that reduces the opportunity for damage or loss of essential blood components (such as albumin). We have further described the potential for this fluid to be repurposed as dialysate. As a critical next step, we are investigating clinically compatible materials to substitute for *Nafion* including PDMS nanostructures and bead beds, which we discussed as part of a recent reveiw.[7] For this approach to become a practical means of obtaining patient- derived dialysate, the ICP-based separation would need to undergo considerable scaling. Hemodialysis treatment of a patient during a 3 h session at a medical center consumes 300− 600 mL min^{-1} of dialysate, which if spread evenly over the week, is equivalent to 15−30 mL min^{-1}. A similar dialysate consumption rate was reported for a clinical trial of the WAK.[3] This volumetric rate is not sustainable if sourced entirely from blood (the human body contains approximately 5 L of peripheral blood). Therefore, a reasonable path to applying this approach may employ slow-flow or low-dialysate consumption hemodialysis in combination with in-line dialysate regeneration.[3] For example, regeneration resulting in a 95% volumetric recovery (i.e., 20-fold enrichment of waste) would reduce fluid consumed by dialysis to about 1.0 mL min^{-1}, which matches a healthy rate of urine production. This figure underscores the inefficiency of hemodialysis relative to a healthy human kidney. Such a dialysate consumption rate could be matched by 50 of the high-throughput devices reported by MacDonald et al. (capable of 20 μL min^{-1} throughput) if operated in parallel.[21] Importantly, this ICP-based approach itself could be employed to regenerate spent patient-derived dialysate and reduce the rate of consumption. Considering these requirements, to progress toward a clinical device, we are focusing on the following three aspects: (1) scaling, (2) ICP- based dialysate regeneration, and (3) clinically compatible materials. Our initial results have demonstrated the feasibility of this strategy, and we believe that it has the potential to have a major positive impact on hemodialysis technology.

References

1. Jones, B.; Bes, M. Bull. *WHO* **2012**, *90*, 718−719.
2. Wanner, C.; Amann, K.; Shoji, T. *Lancet* **2016**, *388*, 276−284.

3. Gura, V.; Rivara, M. B.; Bieber, S.; Munshi, R.; Smith, N. C.; Linke, L.; Kundzins, J.; Beizai, M.; Ezon, C.; Kessler, L.; Himmelfarb, J. *JCI Insight* **2016**, *1*, e86397.
4. Ronco, C.; Davenport, A.; Gura, V. *Nefrologia* **2011**, *31*, 9−16.
5. Johnson, D. G.; Khire, T. S.; Lyubarskaya, Y. L.; Smith, K. J.; Desormeaux, J. P.; Taylor, J. G.; Gaborski, T. R.; Shestopalov, A. A.; Striemer, C. C.; McGrath, J. L. *Adv. Chronic Kidney Dis*. **2013**, *20*, 508−515.
6. Rastogi, A.; Nissenson, A. R. Clin. *J. Am. Soc. Nephrol*. **2009**, *4*, S132−S136.
7. Li, M.; Anand, R. *Analyst* **2016**, *141*, 3496−3510.
8. Kim, M.; Jia, M.; Kim, T. *Analyst* **2013**, *138*, 1370−1378.
9. Mai, J.; Miller, H.; Hatch, A. *ACS Nano* **2012**, *6*, 10206−10215.
10. Yeh, L. H.; Zhang, M.; Qian, S.; Hsu, J. P.; Tseng, S. *J. Phys. Chem. C* **2012**, *116*, 8672−8677.
11. Perdue, R. K.; Laws, D. R.; Hlushkou, D.; Tallarek, U.; Crooks R. M. *Anal. Chem*. **2009**, *81*, 10149−10155.
12. Sheridan, E.; Hlushkou, D.; Knust, K. N.; Tallarek, U.; Crooks, R. M. *Anal. Chem*. **2012**, *84*, 7393−7399.
13. Anand, R. K.; Sheridan, E.; Knust, K. N.; Crooks, R. M. *Anal. Chem*. **2011**, *83*, 2351−2358.
14. Knust, K. N.; Sheridan, E.; Anand, R. K.; Crooks, R. M. *Lab Chip* **2012**, *12*, 4107−4114.
15. Cheow, L. F.; Sarkar, A.; Kolitz, S.; Lauffenburger, D.; Han, J. *Anal. Chem*. **2014**, *86*, 7455−7462.
16. Song, H.; Wang, Y.; Garson, C.; Pant, K. *Microfluid. Nanofluid*. **2014**, *17*, 693−699.
17. Song, H.; Wang, Y.; Garson, C.; Pant, K. *Anal. Methods* **2015**, *7*, 1273−1279.

18. Ko, S. H.; Kim, S. J.; Cheow, L. F.; Li, L. D.; Kang, K. H.; Han, J. *Lab Chip* **2011**, *11*, 1351−1358.

19. Kwak, R.; Kim, S. J.; Han, J. *Anal. Chem.* **2011**, *83*, 7348−7355.

20. Knust, K. N.; Hlushkou, D.; Anand, R. K.; Tallarek, U.; Crooks, R. M. *Angew. Chem., Int. Ed.* **2013**, *52*, 8107−8110.

21. Kim, S. J.; Ko, S. H.; Kang, K. H.; Han, J. *Nat. Nanotechnol.* **2010**, *5*, 297−301.

22. MacDonald, B. D.; Gong, M. M.; Zhang, P.; Sinton, D. *Lab Chip* **2014**, *14*, 681−685.

23. Kim, J.; Cho, I.; Lee, H.; Kim, S. *J. Sci. Rep.* **2017**, *7*, 5091.

24. Shafiee, H.; Caldwell, J. L.; Sano, M. B.; Davalos, R. V. *Biomed. Microdevices* **2009**, *11*, 997−1006.

25. Nakashima, Y.; Hata, S.; Yasuda, T. *Sens. Actuators, B* **2010**, *145*, 561−569.

26. Mohammadi, M.; Madadi, H.; Casals-Terre, J.; Sellares, J. *Anal. Bioanal. Chem.* **2015**, *407*, 4733−4744.

27. Yan, S.; Zhang, J.; Alici, G.; Du, H.; Zhu, Y.; Li, W. *Lab Chip* **2014**, *14*, 2993−3003.

28. McDonald, J. C.; Whitesides, G. M. *Acc. Chem. Res.* **2002**, *35*, 491−499.

29. Kim, K.; Kim, W.; Lee, H.; Kim, S. *Nanoscale* **2017**, *9*, 3466− 3475.

Supporting information

ICP-based separation in blood plasma. A device was prepared as described in the Experimental Section of the main text. After rinsing the channel with 10.0 mM phosphate buffer, the buffer in the inlet reservoir was replaced with 40.0 µL of 0.05 mg mL^{-1} dye-linked albumin in blood plasma. Then, the volume in the outlet reservoirs was adjusted to 14.0 µL to generate pressure driven flow of the plasma through the main channel. Finally, a driving voltage of 40.0 V was applied, as in the experiment described in main text (**Scheme 1a**), and after 1 min, was decreased to 24.0 V. **Figure S1** was obtained approximately 10 min after the driving voltage was decreased and shows the appearance of dye-linked albumin aggregates (bright spots). These results were obtained in a device with dimensions 100 µm width and 19.5 µm channel height.

Evaluation of biofouling at a driving electrode in blood plasma. A voltammetric study was performed to evaluate biofouling of a Pt wire employed as a driving electrode in contact with blood plasma. A cyclic voltammogram (CV) was recorded to evaluate the decrease in the area of the Pt wire accessible for faradaic reactions before the experiment and 1, 3, 5, 7 h after operation in plasma.

Experimental configuration for ICP. A device was prepared as described in the Experimental Section of the main text. After rinsing the main channel with 10.0 mM phosphate buffer, the buffer solution in the inlet was replaced with 60.0 µL of in undiluted blood plasma, which was spiked with 0.05 mg/mL dye-linked albumin. A Pt wire was rinsed with double deionized water, followed by EtOH, and dried under a stream of N2 gas before being positioned in the main channel inlet. Finally, 40.0 V was applied at the inlet reservoir of the main channel versus the auxiliary channel. The Pt wire with protein deposits was gently rinsed with double deionized water before and after each voltammetric measurement.

Voltammetric study. CVs were performed using a Pine WaveDriver 20 Bipotentiostat/Galvanostat system (Durham, NC, USA). The electrochemical cell consisted of the Pt wire working electrode, Ag/AgCl/saturated KCl reference electrode and Pt wire auxiliary electrode. These electrodes were immersed in a 0.1 M KCl solution containing 5.0 mM each potassium ferricyanide and potassium ferrocyanide. Three sequential CV scans were recorded for each timepoint (t = 0, 1, 3, 5, and 7 h). Initial and final potential of the sweep was -0.40 V, scanning to +0.70 V at a sweep rate of 50 mV s^{-1}.

The resulting CVs are presented in **Figure 2a** (main text) along with the ratio of the anodic peak height measured at each time point to its initial value (**Figure 2b**). This data demonstrates that the available electrode area (%) to facilitate the redox reaction decreases by >70% over 7 h of operation in blood.

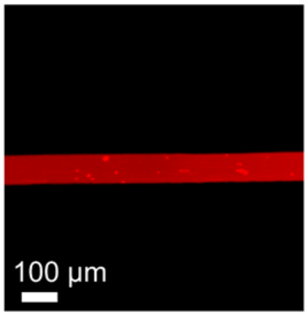

Figure S1. Fluorescence micrograph showing the appearance of protein aggregates (bright spots) in blood plasma in the inlet segment after the application of 40.0 V for 1 min and then 24.0 V for 10 min.

Evaluation of electrode biofouling in the one-electrode scheme during separation in blood plasma. A voltammetric study was performed to verify the absence of biofouling of a Pt wire employed as a single driving electrode positioned in the neutral stream (lower branch) outlet. A CV was recorded to evaluate the decrease in the area of the Pt wire accessible for faradaic reactions before the experiment and 3 h after separation in blood plasma.

Experimental configuration for ICP. A device was prepared as described in the Experimental Section of the main text. A Pt wire was rinsed with double deionized water, followed by EtOH, and dried under a stream of N_2 gas before being positioned in the lower branch outlet. After rinsing the main channel with 10 mM phosphate buffer, 40.0 V was applied at the outlet reservoir of the main channel versus the auxiliary channel. Then, the volume in outlet reservoirs were adjusted to 18 µL. Finally, the buffer solution in the inlet was replaced with 25.0 µL of undiluted blood plasma, which was spiked with 0.05 mg mL^{-1} dye-linked albumin. The initial separation efficiency of 88% increased to 97% over the first 30 s and remained stable over the 3-h period tested (fluorescence micrographs obtained during this separation are shown in **Figure S2**). The volumes of the outlet reservoirs were adjusted every 10 min by increments of 0.1 μL to maintain a stable position of the IDZ boundary. The separation was monitored for 3 h after which the working Pt electrode was evaluated by voltammetry. The Pt wire was gently rinsed with double deionized water before and after each voltammetric measurement. CVs were performed using the same conditions as were employed for the data of **Figure 2**, and the resulting data is shown in **Figure S3**.

Figure S2. Fluorescence micrograph showing the location of dye-linked albumin in undiluted blood plasma. The dye-linked albumin is redirected into the upper branch under an applied voltage (40.0 V).

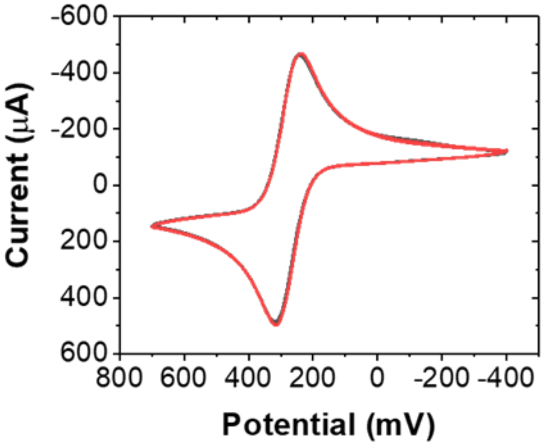

Figure S3. Second and third cycle of CVs obtained in 5.0 mM each ferricyanide and ferrocyanide in 0.1 M KCl using as the working electrode a Pt wire employed in the neutral stream (lower branch) outlet (without contact with blood plasma) to drive ICP for t = 0 (grey), 3 h (red). Potentials are referenced to Ag/AgCl.

Evaluation of device lifetime. The investigation of device lifetime over a period of 12 h (as reported in the main text) was conducted as follows. First, the device was rinsed with 10.0

mM phosphate buffer, and the volumes in the reservoirs were adjusted to 40.0 μL (inlet) and 20.0 μL (both outlets). Second, a 30.0 V driving voltage was applied (one-electrode configuration, Scheme 1b, main text) for 1 min to initiate IDZ formation. Third, the buffer solution in the inlet was replaced with 40.0 μL of 0.05 mg mL^{-1} dye- linked albumin in undiluted blood plasma. The volume of sample solution in the reservoirs was adjusted to 34.0 μL (inlet) and 14.0 μL (outlet of upper branch) to generate flow from left to right. Finally, the driving voltage was adjusted to 40.0 V (defined as t = 0). Repulsion of the albumin at the IDZ boundary was observed as the plasma entered the main channel. The volumes of the outlet reservoirs were adjusted every 20 min by increments of 0.1 μL to maintain a stable position of the IDZ boundary. Note that these adjustments were unnecessary in experiments for which a syringe pump was employed to control the flow rate. The voltage was increased to 55.0 volts after first 5 hours to sustain a stable IDZ. The separation efficiency attained over the course of this experiment was evaluated using mean fluorescence intensity measurements across a line profile 0.2 mm downstream of the Nafion membrane in the images of **Figure S4**. The corresponding separation efficiencies are plotted in Figure S5. These data show that separation efficiencies >90.0% were maintained over a 9-h period. After 10 h the separation efficiency began to decay, reaching 81.7% at 12 h.

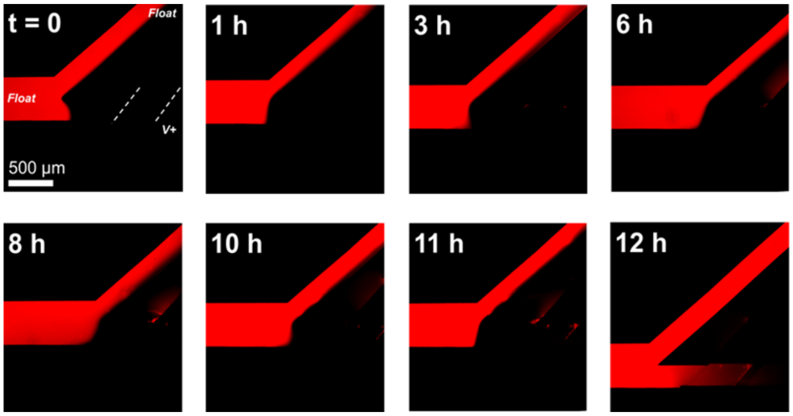

Figure S4. Fluorescence micrograph showing the location of dye-linked albumin in undiluted blood plasma. The dye-linked albumin is redirected into the upper branch under an applied voltage. The white dashed line (added to the image at t = 0) represents the position of the membrane in the lower branch.

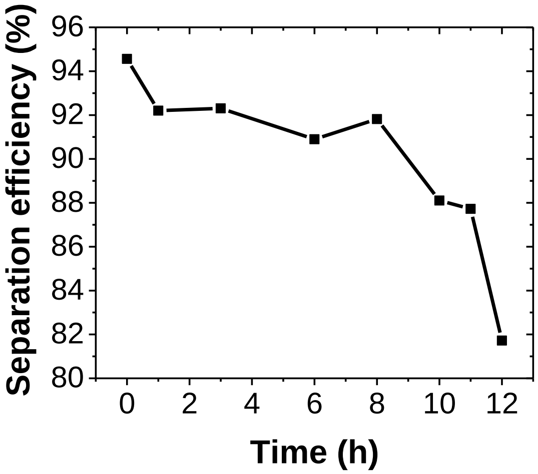

Figure S5. Separation efficiency of dye-linked albumin in undiluted blood plasma over 12 h period.

Evaluation of the impact of flow rate and voltage on separation efficiency. Figures S6a and S6b show the separation efficiency obtained over a range of applied voltages for series of flow rates replicated twice in the same device. For these experiments, a one-electrode configuration (**Scheme 1b**, main text) was employed. A *Nafion* membrane was located in the lower branch at an average lateral distance 0.380 mm downstream of the branching junction. Prior to the experiment, the channels were rinsed with 10 mM phosphate buffer solution. An undiluted blood plasma sample spiked with 0.05 mg mL^{-1} dye-linked albumin was continuously flowed into the device using a syringe pump with a 0.50 mL Hamilton syringe and 1.0 mm outer diameter PTF tubing. After establishing fluid flow at 5.0 nL min^{-1}, a driving voltage of 5.0 V was applied. After 1 min at this voltage, a fluorescence image was acquired. The voltage was then increased in 5.0 V increments to 55.0 V, and an image was acquired after each 1 min interval. The voltage was then turned off, and the flow was increased to 10 nL min^{-1} and allowed to equilibrate for 10 minutes after which the voltage sequence was repeated. In this way, we tested flow rates ranging from 5.0 - 70 nL min^{-1}. **Figure S6a** shows the separation efficiency obtained under each condition. The flow rate was then allowed to equilibrate again to 5.0 nL min^{-1} for 30 minutes before repeating the entire series of flow rates and voltages. The results of this replicate are shown in **Figure S6b**. Figure **S6a** is identical to **Figure 4** (main text) and is included here for comparison. In addition to the conclusions drawn from this data that were discussed in the main text, comparison with **Figure S6b** demonstrates that similar efficiencies are observed from run to run using the same microfluidic device.

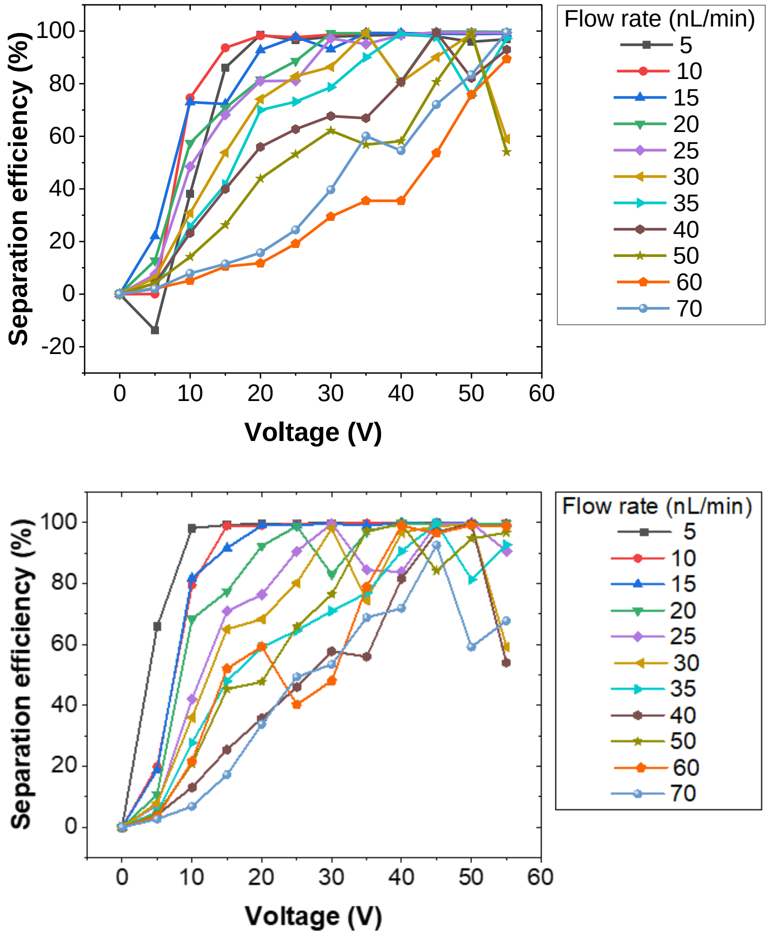

Figure S6. Separation efficiency for dye-linked albumin in undiluted blood plasma at different flow rates over a series of applied voltages (*V*+, **Scheme 1b**, main text). (a) The first series of measurements, and (b) a replicate carried out 30 min later in the same device.

Influence of the membrane location on separation efficiency. Devices in the one-electrode configuration (**Scheme 1b**, main text), were coated with Pluronic and rinsed with 10 mM phosphate buffer as described in the Experimental Section. Separation was characterized in 3 individual microfluidic devices using a 25 nL min^{-1} flow rate over the range of 5.0 to 55.0 V. The flow rate was controlled using a syringe pump and a 0.50 mL syringe with PTF tubing. The devices were identical to each other except for the location of the *Nafion* membrane, made by a single cut, located 380, 650, or 780 µm downstream of the fluidic junction. The difference in separation efficiency among these devices is similar to run-to-run variation for a single device. Therefore, these results imply that device-to-device variance is low given that such similar efficiencies can be attained despite different membrane locations. The key advantage to placing the membrane downstream of the fluidic junction is stable separation. An IDZ boundary originating near the junction can more readily grow to exclude charged species from both upper and lower branches (which is undesirable).

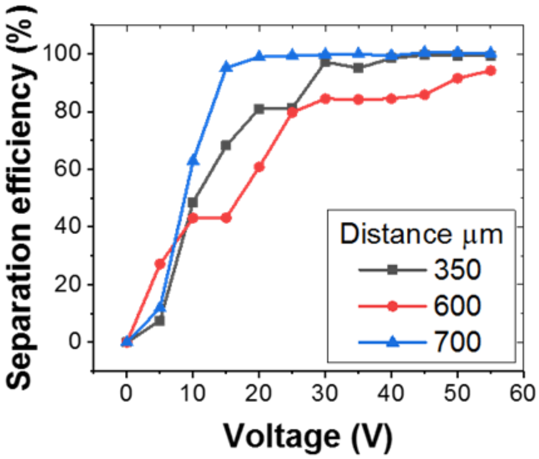

Figure S7. Separation efficiency as a function of applied voltage in three devices at an inlet flow rate of 25 nL min^{-1} over the range of 5.0-55.0 V. The distance of the ion permselective membrane downstream from the fluidic junction is indicated.

System configuration control experiments. Figure S8 shows the behavior of dye-linked albumin (red) and uncharged dye (BODIPY FL, green) near the ion permselective membrane under a potential bias. Fluorescence micrographs were taken in short succession (3 to 6 s apart) for both dyes. **Figures S8a** and **S8b** show the repulsion of both dye-linked albumin and uncharged dye in undiluted blood plasma at 40.0 V (one-electrode configuration). Both species were depleted and directed to the upper branch. Similar behavior of albumin and uncharged dye were observed using the three-electrode configuration (**Figures S8c** and **S8d**), indicating that the configuration does not determine whether the neutral dye depletes in blood plasma.

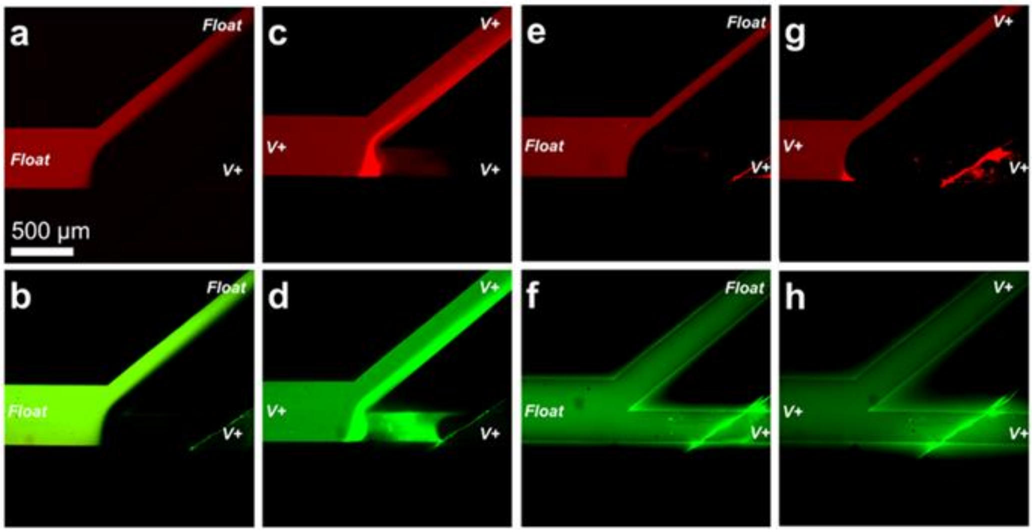

Figure S8. Fluorescence micrographs showing the location of both tracers under 40.0 V (at outlets corresponding channels labeled *V+*) in (a-d) undiluted blood plasma and in (e-h) model blood plasma (containing 0.1% of the albumin content of blood plasma). The results compare the one-electrode (a,b and e,f) and three-electrode (c,d and g,h) configurations. The dye-linked albumin (red, top row) is redirected into the upper branch in all cases, while BODIPY FL was redirected in undiluted plasma only.

These results were compared for an identical set of experiments in model blood plasma (solution that models the pH and salinity of blood). The solution contained 0.05 mg mL^{-1} dye-linked albumin (approximately 0.1% of the concentration of albumin in human blood) and 1.0 µM BODIPY in 50.0 mM NaCl, 5.0 mM KCl, and 20.0 mM carbonate at pH 7.4. In the one-electrode configuration, when 40.0 V were applied, the albumin depleted (Figure S8e), however uncharged dye showed no significant depletion behavior (**Figure S8f**). Similarly using the three-electrode configuration, only albumin showed significant depletion behavior (**Figure S8g** and **S8h**).

CHAPTER 4. CONTINUOUS MICELLAR ELECTROKINETIC FOCUSING OF NEUTRAL SPECIES BY ION CONCENTRATION POLARIZATION

Beatrise Berzina, Robbyn K. Anand

Iowa State University, Department of Chemistry

Modified from a manuscript published in *Lab on a Chip*, **2019**, *19*, 2233-2240.

Abstract

Ion concentration polarization (ICP) has been broadly applied to accomplish electrokinetic focusing of charged species. Despite recent advancements in the ICP field, the ICP-based separation and enrichment of neutral compounds, important for pharmaceutical, biological, and environmental applications, has not yet been reported. Here we report the ICP-based selective and continuous extraction of a neutral compound from aqueous solution by its partition into an ionic micellar phase. Initial results demonstrate the dependence of the separation efficiency on the concentrations of the target compound and the surfactant comprising the micellar phase. As a key feature relevant to the practical application of this method, we show that focusing occurs even an order of magnitude below the critical micelle concentration through the local enrichment and assembly of surfactants into micelles, thus minimizing their consumption. This approach provides access to strategies for selective separation that have been developed in micellar electrokinetic chromatography.

Introduction

Here, we report the continuous extraction of neutral (un- charged) compounds from aqueous solution using an electrokinetic process driven by ion concentration polarization (ICP). This outcome is achieved by the partition of these neutral compounds into an ionic micellar phase, thus conferring them with charge. The results of this study are important for two reasons.

First, this approach provides access to a wide array of strategies that have been developed in the mature field of micellar electrokinetic chromatography (MEKC) for selective separations. Second, we show that focusing occurs even an order of magnitude below the critical micelle concentration (CMC) through the local enrichment and assembly of surfactants into micelles.

ICP is the simultaneous enrichment and depletion of ions at opposing ends of an ion permselective membrane[1] or bipolar electrode[2,3] when an electric field is applied across it. An ion selective membrane may be comprised of charged nanopores or nanochannels that electrostatically exclude co- ions. For example, the pores of a cation selective membrane (e.g., *Nafion*) are lined with negatively charged moieties and therefore exclude anions. When a voltage is applied across the membrane, cations are selectively transported through, while anions migrate towards the anodic driving electrode, resulting in the formation of an ion depletion zone (IDZ) in the anodic compartment. The low ionic conductivity of the IDZ leads to a strong (>10-fold) local enhancement of the electric field and the formation of concentration and electric field gradients at the IDZ boundary. The non-linear migration of ions in these gradients results in further exclusion of charged species from entering the IDZ – a feature that has been leveraged for focusing and continuous separation of charged species.[4]

ICP has had a major impact in several areas of application including desalination,[5–7] enrichment and separation of trace analytes[3,8,9] and bioparticles,[8,10] cellular dielectrophoresis,[11] regeneration of sensing substrates,[12] and mobility shift assays for bioanalysis.[13] Most relevant to the current work is the ability of ICP to continuously separate charged species from an aqueous solution in a branched, flow-through micro- fluidic device (**Scheme 1a**) – a feature that has been employed for desalination[5–7] and for the removal of excess fluid from blood plasma.[14] While ICP has proven to be a versatile approach for enriching and separating charged species, neutral compounds are unaffected by the electric field, thereby limiting its application. This limitation is of particular concern for ICP-based water purification, which requires the removal of uncharged contaminants, and for evaluating the purity of food and pharmaceutical products, where the enrichment of uncharged compounds prior to analysis may be crucial.

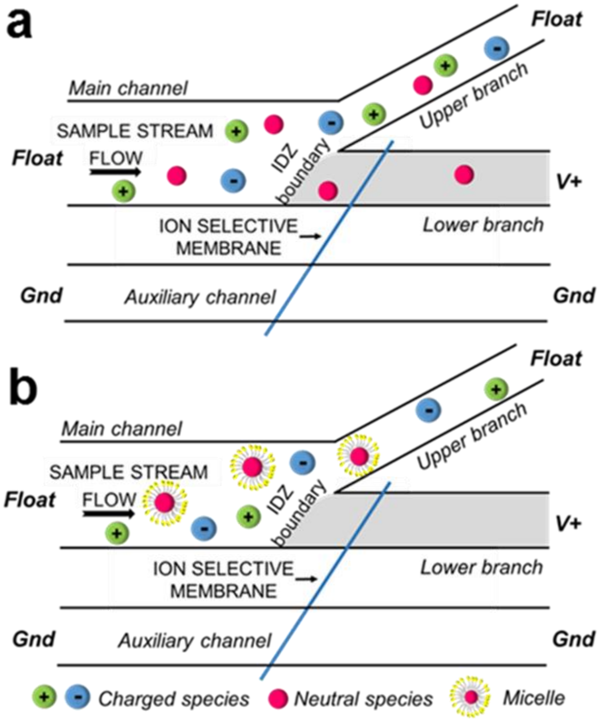

Scheme 1.

Our previously published results indicate that ICP-based separation of neutral species is feasible – we observed electro- static redirection of an uncharged fluorophore in blood plasma, which we attributed to intermolecular interaction of the dye with charged compounds native to blood.[14]

Here, we leverage this phenomenon to address the need for separation and enrichment of neutral species by their partition into an ionic micellar phase (**Scheme 1b**). The addition of ionic surfactants above the CMC has proven to be an effective technique for electrokinetic separation of neutral compounds in capillary electrophoresis.[15–18] In MEKC, micelles act as a pseudostationary phase, into which analytes partition based on their affinity for the functional groups comprising the core (e.g., through hydrophobic or π–π interactions). In this scenario, compounds that are not ionic under experimental conditions can be incorporated into the micelle and then electrophoretically separated by virtue of the charge on the micelles. MEKC techniques leverage anionic, cationic, and non-ionic surfactants, mixed micelles, and additives, such as organic solvents, ionic liquids, and cyclodextrin, to tightly control guest–host interactions. These strategies accomplish electrokinetic separation of compounds that differ in size, hydrophobicity, charge, and conformation – even distinguishing enantiomers. Most relevant to the work reported here is that MEKC has been utilized for sample preconcentration by field-induced sample stacking and sweeping.[16] For example, Palmer et al. reported a method for stacking neutral analytes in micellar capillary electrophoresis.[19] By using a background electrolyte (BGE) less conductive than the sample matrix, they achieved field amplification within the BGE, resulting in stacking of the charged micelles. The stacked micelles complex with neutral analytes efficiently and concentrate them locally thus achieving higher sensitivity. This approach was shown to be particularly relevant for separation of nitroaromatic and nitroamine explosives present in seawater. In comparison to MEKC, longer injection times in conjunction with stacking, lead to improved detection limits to sub mg L^{-1} levels of these compounds. However, the resolution in comparison to MEKC, is decreased.[20]

Here, we demonstrate that in combination with ICP, micelles permit electrokinetic focusing of two uncharged species that partition into the micellar phase, thus leading to their continuous extraction from a flowing solution. We quantify the dependence of the efficiency of this extraction on the input concentration of the surfactant and analyte, the flow rate, and the applied voltage. Critical to the practical application of this method, we have demonstrated neutral analyte extraction at input concentrations of surfactants below the CMC through their local enrichment and assembly into micelles at the IDZ boundary. Collectively, these results demonstrate the capabilities of a new technique for enrichment of neutral targets – continuous micellar electrokinetic focusing (CMEKF).

Materials and methods

Chemicals. Texas Red and CellTracker Green BODIPY dye were obtained from Molecular Probes (Eugene, OR). Sodium dodecylsulfate (SDS), Nafion® perfluorinated resin (20 wt% solution in lower aliphatic alcohols) and Pluronic F-108 (poly(ethylene glycol)-block-poly(propylene glycol)-block-poly(ethylene glycol)) were purchased from Sigma-Aldrich, (St. Louis, MO). Sodium cholate (SC) and pyrene were purchased from Alfa Aesar (Haver- hill, MA). Platinum electrodes (99.95%) were purchased from Strem Chemicals (Newburyport, MD). All solutions were made with reagent grade chemicals (Fisher Scientific, Waltham, MA) and diluted with double deionized water (18.2 MΩ cm, Sartorius Arium Pro, Göttingen, Germany) before use. Spent dialysate (from hemodialysis) was obtained from Mary Greely Hospital (Ames, IA) and used without additional purification.

Device fabrication. The PDMS/glass devices were fabricated using standard soft lithography techniques.21 Briefly, channel molds were patterned using negative photoresist (SU-8 2050, Microchem Corp., Westborough, MD) on a Si substrate. Poly(dimethylsiloxane) (PDMS) (Sylgard 184 elastomer kit, Dow Corning Corp., Midland, MI) was used for microfluidic device fabrication. *Nafion* was used as an ion permselective material. A permselective membrane was incorporated into the device employing a mechanical incision/self-sealing method.[7] Briefly, using a scalpel, an incision (~2 mm deep) was made across the lower branch (Scheme 1) of the micro- channel approximately 300 μm downstream of the branching junction. A 10 μL droplet of the *Nafion* precursor solution was pipetted at one end of the incision, which was gently opened by bending the PDMS monolith to allow the *Nafion* solution to wick into it. The *Nafion* was then cured in an oven at 95 °C for 10 min, and then any excess *Nafion* removed by repeatedly adhering residue-free tape to the PDMS surface. The PDMS layer and glass slide were then treated in an air plasma (PDC-001, Harrick Plasma, Ithaca, NY) for 60 s and finally bonded together. A more detailed description of the device fabrication and dimensions are included in the ESI. Immediately after bonding, all microfluidic devices were rinsed with deionized water and coated by filling the channels with Pluronic solution and incubating at 4.0 °C for at least 18 h. The Pluronic coating was used to suppress electro- osmotic flow. The microfluidic devices were then rinsed with 20.0 mM surfactant solution (SDS or SC) in 10.0 mM phosphate buffer (pH 7.4) for one hour prior to use to ensure uniform wall charge regardless of the surfactant concentration employed in the experiment.

Electrokinetic separation experiments. Prior to ICP experiments, each device was rinsed with 10.0 mM phosphate buffer solution for 15 min to remove excess surfactant. The rinsing solution was then replaced with the sample solution. A driving voltage was applied across the nanojunction using a DC power supply (HY3005D, Mastech and DIGI360, Electro Industries, Westbury, NY) connected to Pt electrode wires positioned in the main (*V*+) and auxiliary (Gnd) channel reservoirs (**Scheme 1**). The concentration, and volume of solution and voltages employed for individual experiments are indicated in the Results and discussion section and in the ESI.

Fluorescence measurements. All fluorescence measurements were performed using an Eclipse Ti-S inverted fluorescence microscope (Nikon Industries, New York, NY) equipped with a digital camera (Orca Flash 4.0, Hamamatsu Corp., Bridgewater, NJ). All images were processed using NIS-Elements 4.6 software (Nikon). Fluorescence measurements used for quantitative comparison of species concentrations were background subtracted.

Results and discussion

Response of neutral species to ICP in the absence of surfactants. We first characterized the behavior of charged and neutral species in ICP-based separation in the absence of surfactant. **Fig. 1** shows the behavior of charged (red) and neutral (green) fluorophores near the ion permselective membrane (dashed line) in a sodium phosphate buffer solution (10.0 mM, pH 7.4) as it is flowed (left to right) into a branched microfluidic channel. An IDZ formed immediately upon ap- plication of a 60.0 V driving voltage (*V*+) versus ground ap- plied in the auxiliary channel (not shown), and as a result, charged species, represented by Texas Red, were re-directed into the upper branch (**Fig. 1a**), while a neutral species (BODIPY) was unaffected (**Fig. 1b**). These results clearly demonstrate that neutral species are not repelled by the IDZ in the absence of surfactant.

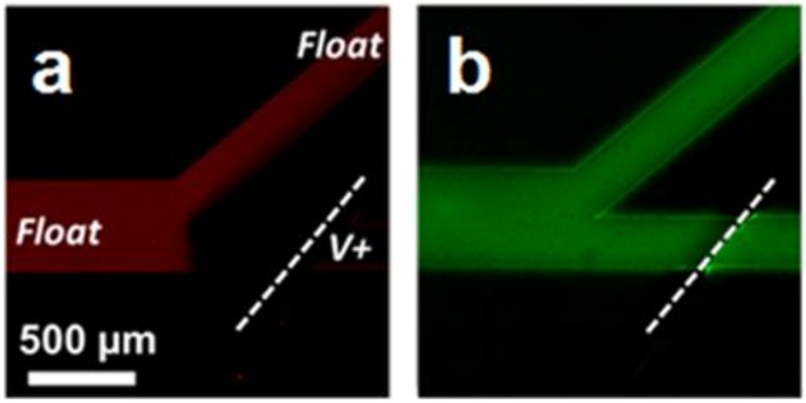

Figure 1. Fluorescence micrographs showing the location of (a) Texas red (1.0 µM) and (b) BODIPY (50 µM) dyes, which are representative of charged and neutral species, respectively, during ICP in 10.0 mM phosphate buffer (pH 7.4); *V*+ = 60.0 V.

Surfactant influence on the extraction of neutral compounds by ICP. Next, we investigated the impact of a surfactant present at several distinct concentrations (**Fig. 2**). It was anticipated that increasing surfactant concentration above the CMC would result in neutral species repulsion from the IDZ and into the upper branch. **Fig. 2a** is a series of fluorescence micrographs that shows the enrichment and extraction of an uncharged dye (BODIPY, at an initial concentration of 50 μM) as a function of the concentration of the anionic surfactant, sodium dodecyl sulfate (SDS), under an applied voltage of 60.0 V.

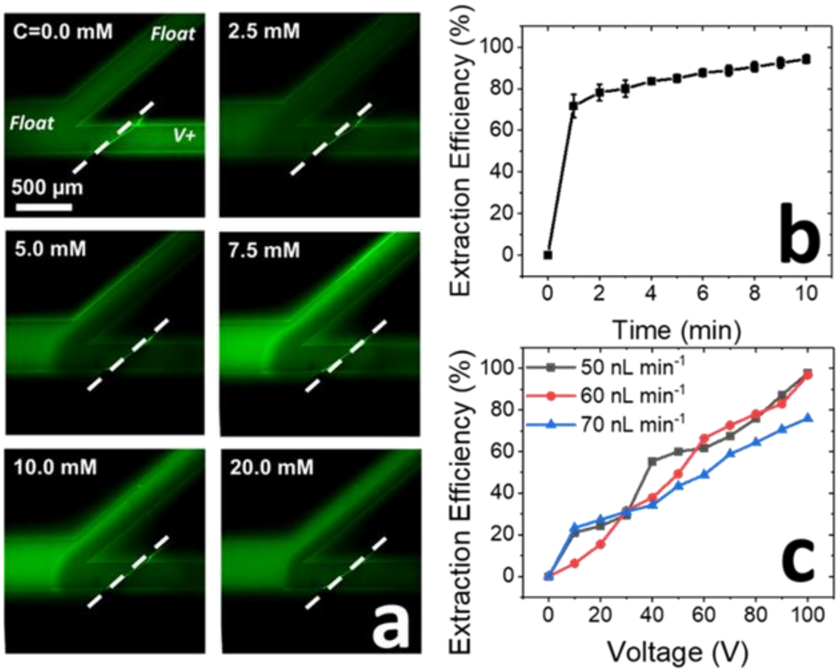

Figure 2. (a) Fluorescence micrographs showing the location of neutral species (BODIPY, 50 μM input) in solutions having distinct SDS concentrations under an applied voltage of 60.0 V. (b) Extraction efficiencies obtained under the same conditions as in (a) (n = 3). (c) Extraction efficiency as a function of flow rate and applied voltage in 10.0 mM SDS (n = 3). Images employed to calculate efficiency obtained 1 min after the application of each voltage.

Extraction efficiency is a commonly used measure in ICP studies to describe the degree of exclusion of a target com- pound from the IDZ under an applied voltage and is defined here as the percent decrease in background subtracted fluorescence intensity in the lower microfluidic branch down- stream of the membrane. Extraction efficiencies above 95% were achieved at an input SDS concentration of 10.0 mM (**Fig. 2b**). We further observed that modest extraction (about 50%) is achieved at an SDS concentration of 2.5 mM – about half of the CMC (4.53 ± 0.03 mM, see ESI†). These results are significant because they highlight the utility of micelles for electrokinetic focusing of neutral species and demonstrate that onset of extraction occurs below the CMC. This latter outcome is attributed to local enrichment of the surfactant near the IDZ boundary.

Next, fixing the SDS concentration at 10.0 mM, we further investigated the dependence of extraction efficiency on flow rate and applied voltage. After establishing each flow rate, the voltage was decreased from 100.0 V in 10.0 V increments at 1 min intervals (detailed procedure in ESI†). **Fig. 2c** demonstrate that extraction efficiency is insensitive to flow rate over the range tested (50–70 nL min^{-1}) and increases monotonically with applied voltage to a maximum of 90–95% at 100.0 V. However, by increasing the time interval between voltages from 1 min to 10 min, the extraction efficiency further increased to 94 ± 2% at voltages as low as 60.0 V (at 60 nL min^{-1}) (Fig. S4†). This result is important because it indicates a delay in increased extraction efficiency in response to an increase in electric field strength – a delay which is attributed here to the time required for a higher concentration of SDS micelles to be established upstream of the IDZ boundary. This phenomenon was further investigated and is further addressed in section 3.4.

Influence of neutral species concentration on extraction efficiency. To ensure high extraction efficiency, the concentration of the micelles must be sufficiently high to avoid saturation with the neutral guest. **Fig. 3** shows the extraction of an uncharged dye present at three distinct concentrations, each in 10.0 mM SDS. In the case that the concentration of this neutral species is lower than or similar to that of the micelles, the extraction efficiency is as high as 95%

(**Fig. 3a** and **c**). The concentration of micelles can be estimated by dividing the surfactant concentration by the aggregation number, which is the number of surfactant molecules per assembled micelle. This value depends sensitively on ionic strength and is on the order of 60–70 for SDS. Therefore, neglecting free surfactant molecules, 10 mM SDS corresponds to a maximum of approximately 0.15 mM micelles. The actual micelle concentration near the IDZ is likely higher, due to its gradual electrokinetic enrichment. When BODIPY concentration surpasses the micelle concentration, the neutral species saturate the micelles, resulting in a sharp decrease in extraction efficiency (**Fig. 3b** and **c**). **Fig. 3c** shows extraction efficiency as a function of neutral species concentration.

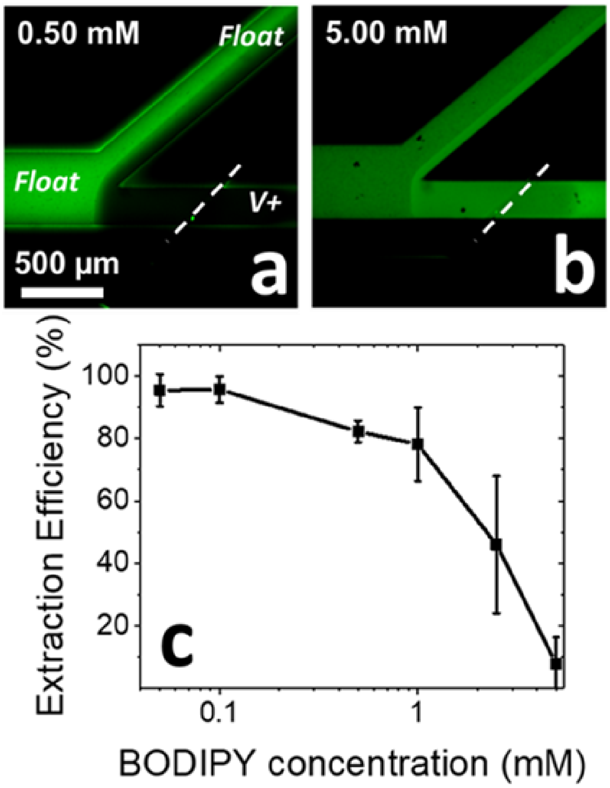

Figure 3. Fluorescence micrographs showing the extraction of a neutral dye (BODIPY) at two distinct concentrations (a) 0.50 and (b) 5.0 mM, each in 10.0 mM SDS (10.0 mM phosphate buffer). Micrographs were obtained 5 min after applying 60.0 V. Flow rate, 60 nL min^{-1}; (c) extraction efficiency as a function of BODIPY dye concentration for the conditions employed in (a and b) (n = 3).

These results clearly demonstrate the limitation of CMEKF at high guest–host ratios and follow the previous finding in MEKC that the capacity of the extraction is directly proportional to the micelle concentration and the solubilization number.[16]

Local formation of micelles by enrichment of surfactant. The results of **Fig. 2** indicate that neutral compounds can be extracted in the presence of surfactant concentrations as low as half of the CMC. Based on these results, we hypothesized that the surfactant is locally enriched to an extent dependent upon the branching geometry at the microfluidic junction – enriching approximately 2-fold at a 1 : 1 branch. This estimate assumes that the flow rate in both branches is equal and that the IDZ is completely contained in the lower branch. To test this hypothesis, the extraction of the uncharged tracer dye (BODIPY) was quantified in devices having a range of channel width ratios between the upper and lower branches (Fig. S2†). **Fig. 4** shows neutral species extraction in the presence of only 1.0 mM SDS (well below the CMC) in three devices with distinct ratios of upper branch to lower branch width (1 : 9, 1 : 4, and 1 : 1, respectively) as a function of time (experimental details, ESI†). In the high channel width ratio devices, extraction efficiencies above 90% were observed 20 min after applying the driving voltage (**Fig. 4a** and **b**). In contrast, only modest local enrichment and extraction of neutral species occurred in the 1 : 1 ratio device (**Fig. 4c**). These results demonstrate that by using high channel width ratio devices, surfactant present at an input concentration well below the CMC exhibits an ability to encapsulate and extract BODIPY to an increasing degree over time. This behavior is attributed to gradual accumulation of SDS upstream of the IDZ boundary and the local formation of guest–host pairs (**Fig. S6**). Using this strategy, extraction was achieved at as low as a full order of magnitude below the CMC (0.5 mM SDS, **Fig. S5**). These results are significant because they indicate that CMEKS can be made effective at low concentrations of surfactant, thus reducing its consumption.

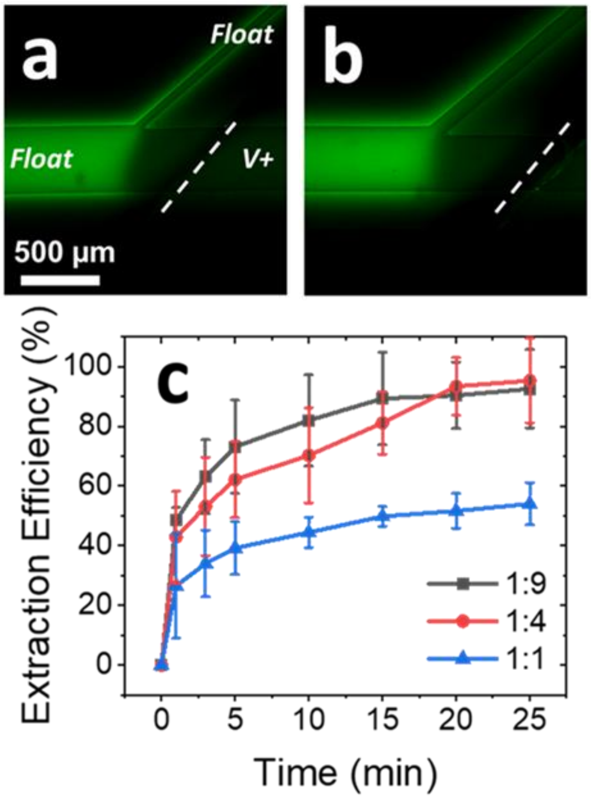

Figure 4. Fluorescence micrographs showing continuous extraction of BODIPY (initial concentration, 50 μM) in the presence of 1.0 mM SDS in (a) 1 : 9, and (b) 1 : 4 channel width ratio devices in 10.0 mM phosphate buffer solution. Images obtained 20 min after applying 60.0 V. Flow rate, 60 nL min^{-1}; (c) extraction efficiency shown for 1 : 9 (black), 1 : 4 (red), and 1 : 1 (blue) ratio branches (n = 3).

Physical and chemical properties of surfactants are of great importance to their ability to bind compounds to be analyzed or separated. To test an alternative surfactant for micelle formation, we chose to use the environmentally benign bile salt, sodium cholate (SC). SC has been used as an additive to enhance the solubilization of hydrophobic compounds in pharmaceuticals,[22] to bind polyaromatic hydrocarbons (PAHs) for water and soil purification,[23,24] and to discriminate analytes in MEKC.[25,26] Due to a relatively flat-shaped hydroxy-substituted steroid portion, and a side-chain with a carboxyl group structure, SC has also proven to be suited for enantiomer separation by MEKC.[26–28] In contrast to SDS, SC has a wide range of reported CMC values and its aggregation number (4–16) is strongly dependent on surfactant concentration (10–60 mM).[23] Typical concentrations of SC employed for separation range from 25 mM to 100 mM.[26,27] Addition- ally, the solubilization of organic compounds increases with cholate concentration up to 60.0 mM.[23] Here, we employ a branched microchannel with a 1 : 9 width ratio to demonstrate local enrichment of 3.0 mM SC to a concentration above the CMC,[23,25] at which it can bind a target compound. **Fig. 5a** is a fluorescence micrograph showing the continuous extraction of BODIPY from a flowing solution at t = 45 min after initiating the driving voltage for the separation.

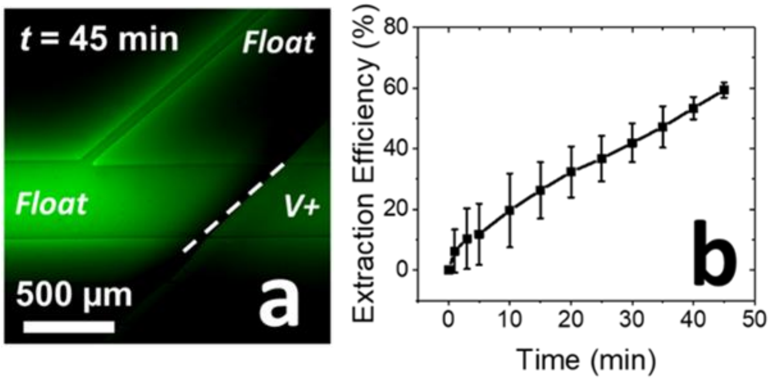

Figure 5. (a) Fluorescence micrograph showing extraction of BODIPY (initial concentration, 50 µM) in the presence of 3.0 mM SC in 10.0 mM phosphate buffer. Flow rate, 60 nL min^{-1}; $V+$ = 60.0 V. (b) Plot of extraction efficiency obtained under these conditions as a function time (voltage applied at t =0; n =3).

Fig. 5b is a plot of the extraction efficiency (percent of BODIPY repelled from the lower branch) over time. The increase in extraction efficiency over time is attributed to gradual accumulation of SC just upstream of the IDZ. Under these conditions, up to 60% extraction was observed (at t =45 min). An improved extraction efficiency (65%) was obtained by increasing the driving voltage to 80.0 V (**Fig. S8**). However, the increased driving voltage is known to increase linear and angular velocity of vortex flow in the IDZ, causing solution mixing, thus disrupting the IDZ boundary.[29] This phenomenon is likely contributing to the limited extraction efficiency.

In comparison to SDS, the lower extraction efficiency can be explained by the lower mobility of SC micelles leading to poorer repulsion at the IDZ.[30–32] Additionally, several physical and chemical parameters such as polarity and the ability to donate or accept hydrogen bonds influences the solvation properties of surfactants, and thus will ultimately impact the neutral species extraction efficiency by ICP.[31,32]

PAHs found in soil and water pose a serious threat to human health and to water-dwelling species. Remediation of PAHs can be accomplished by micellar solubilization.[33] Here, we demonstrate that CMEKF with SC micelles can be employed to both solubilize and continuously extract PAHs from aqueous solution into a concentrated waste stream. It has been reported that the average solubilization number in- creases with the aggregation number of SC, and therefore, the local concentration of SC is critical to this application. For example, pyrene – employed here as a model PAH – has a solubilization number of 0.059 to 0.18 (pyrene molecules per micelle) for SC aggregation numbers of 8.6 and 16, respectively.[23] **Fig. 6a**–**c** show the solubilization and simultaneous extraction of two neutral compounds (pyrene and BODIPY) from an aqueous solution in the presence of 40.0 mM SC. At early timepoints after applying the driving voltage (**Fig. 6a**, t = 30 s), bright fluorescent aggregates of pyrene were observed in the flowing solution. Pyrene solubility increased over a period of five minutes (**Fig. 6c**) as indicated by homogenization of the solution. The extraction efficiency for pyrene achieved at 5 min reached 95%, which may be improved by employing surfactants (or mixed surfactants) that yield a higher partition coefficient for this model PAH.30. **Fig. 6d**–**f** show the location of BODIPY dye at the same timepoints as in **Fig. 6a–c**. BODIPY was added to the sample mixture to verify IDZ formation and local enrichment of the surfactant. Further, once the applied voltage was removed, solution with pyrene aggregates and BODIPY again filled the main channel (**Fig. S10**). These results are important because they indicate that the reported approach may prove to be a useful route to enhance ICP-based water purification. Additionally, the increased solubilization of pyrene over time supports our earlier conclusion that surfactants are locally enriched upstream of the IDZ boundary.

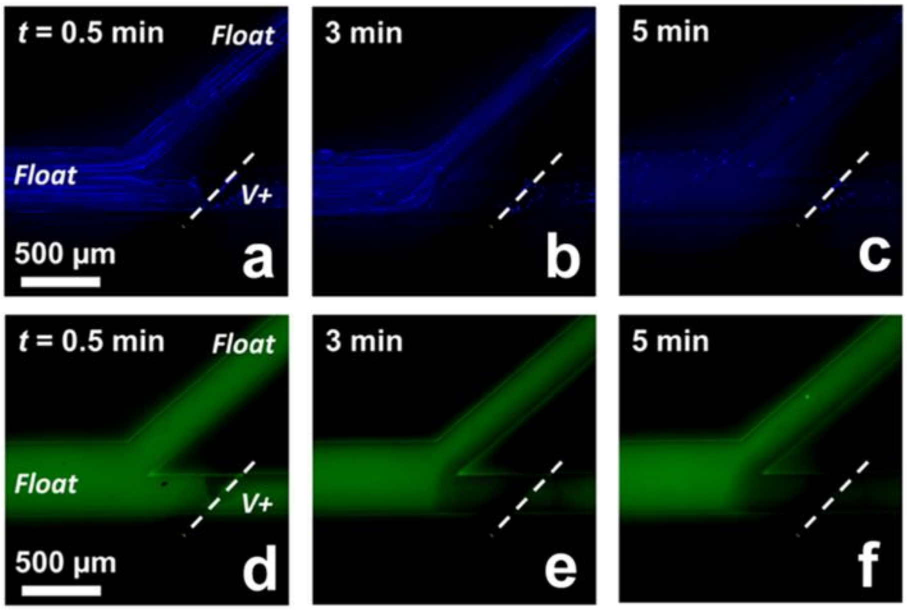

Figure 6. Fluorescence micrographs showing the continuous focusing and solvation of neutral species (a–c) pyrene (blue, 150 μM input concentration) and (d–f) BODIPY (green, 50 μM input concentration) in the presence of 40.0 mM SC in 10.0 mM phosphate buffer (pH 7.4). Flow rate, 60 nL min^{-1}. $V+$ = 60.0 V.

An important point is that many of the strategies currently under investigation to increase the volumetric throughput of ICP-based desalination can be used in conjunction with CMEKF.[5,33] We investigated the ability of CMEKF to proceed in a more complex matrix (spent dialysate) employing a larger channel for increased throughput and microfins to suppress vortex flow patterns.[33] The spent dialysate is saline solution (pH 9.15, 13.9 mS cm^{-2}), with added glucose (122 mg dL^{-1}) and uremic toxins (e.g., urea, creatinine, small proteins, indoles, phenols, aliphatic amines) dialyzed from a patient during hemodialysis. **Fig. S11a–d** demonstrate the extraction of fluorescently tagged bovine serum albumin (negatively charged) and uncharged species (BODIPY) in the presence and absence of SDS (10 mM) in undiluted spent dialysate under an applied voltage of 120.0 V. These results demonstrate the extraction of albumin from spent dialysate in the absence of the surfactant (**Fig. S11a**, 89%), while the neutral species is unaffected by the electric field (**Fig. S11b**). After adding surfactant above the CMC to the sample, both charged species and neutral species were repelled into the upper branch with 87 and 85% efficiency, respectively (**Fig. S11c** and **d**). These results indicate, that CMEKF can be used in more complex matrices.

Conclusions

In summary, we have shown that continuous electrokinetic separation of a neutral species from an aqueous buffer solution can be achieved using charged micelles in combination with ICP. Importantly, 98 ± 2% extraction efficiency can be achieved (in a device with a 1:1 branching ratio) while using SDS concentrations above the CMC. In addition, we demonstrated that high micelle concentration ensures high extraction efficiencies until the micelles become saturated and can accept no further neutral species as guests. A key feature of this approach is that the enrichment of surfactant near to the IDZ allows for local micelle formation, and thus, neutral species extraction can be achieved using low input surfactant concentrations. We have further demonstrated the solubilization and continuous removal of pyrene, a model PAH, from a flowing aqueous solution. Additionally, we have demonstrated that CMEKF can be used in more complex sample matrices like spent dialysate. Based on these results, we anticipate that CMEKF will prove to be a useful method for removal of neutral contaminants during ICP-based purification of water.

Our future work in this area is focused on analytical applications of micelles used in conjunction with ICP. In analytical applications, the specificity of certain micelles to bind targeted compounds can be leveraged to tailor separations. Note that when two neutral solutes are present, if one has a significantly higher micelle-water partition coefficient (K_{mw} = $[solute]_{micelle}/[solute]_{water}$), then it will be selectively focused and enriched. K_{mw} is a highly sensitive indicator of molecular structure and varies over a wide range. For example, K_{mw} for a series of aliphatic alcohols in SDS increases by an order of magnitude for every two methylene units added (2.4, 18.3, and 193.9 for ethanol, butanol, and hexanol). Common beta blockers atenolol and propranolol have widely differing K_{mw} for SDS micelles of 389 and 19 055. Indeed, micellar phases that are much more selective than SDS have been devised for specific systems.[28,34] Therefore, we anticipate that continuous and selective electrokinetic separation of one or more neutral compounds from a mixture by CMEKF is attainable. In our ongoing studies, we are developing such selective separations by CMEKF and further leveraging a non-branching device[35] to achieve ‘static’ electrokinetic focusing of uncharged compounds into discrete bands.

References

1. M. Li and R. K. Anand, *Analyst*, **2016**, *141*, 3496–3510.
2. R. K. Perdue, D. R. Laws, D. Hlushkou, U. Tallarek and R. M. Crooks, *Anal. Chem.*, **2009**, ***81,*** 10149–10155.
3. R. K. Anand, E. Sheridan, K. N. Knust and R. M. Crooks, *Anal. Chem.*, **2011**, *83*, 2351–2358.
4. W. Ouyang, X. Ye, Z. Li and J. Han, *Nanoscale*, **2018**, *10*, 15187–15194.
5. B. D. MacDonald, M. M. Gong, P. Zhang and D. Sinton, *Lab Chip*, **2014**, *14*, 681–685.

6. K. N. Knust, D. Hlushkou, R. K. Anand, U. Tallarek and R. M. Crooks, *Angew. Chem., Int. Ed.*, **2013**, *52*, 8107–8110.
7. S. J. Kim, S. H. Ko, K. H. Kang and J. Han, Nat. *Nanotechnol*., **2010**, *5*, 297–301.
8. R. Kwak, J. Y. Kang and T. S. Kim, *Anal. Chem*., **2016**, *88*, 988–996.
9. H. Jeon, H. Lee, K. H. Kang and G. Lim, *Sci. Rep*., **2013**, *3*, 1–7.
10. R. Kwak, S. J. Kim and J. Han, *Anal. Chem*., **2011**, *83*, 7348–7355.
11. R. K. Anand, E. S. Johnson and D. T. Chiu, *J. Am. Chem. Soc*., **2015**, *137*, 776–783.
12. D.-T. Phan, L. Jin, S. Wustoni and C.-H. Chen, *Lab Chip*, **2018**, *18*, 3962–3979.
13. L. F. Cheow, A. Sarkar, S. Kolitz, D. Lauffenburger and J. Han, *Anal. Chem*., **2014**, *86*, 7455–7462.
14. B. Berzina and R. K. Anand, *Anal. Chem*., **2018**, *90*, 3720–3726.
15. P. G. Muijselaar, K. Otsuka and S. Terabe, *J. Chromatogr. A*, **1997**, *780*,41–61.
16. S. Terabe, *Anal. Chem*., **2004**, *76*, 240 A–246 A.
17. S. I. Wakida, K. Fujimoto, H. Nagai, T. Miyado, Y. Shibutani, S. Takeda, *J. Chromatogr. A*, **2006**, *1109*, 179–182.
18. S. Shen, Y. Li, S. I. Wakida and S. Takeda, *Environ. Monit. Assess*., **2009**, *153*, 201–208.
19. J. Palmer, N. J. Munro and J. P. Landers, *Anal. Chem*., **1999**, *71*, 1679–1687.
20. B. C. Giordano, C. L. Copper and G. E. Collins, *Electrophoresis*, **2006**, *27*, 778–786.
21. J. C. McDonald and G. M. Whitesides, *Acc. Chem. Res*., **2002**, *35*, 491–499.
22. G. Hancu, B. Simon, A. Rusu, E. Mircia and Á. Gyéresi, *Adv. Pharm. Bull*., **2013**, *3*,1–8.
23. H. Sugioka and Y. Moroi, *Biochim. Biophys. Acta, Lipids Lipid Metab*., **1998**, *1394*, 99–110.
24. A. Shah, S. Shahzad, A. Munir, M. N. Nadagouda, G. S. Khan, D. F. Shams, D. D. Dionysiou and U. A. Rana, *Chem. Rev*., **2016**, *116*, 6042–6074.

25. E. Fuguet, C. Ràfols, M. Rosés and E. Bosch, *Anal. Chim. Acta*, **2005**, *548*, 95–100.

26. A. L. C. Navazo, M. L. Marina and M. J. Gonzalez, *Electrophoresis*, **2005**, *19*, 2113–2118.

27. E. Fuguet, C. Ràfols, E. Bosch and M. Rosés, *Electrophoresis*, **2002**, *23*, 93–101.

28. K. Otsuka and S. Terabe, *J. Chromatogr. A*, **2000**, *875*, 163–178.

29. S. J. Kim, Y.-C. Wang, J. H. Lee, H. Jang and J. Han, *Phys. Rev. Lett.*, **2007**, *99*, 1–9.

30. L. Hao, R. Lu, D. G. Leaist and P. R. Poulin, *J. Solution Chem.*, **1997**, *26*, 113–125.

31. E. Fuguet, C. Ràfols and M. Rosés, *Langmuir*, **2003**, *19*, 6685–6692.

32. E. Fuguet, C. Ràfols, E. Bosch and M. Rosés, *Langmuir*, **2003**, *19*, 55–62.

33. M. K. Gupta, R. K. Srivastava and A. K. Singh, *E-J. Chem.*, **2010**, *7*, 73–80.

34. K. L. Rundlett and D. W. Armstrong, *Anal. Chem.*, **1995**, *67*, 2088–2095.

35. U. Tallarek, R. K. Perdue, R. M. Crooks, D. Hlushkou and D. R. Laws, *Anal. Chem.*, **2009**, *81*, 8923–8929.

Supporting information

This Supporting Information (SI) includes details of the experimental procedures for 1) conductivity measurements employed to determine the critical micelle concentration (CMC) of sodium dodecyl sulfate (SDS) solutions in 10.0 mM sodium phosphate buffer with and without the addition of BODIPY dye, 2) microfluidic device design and fabrication, and 3) ICP-based extraction experiments that evaluate the impact of concentration (of surfactant and neutral species), flow rate, voltage, and channel geometry on extraction efficiency. Experimental results presented in the SI include fluorescence micrographs that show the extraction process as a function of applied voltage (**Figure S4**), time dependence of extraction efficiency after initiation of driving voltage (**Figure S5**), and extraction efficiency in the presence of surfactant one order of magnitude below the CMC (**Figure S6, S7, S8**) in a device with a 1:9 channel width ratio between upper and lower branches (**Figure S2c**).

Determination of critical micelle concentration. Conductivity measurements were performed to verify the CMC of SDS in 10.0 mM sodium phosphate buffer (pH 7.4, 22 ºC) with and without added BODIPY. The conductivity was measured using an Orion Star A215 pH/Conductivity meter (Thermo Scientific, Waltham, MA). A 25.00 mL solution of SDS (20.0 mM) in sodium phosphate buffer (10.0 mM, pH 7.4, 22 ºC) was serially diluted under vigorous stirring (1200 rpm). Measurements were taken every minute after each change in concentration. The CMC obtained for SDS in sodium phosphate buffer is 4.53± 0.03 mM. These values are in good agreement with those previously published.[1] The CMC of SDS in 10.0 mM sodium phosphate buffer remained in the previously published range even when BODIPY was added (CMC_{SDS}+BODIPY = 4.53 mM, for both 0.05 mM and 0.10 mM BODIPY).

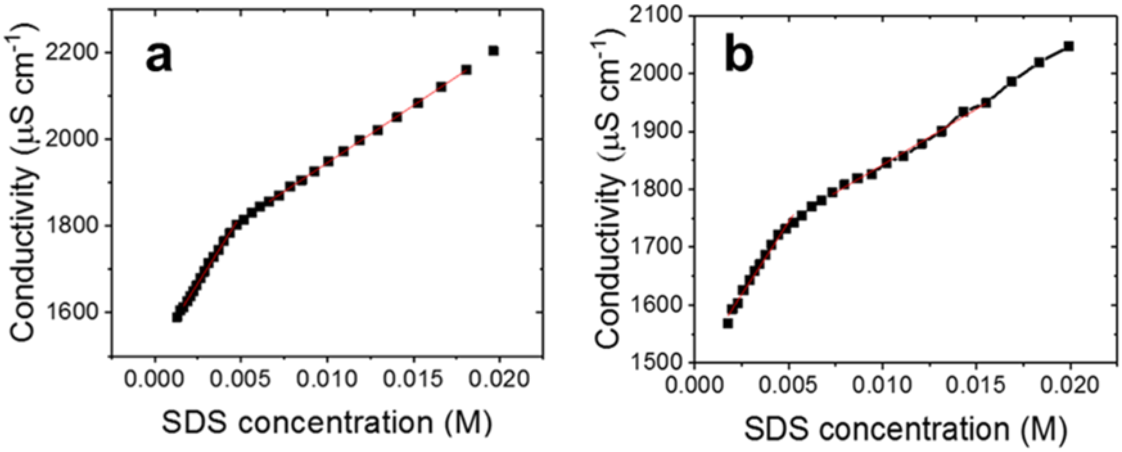

Figure S1. Solution conductivity as a function of SDS concentration in the absence (a) and presence (b) of 50 μM BODIPY dye. Both (a and b) in 10.0 mM sodium phosphate buffer (pH 7.4).

Device fabrication. The microfluidic devices were fabricated using standard photolithographic processes.[2] Channel molds were patterned using negative photoresist (SU-8

2050, Microchem Corp., Westborough, MD) on Si substrate. Poly(dimethylsiloxane) (PDMS) (Sylgard 184 elastomer kit, Dow Corning Corp., Midland, MI) was used for device fabrication. All microchannels were 46.0 µm tall with a distance of 10.0 mm between the inlet and each outlet and having 500 µm-wide main channel that branched into two channels (each 250 µm wide for 1:1 channel width ratio between upper and lower branches) (**Figure S2a**). A second channel (auxiliary channel) 10.0 mm long and 500 µm wide was located parallel to the separation channel at a distance of 300 µm. A 4.0 mm-diameter biopsy punch was used to create the inlet and outlet reservoirs, unless noted otherwise. A mechanical incision was made using a scalpel blade across the lower branch and auxiliary channel, and subsequently filled with 10.0 µL of *Nafion*. The membrane was then cured at 95ºC for 10 min. Excess *Nafion* was removed by applying and peeling away low residue tape. The PDMS layer and glass slide were treated with air plasma (PDC-001, Harrick Plasma, Ithaca, NY) for 60 s (medium RF power) and then bonded together. All microfluidic devices were rinsed with double deionized water and coated with Pluronic (3.0 µM in 10.0 mM phosphate buffer) for at least 18 h. The Pluronic solution was used to suppress the electroosmotic flow. The microfluidic devices were then rinsed with 20.0 mM surfactant solution for 1 h before use to ensure uniform wall charge regardless of the surfactant concentration employed in the experiment. Then just before use, the device was rinsed with 10.0 mM sodium phosphate buffer (pH 7.4) for 15 min to remove the 20 mM surfactant solution. In each experiment, the driving voltage was applied between the outlet of the lower branch (*V+*, **Figure S2**) and both ends of the auxiliary channel (*Gnd*, **Figure S2**). Microfluidic devices with high channel width ratio between the upper and lower branches (**Figure S2b,c**) were fabricated and operated using the same procedure.

Calibration of neutral dye (BODIPY) fluorescence intensities in microfluidic device. The device used for calibration was fabricated with the same dimensions and procedure as the devices employed to obtain the data in the main text. The device was rinsed with double deionized water and coated with Pluronic (3.0 µM in 10.0 mM phosphate buffer) for 18 h. The microfluidic device was then rinsed with 20.0 mM SDS solution for 1 h, and then just before use, rinsed with 10.0 mM sodium phosphate buffer (pH 7.4) for 15 min to remove the surfactant solution. The rinsing solution was then replaced with 0.01 mM BODIPY solution in 10.0 mM sodium phosphate buffer (pH 7.4), and fluorescence micrographs were taken to measure mean fluorescence intensity across the lower branch of the microfluidic device 300 μm downstream from the ion selective membrane. Subsequently, the device was rinsed thoroughly with 10.0 mM phosphate buffer for 15 min and imaged to ascertain the background fluorescence intensity of the channel walls and to account for residual BODIPY adsorption. This procedure was repeated to obtain background subtracted fluorescence intensities for BODIPY concentrations of 0.025, 0.05, 0.075 mM. **Figure S3** demonstrates the linear relationship between background subtracted fluorescence intensity and various BODIPY concentrations.

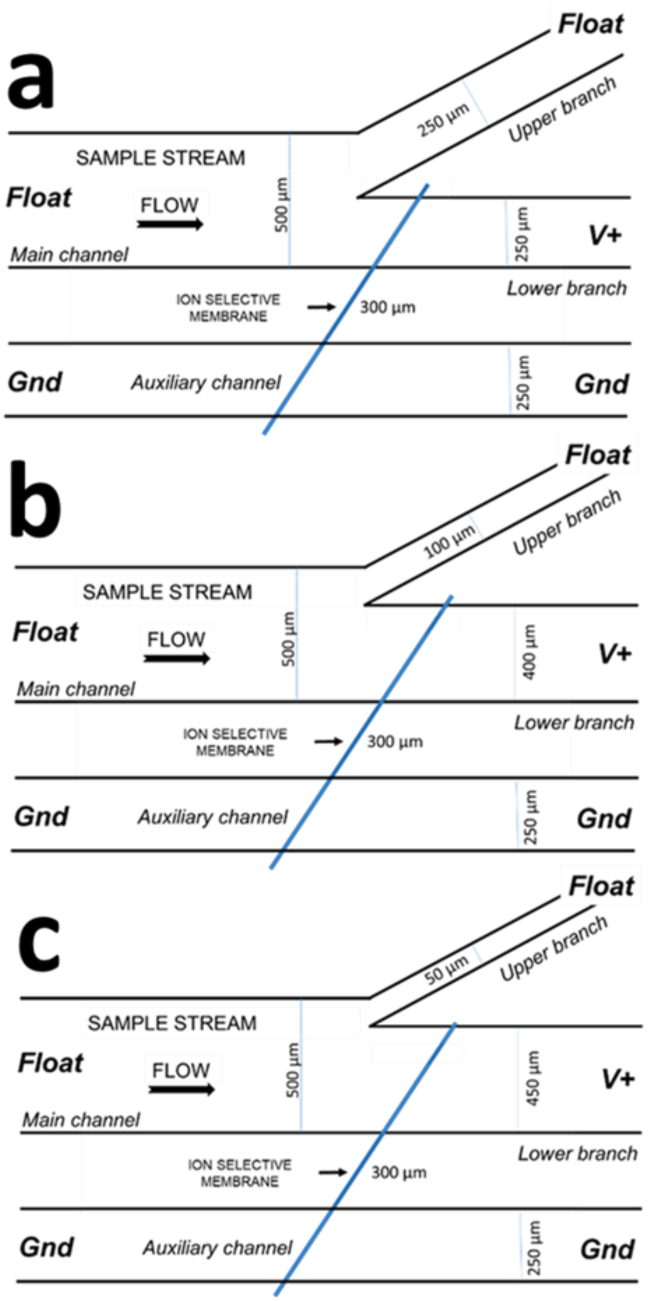

Figure S29. Microfluidic device design schematics with dimensions and experimental setup for continuous ICP separation experiments. Devices with 1:1 (a), 1:4 (b), and 1:9 (c) channel width ratio between the upper and lower branches, respectively.

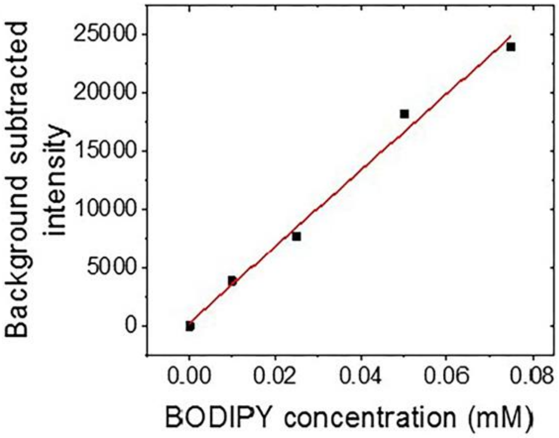

Figure S3. Calibration curve of background subtracted fluorescence intensities for various BODPIY dye concentrations. y = 327384x + 294.12; R^2 = 0.990.

ICP based extraction of neutral species in the absence of surfactants. The device was rinsed with 10.0 mM sodium phosphate buffer (pH 7.4) for 15 min. The buffer in the inlet reservoir was then replaced with 35.0 µL (resulting height difference ~2.8 mm, concave meniscus) of 0.05 mM BODIPY and 1.0 µM Texas Red solution in 10.0 mM sodium phosphate buffer. Then, the volume in the outlet reservoirs was adjusted to 20.0 µL (resulting height difference ~ 1.6 mm, concave meniscus) to generate pressure driven flow of the solution in the main channel. Finally, a driving voltage of 60.0 V was applied. Fluorescence micrographs (Figure 1a-b, main text) were taken 5 min after the driving voltage was applied.

Micellar electrokinetic focusing of a neutral tracer dye by ICP. After the channels were rinsed, the buffer in the inlet reservoir was replaced with 35.0 µL (resulting height difference ~2.8 mm, concave meniscus) of SDS solution (0.0-20.0 mM) and 50 *µ*M BODIPY in sodium phosphate buffer (10.0 mM, pH 7.4). Then, the volume in the outlet reservoirs was adjusted to 20.0 µL (resulting height difference ~ 1.6 mm, concave meniscus) to generate pressure driven flow of the solution in the main channel. Finally, a driving voltage of 60.0 V was applied. Fluorescence micrographs were taken 5 min after the driving voltage was applied (Figure 2a, main text). The device was rinsed thoroughly with 10.0 mM phosphate buffer, re-coated for 15 min using 20.0 mM SDS solution in 10.0 mM sodium phosphate buffer, re-rinsed with phosphate buffer (10.0 mM, pH 7.4) in between trials and imaged to ascertain the background fluorescence intensity of the channel walls and to account for residual BODIPY adsorption. Mean fluorescence intensity across the lower branch of the microfluidic device was measured 300 μm downstream from the ion selective membrane and used for quantitative analysis. All fluorescence intensities were background subtracted. Extraction efficiency (EE) was calculated by comparing the intensity (I) at this location to that obtained prior to initiation of ICP (I_0) such that EE = 100%($1 - I/I_0$).

Evaluation of the impact of flow rate and voltage on extraction efficiency. For these sets of experiments, a 1.0 mm-diameter biopsy punch was used to create the device inlet reservoir (4.0 mm-diameter outlet). A 10.0 mM SDS solution in sodium phosphate buffer (10.0 mM, pH 7.4) spiked with 0.050 mM BODIPY was continuously flowed into the device using a 0.50 mL Hamilton syringe through a 1.0 mm outer diameter PTF tubing. The 11 Pico Plus Elite Programmable Syringe Pump (Harvard Apparatus, Holliston, MA) was used to control the flow rate. After establishing a flow rate of 50 nL min^{-1} a driving voltage of 100.0 V was applied. After 1 min at this voltage, a fluorescence image was taken. The voltage was then turned off for 1 min. This pattern was subsequently repeated such that the voltage was decreased by 10.0 V increments to 10.0 V and images were acquired 1 min after each voltage step (**Figure S4**). These experiments were repeated three times each at flow rates of 50, 60 and 70 nL min^{-1}. In each case, the mean fluorescence intensity across the lower branch of the microfluidic device was measured 300 μm downstream from the ion selective membrane and used for quantitative analysis. After the full voltage sequence, the device was thoroughly rinsed for 15 min using phosphate buffer (10.0 mM, pH 7.4), and imaged to obtain background fluorescence intensity of the channel walls. Background subtracted fluorescence intensities were used to quantify extraction efficiency at each voltage. **Figure 2c** in the main text shows the average extraction efficiency obtained over a range of applied voltages over this series of flow rates.

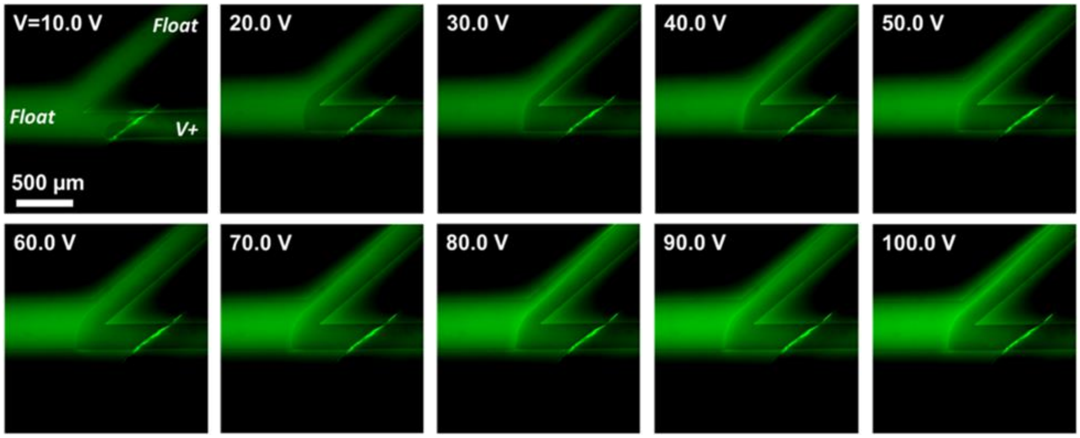

Figure S4. Fluorescence micrographs showing the location of neutral analyte in the presence of 10.0 mM SDS and flow rate of 50 nL min^{-1} for voltage sequence 10.0-100.0 V.

Evaluation of the impact of flow rate and voltage on extraction efficiency at longer periods of time. For these sets of experiments, a 1.0 mm-diameter biopsy punch was used to create the device inlet (4.0 mm outlet). A solution of 0.050 mM BODIPY and 10.0 mM SDS in sodium phosphate buffer (10.0 mM, pH 7.4) was continuously flowed into the device using a 0.50 mL Hamilton syringe through 1.0 mm O.D. PTF tubing. The syringe pump was used to control the flow rate. After establishing a flow rate of 60 nL min^{-1} a driving voltage of 60.0 V was applied. A fluorescence image was taken every 1 min after ICP initiation for a total of 10 min (**Figure S5**). After the full voltage sequence, the device was thoroughly rinsed for 15 min using phosphate buffer (10.0 mM, pH 7.4), and imaged to obtain the background fluorescence intensity of the channel walls. These experiments were repeated three times. **Figure S5** shows the average extraction efficiency obtained over a time period of 10 min. The mean fluorescence intensity across the lower branch of microfluidic device was measured 300 μm downstream from the ion selective membrane and used for quantitative analysis. All fluorescence intensities were background subtracted.

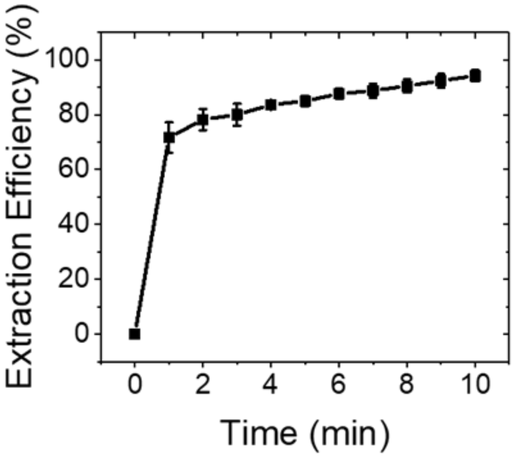

Figure S5. Neutral species extraction efficiency at different time points after initiation of ICP. Results demonstrated using 10.0 mM SDS in 10.0 mM phosphate buffer at flow rate of 60 nL min^{-1}, and under applied voltage of 60.0 V. Error bars represent the standard deviation for three replicates.

Influence of the concentration of the neutral species on the efficiency of CMEKS.

After treatment with SDS and rinsing with phosphate buffer, the buffer in the inlet reservoir was replaced with 35.0 μL (resulting height difference ~2.8 mm, concave meniscus) of 10.0 mM SDS in sodium phosphate buffer (10.0 mM, pH 7.4) with BODIPY at 0.05, 0.10, 0.50, 1.0 or 5.0 mM. Then, the volume in the outlet reservoirs was adjusted to 20.0 μL (resulting height difference ~ 1.6 mm, concave meniscus) to generate pressure driven flow of the solution in the main channel. Finally, a driving voltage of 60.0 V was applied. Fluorescence micrographs were taken 5 min after the driving voltage was applied (**Figure 3**, main text). Then, the voltage was turned off, and the device was rinsed 3 times with 10.0 mM phosphate buffer, re-coated for 15 min using 20.0 mM SDS in 10.0 mM sodium phosphate buffer, and imaged to obtain background fluorescence intensity of the channel walls in between the trials. Extraction efficiency was calculated as described in the preceding paragraphs.

ICP enrichment and extraction of neutral species at surfactant concentrations below the CMC (1.0 and 0.5 mM SDS). For these experiments, a 1.0 mm-diameter biopsy punch was used to create the device inlet. A 1.0 mM SDS solution in sodium phosphate buffer (10.0 mM, pH 7.4) spiked with 0.050 mM BODIPY was continuously flowed into the device using a 0.50 mL Hamilton syringe and 1.0 mm O.D. PTF tubing. The syringe pump was used to control the flow rate. After establishing a flow rate of 60.0 nL min^{-1} a driving voltage of 60.0 V was applied. A series of fluorescence micrographs was acquired over a period of 25 min (images taken at 1, 3, 5, 10, 15, 20, and 25 min) after the start of the experiment. The device was thoroughly rinsed with 10.0 mM phosphate buffer for 15 min and imaged to obtain the background fluorescence intensity of the channel walls. Separation efficiency was calculated as described in the preceding paragraphs. **Figure S6** shows the resulting extraction efficiency obtained for 0.050 mM BODIPY dye in the presence of 0.50 mM SDS over a period of 25 min. **Figure S7** shows the increase of background subtracted intensity across IDZ boundary obtained for 0.050 mM BODIPY dye in the presence of 1.0 mM SDS over a period of 25 min.

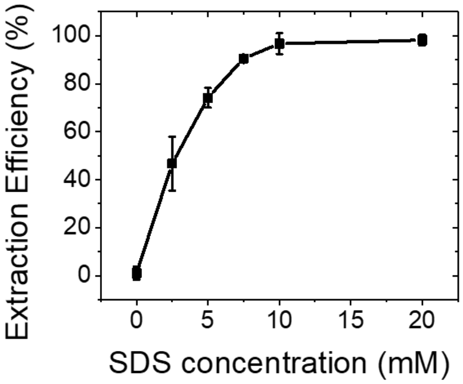

Figure S6. Neutral species extraction efficiency at different time points after initiation of ICP in a device with a branching ratio of 1:9. Results demonstrated using 0.50 mM SDS in 10.0 mM phosphate buffer at flow rate of 60 nL min-1, and under applied voltage of 60.0 V.

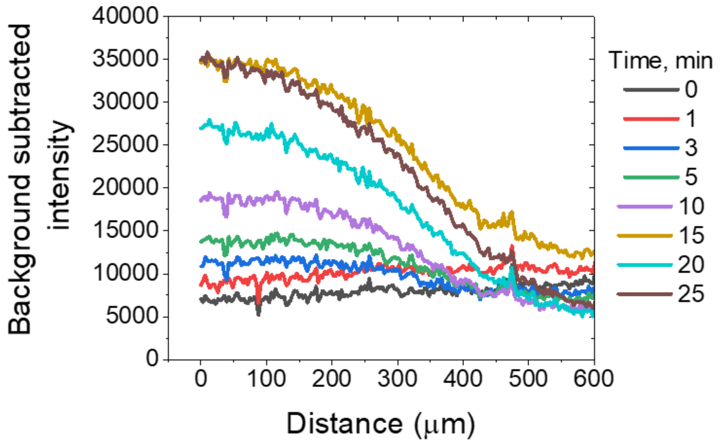

Figure S7. Increase of background subtracted intensity across IDZ boundary of neutral species at different time points after initiation of ICP in a device with a branching channel width ratio of 1:9. Results demonstrated using 1.0 mM SDS in 10.0 mM phosphate buffer at flow rate of 60 nL min^{-1}, and under applied voltage of 60.0 V.

ICP enrichment and extraction of neutral species at sodium cholate concentrations below the CMC. For these experiments, a 1.0 mm-diameter biopsy punch was used to create the device inlet. A 3.0 mM SC solution in sodium phosphate buffer (10.0 mM, pH 7.4) spiked with 0.050 mM BODIPY was continuously flowed into the device using a 0.50 mL Hamilton syringe and 1.0 mm O.D. PTF tubing. A syringe pump was used to control the flow rate. After establishing a flow rate of 60.0 nL min^{-1} a driving voltage of 80.0 V was applied. A series of fluorescence micrographs was acquired over a period of 45 min (images taken at 1, 3, 5, 10, 15, 20, 25, 30, 35, 40 and 45 min) after the start of the experiment. The device was thoroughly rinsed with 10.0 mM phosphate buffer for 15 min and imaged to obtain background fluorescence intensity of the channel walls. Extraction efficiency was calculated as described in the preceding paragraphs. Figure S8 shows the resulting separation efficiency obtained for 0.050 mM BODIPY dye in the presence of 3.0 mM sodium cholate over a period of 45 min. **Figure S9** shows the fluorescence micrographs of neutral analyte (0.050 mM BODIPY) at different time points in the presence of 3.0 mM sodium cholate over a period of 45 min.

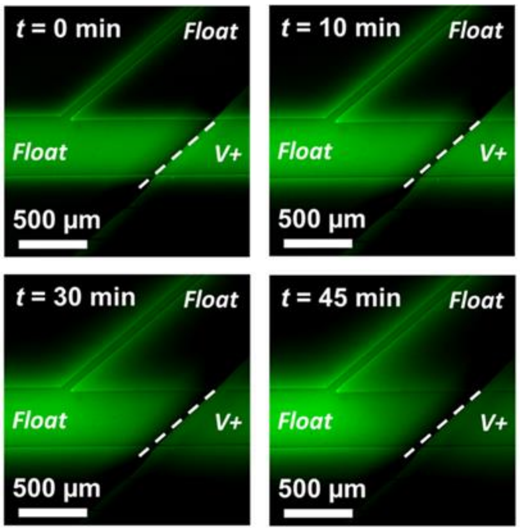

Figure S8. Neutral species extraction efficiency at different time points after initiation of ICP in a device with a branching channel width ratio of 1:9. Results demonstrated using 3.0 mM sodium cholate in 10.0 mM phosphate buffer at flow rate of 60 nL min^{-1}, and under applied voltage of 80.0 V.

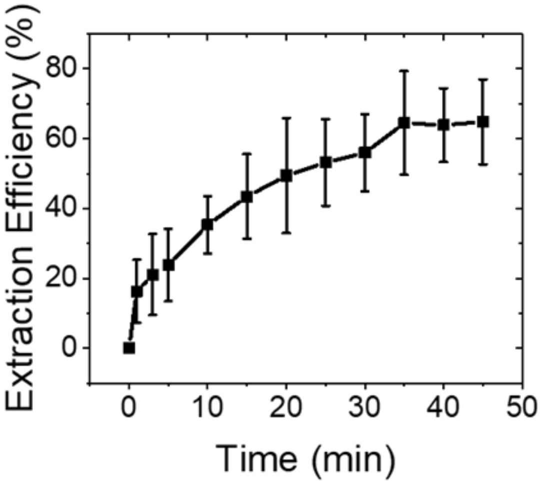

Figure S9. Fluorescence micrographs showing the location of neutral analyte (0.050 mM BODIPY) at different time points in the presence of 3.0 mM SC at a flow rate of 60 nL min^{-1}, and under applied voltage of 60.0 V.

Simultaneous solubilization and extraction of two neutral species (BODIPY and pyrene) from solution by continuous micellar electrokinetic focusing. The device was rinsed with 20.0 mM sodium cholate solution in phosphate buffer (10.0 mM) for 1 h. Further, the device was rinsed with 10.0 mM sodium phosphate buffer (pH 7.4) for 15 min to remove excess surfactant. The buffer in the inlet reservoir was then replaced with 35.0 µL (resulting height difference ~2.8 mm, concave meniscus) of the sample solution (0.05 mM BODIPY, 0.15 mM pyrene, and 40.0 mM sodium cholate, in 10.0 mM sodium phosphate buffer). Then, the volume in the outlet reservoirs was adjusted to 20.0 µL (resulting height difference ~ 1.6 mm, concave meniscus) to generate pressure driven flow of the solution in the main channel. Finally, a driving voltage of 60.0 V was applied. Fluorescence micrographs (**Figures 6a-f**, main text) were taken at the times indicated after the driving voltage was applied. **Figure S10** demonstrates the filling of the main channel with fresh solution from the inlet 1 min after releasing the driving voltage.

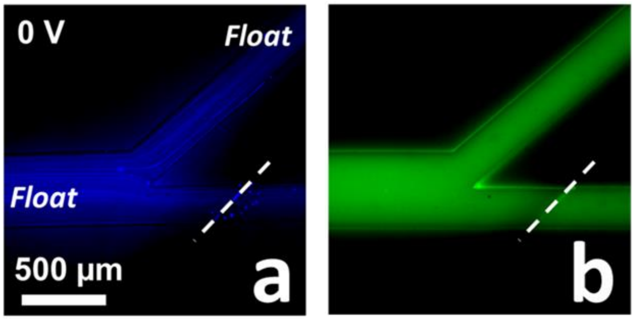

Figure S10 Fluorescence micrographs showing the neutral species (green – BODIPY, 50 µM input concentration; blue – pyrene, 150 µM input concentration) in the presence of 40.0 mM sodium cholate. Image taken 1 min after releasing the driving voltage (*V*+ = 0).

ICP based focusing of charged and neutral species in complex matrices (spent dialysate). An ICP-based device yielding increased volumetric throughput was fabricated according to a previously described procedure. The microchannel had a distance of 10.0 mm between the inlet and each outlet and a 2.1 µm-wide main channel that branched into two channels (0.1 mm and 2.0 mm wide). Microfin structures were 0.5 mm long and 0.020 mm wide with a 0.030 mm gap between microslits). A second channel (auxiliary channel) 10.0 mm long and 0.5 µm wide was located parallel to the separation channel at a distance of 300 µm. A 1.0 mm-diameter biopsy punch was used to create the inlet reservoir. A 4.0 mm-diameter biopsy punch was used to create the outlet reservoirs. A mechanical incision was made using a scalpel blade across the lower branch and auxiliary channel, and subsequently filled with 20.0 µL of Nafion®. The membrane was then cured at 95ºC for 10 min. Excess Nafion® was removed by applying and peeling away low residue tape. The PDMS layer and glass slide were treated with air plasma (PDC-001, Harrick Plasma, Ithaca, NY) for 60 s (medium RF power) and then bonded to a glass slide to form the channel floor. The microfluidic device was rinsed with double deionized water and coated with Pluronic (3.0 µM in 10.0 mM phosphate buffer) for at least 18 h. The microfluidic device was then rinsed with 20.0 mM SDS solution for 1 h before use. Then just before use, the device was rinsed with 10.0 mM sodium phosphate buffer (pH 7.4) for 15 min to remove the 20 mM SDS solution. Undiluted spent dialysate was spiked with BODIPY (to 0.050 mM) and dye-linked albumin (0.1 mg mL^{-1}). This solution was continuously flowed into the device using a 0.50 mL Hamilton syringe and 1.0 mm O.D. PTF tubing. A syringe pump was used to control the flow rate. After establishing a flow rate of 0.2 µL min^{-1}, a driving voltage of 120.0 V was applied. Fluorescence micrographs (**Figures S11a,b**) were obtained 5 min after applying the driving voltage. Further, the device was thoroughly rinsed with 10.0 mM phosphate buffer for 15 min and imaged to obtain background fluorescence intensity of the channel walls. Further, the device was used to repeat the experiment employing spent dialysate spiked with 10.0 mM SDS, 0.050 mM BODIPY and 0.1 mg mL^{-1} dye linked albumin.

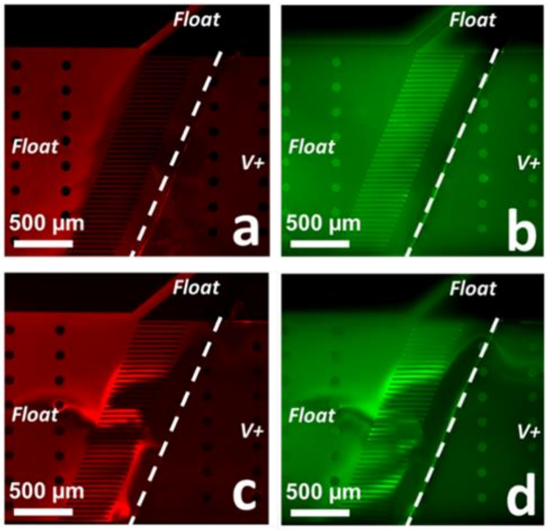

Figure S11. Fluorescence micrographs showing neutral species (green – BODIPY, 50 µM input concentration; red –dye-linked albumin, 0.1 mg mL^{-1} input concentration) in the absence (a,b) and presence (c,d) of 10.0 mM SDS. Flow rate, 0.2 µL min^{-1}.; *V*+ = 120.0 V. Images taken 5 min after applying the driving voltage.

References

1. Fuguet, E.; Ràfols, C.; Rosés, M.; Bosch, E. *Anal. Chim. Acta* **2005**, *548*, 95–100.

2. McDonald, J. C.; Whitesides, G. M. *Acc. Chem. Res*. **2002**, *35*, 491–499.

CHAPTER 5. ENRICHMENT OF CHARGED SPECIES BY OUT OF PLANE FARADAIC ION CONCENTRATION POLARIZATION

Beatrise Berzina, Robbyn K. Anand

Iowa State University, Department of Chemistry

Modified from a manuscript prepared for publication

Abstract

Ion concentration polarization (ICP) is the simultaneous enrichment and depletion of ions at opposing ends of an ion permselective structure under a voltage bias. The steep electric field gradient at the boundary of the ion depleted zone (IDZ) has been leveraged for counter-flow focusing of charged species in applications ranging from highly sensitive bioanalysis to water purification. Despite rapid advancement in ICP-based techniques, there are several important limitations that remain including fluidic instability incurred in scale-up and few options for in situ analysis of focused analytes. Here, we address these challenges with the development out-of-plane faradaic ICP (fICP), in which IDZ formation is driven by charge transfer reactions at a three-dimensional (3D) electrode comprised of metallic microbeads. Relative to fICP at a planar electrode, this 3D-electrode maintains high efficiency focusing by distributing the IDZ across the channel cross section. Further, several geometric features of the bead bed increase fluidic stability, thereby allowing for higher volumetric throughput. Finally, by incorporating a second bed of bioconjugated microbeads upstream of the 3D-electrode, we accomplish highly sensitive in situ quantification of electrokinetically enriched nucleic acids by both fluorescence and non-optical (electrical) detection. We demonstrate detection of 200 pM tumor DNA, following a 1-h single step of enrichment and hybridization. We anticipate that these results will enable a route for high-throughput enrichment, separation, and analysis of biologically and clinically relevant samples.

Introduction

Point-of-care (POC) testing allows for rapid detection, monitoring, and management of disease and is especially important in hospitals, clinics, and remote areas where healthcare facilities and personnel are limited. However, biomarkers that serve as indicators for disease detection are often present at a low concentration (fM-pM) and therefore, require preconcentration. Electrokinetic methods of analyte preconcentration are advantageous for integration with POC testing because they provide efficient transport of charged species in small sample volumes.[1] Over the past two decades, electrokinetic methods of focusing that employ ion concentration polarization (ICP) (**Scheme 1a**) and faradaic ICP (fICP) (**Scheme 1b**) have been developed for enrichment and separation of a wide range of disease biomarkers, including nucleic acids,[2–4] proteins,[5,6] enzymes,[7,8] exosomes,[9] and biological cells.[10–12] Concentration enrichment ranging from 10^2-fold for simple devices to even 10^9-fold for multistage hierarchical preconcentrators[2] has been reported.

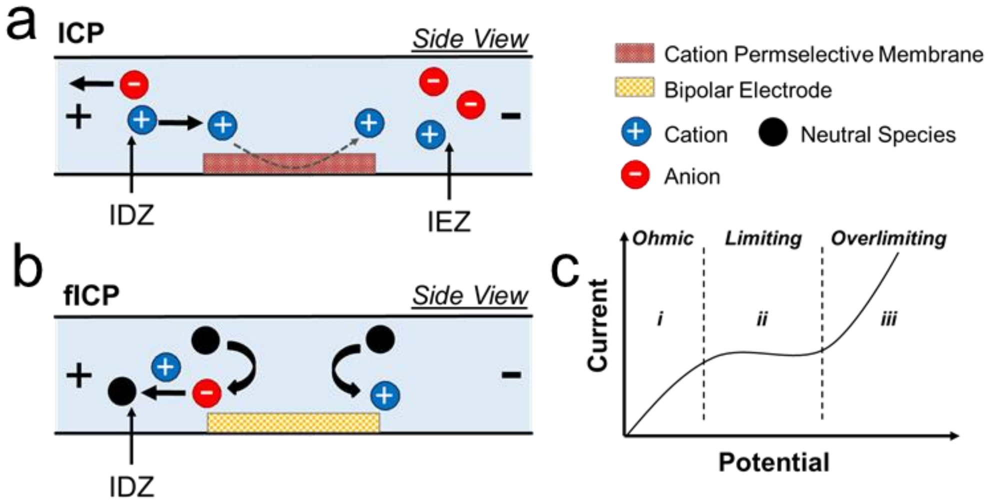

Scheme 1. Illustration of the mechanisms of a) ICP and b) fICP. c) Schematic representation of a current-voltage curve (CVC) displaying characteristic i) ohmic, ii) limiting, and iii) overlimiting regions.

Despite the success of these preconcentration methods, some aspects remain challenging.[13] Many existing ICP-based preconcentrators operate at > 100 V, which hinders integration into POC devices. Further, improvement of volumetric throughput,[2,14,15] integration with downstream analysis,[16–19] and the development of strategies to decrease fluidic instability are active areas of research.[20,21] Fluidic instability (vortex flow), which is exacerbated by increased device dimensions, leads to unwanted mixing, ultimately limiting sensitivity.

In this paper, we introduce out-of-plane fICP, in which electrokinetic enrichment of charged analytes is driven by a 3-dimensional (3D) flow-through electrode comprising a bed of metallic beads. This approach has several distinct advantages. First, the faradaic mechanism allows for a low applied voltage – here, 5.0 to 10.0 V – making it appropriate for point-of-care (POC) application. Second, the 3D electrode distributes the electric field gradient, used for enrichment, across the entire channel cross section, thereby facilitating scale-up of channel dimensions without a loss in analyte retention. Third, we show that incorporation of a second bed, upstream of this electrode, comprised of probe-modified beads facilitates in situ quantification of enriched nucleic acids based on either fluorescence or electrical (non-optical) detection. A key point is that this method offers ‘plug-and-play’ enrichment and detection of unlabeled biomolecules because it is compatible with commercially available conjugated beads. Finally, the geometry of these bead beds mitigates fluidic instability that leads to unwanted mixing. These advancements are significant because they address the most pressing challenges to the application of ICP-based preconcentrators at the point of care.

Both ICP and fICP achieve electrokinetic enrichment by localized depletion of the background electrolyte (BGE), leading to an electric field gradient. Charged analytes are focused at distinct axial locations along this gradient, at which their electrophoretic velocities balance opposing convection. Existing fICP preconcentrators have used thin film electrodes to facilitate electrochemical reactions that generate an ion depleted zone (IDZ). However, in a tall microchannel or under rapid fluid flow, the IDZ does not extend the full height of the microchannel from the planar electrode, and therefore, a fraction of the analyte escapes, carried over the IDZ by convection. This phenomenon decreases the efficiency of enrichment.[22] In prior reports, this challenge has been addressed by decreasing the microchannel height and increasing the applied electric field to augment the IDZ size.[23] However, these approaches sacrifice volumetric throughput and are limited by gas bubble formation, respectively. In a device employed for desalination by ICP, MacDonald and coworkers achieved throughput of up to 20 μL min^{-1} by using an out-of-plane device, in which a vertical nanoporous membrane was integrated into the wall of a microchannel, thereby increasing the exposed area available for ion transport.[14] Based on this result, we anticipated that a 3D electrode could facilitate increased scale in fICP.

We couple this out-of-plane preconcentrator with a bead-based assay for nucleic acids. Electrokinetic enrichment of biomolecules has been shown previously to increase the sensitivity of bead-based immunoassays. Wang et al. reported an approximate 500-fold increase in the sensitivity of R-phycoerythrin protein detection following 30 min of preconcentration followed by a 30 min binding step to antibody-modified particles.[24] In related work, Park and coworkers developed a platform combining dielectrophoretic capture of freely suspended biotin-conjugated beads with ICP based preconcentration step. This approach increased the sensitivity for detection of avidin at biotin-conjugated particles by 3-fold and opened a route to control bead positioning for localized sensor development.[25] Most recently, Lu et al. reported 162-fold enhanced sensitivity for fluorescently-tagged inflammatory cytokines using a silicon nanogap preconcentrator.[26] These results demonstrate that ICP-based preconcentration can enhance the speed and sensitivity of immunoassays, which is advantageous for POC applications. Nevertheless, these assays are limited in scope because they require the analyte to be fluorescent or to be tagged with a fluorescent label.

To address this challenge, Senapati et al. developed a label-free non-optical sensor, which employs ICP itself as a reporting mechanism.[27] Ion selective structures exhibit distinct non-linear current-voltage characteristics (**Scheme 1c**). These authors showed that binding of nucleic acids on the surface of an ion permselective membrane produces a change in ionic current and, in turn, causes a shift in the current-voltage curve (CVC). This sensor was operated by simply incubating the sample with the membrane for a period of 15 min prior to reading the CVC – there was no electrokinetic preconcentration step. This procedure resulted in a detection limit in the range of 10-100 nM for a 27 bp sequence for a 3.5 mm^2 and 1 pM for a 1 mm^2 sensor. Chang and coworkers developed this approach further, demonstrating sensitive and selective detection of four dengue virus serotypes following RNA extraction from blood plasma and amplification by reverse transcriptase polymerase chain reaction (RT-PCR).[28] It is notable that there was still no electrokinetic pre-enrichment step. The LOD for the combination of RT-PCR and the sensor was 100 copies of viral RNA per 1 mL of plasma. The key point is that these detection limits are competitive with fluorescence-based methods but require only simple electrical equipment.

For many such biomedical applications, sensitivity is limited by the volume of fluid that can be ‘swept’ for the analyte within a reasonable timeframe. Fluidic instability is the primary limitation to scaling devices up for increased volumetric throughput. When the channel cross section becomes large, mixing driven by fluid vortices drastically decreases the efficiency of enrichment and separation. To understand how to mitigate this detrimental process, several research groups have proposed theoretical models describing mechanisms for vortex flow formation indicating that the dominant mechanism can vary based on the critical dimensions of microchannel and the concentration of background electrolyte.[29] Experimental approaches have been developed to control vortex formation, including geometric constriction of the fluid in microslits,[20] creation of an alternative current path through the IDZ by coating the channel with a highly conductive polymer,[21] and addition of microposts to augment surface conduction within the IDZ.[20] Chang and coworkers have further demonstrated that increased surface area of a permselective membrane leads to smaller vortices due to a decrease in the current demand per area.[30] Another recent approach is to microstructure the surface of the ion selective membrane.[31] Valença et al. demonstrated that the applied potential that is required to start and sustain electroconvection is strongly affected by the geometry of a membrane, indicating that the position and size of vortices can be controlled.[31] A reduction in the resistance of approximately 50% was demonstrated when using membranes with structure sizes (100 to 400 µm) close to the dimensions of the mixing layer, resulting in more confined microvortices with less lateral motion in comparison to flat membranes. These smaller and confined vortices can suppress the development of larger instabilities. This behavior can be recognized by a signature alteration to the shape of the CVC.[30]

Here, we combine the design principles from these prior studies to achieve stable, high-throughput preconcentration of nucleic acids coupled to in situ, non-optical sensing at probe-modified polystyrene beads. Specifically, we demonstrate that a 3D electrode, comprising a bed of Ag microbeads overlying a Au microband (‘Ag/Au’, **Scheme 2b**,**c**), generates an IDZ, leading to an electric field gradient distributed across the whole cross section of a microchannel. In this system, IDZ formation is driven by neutralization of a buffer cation (blue circle, **Scheme 2a**) by electrochemically generated OH- (red circle, **Scheme 2a**). The formation of small, non-disruptive fluid vortices is supported by microstructuring of this bead bed and its large surface area, which supports decreased current density. To further restrict vortex flow, we employ a secondary bead bed comprised of polystyrene carboxylate (PSC) beads, located upstream of the 3D electrode (‘PSC/Ag/Au’, **Scheme 2d,e**).

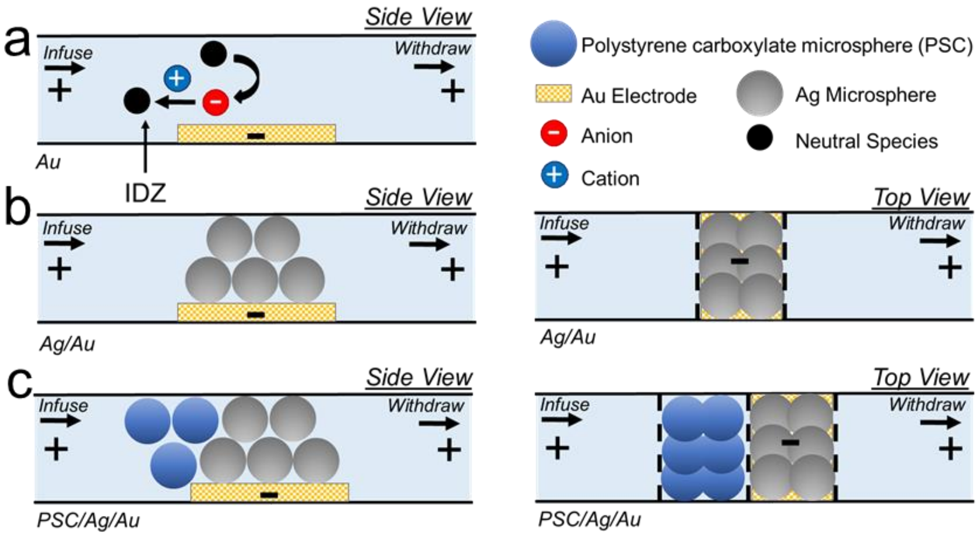

Scheme 2. Side and top views of fICP device designs and operating procedure of a) planar Au; b) Ag/Au and c) PSC/Ag/Au systems.

This secondary bed geometrically confines fluid laminae and enhances surface conduction of ions from the bulk solution to the electrode. We compare these device designs to one having a conventional planar Au electrode (‘Au’, **Scheme 2a**). We first evaluate the enrichment of a small molecule fluorophore and a dye-linked protein, at a planar Au electrode, and demonstrate the presence of three distinct regions in the CVC (as illustrated in **Scheme 1c**). Second, the rate and morphology of IDZ growth, current transients, and the shape of the CVCs are compared for the Au, Ag/Au, and PSC/Ag/Au devices. These experiments show that the bead bed designs facilitate formation of both an IDZ that fills the channel cross section and small fluid vortices that support overlimiting current. Next, we observed that the rate of enrichment of a small molecule fluorophore is greater in both bead bed designs but more dramatically for the PSC/Ag/Au – a result, which is attributed to the higher electric field strength within the resistive PSC bead bed. This performance is retained when throughput is doubled by using to a 2X wider PSC/Ag/Au device. Lastly, we employ bioconjugated PSC beads in the PSC/Ag/Au device to facilitate a nucleic acid enrichment. We anticipate that this approach will allow for high-throughput enrichment and in situ electrochemical detection of a wide range of biologically and clinically relevant analytes by simply selecting the appropriate bioconjugated beads.

Results and discussion

Mechanism of faradaic ion concentration polarization. ICP is the simultaneous enrichment and depletion of ions at opposing ends of an ion permselective membrane (e.g., Nafion) when an electric field is applied across it (**Scheme 1a**). A key feature of the IDZ is its low ionic conductivity, which leads to a strong local enhancement of the electric field and formation of an extended electric field gradient along which charged species can be focused based on their migration against opposing convection.[32,33] Depletion can likewise proceed via faradaic (charge transfer) reactions that occur at an electrode – a process called faradaic ICP (fICP) (**Scheme 1b**).[23] fICP is analogous to selective charge transport at a permselective membrane with the exception that the local concentration of the background electrolyte (BGE) is modulated electrochemically. fICP has been demonstrated as an alternative to conventional ICP for separation of particles,[34,35] dielectrophoresis,[12] and enrichment of charged species for analysis,[22,23,36–38] where the latter has been carried out in paper-based POC devices.[39] In these applications, electrochemical reactions are most commonly facilitated by a bipolar electrode (BPE).[40–42] **Scheme 1b** depicts a route to fICP that proceeds via base neutralization of buffer ions comprising the BGE in a single microfluidic channel with an embedded planar BPE. Here, at the BPE cathodic pole, water is reduced to generate OH^- (red circle), which goes on to accept a proton from a buffer cation (blue circle, e.g., $TrisH^+$) to generate a neutral species (black circle, e.g., Tris). The removal of ions of the BGE results in a local decrease in ionic strength and creation of an IDZ, which can extend several hundred microns upstream of the electrode. This cathodic reaction is coupled to an oxidation reaction at the BPE anodic pole.[22] This overall process resembles the transport of a cation from the anodic to cathodic microchannel compartments through a cation selective membrane. Ion depletion has also been carried out at a single pole, such as a membrane-coated electrode in 'half-cell' ICP,[43] or in the current work, at a single cathodic electrode located within a microchannel. A key advantage of fICP is that charge transfer resistance, instead of the ionic resistance of a membrane, dictates the required potential bias and is often lower, allowing a smaller power supply or batteries to be used.

Prior to evaluating enrichment, we confirmed that the IDZ was formed by this mechanism of faradaically-driven acid-base neutralization of buffer ions. In a device with only a planar Au electrode, the presence or absence of an IDZ was determined in three distinct BGE solutions: $Tris \cdot HClO_4$ (40.0 mM, pH 8.3), KNO_3 (10.0 mM) and phosphate buffer (10.0 mM), each spiked with two fluorescent tracers (10 µM $BODIPY^{2-}$ and 300 nM TxRed-BSA). First, we evaluated the CVCs obtained when a series of voltages was applied between driving electrodes, located in the inlet and outlet of the microchannel, and a wire lead connected to the Au microband, which crossed underneath the channel at its midpoint. The details of this experiment are included in the Supporting Information (SI). **Figure S1** is a plot of the CVCs obtained for these three solutions. Ohmic, limiting, and overlimiting regions, corresponding to three distinct slopes were observed only in the Tris buffer solution. This result supports the proposed mechanism because the anions of the other two BGE solutions, NO^{3-} and $HPO_4^{2-}/H_2PO_4^-$, do not react with OH^- to form an uncharged product as does $TrisH^+$.

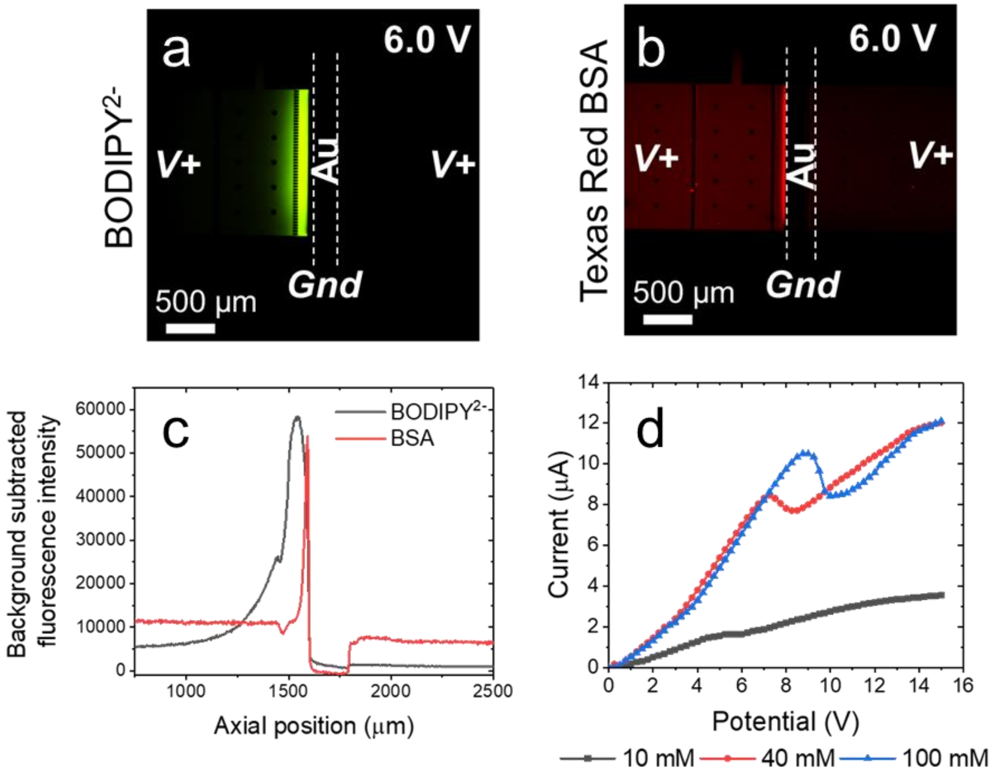

Figure 1. Fluorescence micrographs showing the distribution of a) $BODIPY^{2-}$ and b) dye-linked albumin (Texas Red BSA) in 40 mM Tris buffer (pH 8.3) in a device with a planar Au microband. White dashed lines indicate the position of the microband. These images were obtained at t = 10 min following application of $V+$ = 6.0 V. Flow rate, 100 nL min^{-1} (left to right). The initial concentrations of these two anionic fluorophores were 10 µM $BODIPY^{2-}$ and 0.3 µM dye-linked albumin. c) Background subtracted fluorescence intensities measured along cut lines located across the IDZ boundary in the images shown in (a and b). d) CVCs measured between the Au microband and the driving electrodes in a microchannel filled with 10 (black), 40 (red) and 100 (blue) mM Tris buffer. The voltage was stepped in 0.25 V increments every 0.33 s.

We next evaluated the distribution of the two anionic dyes in these solutions under conditions appropriate for electrokinetic enrichment. First, the channel was filled with the BGE, and then a constant flow rate of 100 nL min^{-1} was established by a syringe pump connected to the inlet reservoir. Next, a voltage bias of $V+$ = 6.0 V was applied between a driving electrode in the microchannel inlet and a wire lead connected to the Au microband. Finally, a series of fluorescence micrographs was obtained to monitor the distribution of the dyes. **Figure 1a** and **1b** are fluorescence micrographs obtained following 10 min of enrichment these dyes in the Tris buffer. The anionic dyes accumulated upstream of the microband, indicating that an IDZ and electric field gradient have formed. Since each dye is focused at an axial location at which its electrophoretic and convective velocities are equal, but opposite, BODIPY^{2-}, which has a higher electrophoretic mobility, forms an enriched plug further upstream than does the dye-linked albumin (**Figure 1c**). Focusing of these dyes by fICP was not observed in KNO_3 or phosphate buffer solutions. However, the dye-linked albumin accumulated upstream of the Au microband cathode in KNO_3 solution – a result attributed to isoelectric focusing of the protein following the formation of a pH gradient (**Figure S2**).

We next investigated CVC characteristics obtained at a planar Au electrode as a function of the concentration of Tris buffer. Resistance dictated by ion transport to the electrode or by charge transfer reactions can be observed in the CVC (**Scheme 1c**).[30,44,45] At low voltages, current increases linearly with the applied potential bias showing ohmic behavior (*i*). A further increase in applied voltage leads to ion depletion at the cathodic microband, and the current reaches a limiting value that is reflected by a sharp decrease in the slope of the CVC (*ii*). Here, increasing voltage leads to growth of the resistive IDZ, preventing further gains in current. At high voltages, rapid vortex flow is initiated within the IDZ leading to a sudden increase in the slope of the CVC, called the overlimiting region (*iii*).

Figure 1d shows CVCs obtained in 10.0, 40.0 and 100.0 mM Tris buffer under low flow conditions (10 nL min^{-1}) in a device with a planar Au microband. Each curve exhibits clear variations in the slope that delineate the three characteristic regimes. A shift in the onset of limiting and overlimiting behavior to higher voltages is observed with increasing Tris buffer concentration, which is in qualitative agreement with previously published results for nanoporous membranes and nanochannels.[46,47]

3D structures for fICP. Next, we compared IDZ formation at this planar Au electrode to devices with a three-dimensional electrode in the absence (Ag/Au) and presence (PSC/Ag/Au) of an additional PSC bead bed. Previous studies have shown that microstructured ion selective features with increased conductive or geometric heterogeneities reduce the limiting-current window, and have localized space charge regions that can sustain corner vortex pairs, and moreover, show increased ion flux with an enhanced field gradient.[30,48]

It was anticipated that placing conductive Ag beads on top of the planar Au electrode would create a 3D flow-through electrode, and that extension into the z-direction would distribute the electric field gradient to the full channel height. Ag-coated microspheres (10-20 μm diameter) are commercially available and the potential for water reduction (to generate OH^-) is comparable on Ag and Au (**Figure S6**, SI). The 300 μm-wide bead bed was defined by a row of narrowly spaced posts (20.0 μm wide with 10.0 μm gaps). The projected area and shape of the IDZ, as visualized with an anionic tracer ($BODIPY^{2-}$), was monitored over time for these three device architectures. **Figure 2a-c** are each a series of fluorescence micrographs showing the distribution of the tracer, at t = 0, 5, 20, and 30 s following application of $V+ = 5.0$ V in planar Au (**Figure 2a**), Ag/Au (**Figure 2b**), and PSC/Ag/Au (**Figure 2c**) devices filled with a solution of 10.0 μM $BODIPY^{2-}$ in 40.0 mM Tris buffer.

Based on qualitative evaluation of these micrographs, the planar Au device exhibits larger vortices, indicated by a larger radius of curvature in the distorted IDZ boundary (**Figure**

2a). In the Ag/Au device (**Figure 2b**), smaller vortices are observed (many vortices with small radius of curvature) and the IDZ boundary has a more uniform shape.

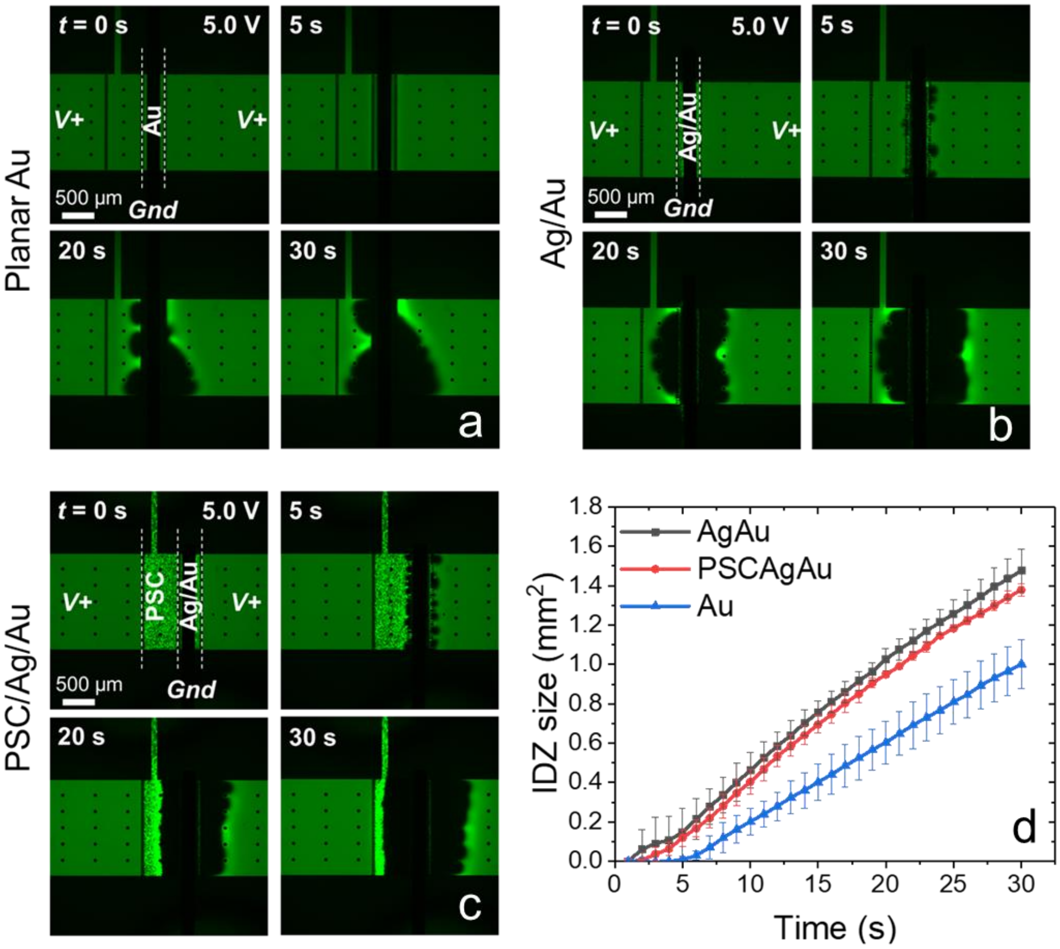

Figure 2. Fluorescence micrographs demonstrating IDZ growth at a) planar Au, b) Ag/Au and c) PSC/Ag/Au devices under an applied voltage of *V*+ = 5.0 V in a solution of 10 µM BODIPY2- in 40.0 mM Tris buffer (pH 8.3). Flow rate, 10 nL min-1 (left to right). d) IDZ growth as a function of time in planar Au (blue), AgAu (black), and PSC/Ag/Au (red) devices under the same conditions (n = 3 separate devices for each). White dashed lines indicate the position of the electrode and PSC bead bed.

Additionally, based on measurements of the projected area of the IDZ (**Figure 2d**), the onset time for stable IDZ growth is earlier for Ag/Au (1 s) versus the planar Au system (5 s). We attribute this lag to the time required for the IDZ to extend to the full height of the channel (z-direction) before propagating upstream and downstream from the electrode.

Next, we added secondary bead bed PSC microspheres (20 µm diameter) to confine the vortices and to facilitate surface conduction of ions to the electrode. **Figure 2c** is a series of fluorescence micrographs showing the evolution of the IDZ in this PSC/Ag/Au device under an applied potential of 5.0 V. Under these conditions, the IDZ boundary has a stable, plug-like shape and was maintained within the secondary bead bed (did not propagate further upstream). The IDZ growth over time was comparable to the Ag/Au system (compare black and red traces, Figure 2d). An increase in the time to the initiation of ion depletion (to ~2 s) is attributed to an increase in the overall resistance of the device due to the volume occupied by the PSC beads. IDZ growth was also investigated under applied potential of 7.0 and 10.0 V (**Figure S3**, SI) for all device designs. Faster IDZ growth is observed with increased potential and difference in IDZ growth decreases between device designs. Additionally, further stabilization of IDZ boundary can be achieved by flanking the 3D electrode from both sides with secondary structures of bead beds (SI). However, by adding secondary bead beds, overall resistance of the device increases.

Comparison of current transients and CVCs for the three device architectures. **Figure 3a** shows current transients obtained, for all three device architectures, with the microchannel filled with 40.0 mM Tris buffer and under an applied voltage of 7.0 V. The current transient obtained with the planar Au device (blue line, **Figure 3a**) shows a stepwise decay, while both 3D-structured devices exhibit gradual decay (red and black lines, **Figure 3a**). We attribute this stepwise decay to initial growth of the IDZ in the z-direction from the planar electrode until it makes contact with the channel 'ceiling', which leads to a sudden increase in resistance (drop in current), followed by outward propagation.

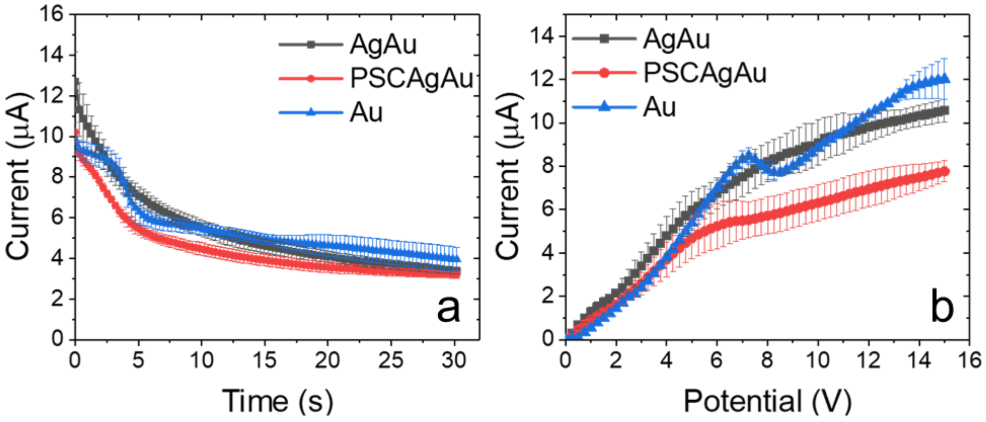

Figure 3. a) Current transients and b) CVCs obtained with planar Au (blue), Ag/Au (black), and PSC/Ag/Au (red) device architectures in 40.0 mM Tris buffer. *V*+ = 7.0 V. Flow rate, 10 nL min^{-1}. In all cases, n = 3 devices.

Next, CVCs were obtained for these device architectures, and the onset potentials and slopes (conductance) of the ohmic, limiting and overlimiting regimes were compared. In the planar Au device, three distinct regimes are observed in the CVC (blue line, **Figure 3b**). In the Ag/Au device (red line, **Figure 3b**), there is a direct transition from the ohmic to overlimiting regime. This absence of limiting behavior has been demonstrated previously in an ICP-based preconcentrator having nanoslit structures.[30] A secondary bead bed (PSC/Ag/Au device) yields a comparable CVC to the Ag/Au device, but the currents are shifted lower due to increased overall resistance (black line, **Figure 3b**).

Enrichment of charged species under constant flow. Having demonstrated the electronic and fluidic properties of these systems, we compared their ability to focus of charged species. In these experiments, first, the channel was filled with 0.1 μM $BODIPY^{2-}$ in 20.0 mM Tris buffer, which was kept under constant flow at 100 nL min^{-1}. Then, a potential of *V*+ = 7.0 V was applied between both driving electrodes and the electrode within the microchannel (planar

Au or bead bed). **Figure 4a**,**b** are fluorescence micrographs showing the enrichment of BODIPY^{2-} in the PSC/Ag/Au device obtained at t = 5 min and 15 min after applying the voltage. **Figure 4c** is a plot of enrichment factor (EF) as a function of time observed in the three device architectures. EF was calculated by comparing the brightest region of the enriched plug (average of 10 neighboring pixels) to the initial fluorescence intensity. Fluorescence intensities were background subtracted. An important point is that the EF of an enriched plug confined to the PSC bead bed was calculated by comparing to the initial intensity measured within the bed. These results indicate that higher EF (up to 115-fold within 15 min) can be obtained by employing the PSC/Ag/Au device, in comparison to Au or Ag/Au, for which EFs of 30 and 40 fold were obtained, respectively. The increased enrichment observed with the addition of a Ag bead-bed electrode to the Au microband is attributed to the full height of the electrode and its stabilization of the IDZ. This difference is expected to become more dramatic as the height of the microchannel (here, 20 μm) is increased. The PSC/Ag/Au device yields a greater increase in the rate of enrichment for two reasons. First, the PSC bead bed provides fluidic stabilization within the entire IDZ volume by geometric restriction and surface conduction mechanisms. Second, both the fluid velocity and the electric field are enhanced in the bead-occupied channel segment due to its increased fluidic and electrical resistance. Dispersion is also expected to be mitigated by the beads.

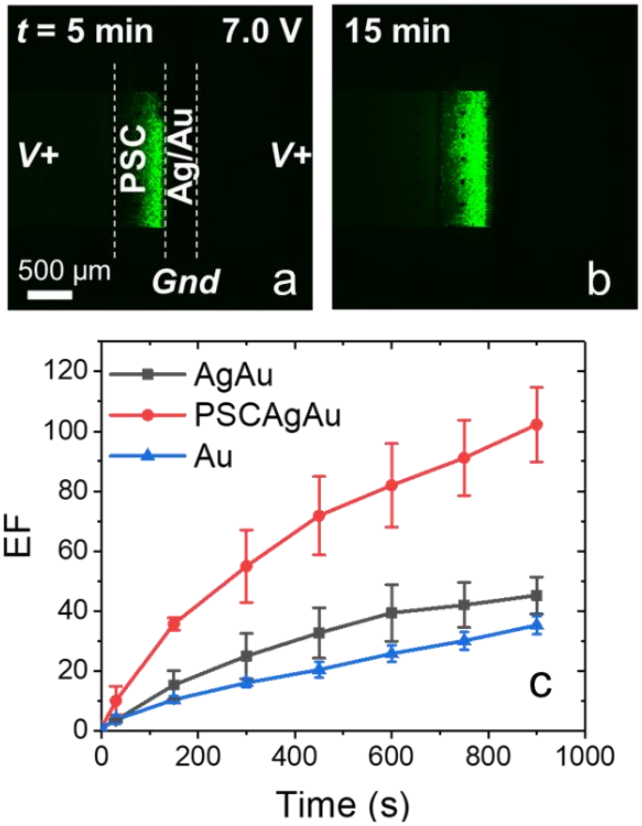

Figure 4. Fluorescence micrographs obtained at a) 5 min and b) 15 min after initiating enrichment of BODIPY^{2-} in the PSC/Ag/Au device. c) A plot showing the evolution of EF over time in the three device architectures: planar Au (blue line), Ag/Au (black line), and PSC/Ag/Au (red line). In all cases, the channel was filled with 0.1 µM BODIPY^{2-} in 20.0 mM Tris buffer (pH 8.3). $V+ = 7.0$ V applied at $t = 0$ s. Flow rate, 100 nL min^{-1}.

Scalability of the PSC/Ag/Au device. We next investigated the impact of device scale on concentration enrichment in the PSC/Ag/Au device. Here, both the flow rate and channel width were doubled to 3.0 mm and 200 nL min^{-1}. The channel was filled with 0.1 µM BODIPY^{2-} in 40.0 mM Tris buffer, and constant fluid flow was established. Then, $V+ = 7.0$ V was applied. **Figure 5a** is a fluorescence micrograph of the resulting enriched band of tracer dye positioned within the PSC bead bed at $t = 450$ s following initiation of the applied voltage. **Figure 5b** shows the evolution of the EF over this time period. The 80-fold enrichment obtained over 450 s is a rate of 0.18-fold/s, which is comparable to the rate (0.13-fold/s) observed in the narrower (1.48

mm-wide) device. This result indicates that out-of-plane fICP is scalable. Over longer periods of time, hydrogen gas bubble formation disrupts the IDZ boundary, which leads to a decrease in the enrichment of charged species. To avoid rapid hydrogen gas formation, a less conductive BGE can be employed. Alternatively, the driving voltage (*V*+) can be applied to the inlet or outlet alone (and the other left floating), instead of being applied to both, so that the bead bed/microband electrode does not have to support the current from both halves of the device.

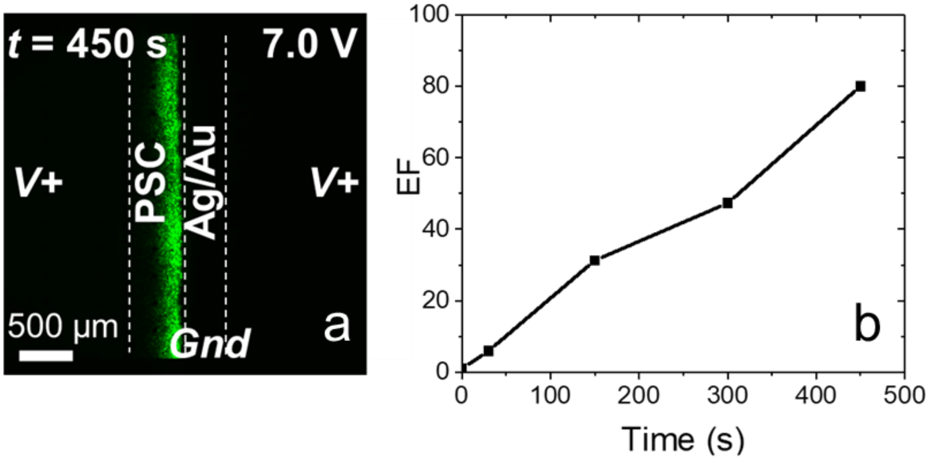

Figure 5. a) Fluorescence micrograph showing an enriched band of BODIPY^{2-} at t = 450 s after initiation of an applied voltage of *V*+ = 7.0 V in the PSC/Ag/Au device. b) Plot of EF as a function of time for the same experiment. Initial concentration, 0.1 µM BODIPY^{2-} in 40.0 mM Tris buffer (pH 8.3). Flow rate, 200 nL min^{-1}.

Electrokinetic enrichment of nucleic acids. The location of the focused band of analyte within the PSC bead bed provides an opportunity to interface concentration enrichment with a bead-based assay. To explore this possibility, we replaced the PSC beads with streptavidin-coated microspheres (15 µm diameter) modified with a biotinylated oligonucleotide probe (1° probe) and performed electrokinetic enrichment of a target ssDNA (210 bases). The targeted gene (BRAF-mut) encodes the BRAF enzyme, which participates in a signaling pathway responsible for cell growth. The V600E mutation leads to increased activity of the BRAF enzyme, and ultimately causes uncontrolled growth and spread of tumor cells. The detection of this mutation in tumor tissue or as circulating tumor DNA (ctDNA) in blood plasma has diagnostic value and is a pharmacodynamic indicator for treatment with drugs that inhibit BRAF enzyme.

The experiment proceeded as follows. First, the channel was filled with 20.0 mM Tris buffer, and a fluorescence image was obtained. Second, the channel was infused with a solution containing 0.4 μM 2° probe and 20 pM BRAF-Mut ssDNA in 20.0 mM Tris buffer ('assay solution') at a flow rate of 100 nL min^{-1}. This flow rate was maintained for 1 h, and then the channel was rinsed with blank solution (20.0 mM Tris buffer) and an additional fluorescence image obtained. No increase in the fluorescence intensity across the secondary bead bed was observed during or after this step. Third, the assay solution was introduced into the channel again, and a constant flow rate of 100 nL min^{-1} was established. Third, $V+$ = 7.0 V was applied between the driving electrodes and the wire lead connected to the Ag bead bed, and accumulation of the FL-tagged 2° probe was monitored by fluorescence microscopy.

Figure 6a is a time series of fluorescence micrographs demonstrating the formation of an enriched plug of the FL-tagged 2° probe within the 1° probe-modified bead bed at t = 1, 30, and 60 min after application of a voltage bias. **Figure 6b** is a plot of the calculated EF as a function of time. 300-fold enrichment of the 2° probe was achieved within 60 min. We anticipate that this approach will further enable the development of an optical and non-optical approach to sense the target DNA following hybridization to the probe-modified beads.

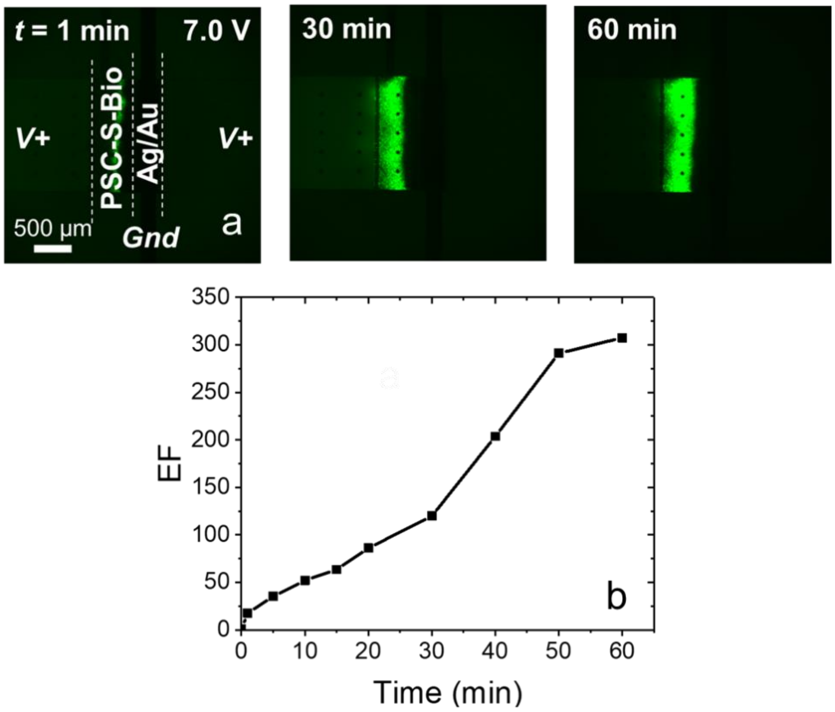

Figure 6. a) Time series of fluorescence micrographs showing co-enrichment of the FL-tagged 2° probe and BRAF-Mut ssDNA at t = 1, 30, and 60 min following initiation of an applied voltage of *V*+ = 7.0 V to a PSC/Ag/Au device, in which the PSC beads were modified with 1° probe. During this experiment, the channel was continuously infused with 0.4 µM 2° probe and 20 pM BRAF-Mut in 20.0 mM Tris buffer (pH 8.3) at 100 nL min^{-1}. b) Plot of EF versus time observed for the 2° probe.

Conclusions

In this article, we have reported several key findings. First, we demonstrated out-of-plane fICP, which employs a 3D flow-through electrode to distribute the IDZ across the entire channel cross section. This result is important because it opens a route for scale-up of fICP-based preconcentrators. Second, we show that the microstructured surface of the Ag bead-bed electrode facilitates overlimiting current through the formation of small, non-disruptive vortices and increased surface area. This advancement allows for increased fluidic stability in the IDZ, preventing unwanted mixing that is detrimental to the enrichment of charged analytes. Third, our results demonstrate that a secondary bead bed further stabilizes the IDZ through geometric confinement of fluid laminae and enhanced surface conduction of ions. Fourth, we show that under conditions appropriate for analyte focusing, higher EFs are achieved with the addition of a Ag bead bed, and more dramatically improved in the device having a secondary bead bed (PSC/Ag/Au). Further, we anticipate that a secondary bed comprising bioconjugated microbeads can be used to tune the developed approach towards in situ quantification of enriched nucleic acids based on either fluorescence or electrical (non-optical) detection. These results will present a significant advancement towards electrokinetically enhanced non-optical sensing in POC applications.

References

1. Breadmore, M. C. Recent Advances in Enhancing the Sensitivity of Electrophoresis and Electrochromatography in Capillaries and Microchips. *Electrophoresis* **2007**, *28*, 254–281.
2. Ouyang, W.; Han, J. Universal Amplification-Free Molecular Diagnostics by Billion-Fold Hierarchical Nanofluidic Concentration. *Proc. Natl. Acad. Sci*. **2019**, *116*, 16240–16249.
3. Song, H.; Wang, Y.; Garson, C.; Pant, K. Concurrent DNA Preconcentration and Separation in Bipolar Electrode-Based Microfluidic Device. *Anal. Methods* **2015**, *7*, 1273–1279.
4. Hong, S. A.; Kim, Y.-J.; Kim, S. J.; Yang, S. Electrochemical Detection of Methylated DNA on a Microfluidic Chip with Nanoelectrokinetic Pre-Concentration. *Biosens. Bioelectron*. **2018**, *107*, 103–110.
5. Wang, Y. C.; Stevens, A. L.; Han, J. Million-Fold Preconcentration of Proteins and Peptides by Nanofluidic Filter. *Anal. Chem*. **2005**, *77*, 4293–4299.
6. Cheow, L. F.; Han, J. Continuous Signal Enhancement for Sensitive Aptamer Affinity Probe Electrophoresis Assay Using Electrokinetic Concentration. *Anal. Chem*. **2011**, *83*, 7086–7093.

7. Jeong, H. L.; Cosgrove, B. D.; Lauffenburger, D. A.; Han, J. Microfluidic Concentration-Enhanced Cellular Kinase Activity Assay. *J. Am. Chem. Soc.* **2009**, *131*, 10340–10341.
8. Cheow, L. F.; Sarkar, A.; Kolitz, S.; Lauffenburger, D.; Han, J. Detecting Kinase Activities from Single Cell Lysate Using Concentration-Enhanced Mobility Shift Assay. *Anal. Chem.* **2014**, *86*, 7455–7462.
9. Marczak, S.; Richards, K.; Ramshani, Z.; Smith, E.; Senapati, S.; Hill, R.; Go, D. B.; Chang, H. C. Simultaneous Isolation and Preconcentration of Exosomes by Ion Concentration Polarization. *Electrophoresis* **2018**, *39*, 2029–2038.
10. Kim, M.; Jia, M.; Kim, T. Ion Concentration Polarization in a Single and Open Microchannel Induced by a Surface-Patterned Perm-Selective Film. *Analyst* **2013**, *138*, 1370.
11. Kwak, R.; Kim, S. J.; Han, J. Continuous-Flow Biomolecule and Cell Concentrator by Ion Concentration Polarization. *Anal. Chem.* **2011**, *83*, 7348–7355.
12. Anand, R. K.; Johnson, E. S.; Chiu, D. T. Negative Dielectrophoretic Capture and Repulsion of Single Cells at a Bipolar Electrode: The Impact of Faradaic Ion Enrichment and Depletion. *J. Am. Chem. Soc.* **2015**, *137*, 776–783.
13. Li, M.; Anand, R. K. Recent Advancements in Ion Concentration Polarization. *Analyst* **2016**, *141*, 3496–3510.
14. MacDonald, B. D.; Gong, M. M.; Zhang, P.; Sinton, D. Out-of-Plane Ion Concentration Polarization for Scalable Water Desalination. *Lab Chip* **2014**, *14*, 681–685.
15. Papadimitriou, V. A.; Segerink, L. I.; Eijkel, J. C. T. Free Flow Ion Concentration Polarization Focusing (FF-ICPF). *Anal. Chem.* **2020**, *92*, 4866–4874.

16. Hong, S. A.; Kim, Y. J.; Kim, S. J.; Yang, S. Electrochemical Detection of Methylated DNA on a Microfluidic Chip with Nanoelectrokinetic Pre-Concentration. *Biosens. Bioelectron*. **2018**, *107*, 103–110.

17. Lee, H.; Choi, J.; Jeong, E.; Baek, S.; Kim, H. C.; Chae, J. H.; Koh, Y.; Seo, S. W.; Kim, J. S.; Kim, S. J. DCas9-Mediated Nanoelectrokinetic Direct Detection of Target Gene for Liquid Biopsy. *Nano Lett*. **2018**, *18*, 7642–7650.

18. Zhang, C.; Sun, G.; Senapati, S.; Chang, H. C. A Bifurcated Continuous Field-Flow Fractionation (BCFFF) Chip for High-Yield and High-Throughput Nucleic Acid Extraction and Purification. *Lab Chip* **2019**, *19*, 3853–3861.

19. Yin, Z.; Ramshani, Z.; Waggoner, J. J.; Pinsky, B. A.; Senapati, S.; Chang, H. C. A Non-Optical Multiplexed PCR Diagnostic Platform for Serotype-Specific Detection of Dengue Virus. *Sensors Actuators, B Chem*. **2020**, *310*, 127854.

20. Kim, K.; Kim, W.; Lee, H.; Kim, S. J. Stabilization of Ion Concentration Polarization Layer Using Micro Fin Structure for High-Throughput Applications. *Nanoscale* **2017**, *9*, 3466–3475.

21. Kim, J.; Cho, I.; Lee, H.; Kim, S. J. Ion Concentration Polarization by Bifurcated Current Path. *Sci. Rep*. **2017**, *7*, 1–12.

22. Hlushkou, D.; Perdue, R. K.; Dhopeshwarkar, R.; Crooks, R. M.; Tallarek, U. Electric Field Gradient Focusing in Microchannels with Embedded Bipolar Electrode. *Lab Chip* **2009**, *9*, 1903–1913.

23. Anand, R. K.; Sheridan, E.; Knust, K. N.; Crooks, R. M. Bipolar Electrode Focusing: Faradaic Ion Concentration Polarization. *Anal. Chem*. **2011**, *83*, 2351–2358.

24. Wang, Y. C.; Han, J. Pre-Binding Dynamic Range and Sensitivity Enhancement for Immuno-Sensors Using Nanofluidic Preconcentrator. *Lab Chip* **2008**, *8*, 392–394.

25. Park, S.; Yossifon, G. Combining Dielectrophoresis and Concentration Polarization-Based Preconcentration to Enhance Bead-Based Immunoassay Sensitivity. *Nanoscale* **2019**, *11*, 9436–9443.

26. Lu, B.; Maharbiz, M. M. Ion Concentration Polarization (ICP) of Proteins at Silicon Micropillar Nanogaps. *PLoS One* **2019**, *14*, 1–17.

27. Senapati, S.; Slouka, Z.; Shah, S. S.; Behura, S. K.; Shi, Z.; Stack, M. S.; Severson, D. W.; Chang, H. C. An Ion-Exchange Nanomembrane Sensor for Detection of Nucleic Acids Using a Surface Charge Inversion Phenomenon. *Biosens. Bioelectron*. **2014**, *60*, 92–100.

28. Yin, Z.; Ramshani, Z.; Waggoner, J. J.; Pinsky, B. A.; Senapati, S.; Chang, H. C. A Non-Optical Multiplexed PCR Diagnostic Platform for Serotype-Specific Detection of Dengue Virus. *Sensors Actuators, B Chem*. **2020**, *310*, 127854.

29. Ouyang, W.; Li, Z.; Ye, X.; Han, J. Theoretical Limits and Scaling Laws for Electrokinetic Molecular Concentration via Ion Concentration Polarization, **2018**, *10*, 15187–15194.

30. Yossifon, G.; Mushenheim, P.; Chang, Y. C.; Chang, H. C. Eliminating the Limiting-Current Phenomenon by Geometric Field Focusing into Nanopores and Nanoslots. *Phys. Rev. E*. **2010**, *81*, 1–13.

31. De Valença, J.; Jõgi, M.; Wagterveld, R. M.; Karatay, E.; Wood, J. A.; Lammertink, R. G. H. Confined Electroconvective Vortices at Structured Ion Exchange Membranes. *Langmuir* **2018**, *34*, 2455–2463.

32. Zangle, T. A.; Mani, A.; Santiago, J. G. Theory and Experiments of Concentration Polarization and Ion Focusing at Microchannel and Nanochannel Interfaces. *Chem. Soc. Rev.* **2010**, *39*, 1014.
33. Mani, A.; Zangle, T. A.; Santiago, J. G. On the Propagation of Concentration Polarization from Microchannel-Nanochannel Interfaces. Part I: Analytical Model and Characteristic Analysis. *Langmuir* **2009**, *25*, 3898–3908.
34. Davies, C. D.; Yoon, E.; Crooks, R. M. Continuous Redirection and Separation of Microbeads by Faradaic Ion Concentration Polarization. *Chem Electro Chem* **2018**, *5*, 877–884.
35. Davies, C. D.; Crooks, R. M. Focusing, Sorting, and Separating Microplastics by Serial Faradaic Ion Concentration Polarization. *Chem. Sci*. **2020**.
36. Perdue, R. K.; Laws, D. R.; Hlushkou, D.; Tallarek, U.; Crooks, R. M. Bipolar Electrode Focusing: The Effect of Current and Electric Field on Concentration Enrichment. *Anal. Chem*. **2009**, *81*, 10149–10155.
37. Knust, K. N.; Sheridan, E.; Anand, R. K.; Crooks, R. M. Dual-Channel Bipolar Electrode Focusing: Simultaneous Separation and Enrichment of Both Anions and Cations. *Lab Chip* **2012**, *12*, 4107.
38. Tallarek, U.; Perdue, R. K.; Crooks, R. M.; Hlushkou, D.; Laws, D. R. Bipolar Electrode Focusing: Simultaneous Concentration Enrichment and Separation in a Microfluidic Channel Containing a Bipolar Electrode. *Anal. Chem*. **2009**, *81*, 8923–8929.
39. Li, X.; Luo, L.; Crooks, R. M. Faradaic Ion Concentration Polarization on a Paper Fluidic Platform. *Anal. Chem.* **2017**, *89*, 4294–4300.
40. Crooks, R. M. Principles of Bipolar Electrochemistry. *Chem Electro Chem* **2016**, *3*, 357–359.

41. Koefoed, L.; Pedersen, S. U.; Daasbjerg, K. Bipolar Electrochemistry—A Wireless Approach for Electrode Reactions. *Curr. Opin. Electrochem.* **2017**, 2, 13–17.
42. Fosdick, S. E.; Knust, K. N.; Scida, K.; Crooks, R. M. Bipolar Electrochemistry. *Angew. Chemie - Int. Ed.* **2013**, *52*, 10438–10456.
43. Kwak, R.; Han, J. Half-Cell Ion Concentration Polarization on Nafion-Coated Electrode. *J. Phys. Chem. Lett.* **2018**, *9*, 2991–2999.
44. Rubinstein, I.; Shtilman, L. Voltage against Current Curves of Cation Exchange Membranes. *J. Chem. Soc. Faraday Trans. 2 Mol. Chem. Phys.* **1979**, *75*, 231–246.
45. Yossifon, G.; Mushenheim, P.; Chang, Y. C.; Chang, H. C. Nonlinear Current-Voltage Characteristics of Nanochannels. *Phys. Rev. E.* **2009**, *79*, 1–9.
46. Kim, S. J.; Wang, Y.-C.; Lee, J. H.; Jang, H.; Han, J. Concentration Polarization and Nonlinear Electrokinetic Flow near Nanofluidic Channel. *Phys. Rev. Lett.* **2007**, *99*, 1–9.
47. Maletzki, F.; Rösler, H. W.; Staude, E. Ion Transfer across Electrodialysis Membranes in the Overlimiting Current Range: Stationary Voltage Current Characteristics and Current Noise Power Spectra under Different Conditions of Free Convection. *J. Memb. Sci.* **1992**, *71*, 105–116.
48. Balster, J.; Yildirim, M. H.; Stamatialis, D. F.; Ibanez, R.; Lammertink, R. G. H.; Jordan, V.; Wessling, M. Morphology and Microtopology of Cation-Exchange Polymers and the Origin of the Overlimiting Current. *J. Phys. Chem. B* **2007**, *111*, 2152–2165.
49. Ascierto, P. A.; Kirkwood, J. M.; Grob, J. J.; Simeone, E.; Grimaldi, A. M.; Maio, M.; Palmieri, G.; Testori, A.; Marincola, F. M.; Mozzillo, N. The Role of BRAF V600 Mutation in Melanoma. *J. Transl. Med.* **2012**, *10*, 1–9.

Supporting Information

This supporting information includes detailed information and procedures regarding 1) device designs and fabrication, 2) verification of the mechanism of fICP, 3) assessment of the projected area and growth rate of the IDZ, 4) collection of current transients and current-voltage curves (CVCs), 5) measurement of the onset potential of water reduction on several distinct electrode materials, 6) electrokinetic enrichment of charged species, and 7) preparation of bioconjugated beads and performance of nucleic acid assays.

Chemicals. The charged fluorophore, BODIPY^{2-} (4,4-fluoro-1,3,5,7,8-pentamethyl-4-bora-3a,4a-diaza-S-indacene-2,6-disulfonic acid, disodium salt) and Texas Red dye-linked bovine serum albumin (Texas Red BSA) were obtained from Invitrogen (Carlsbad, CA). All other solutions were prepared using reagent grade chemicals (Fisher Scientific, Waltham, MA) and diluted with double deionized water (18.2 MΩ·cm, Sartorius Arium Pro, Göttingen, Germany) to desired concentration. Poly(dimethylsiloxane) (Sylgard 184 elastomer kit, Dow Corning Corp., Midland, MI) was used for device fabrication. Polystyrene carboxylate beads (diameter, d = 20 μm) were purchased from Polysciences Inc. (Warrington, PA). Conductive silver-coated hollow glass microspheres (d = 10-20 μm, 0.67 g/cc) were purchased from Cospheric (Santa Barbara, CA). Gold-coated glass slides with a Cr adhesion layer (1” x 3” x 0.40”; 50 Å Cr, 1,000 Å Au) were purchased from Evaporated Metal Films (Ithaca, NY) and were used for fabrication of patterned thin film electrodes.

Fluorescence imaging and data processing. All fluorescence measurements were obtained using an Eclipse Ti-S inverted fluorescence microscope (Nikon Industries, New York, NY) equipped with a digital camera (Orca Flash 4.0, Hamamatsu Corp., Bridgewater, NJ). All images were processed using NIS-Elements 4.6 software (Nikon) and ImageJ (NIH). Fluorescence intensities used for quantitative comparison of IDZ growth and for calculation of EF were background subtracted and processed using MatLab (The MathWorks Inc. Natick, MA) and NIS-Elements 4.6 software.

Device design and fabrication. The microfluidic devices were fabricated using standard photolithographic processes.[1] Channel molds were patterned using negative photoresist (SU-8 2050, Microchem Corp., Westborough, MD) coated on a Si substrate followed by casting with PDMS. Scheme S1 depicts the device design and setup all three device architectures. The main channel was 19.5 µm tall, 11.0 mm long, and 1.48 mm wide. The width of the bead bed was 0.30 mm, and there were 10.0 µm gaps between the posts (20 µm wide) used to retain the bead. Auxiliary channels used for packing the bead beds were 0.20 mm wide and 2.5 mm long. A 1.0 mm diameter biopsy punch was used to create the inlet and outlet reservoirs of the main channel, and the inlet of the auxiliary channels for bead bed packing.

Au electrodes were microfabricated on glass slides using a previously published method.[2] The patterned Au electrode width was 0.2 mm and it was centered at the midpoint of the main channel, underneath the primary (conductive) bead bed. This electrode was sufficiently long to extend out from under the PDMS monolith to make contact to a wire lead. The PDMS layer and glass slide with patterned Au film were treated in an air plasma (PDC-001, Harrick Plasma, Ithaca, NY) for 60 s and then placed in contact to bond. To enhance the bond strength, the device was incubated at 65°C for at least 18 h.

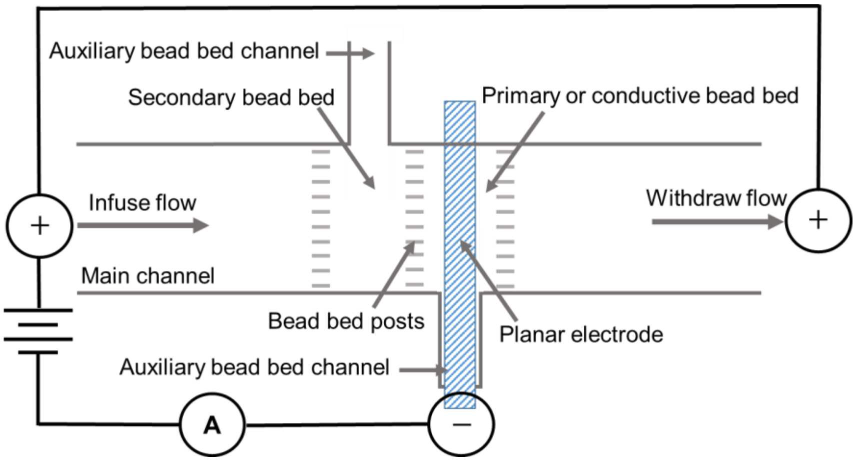

Scheme S1. Schematic representation of the device design near the center of the main channel including the planar electrode, bead beds, and the auxiliary channels employed to pack the beads. The channel segments leading to the inlet and outlet are not depicted. The voltage bias was applied between the driving electrodes (indicated by '+') and the wire lead connected to the planar electrode ('-' sign). The sample solution is infused into the inlet (at left) and withdrawn from the outlet (at right).

A suspension of the conductive Ag-coated beads in DDI (5.0 µL, w/v = 22 mg mL^{-1}) was packed into the primary bead bed by pipetting them into the inlet and applying pressure. When a secondary bead bed was used, a suspension of polystyrene carboxylate (PSC) beads (10 µL, 10 v/v% in DDI) was packed into the inlet of the auxiliary channel of the secondary bead bed using the same method. The inlets of these auxiliary channels were then sealed by adding a drop (approx. 20 µL) of PDMS, which was subsequently cured by incubating the device at 65ºC for 3 h. Devices were filled with buffer at concentration matching that utilized in subsequent experiments prior to use. The driving electrodes were comprised of 1 mm O.D. stainless steel tubing that connected the inlet and outlet of each device to PTFE tubing. An identical device design with increased width of the main channel (3.0 mm), used to demonstrate scalability of out-of-plane fICP devices. The dimensions for both devices are summarized in **Table 1**.

Table 1. Device design dimensions

Device design	Channel width, mm	Channel length, mm	Channel height, µm	Primary or conductive bead bed width, µm	Secondary bead bed with, µm	Gap between bead bed posts, µm
1	1.48	11.0	19.5±0.5	300	500	10
2	3.00	11.0	19.8±0.5	300	500	10

Verification of IDZ generation by the fICP mechanism. In these experiments, the microchannel was rinsed for 20 min with Tris buffer before filling the inlet reservoir with 10.0 µL of running solution (see the following paragraph), spiked with 0.3 µM Texas Red BSA and 10 µM BODIPY2-. Prior to use, devices were conditioned at 3.0 V for 5 min, at 200 nL min^{-1}. Flow was established using two syringe pumps (Pump 11 PicoPlus Elite, Harvard apparatus, Holliston, MA), each of which were equipped with a glass syringe (500 µL) connected to the device with 1.0 mm i.d. PTFE tubing. Importantly, uniform pressure driven flow was ensured by setting one pump to infuse into the inlet and the other pump to withdraw from the outlet reservoir. For IDZ growth measurements, the flow rate was decreased to 10 nL min^{-1} allowing the flow to equilibrate for 10 min. Then, a potential between 0 V and 15.0 V was applied (6487 Picoammeter/Voltage source, Keithley, Cleveland, OH) and the current measured between the driving electrodes and Au microband. The current was recorded using ExceLINX (Keithley, Cleveland, OH) software. After each trial, the device was rinsed thoroughly with DDI, followed by running solution.

The running solutions tested include KNO_3 (10.0 mM, 1588 µS cm^{-1}), phosphate buffer (10.0 mM, pH 7.4, 2642 µS cm^{-1}), Tris buffer (10.0 mM, pH 8.3, 260 µS cm^{-1}), Tris buffer (40.0 mM, pH 8.3, 878 µS cm^{-1}), and Tris buffer (100.0 mM, pH 8.3, 2109 µS cm^{-1}). **Figure S1** depicts CVCs obtained for three different solutions – Tris buffer (40.0 mM), KNO_3 (10.0 mM) and phosphate buffer (10.0 mM) using the planar Au device (no beads). **Figure S2** is a fluorescence micrograph obtained when the KNO$_3$ running solution was used. Stacking of dye-linked albumin occurred, which we attribute to isoelectric focusing in a pH gradient generated by water electrolysis at the driving and planar Au electrodes. The image was obtained at t = 180 s after applying the driving voltage (6.0 V, flow rate 100 nL min^{-1}).

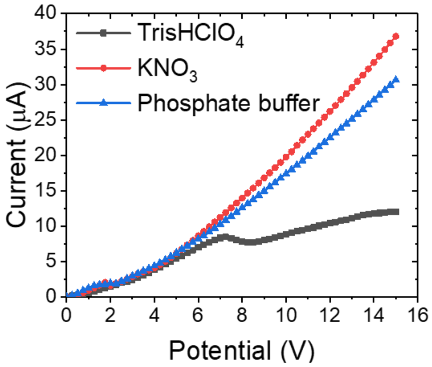

Figure S1. Graph demonstrating current-voltage curves for TrisHClO$_4$ (40.0 mM, black), KNO$_3$ (10.0mM, red) and phosphate (10.0 mM, blue) systems obtained using planar Au electrode device design. Voltage range 0-15.0 V, 0.25 V/step, 0.33s/step. Flow rate 10 nL min^{-1} (infuse, withdraw).

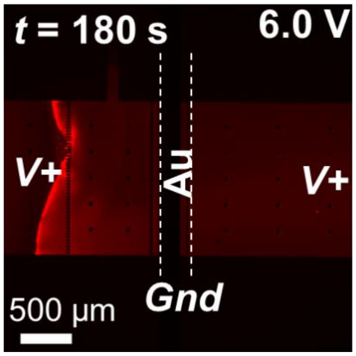

Figure S2. Fluorescence micrograph demonstrating stacking of dye linked albumin in KNO$_3$ solution (10.0 mM), under applied potential of 6.0 V and 100 nL min^{-1} flow rate (infuse, withdraw).

Measurements of IDZ growth over time. To facilitate filling, devices were evacuated in a vacuum desiccator for 20 min prior filling with Tris buffer. Prior to each experiment, the microchannels were rinsed for 20 min with Tris·HClO4 buffer (40.0 mM, pH 8.3). The reservoirs were then filled with 40.0 mM Tris buffer with 10.0 μM BODIPY^{2-}. Prior to use, devices were conditioned for 5 min at 3.0 V under a flow rate of 200 nL min^{-1}. As described in the preceding section, uniform pressure driven flow was ensured using infusion and withdrawal from the inlet and outlet reservoirs, respectively. Prior to IDZ growth measurements, the flow rate was decreased to 10 nL min-1 and allowed to equilibrate for 10 min. To initiate fICP, a voltage bias of 5.0 V was applied and projected area of the IDZ was measured as the region over which the fluorescence intensity was ≤ 0.5-fold the initial fluorescence intensity. These measurements were repeated at a voltage bias of 7.0 and 10.0 V. Between each of these experiments, the device was refreshed by increasing the flow rate to 200 nL min^{-1} for 20 s. The flow rate was once again decreased to 10 nL min-1 and allowed to equilibrate for 10 min, before initiating the next experiment. All image sequences were processed using a MatLab program developed in-house. **Figure S3a-b** demonstrate IDZ growth over time using planar Au, Ag/Au and PSC/Ag/Au devices, repeated in three individual microfluidic devices for each of the device architectures. The plots of IDZ growth obtained at 5.0 V are shown in the main manuscript (**Figure 2**). **Figure S4** shows IDZ growth in a device having two secondary (PSC) bead beds flanking the Ag/Au electrode.

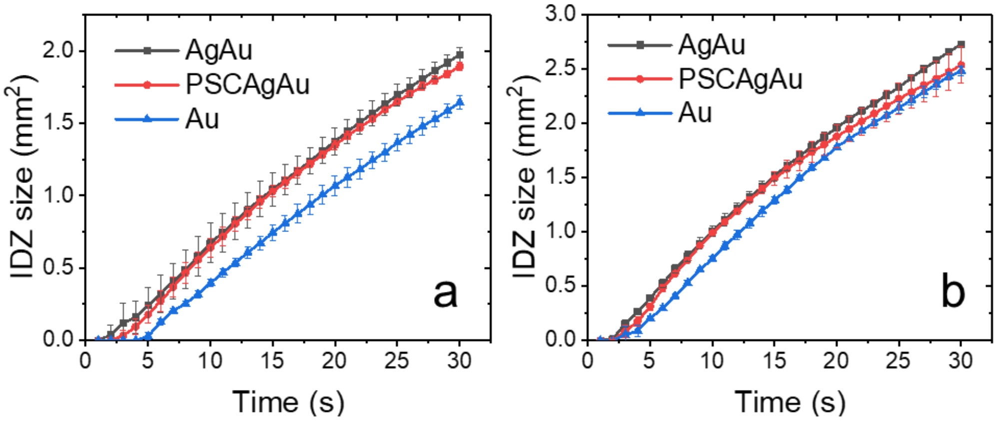

Figure S3. Graphs demonstrating IDZ growth over time measurements for planar Au (blue), PSC/Ag/Au (red), and Ag/Au (black) devices at flow rate of 10 nL min^{-1}, and applied potential of a) 7.0 V, b) 10.0 V.

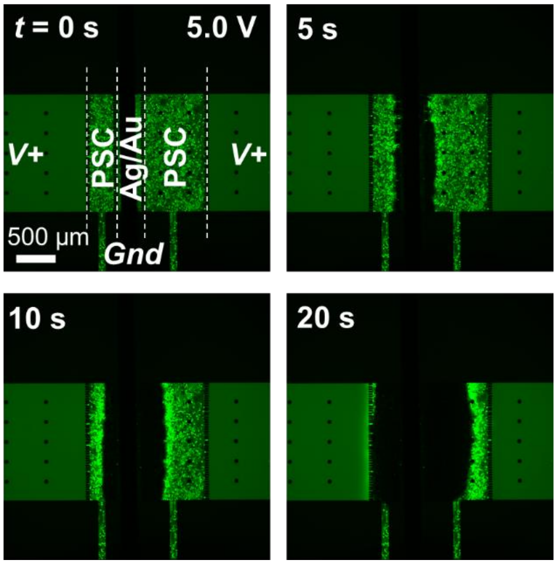

Figure S4. Fluorescence micrographs showing the IDZ at t = 0, 5, 10, and 20 s in a device with two PSC bead beds flanking the Ag/Au electrode. Experimental conditions: 5.0 V, 10 nL min^{-1}, 10.0 µM BODIPY^{2-} in 40.0 mM Tris buffer (pH 8.3).

Measurement of current transients and CVCs. To facilitate device filling, devices were evacuated in a vacuum desiccator for 20 min prior to filling with Tris buffer. Prior to each experiment, the microchannels were rinsed for 20 min with Tris buffer (40.0 mM, pH 8.3). The reservoirs were then filled with 10 µM BODIPY^{2-} in 40.0 mM Tris buffer. **Scheme 2** (main manuscript) depicts the device designs used for measurement of current transients and CVCs. Prior to use, devices were conditioned at 3.0 V for 5 min, at 200 nL min^{-1}. Then, the flow rate was decreased to 10 nL min^{-1} and allowed to equilibrate for 10 min. In between measurements, devices were refreshed by increasing the flow rate to 200 nL min^{-1} for 20 s, and then decreasing to 10 nL min^{-1} and allowing the flow to equilibrate for 10 min.

Current transients. Measurements proceeded as follows. First, the driving electrodes and Au planar microband were connected by power supply in series with a picoammeter (6487 Picoammeter/Voltage source, Keithley, Cleveland, OH). Second, 5.0 V were applied. The resulting current at the electrode was measured for 30 s using ExceLINX (Keithley, Cleveland, OH) software. Further, the device was rinsed according to the procedure described in the preceding paragraph before repeating at 7.0 and 10.0 V. **Figure S5a-b** shows current transients obtained in three individual devices for each architecture.

Obtaining CVCs. Evaluation of current-voltage relationship for each device architecture proceeded as follows. First, the driving electrodes and planar Au microband were connected by a power supply in series with a picoammeter. Second, a series of voltage steps from 0 V to 20.0 V were applied in 0.25 V increments at a rate of 0.33 s per step. The resulting current at the electrode was using ExceLINX (Keithley, Cleveland, OH) software. Between each CVC, the device was rinsed according to the procedure described in the preceding paragraphs. **Figure 3** (main text) demonstrates CVCs obtained in three individual devices for each of the three device architectures

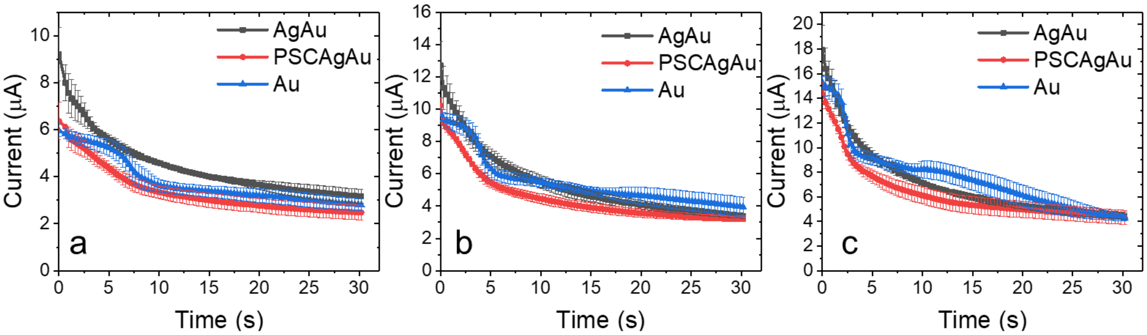

Figure S5. Graphs demonstrating current transients for planar Au (blue), PSC/Ag/Au (red), and Ag/Au (black) devices. Measurements taken at a) 5.0 V, b) 7.0 and c) 10.0 V, Flow rate 10 nL min^{-1}.

Measurement of the potential of water reduction at four electrode materials. A voltammetric study was performed to determine the onset potential for water reduction using four different working electrode materials: Pt disk (d = 3.0 mm), Au disk (d = 3.0 mm), and glassy carbon (GCE) disk (d = 3.0 mm) microelectrodes and a Ag wire (17 mm long, d = 1.0 mm) immersed in 40.0 mM Tris·HClO$_4$ buffer (pH 8.3, 878 μS cm^{-1}).

Voltammetric study. Measurements were recorded using a Pine WaveDriver 20 Bipotentiostat/ Galvanostat (Pine Instruments, Durham, NC, US). The electrochemical cell consisted of the driving electrode (Pt, Au, GCE or Ag wire), Ag/AgCl reference electrode and Pt mesh auxiliary electrode. Prior to experiments, electrodes were polished using a published method[3] and dried with a stream of N_2 gas. To further condition the Au microelectrode, cyclic voltammetric scans (60 scans, 0.50 mV s^{-1}, -0.40 V to 1.75 V vs. Ag/AgCl reference) were performed in a cell containing 0.5 M H_2SO_4 solution.

Onset of water reduction at each working electrode material. 40.0 mM Tris·$HClO_4$ buffer (pH 8.3, 878 µS cm^{-1}) was sparged with N_2 for 15 min. Further, a N_2 stream was positioned above the solution while a linear sweep voltammogram was obtained to observe water reduction. The working electrode was then exchanged for the next material, and N_2 sparging was repeated for 5 min in between the trials. Three sequential voltammograms were recorded, at a sweep rate of 50 mV s^{-1} for each of the working electrodes (**Figure S6**). Onset of water reduction was observed at -0.51 V (Pt), -0.97 V (Au), -0.97 V (Ag), and -1.31 V (GCE).

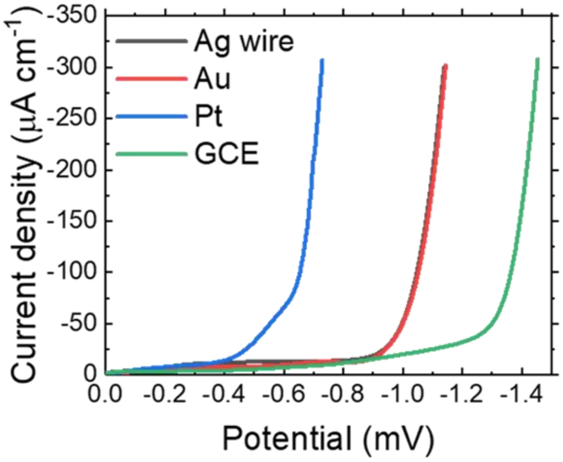

Figure S6. Linear sweep voltammogram obtained for water reduction in 40.0 mM Tris·HClO4 buffer employing various working electrode materials: Pt (blue), glassy carbon (GCE, green), Au (red), and Ag (black) in 3-electrode cell with a Ag/AgCl reference electrode and a Pt mesh counter electrode. Sweep rate, 50 mV s^{-1}.

Charged species electrokinetic enrichment by fICP. To facilitate device filling, devices were evacuated in a vacuum desiccator for 20 min prior to filling with Tris buffer. Prior to experiments, the microchannels were rinsed for 20 min with Tris·$HClO_4$ buffer (20.0 mM, pH 8.3). The reservoirs were then filled with 0.1 µM $BODIPY^{2-}$ in 20.0 mM $TrisHClO_4$. Next, devices were conditioned at 3.0 V for 5 min, at a flow rate of 200 nL min^{-1}. The flow rate was then decreased to 100 nL min^{-1} and allowed to equilibrate for 10 min. Finally, a driving voltage of 7.0 V was applied. Fluorescence micrographs were taken every 30 s for 15 min after initiation of the driving voltage. Fluorescence intensity used for EF calculations was background subtracted. The mean of the 10 pixels with the highest intensity was used to calculate EF. **Figure S7a,b** are two series of fluorescence micrographs obtained at t = 5, 10, and 15 min after applying *V*+ = 7.0 V in a a) planar Au and b) Ag/Au device.

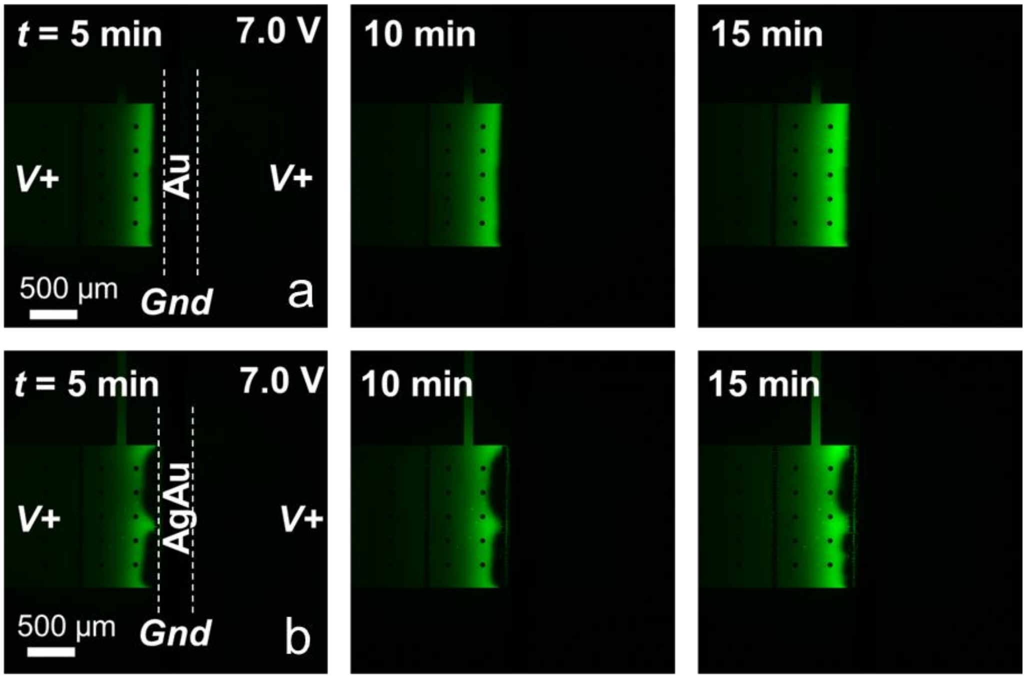

Figure S7. Fluorescence micrographs in a) the planar Au and b) Ag/Au devices filled with $BODIPY^{2-}$ (0.1 µM) in 20.0 mM Tris buffer at t = 5, 10, and 15 min following application of *V*+ = 7.0 V. Flow rate 100 nL min^{-1}.

Electrokinetically enhanced assays for single-stranded nucleic acids at a probe-modified bead bed. Oligonucleotides used in this study were as follows: Biotin-ATATAAAGAAGTACTTCTGGAGTG (1° probe), AGATCGATGTCTCTTTAGAGCTAC-FL (2° probe), and BRAF mutant 5’-TATATTTCTTCATGAAGACCTCACAGTAAAAA TAGGTGATTTTGGTCTAGCTACAGAGAAATCTCGATGGAGTGGGTCCCATCAGTTTG AACAGTTGTCTGGATCCATTTTGTGGATGGTAAGAATTGAGGCTATTTTTCCACTGAT TAAATTTTTGGCCCTGAGATGCTGCTGAGTTACTAGAAAGTCATTGAAGGTCTCAAC TATAGT-3' (BRAF-Mut). All oligonucleotide sequences were purchased from Integrated DNA Technologies (Coralville, IA).

Attachment of biotinylated oligonucleotide to streptavidin coated microspheres. Biotinylated oligonucleotide (1° probe) was bound to the streptavidin-modified beads following a published procedure.[4] First, 100 µL of the bead suspension (Bangs Laboratories, Fishers, IN) was rinsed two times with 100 µL of a wash buffer (20.0 mM Tris buffer, pH 7.5, 1.0 M NaCl, 1.0 mM EDTA, and 0.0005% Triton™ X-100) by centrifuging the beads at 5000 rpm for 3 min, and decanting the supernatant. Second, the beads were resuspended into 20 µL of wash buffer and 7.6 µg of 1° probe. The beads were incubated at 800 rpm (ThermoMixer C, Eppendorf, Hauppauge, NY) for 30 min at 20ºC. Third, unbound 1° probe was removed by rinsing two times with 100 µL of the wash buffer, centrifuging the beads at 5000 rpm for 3 min, and decanting the supernatant. Lastly, these oligo-bound microspheres were re-suspended in 100 µL of wash buffer and stored at 4ºC.

Device design. Microfluidic chips were fabricated according to the procedure described in the first section of this Supporting Information. Instead of PSC beads, oligo-bound microspheres were packed into the secondary bead bed, and the bead-inlet was sealed using

PDMS. It is very important that this PDMS was cured at room temperature overnight to prevent degradation of the modified beads. Prior to use, devices were thoroughly rinsed with DDI (18.2 MΩ·cm), followed by a running solution (20.0 mM Tris·$HClO_4$, 20 pM BRAF-Mut, 0.4 µM 2° probe). Running solution was freshly prepared immediately prior to use.

Electrokinetic nucleic acid enrichment. To facilitate device filling, devices were evacuated under vacuum for 20 min prior to rinsing for 20 min with DDI, followed by Tris·$HClO_4$ buffer (20.0 mM, pH 8.3). Prior to use, devices were conditioned at 3.0 V for 5 min, at 200 nL min^{-1}, and a fluorescence image was obtained. Second, solution containing 0.4 µM 2° probe and 20 pM BRAF-Mut ssDNA in 20.0 mM Tris buffer ('assay solution') at a flow rate of 100 nL min^{-1}. This flow rate was maintained for 1 h, and then the channel was rinsed with blank solution (20.0 mM Tris buffer) and an additional fluorescence image obtained. Third, the assay solution was introduced into the channel again, and a constant flow rate of 100 nL min^{-1} was established. Then, $V+ = 7.0$ V was applied between the driving electrodes and the wire lead connected to the Ag bead bed, and accumulation of the FL-tagged 2° probe was monitored by fluorescence microscopy. Fluorescence micrographs were taken every min for 60 min after the driving voltage was applied. Images obtained at selected time points are shown in **Figure 6** (main text) and in **Figure S8**. This fluorescence intensity was then compared to the background intensity obtained prior to the experiment in the bead bed of the channel when it contained buffer alone.

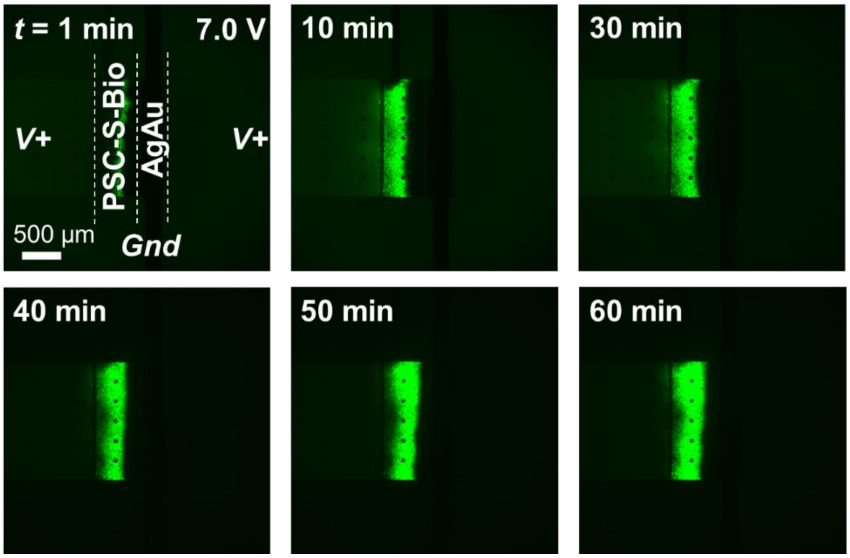

Figure S8. Fluorescence micrographs demonstrating enrichment of fluorescently tagged nucleotides (2° probe) from an initial concentration of 0.4 µM in 20 pM BRAF-Mut and 20.0 mM Tris·$HClO_4$ at t = 1, 10, 30, 40, 50, and 60 min after initiation of *V*+ = 7.0 V. PSC/Ag/Au device containing 1° probe-modified PSC beads. Flow rate, 100 nL min^{-1}.

References

1. McDonald, J. C.; Whitesides, G. M. Poly (Dimethylsiloxane) as a Material for Fabricating Microfluidic Devices. *Acc. Chem. Res*. **2002**, *35*, 491–499.
2. Xia, Y.; Whitesides, G. M. Soft Lithography. *Annu. Rev. Mater. Sci*. **1998**, *28*, 153–184.
3. Elgrishi, N.; Rountree, K. J.; McCarthy, B. D.; Rountree, E. S.; Eisenhart, T. T.; Dempsey, J. L. A Practical Beginner's Guide to Cyclic Voltammetry. *J. Chem. Educ*. **2018**, *95*, 197–206.
4. Fishers, B. L. Streptavidin Coated Microspheres. *Prod. data sheet* **2004**, *No. 721*, 1–3.

CHAPTER 6. GENERAL CONCLUSIONS

In this dissertation, fundamental and practical aspects, relevant to the implementation of ICP and fICP for bioanalytical applications are discussed. The main experimental challenges that prevent broad implementation of ICP, e.g., ICP in high conductivity media, neutral species focusing, fluidic instabilities and mixing in a high electric field, and limited throughput are partially or fully addressed.

The high conductivity of biological fluids results in high currents under an applied electric field, leading to water electrolysis and Joule heating that can damage the sample, electrode, or ion-selective membrane. Previously, this challenge has been addressed by diluting samples with low conductivity electrolytes,[84,85] or by changing the design of the device to prevent contact between biological species and the electrode.[85-87] In this dissertation, an electrokinetic route for the separation of charged from neutral species in highly conductive media (e.g., blood plasma) is reported. The method demonstrates the potential application of this approach for sourcing dialysate fluid from patients' blood plasma. The described microfluidic device reduces the opportunity to damage plasma proteins and prevents electrode biofouling, which is important for the retention of albumin and the successful separation of metabolites during dialysis This latter goal is achieved by using a device design that avoids direct contact between blood plasma and the electrode. Moreover, the same method can be used not only for sourcing excess fluid from patients' blood, but also for the regeneration of spent dialysate. However, for such an electrokinetic approach to become practical for obtaining patient-derived dialysate and dialysate regeneration, a few important challenges needed to be addressed. First, the ICP-based separation will need to undergo considerable scaling to meet the volumetric demands of clinical dialysis, and second, a strategy for the separation of uncharged metabolites will need to be developed as neutral species are unaffected by the electric field, thereby limiting the application of ICP for dialysate regeneration.

In order to attain the extraction of neutral compounds from aqueous solution, a continuous micellar electrokinetic focusing method was established. Neutral species focusing by ICP is achieved by their partition into an ionic micellar phase. Initial results presented in this dissertation demonstrate the dependence of the extraction efficiency on the concentrations of the target compound and the surfactant comprising the micellar phase. Importantly, an ionic micellar phase is generated in situ during ICP focusing, thus reducing the initial concentration of surfactant required. It is anticipated that this approach can be generalized to any intermolecular interaction that would assign charge and change species mobility, thus expanding the applicability of ICP to previously unattainable or low mobility species. The later aspect is a key feature of the established method, relevant to pharmaceutical, biological, and environmental applications.

Lastly, a strategy to decrease the magnitude of the applied potential to drive ICP, increase the stability of ICP, and thereby increase the device throughput, is presented. These challenges are addressed by employing out-of-plane fICP that allows for the reduction of the magnitude of the applied electric field due to the electrochemical mechanism of ion depletion. fICP maintains a high analyte enrichment factor by distributing the depletion zone across the channel cross section using a three-dimensional flow-through electrode. Further, fluid mixing, the primary cause for decreased stability and low throughput in ICP devices, is addressed by using three-dimensional structures comprised from beads located upstream from the electrode. This approach suppresses the limiting current behavior and increases the fluidic stability of the device. However, additional improvements, such as further scale-up of the device and the dimensions of the ion-selective feature, are necessary to suit the requirements of a commercial devices. This goal could be achieved by using 3D-printed microfluidic chips with high surface area biocompatible ion-selective features.[88,89] It is believed that this platform both offers important advantages for POC assay and will enable further advancement of portable dialysate recyclers.

REFERENCES

1. Yamini, Y.; Seidi, S.; Rezazadeh, M. Electrical Field-Induced Extraction and Separation Techniques: Promising Trends in Analytical Chemistry - A Review. *Anal. Chim. Acta* **2014**, *814*, 1–22.
2. Collins, C. J.; Arrigan, D. W. M. A Review of Recent Advances in Electrochemically Modulated Extraction Methods. *Analytical and Bioanalytical Chemistry*. **2009**, *393*, 835–845.
3. Simonet, M.; Morales, G.; Ca, S.; Valca, M. Sample Treatments Improved by Electric Fields. *Trends Anal. Chem*. **2010**, *29*, 158–165.
4. Drouin, N.; Kubáň, P.; Rudaz, S.; Pedersen-Bjergaard, S.; Schappler, J. Electromembrane Extraction: Overview of the Last Decade. TrAC - *Trends Anal. Chem*. **2019**, *113*, 357–363.
5. Huotari, H. M.; Trägårdh, G.; Huisman, I. H. Crossflow Membrane Filtration Enhanced by an External DC Electric Field: A Review. *Chem. Eng. Res. Des*. **1999**, *77*, 461–468.
6. Groenewegen, M. G. M.; van de Merbel, N. C.; Slobodnik, J.; Lingeman, H.; Brinkman, U. A. T. Automated Determination of Weakly Acidic and Basic Pollutants in Surface Water by On-Line Electrodialysis Sample Treatment and Column Liquid Chromatography. *Analyst* **1994**, *119*, 1753–1758.
7. Jajuli, M. N.; Hussin, M. H.; Saad, B.; Rahim, A. A.; Hébrant, M.; Herzog, G. Electrochemically Modulated Liquid-Liquid Extraction for Sample Enrichment. *Anal. Chem*. **2019**, *91*, 7466–7473.

8. Yates, B. J.; Temsamani, K. R.; Ceylan, A.; Öztemiz, S.; Gbatu, T. P.; LaRue, R. A.; Tamer, U.; Mark, H. B. Electrochemical Control of Solid Phase Micro-Extraction: Conducting Polymer Coated Film Material Applicable for Preconcentration/Analysis of Neutral Species. *Talanta* **2002**, *58*, 739–745.
9. Morales, G.; Simonet, B. M. Electrical Field-Assisted Solid-Phase Extraction Coupled On-Line to Capillary Electrophoresis-Mass Spectrometry. *Electrophoresis* **2008**, *29*, 2033–2040.
10. Voeten, R. L. C.; Ventouri, I. K.; Haselberg, R.; Somsen, G. W. Capillary Electrophoresis: Trends and Recent Advances. *Anal. Chem*. **2018**, *90*, 1464–1481.
11. Giordano, B. C.; Copper, C. L.; Collins, G. E. Micellar Electrokinetic Chromatography and Capillary Electrochromatography of Nitroaromatic Explosives in Seawater. *Electrophoresis* **2006**, *27*, 778–786.
12. Dolník, V.; Liu, S.; Jovanovic, S. Capillary Electrophoresis on Microchip. *Electrophoresis* **2000**, *21*, 41–54.
13. Stachowiak, T. B.; Svec, F.; Fréchet, J. M. J. Chip Electrochromatography. *J. Chromatogr. A* **2004**, *1044*, 97–111.
14. Breadmore, M. C. Recent Advances in Enhancing the Sensitivity of Electrophoresis and Electrochromatography in Capillaries and Microchips. *Electrophoresis* **2007**, *28*, 254–281.
15. Jung, B.; Bharadwaj, R.; Santiago, J. G. Thousand-fold Signal Increase Using Field-Amplified Sample Stacking for on-Chip Electrophoresis. *Electrophoresis* **2003**, *24*, 3476–3483.
16. Jung, B.; Bharadwaj, R.; Santiago, J. G. On-Chip Millionfold Sample Stacking Using Transient Isotachophoresis. *Anal. Chem*. **2006**, *78*, 2319–2327.

17. Cui, H.; Horiuchi, K.; Dutta, P.; Ivory, C. F. Isoelectric Focusing in a Poly(Dimethylsiloxane) Microfluidic Chip. *Anal. Chem*. **2005**, *77*, 1303–1309.
18. Humble, P. H.; Kelly, R. T.; Woolley, A. T.; Tolley, H. D.; Lee, M. L. Electric Field Gradient Focusing of Proteins Based on Shaped Ionically Conductive Acrylic Polymer. *Anal. Chem*. **2004**, *76*, 5641–5648.
19. Song, S.; Singh, A. K. On-Chip Sample Preconcentration for Integrated Microfluidic Analysis. *Anal. Bioanal. Chem*. **2006**, *384*, 41–43.
20. Koegler, W. S.; Ivory, C. F. Focusing Proteins in an Electric Field Gradient. *J. Chromatogr. A* **1996**, *726*, 229–236.
21. Ouyang, W.; Han, J. Universal Amplification-Free Molecular Diagnostics by Billion-Fold Hierarchical Nanofluidic Concentration. *Proc. Natl. Acad. Sci*. **2019**, *116*, 16240–16249.
22. Li, M.; Anand, R. K. Recent Advancements in Ion Concentration Polarization. *Analyst* **2016**, *141*, 3496–3510.
23. Perdue, R. K.; Laws, D. R.; Hlushkou, D.; Tallarek, U.; Crooks, R. M. Bipolar Electrode Focusing: The Effect of Current and Electric Field on Concentration Enrichment. *Anal. Chem*. **2009**, *81*, 10149–10155.
24. Tallarek, U.; Perdue, R. K.; Crooks, R. M.; Hlushkou, D.; Laws, D. R. Bipolar Electrode Focusing: Simultaneous Concentration Enrichment and Separation in a Microfluidic Channel Containing a Bipolar Electrode. *Anal. Chem*. **2009**, *81*, 8923–8929.
25. Anand, R. K.; Sheridan, E.; Knust, K. N.; Crooks, R. M. Bipolar Electrode Focusing: Faradaic Ion Concentration Polarization. *Anal. Chem*. **2011**, *83*, 2351–2358.
26. Ghosal, S. Electrokinetic Flow. In Encyclopedia of Microfluidics and Nanofluidics; Li, D., Ed.; Springer US: Boston, MA, **2008**; 496–506.

27. Erickson, D. Electroosmotic Flow (DC). In Encyclopedia of Microfluidics and Nanofluidics; Li, D., Ed.; Springer US: Boston, MA, **2008**; 560–567.

28. Dorfman, K. D. Electrophoresis. In Encyclopedia of Microfluidics and Nanofluidics; Li, D., Ed.; Springer US: Boston, MA, **2008**; 580–588.

29. Jin, X.; Joseph, S.; Gatimu, E. N.; Bohn, P. W.; Aluru, N. R. Induced Electrokinetic Transport in Micro-Nanofluidic Interconnect Devices. *Langmuir* **2007**, *23*, 13209–13222.

30. Ghosal, S. Electrokinetic Flow and Ion Transport in Nanochannels. Encycl. *Microfluid. Nanofluidics* **2013**, *16*, 1–15.

31. You, A.; Be, M. A. Y.; In, I. Surface-Charge-Induced Asymmetric Electrokinetic Transport in Confined Silicon Nanochannels. *Appl. Phys. Lett.* **2005**, *86*, 1–3.

32. Qiao, R.; Aluru, N. R. Scaling of Electrokinetic Transport in Nanometer Channels. *Langmuir* **2005**, *21*, 8972–8977.

33. Qiao, R.; Aluru, N. R. Charge Inversion and Flow Reversal in a Nanochannel Electro-Osmotic Flow. *Phys. Rev. Lett*. **2004**, *92*, 198301.

34. Baldessari, F.; Santiago, J. G. Electrophoresis in Nanochannels: Brief Review and Speculation. *Journal of Nanobiotechnology* **2006**, *4*, 1–6.

35. Pennathur, S.; Santiago, J. G. Electrokinetic Transport in Nanochannels. 1. Theory. *Anal. Chem*. **2005**, *77*, 6772–6781.

36. Pennathur, S.; Santiago, J. G. Electrokinetic Transport in Nanochannels. 2. Experiments. *Anal. Chem*. **2005**, *77*, 6782–6789.

37. Dydek, E. V.; Zaltzman, B.; Rubinstein, I.; Deng, D. S.; Mani, A.; Bazant, M. Z. Overlimiting Current in a Microchannel. *Phys. Rev. Lett*. **2011**, *107*, 1–5.

38. Zaltzman, B.; Rubinstein, I. Electro-Osmotic Slip and Electroconvective Instability. *J. Fluid Mech*. **2007**, *579*, 173–226.

39. Ouyang, W.; Li, Z.; Ye, X.; Han, J. Theoretical Limits and Scaling Laws for Electrokinetic Molecular Concentration via Ion Concentration Polarization. **2018**, *10*, 15187–15194.

40. John, A. S.; P Price, C. Existing and Emerging Technologies for Point-of-Care Testing. *Clin. Biochem. Rev*. **2014**, *35*, 155–167.

41. Kozel, T. R.; Burnham-marusich, A. R. Point-of-Care Testing for Infectious Diseases: Past, Present, and Future. *J. Clin. Microbiol*. **2017**, *55*, 2313–2320.

42. Vashist, S. K. Point-of-Care Diagnostics: Recent Advances and Trends. *Biosensors* **2017**, *7*, 10–13.

43. Market and Market. Point of Care Diagnostics Market by Product (Glucose, Infectious Disease (Hepatitis C, Influenza, Respiratory), Coagulation), Platform (Microfluidics, Immunoassays), Mode (Prescription & OTC), End- User (Hospitals, Home Care) - Global Forecast to 2024. Online-source **2019**, No. MD 2702. www.marketsandmarkets.com/Market-Reports/point-of-care-diagnostic-market-106829185.html.

44. Anand, R. K.; Johnson, E. S.; Chiu, D. T. Negative Dielectrophoretic Capture and Repulsion of Single Cells at a Bipolar Electrode: The Impact of Faradaic Ion Enrichment and Depletion. *J. Am. Chem. Soc.* **2015**, *137*, 776–783.

45. Cheow, L. F.; Sarkar, A.; Kolitz, S.; Lauffenburger, D.; Han, J. Detecting Kinase Activities from Single Cell Lysate Using Concentration-Enhanced Mobility Shift Assay. *Anal. Chem.* **2014**, *86*, 7455–7462.

46. Li, M.; Anand, R. K. Integration of Marker-Free Selection of Single Cells at a Wireless Electrode Array with Parallel Fluidic Isolation and Electrical Lysis. *Chem. Sci*. **2019**, *10*, 1506–1513.

47. Berzina, B.; Anand, R. K. Continuous Micellar Electrokinetic Focusing of Neutral Species Driven by Ion Concentration Polarization. *Lab Chip* **2019**, *19*, 2233-2240.

48. Kim, S.; Ganapathysubramanian, B.; Anand, R. K. Concentration Enrichment, Separation, and Cation Exchange in Nanoliter-Scale Water-in-Oil Droplets. *J. Am. Chem. Soc*. **2020**, *142*, 3196–3204.

49. Choi, J.; Huh, K.; Moon, D. J.; Lee, H.; Son, S. Y.; Kim, K.; Kim, H. C.; Chae, J. H.; Sung, G. Y.; Kim, H. Y.; et al. Selective Preconcentration and Online Collection of Charged Molecules Using Ion Concentration Polarization. *RSC Adv*. **2015**, *5*, 66178–66184.

50. Papadimitriou, V. A.; Segerink, L. I.; Eijkel, J. C. T. Free Flow Ion Concentration Polarization Focusing (FF-ICPF). *Anal. Chem*. **2020**, *92*, 4866–4874.

51. Han, S. Il; Yoo, Y. K.; Lee, J.; Kim, C.; Lee, K.; Lee, T. H.; Kim, H.; Yoon, D. S.; Hwang, K. S.; Kwak, R. High-Ionic-Strength Pre-Concentration via Ion Concentration Polarization for Blood-Based Biofluids. *Sensors and Actuators, B: Chemical*. **2018**, *268*, 485–493.

52. Cheow, L. F.; Ko, S. H.; Kim, S. J.; Kang, K. H.; Han, J. Increasing the Sensitivity of ELISA Using Multiplexed Electrokinetic Concentrator. *Anal. Chem*. **2010**, *82*, 3383–3388.

53. Wang, Y. C.; Han, J. Pre-Binding Dynamic Range and Sensitivity Enhancement for Immuno-Sensors Using Nanofluidic Preconcentrator. *Lab Chip* **2008**, *8*, 392–394.

54. Lee, J. H.; Song, Y. A.; Tannenbaum, S. R.; Han, J. Increase of Reaction Rate and Sensitivity of Low-Abundance Enzyme Assay Using Micro/Nanofluidic Preconcentration Chip. *Anal. Chem*. **2008**, *80*, 3198–3204.

55. Jeong, H. L.; Cosgrove, B. D.; Lauffenburger, D. A.; Han, J. Microfluidic Concentration-Enhanced Cellular Kinase Activity Assay. *J. Am. Chem. Soc*. **2009**, *131*, 10340–10341.
56. Wang, C.; Wang, Y.; Zhou, Y.; Wu, Z. Q.; Xia, X. H. High-Performance Bioanalysis Based on Ion Concentration Polarization of Micro-/Nanofluidic Devices. *Anal. Bioanal. Chem*. **2019**, *411*, 4007–4016.
57. Senapati, S.; Slouka, Z.; Shah, S. S.; Behura, S. K.; Shi, Z.; Stack, M. S.; Severson, D. W.; Chang, H. C. An Ion-Exchange Nanomembrane Sensor for Detection of Nucleic Acids Using a Surface Charge Inversion Phenomenon. *Biosens. Bioelectron*. **2014**, *60*, 92–100.
58. Slouka, Z.; Senapati, S.; Shah, S.; Lawler, R.; Shi, Z.; Stack, M. S.; Chang, H. C. Integrated, DC Voltage-Driven Nucleic Acid Diagnostic Platform for Real Sample Analysis: Detection of Oral Cancer. *Talanta* **2015**, 145, 35–42.
59. Marczak, S.; Senapati, S.; Slouka, Z.; Chang, H. C. Induced Nanoparticle Aggregation for Short Nucleic Acid Quantification by Depletion Isotachophoresis. *Biosens. Bioelectron*. **2016**, *86*, 840–848.
60. Yin, Z.; Ramshani, Z.; Waggoner, J. J.; Pinsky, B. A.; Senapati, S.; Chang, H. C. A Non-Optical Multiplexed PCR Diagnostic Platform for Serotype-Specific Detection of Dengue Virus. *Sensors Actuators, B Chem*. **2020**, *310*, 127854.
61. Jones, B.; Bes, M. Keeping Kidneys. *Bull. World Health Organ*. **2012**, *90*, 718–719.
62. Wanner, C.; Amann, K.; Shoji, T. The Heart and Vascular System in Dialysis. *Lancet* **2016**, *388*, 276–284.
63. Fissell, W. H.; Fleischman, A. J.; Humes, H. D.; Roy, S. Development of Continuous Implantable Renal Replacement: Past and Future. *Transl. Res*. **2007**, *150*, 327–336.

64. Davenport, A. Portable and Wearable Dialysis Devices for the Treatment of Patients with End-Stage Kidney Failure : Wishful Thinking or Just over the Horizon? *Pediatr. Nephrol.* **2015**, *30*, 2053–2060.
65. Gura, V.; Rivara, M. B.; Bieber, S.; Munshi, R.; Smith, N. C.; Linke, L.; Kundzins, J.; Beizai, M.; Ezon, C.; Kessler, L.; et al. A Wearable Artificial Kidney for Patients with End-Stage Renal Disease. *JCI Insight* **2016**, *1*, 1–15.
66. Davenport, A.; Gura, V.; Ronco, C.; Beizai, M.; Ezon, C.; Rambod, E. Articles A Wearable Haemodialysis Device for Patients with End-Stage Renal Failure: A Pilot Study. *Lancet* **2007**, *370*, 2005–2010.
67. Ronco, C.; Davenport, A.; Gura, V. The Future of the Artificial Kidney: Moving towards Wearable and Miniaturized Devices. *Nefrologia* **2011**, *31*, 9–16.
68. Ronco, C.; Fecondini, L. The Vicenza Wearable Artificial Kidney for Peritoneal Dialysis (ViWAK PD). *Blood Purif*. **2007**, *25*, 383–388.
69. Roberts, M.; Ash, S. R.; Lee, D. B. N. Innovative PD Flow and Regeneration. *ASAIO Journal*, **1999**, 372-378.
70. Ronco, C.; La Greca, G. Sorbent Augmented Dialysis Systems. *Hemodial. Technol*. **2002**, *137*, 170–180.
71. Winchester, J. F.; Ronco, C. Sorbent Augmented Hemodialysis Systems: Are We There Yet? *J. Am. Soc. Nephrol*. **2010**, *21*, 209–211.
72. Wester, M.; Gerritsen, K. G.; Simonis, F.; Boer, W. H.; Hazenbrink, D. H.; Vaessen, K. R.; Verhaar, M. C.; Joles, J. A. A Regenerable Potassium and Phosphate Sorbent System to Enhance Dialysis Efficacy and Device Portability: A Study in Awake Goats. *Nephrol. Dial. Transplant*. **2017**, *32*, 951–959.

73. Roberts, M. The Regenerative Dialysis (REDY) Sorbent System. *Nephrology* **1998**, *4*, 275–278.

74. Agar, J. W. M. Review: Understanding Sorbent Dialysis Systems. *Nephrology* **2010**, *15*, 406–411.

75. Bäuerlein, P. S.; Mansell, J. E.; Ter Laak, T. L.; De Voogt, P. Sorption Behavior of Charged and Neutral Polar Organic Compounds on Solid Phase Extraction Materials: Which Functional Group Governs Sorption? *Environ. Sci. Technol*. **2012**, *46*, 954–961.

76. Urbańczyk, E.; Sowa, M.; Simka, W. Urea Removal from Aqueous Solutions—a Review. *J. Appl. Electrochem*. **2016**, *46*, 1011–1029.

77. Michaels, A.; Appleby, A.; Wright, J. Flow through Electrochemical Hemodialysate Regeneration. 4473449, **1985**.

78. Hedayat, A.; Peace, R.; Elmoselhi, H.; Shoker, A. Study of Uremic Toxin Fluxes Across Nanofabricated Hemodialysis Membranes Using Irreversible Thermodynamics. Comput. Struct. *Biotechnol. J*. **2013**, *6*, e201303005.

79. Detrick, R. S.; Mudie, J. D.; Luyendyk, B. P.; Macdonald, K. C. Publishing Group. *Nat. Phys. Sci*. **1973**, *243*, 232.

80. Meng, E., Sheybani, R. Lab on a Chip Insight: Implantable Medical Devices. *Lab Chip* **2014**, *14*, 3233–3240.

81. Wu, J.; Dong, M.; Rigatto, C.; Liu, Y.; Lin, F. Lab-on-Chip Technology for Chronic Disease Diagnosis. *Digit. Med*. **2018**, *1*, 1–11.

82. McAdams, B. H.; Rizvi, A. A. An Overview of Insulin Pumps and Glucose Sensors for the Generalist. *J. Clin. Med*. **2016**, *5*, 1–17.

83. Kim, W.; Kim, K.; Lee, H.; Kim, Y. S.; Lee, J. C.; Sung, G. Y.; Kim, S. J. Nanoelectrokinetic Purification Device for a Continuous Peritoneal Dialysate Recycler. Proc. *IEEE Int. Conf. Micro Electro Mech. Syst*. **2017**, 319–322.

84. Gao, H.; Liu, J. J.; Liu, Y. Q.; Wu, Z. Y. Detection of Urine Protein by a Paper-Based Analytical Device Enhanced with Ion Concentration Polarization Effect. *Microfluid. Nanofluidics* **2019**, *23*, 1–7.

85. Han, S. Il; Yoo, Y. K.; Lee, J.; Kim, C.; Lee, K.; Lee, T. H.; Kim, H.; Yoon, D. S.; Hwang, K. S.; Kwak, R.; et al. High-Ionic-Strength Pre-Concentration via Ion Concentration Polarization for Blood-Based Biofluids. *Sensors and Actuators, B: Chemical*. **2018**, *268*, 485–493.

86. Marczak, S.; Senapati, S.; Slouka, Z.; Chang, H. C. Induced Nanoparticle Aggregation for Short Nucleic Acid Quantification by Depletion Isotachophoresis. *Biosens. Bioelectron.* **2016**, *86*, 840–848.

87. Marczak, S.; Richards, K.; Ramshani, Z.; Smith, E.; Senapati, S.; Hill, R.; Go, D. B.; Chang, H. C. Simultaneous Isolation and Preconcentration of Exosomes by Ion Concentration Polarization. *Electrophoresis* **2018**, *39*, 2029–2038.

88. Farghaly, A. A.; Lam, M.; Freeman, C. J.; Uppalapati, B.; Collinson, M. M. Potentiometric Measurements in Biofouling Solutions: Comparison of Nanoporous Gold to Planar Gold. *J. Electrochem. Soc*. **2016**, *163*, H3083–H3087.

89. Khan, R. K.; Gadiraju, S. P.; Kumar, M.; Hatmaker, G. A.; Fisher, B. J.; Natarajan, R.; Reiner, J. E.; Collinson, M. M. Redox Potential Measurements in Red Blood Cell Packets Using Nanoporous Gold Electrodes. *ACS Sensors* **2018**, *3*, 1601–1608.